



Forschungszentrum Karlsruhe
Technik und Umwelt

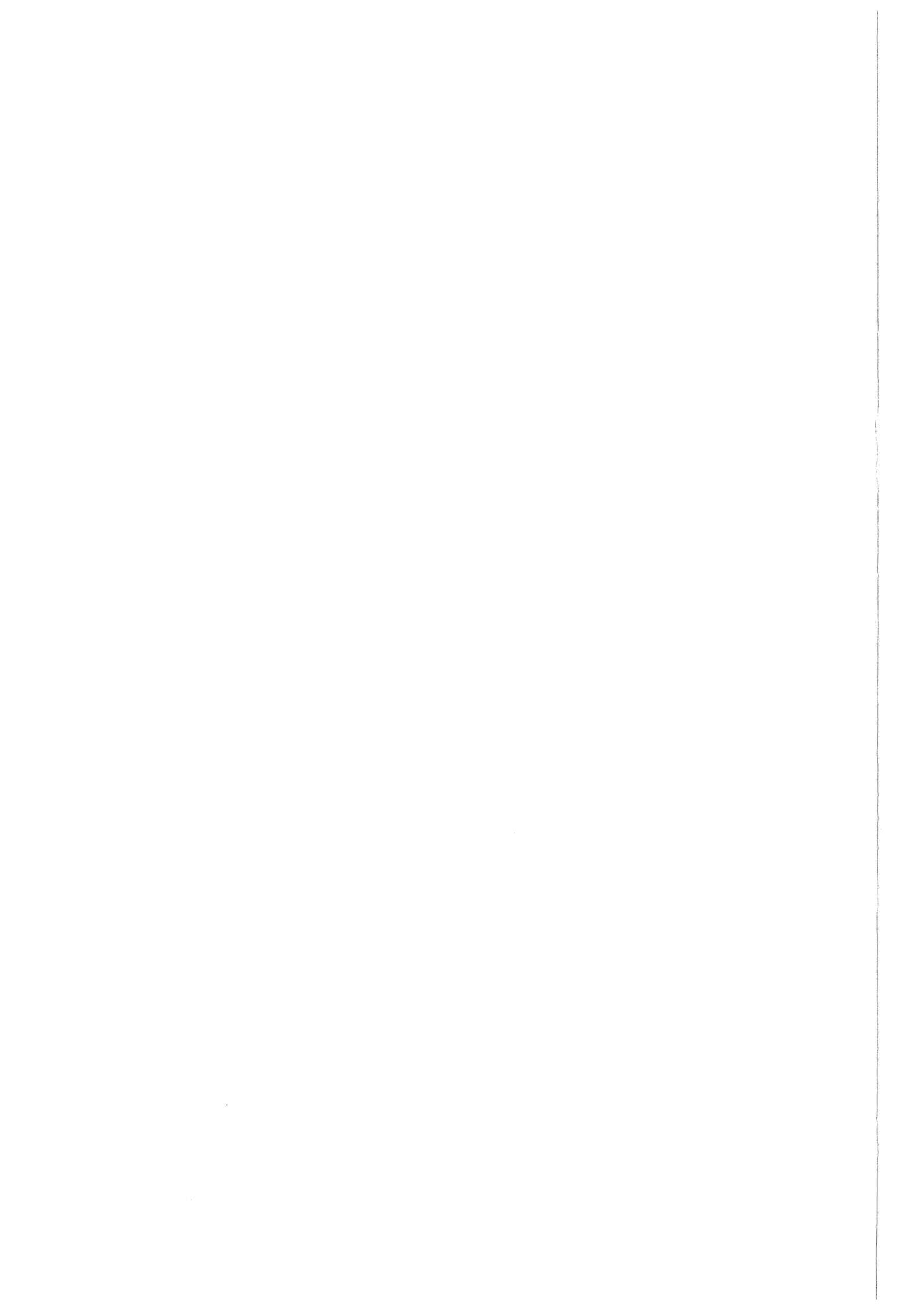
Wissenschaftliche Berichte
FZKA 6358

**Reactor Pressure Vessel
under Severe Accident
Loading (RPVSA)**
**FINAL REPORT of EU-Project
Contract FI4S-CT95-0002**

R. Krieg

Institut für Reaktorsicherheit
Projekt Nukleare Sicherheitsforschung

Dezember 1999



Forschungszentrum Karlsruhe

Technik und Umwelt

Wissenschaftliche Berichte

FZKA 6358

REACTOR PRESSURE VESSEL
UNDER SEVERE ACCIDENT LOADING
(RPVSA)

Final Report of EU-Project
Contract FI4S-CT95-0002

compiled by
Rolf Krieg

Institut für Reaktorsicherheit
Projekt Nukleare Sicherheitsforschung

Als Manuskript gedruckt
Für diesen Bericht behalten wir uns alle Rechte vor
Forschungszentrum Karlsruhe GmbH
Postfach 3640, 76021 Karlsruhe
Mitglied der Hermann von Helmholtz-Gemeinschaft
Deutscher Forschungszentren (HGF)
ISSN 0947-8620

Co-ordinator:

Forschungszentrum Karlsruhe (FZK), Germany

Contractor:

Commissariat à l'Energie Atomique (CEA), France

Ente per le Nuove Tecnologie l'Energia e l'Ambiente (ENEA), Italy

Joint Research Centre of the European Commission (JRC)

Forschungszentrum Jülich (KFA), Germany

Paul Scherrer Institut (PSI), Switzerland

Sub-contractor:

Servizi di Ricerche e Sviluppo (SRS), Italy

Summary and main results

The mechanical behaviour of the reactor pressure vessel strongly influences the environmental consequences of a core melt-down accident. If unfavourable large-scale failure of the vessel could be ruled out, this accident would lose much of its catastrophic character. Therefore, thorough investigations of the most vulnerable parts of the reactor pressure vessel under severe accident loading have been carried out.

In the 1st section the lower vessel head is assumed to be heated intensely by contact with a corium pool. As a result the lower head will undergo a transient temperature rise with very non-uniform spatial distributions causing complex creep deformations and material damage. The main question concerns the possible lower head failure.

In a first step the natural convection and the temperature field in the corium pool as well as the coupled temperature distribution in the lower head has been investigated by extensive computations. Different decay heat levels and heat removal by outside cooling has been assumed. Quite difficult conditions such as a possible pool stratification with an upper metal layer and the formation of a corium crust or partial melting of the lower head have been considered.

The results, obtained for a large range of the Rayleigh number, show strong variation of the heat flux along the pool/vessel interface with a peak near the equatorial region that increases and narrows with increasing Rayleigh number. Usually the corium pool is bounded by a corium crust which hinders the local heat removal significantly, except for the metal layer where no crust is formed and a strong focusing effect occurs with high heat removal. In front of the metal layer local melting of the lower head and high temperature gradients in the remaining structure have been observed. In any case this equatorial section of the lower head is crucial. The temperature distribution in this section has been calculated for various conditions.

In a second step the creep deformation and the resulting material damage in the lower head has been addressed. Because of the strong non-uniform temperature distribution with a very high temperature maximum, basic research was necessary. In the RUPATHER experiments excessive creep deformations and creep rupture of a shell (circular tube) with varying temperature along the shell surface (along the tube axis) and loaded by internal pressure has been investigated. In the FASTHER experiments the corresponding problem with a strong temperature gradient across the shell thickness (across the tube thickness) and a superimposed tangential stretching (axial stretching) has been studied. The results were used as benchmarks to check and improve different computational models.

The strong influence of the temperature field and the need of adequate material parameters are underlined. Constitutive equations covering both, time independent elastic-plastic behaviour and viscoplastic behaviour must be considered. The use of a large strain hypothesis and the updating of the pressure vector with respect to the growing deformation are recommended.

The predicted material damage varied by one order of magnitude. Consequently, the calculations of the failure time was rather inaccurate; in many cases the predicted failure time was too long. Both very simple and more sophisticated failure criteria may yield satisfactory results provided an adequate material data base is available. Here the results of the RUPATHER and FASTHER experiments were very helpful. They could be used to adjust and validate various computational models which now are applicable to the lower head creep rupture problem with more confidence.

In the 2nd section the lower vessel melt-through failure was investigated by the CORVIS experiments, where a high temperature alumina/iron thermite as a corium substitute was poured on a thick steel plate simulating the lower head wall. The decay heating could be simulated by an electric arc submerged in the resulting thermite pool. The results confirmed that oxide melt will form a crust which protects the lower head. Thermally or mechanically induced deformations may cause a gap between the crust and the lower head which reduces the heat flux additionally. Furthermore, the behaviour of nozzles and tubes in the lower head could be studied. It was concluded that the corium may penetrate into such tubes over long distances and that depending on the structural details the tubes may fail due to creep damage.

In the 3rd section the lower head region mechanical processes during a postulated in-vessel steam explosion has been addressed. It will be studied by the model experiments BERDA II. Of special interest is the formation of an upward moving corium slug. The experiments have been prepared and theoretical assessments have been done. Depending on the configuration of the corium located above the core support plate some of the corium will spread in radial direction. Thus only a fraction of the mechanical energy released during the steam explosion will be transferred into kinetic energy of the upward moving slug. A formula to assess this fraction has been developed.

In the 4th section the upper head dynamic response during a postulated in-vessel steam explosion has been investigated by the model experiments BERDA I. Here it is assumed that an upward moving corium slug will impact against the upper head. The corium slug has been simulated by liquid metal. The mitigating influence of the upper internal structures has been considered. Since the development of corresponding computational models is very difficult, the experiments were designed to fulfil essential similarity conditions. Thus the results could be transferred to reactor dimensions using similarity rules.

The application of this method has been checked by the similarity experiments FLIPPER where a simplified liquid structure impact was studied in different scales. It turned out that the deviations from the similarity rules were moderate but the scatter requires attention. For a better interpretation of the BERDA I results various computational models have been applied, among them the code PLEXUS, where the liquid slug is simulated by an assemblage of many discrete particles. The work has been completed by the SKIPPY tests. Major questions of the impact could be answered. It has been confirmed, that detailed computational models are only applicable in cases without upper internal structures.

The results showed that the impact force due to a liquid slug is smaller by a factor 3 – 4 in comparison to a solid slug. The upper internal structures provide a similar reduction. The material properties of these structures which depend on their temperature under accident conditions have only moderate influence.

Requiring that the upper head must not fail such that the containment cannot be endangered by broken head missiles, the admissible (tolerable) corium slug energies could be determined. In the absence of upper internal structures the admissible corium slug energy is 0.1 GJ; if only the upper support grid is available, the value is 0.4 GJ and if the complete structures are present it is 0.8 GJ. Based on the assessments within the 3rd section which are going to be checked by the experiments BERDA II, the tolerable energy releases by a postulated steam explosion are 0.2, 1.0 and 2.0 GJ, respectively. Thus considering that maximum mechanical energy release from an in-vessel steam explosion will hardly exceed 1.0 GJ and that at least the upper support grid should be available, the investigations of this project confirm that the reactor containment will not be endangered by broken head missiles.

In the 5th section the mechanical material properties required for the lower and upper head problem, have been investigated by corresponding material test programs. Results related to the lower head problem indicated a material phase change between 690 and 825°C. It effects the material properties. Dynamic tests related to the upper head problem showed the effect of temperature, strain rate, and specimen size on the stress-strain diagram. The data were used to convert the results of the BERDA tests carried out at room temperature and causing high strain rates to the reactor conditions with elevated temperatures but smaller strain rates according to the scaling rules.

Contents

1. Lower head heated by corium and loaded by quasi-static internal pressure	1
1.1 Analysis of temperature distribution in the lower head	1
1.1.1 Discussion of the problem	1
1.1.2 Objectives	3
1.1.3 Main results	4
1.1.4 Conclusions	5
1.2 Creep experiment RUPATHER	12
1.2.1 Objectives	12
1.2.2 Experimental set-up for RUPATHER	12
1.2.3 Test conditions	14
1.2.4 Temperature control	14
1.2.5 Tube response during the test	14
1.2.6 Conclusions from RUPATHER test #9	18
1.3 Validation of computational models (RUPATHER benchmark)	18
1.3.1 Introduction	18
1.3.2 Table of participants and main options of the FE codes used	18
1.3.3 Predicted uniaxial creep curves at 700°C	20
1.3.4 Thermal loading	21
1.3.5 Diametral deformation	23
1.3.6 Damage evolution	24
1.3.7 Comparison and discussion of the results	28
1.4 Creep experiment FASTHER	30
1.4.1 Test conditions	30
1.4.2 Experimental facility and instrumentation	31
1.4.3 Results	33
1.5 Validation of computational models (FASTHER benchmark)	37
1.5.1 Introduction	37
1.5.2 Thermal loading	37
1.5.3 Global mechanical behaviour	38
1.5.4 Prediction of failure initiation	40
1.5.5 Conclusions from the FASTHER benchmark	43
2. Lower head melt-through failure caused by the attack of molten core material	44
2.1 Melt-through experiments CROVIS	44
2.1.1 Experiment 01/11 (March 28, 1996)	46
2.1.2 Experiment 03/2 (May 30, 1996)	48
2.1.3 Experiment 04/1 (September 19, 1996)	49
2.1.4 Summary of major findings	50
2.2 Validation of computational models	59
2.2.1 Thermal transport within the molten pool	59
2.2.2 Crust formation by freezing of ceramic melt	59
2.2.3 Freezing of ceramic melt in penetration tubes	59
2.2.4 Gap between crust and structures	60

3.	Lower head region loaded by dynamic pressure during a postulated steam explosion	65
3.1	Preparation of the experiments BERDA II to investigate the acceleration of an upward moving corium slug	65
3.2	Analysis of the acceleration of an upward moving corium slug	68
4.	Upper head region loaded by a corium slug impact during a postulated steam explosion	71
4.1	Model experiments BERDA I to determine the admissible kinetic energy of the corium slug	71
4.1.1	Impact of slugs consisting of lead spheres, upper internal structures neglected, test 01 and 02	73
4.1.2	Impact of a solid slug, upper internal structures neglected, test 03	73
4.1.3	Impact of liquid metal slugs, upper internal structures neglected, test 04 to 07 and 09	74
4.1.4	Impact of liquid metal slugs, upper internal structures of original steel considered, test 08, 10, 12 and 15	74
4.1.5	Impact of liquid metal slugs, upper internal structures of red brass considered, test 11, 13 and 16	75
4.1.6	Impact of a liquid metal slug, only an upper support grid of steel considered, test 14	75
4.1.7	Impact of liquid metal slugs, only upper support grid of steel considered, test 17	75
4.1.8	Major findings from the BERDA I tests	75
4.2	Simplified slug impact experiments	87
4.2.1	Similarity experiments FLIPPER	87
4.2.2	Impact tests SKIPPY	88
4.3	Analysis of slug impact and slug penetration	93
4.3.1	Introduction	93
4.3.2	Calculations for BERDA test 07 with the particle model in PLEXUS	93
4.3.3	FLIP: Fluid impact experiment under well known boundary conditions	94
4.3.4	Application of the special code SIMSIC	94
4.3.5	Structural mechanics calculations for interpretation of BERDA tests 07 and 09	95
4.4	Conversion of results from the BERDA scale to the reactor scale	100
5.	Material properties for the lower and the upper head problem	102
5.1	Creep tests	102
5.1.1	Uni-axial tests	102
5.1.2	Tube tests	104
5.2	Dynamic tests	109
5.2.1	Objectives	109
5.2.2	Experimental apparatus	109
5.2.3	Specimens	110
5.2.4	Data elaboration	111
5.2.5	Recorded and calculated data	115
5.2.6	Experimental results – austenitic steel X6CrNiNB1810 (1.4550)	116
5.2.7	Experimental results – ferritic steel 20MnMoNi55 (1.6310)	125

5.2.8 Experimental results – ferritic steel 26NiCrMo146 (1.6958)	134
5.2.9 Experimental results – bronze G-CuSn 12	138
5.2.10 Essential results and conclusions	139
Acknowledgement	140
References	141

1. Lower head heated by corium and loaded by quasi-static internal pressure

C. Caroli and A. Miliozzi, ENEA, Italy; P. Mongabure, L. Nicolas, L. Le Ber, J. Devos and C. Sainte Catherine, CEA Saclay, DRN-DMT-SEMT, France; H. Lämmer, B. Ritter, and C. Tsakmakis, FZK-IMF, Germany; S. Bhandari, FRAMATOME, France; M. Niffenegger and G. Duijvestijn, PSI, Switzerland; P. Dupas and C. Messelier-Gouze, EDF-DER, France

1.1 Analysis of temperature distribution in the lower head

1.1.1 Discussion of the problem

In a severe accident with core melt down in a PWR the lower head will be heavily attacked by the corium. The extent of the attack is a complex function of the corium relocation sequence, of the external vessel cooling during the accident, of the number and position of penetrations in the lower head, of the corium composition and configuration, of the natural convection in the corium pool, of the corium crust and of a possible gap between the crust and the vessel wall. This is a wide spectrum of different phenomena that need different methodologies and capabilities to be analysed. Here we restrict our interest to the molten pool configuration without penetrations in the lower head. Some research has been done in the last decade to analyse this problem and some knowledge has been achieved with substantial confidence on its correctness.

External Cooling – Although during the Three-Miles-Island (TMI) accident no external cooling of the vessel has been provided, it is known that only in case of small amount of relocated material and/or a reduced level of the residual decay power, the vessel wall can withstand the corium thermal attack without external water cooling. When external water cooling is provided its effectiveness is strongly related to the boiling mechanism at the external vessel surface. For nucleate boiling very high heat fluxes can be evacuated with a moderate temperature drop (about 10 – 20 K) between wall and water (i.e. with very low temperature of the external vessel surface). For film boiling a drastic reduction of the heat flux coefficient is observed and high heat fluxes can be evacuated only with a high temperature drop between wall and water normally out of the range of practical interest.

Critical Heat Flux (CHF) distribution – For the above considerations the CHF distribution around the lower head is practically the cooling limit for a vessel under accidental condition. The CHF depends in general on the vessel pit layout and on the external surface of the vessel. Several experimental investigations have been carried out to determine the CHF distribution; El-Genk (1992 and 1996), Theofanous (1995). Considering natural convection of the external cooling water, the CHF has its minimum at the vessel axis and increases toward the equatorial region reaching its maximum at the connection to the cylindrical part of the vessel. The CHF distribution is very useful, because a practical way to analyse the safety margins is to compare the heat flux from the molten pool boundary with the CHF.

Corium crust – The corium has a high melting point whose exact value depends on its composition but in general it is much higher than the steel melting point. For this reason usually the oxide molten pool is totally bounded by a corium crust that avoids direct contact between the vessel wall and the pool and behaves as a protective layer for the vessel. The corium crust has a quite low thermal conductivity and high temperature gradients establish through the corium crust. Its thickness is related to the heat flux level.

Gap between the corium crust and the vessel – The formation of a gap between the corium crust and the vessel wall, as shown in the TMI accident, has a beneficial effect for the vessel. In presence of water in the lower head, the water circulating through the gap cools the

crust and reduces the heat conducted through the vessel wall. In case of a dry lower head the gap behaves as a thermal resistance between the crust and the vessel. The importance of these effects is largely dependent on the gap dimension. Although several experimental and theoretical research activities have addressed the mechanisms of formation of the gap, a general model of the gap evolution does not exist and the gap formation and its dimension are nowadays quite unpredictable. For these reasons many safety analyses leave aside the presence of the gap.

Beside these phenomena some uncertainties are present concerning the configuration assumed for the molten corium and its influence on the vessel behaviour. The corium composition should include oxide as UO_2 or ZrO_2 arising from the melting of the fuel elements and the vessel internals. The density differences between the corium materials could cause the separation of the molten material in two separate layers, the upper essentially composed of light metals, the lower essentially composed of heavy oxide. This hypothesis is also confirmed by some experimental tests carried out within the frame of the RASPLAV project where a partial segregation of the different materials has been observed in the re-solidified corium. However, even if there is not an irrefutable experimental evidence that the debris will form two separate layers, this possibility cannot be completely excluded. Thus the major questions arising are:

- What are the consequences of a stratification on the heat transfer mechanism from the molten pool?
- How is the heat transfer mechanism influenced by the thickness of the upper metal layer?
- What is the decay power distribution between the two layers?
- How does the decay power distribution influence the vessel behaviour?

Some qualitative answers can be given to these questions. An influence of the pool stratification on the heat transfer mechanism is expected especially for the upper part of the pool because of a different convective configuration (two separate convective layers instead of one) and because of different material properties (the upper metal layer will be more conductive than the lower). The stratified configuration can be thought as derived from the homogeneous distribution with the superposition of a metal layer. In this case the lower oxide layer should behave (with minor differences) like the homogeneous pool. The heat evacuated from the upper boundary of this layer is now transferred to the metal layer, and then partially radiated by its upper surface to the upper head and partially transported toward the vessel wall. The heat flux partition between the upper and the lateral boundary of the metal layer will probably depend on the radiating properties of the upper boundary and on the radial heat conduction including the natural convection within the metal layer. Its thickness should thus also influence the heat partition. The decay power distribution in the two layers depends on the distribution of unstable fission products in the upper and the lower layer. If the segregation is driven by density difference, the presence of decaying materials in the upper layer can not be excluded, as also indicated by some experimental work. The determination of the power distribution between the two layers requires refined models of the segregation phenomena that should be supported by an experimental program.

From previous research work on the homogeneous configuration and from the considerations reported above, one can expect that the vessel wall close to the metal layer should undergo the strongest thermal attack. Of course, the presence of decay power in the metal layer should make things worse. All these phenomena, reported here in a qualitative form, need more accurate analysis to quantify the safety margins.

1.1.2 Objectives

The work is aimed to investigate the molten pool behaviour and to point out the main differences between the case of a homogeneous and a stratified molten pool. Of special interest is the molten pool natural convection and the vessel wall thermal attack for different corium configurations. The influence of those physical properties whose values are not always precisely known are investigated by parametric analyses. Special attention is given to the influence that the metal layer thickness and the decay power partition have on the safety margin of a PWR in accidental condition with flooding of the reactor pit. In this way a general methodology is developed for refined analyses of accidental scenarios in a PWR. Intentionally, the analyses are not referred to a particular reactor. Thus the results and conclusions will have a wider validity. The work has been divided in two stages:

First the pure natural convection in hemispherical pools internally heated is analysed, with constant temperature at the boundaries, in homogeneous and stratified configurations and for a wide range of the internal Rayleigh number.

In a successive stage more realistic configurations are considered accounting for the thermal interactions between the vessel and the molten corium, the external water cooling, the corium solidification and the vessel melting.

The first stage is justified by the need of using very refined models to describe the natural convection, characterised in this kind of phenomena by instabilities and strongly influenced by the turbulence. In the real case of a homogeneous molten pool contained in the lower head, the natural convection develops in a pool bounded by the corium crust at a fixed temperature corresponding to the corium melting point. The pure natural convection can therefore be considered as a limit case of the real situation of a homogeneous pool. Focusing the attention on the convection without considering the phase changes and the interactions with the wall, it is possible to analyse in detail the heat flux distribution from the pool boundary, the pool temperature and the velocity fields and their dependence on the Rayleigh number (i.e. their dependence on the corium physical properties, pool dimensions and on the decay power level), and the variation induced in the heat transfer mechanism by the different thermal conductivity of the two layers.

In the second stage the attention is focused on the interactions between pool and vessel and on the effect of the external water cooling. The model has been enriched to account for the phase changes and for the external water cooling but simplified regarding the turbulence models. The cooling transients for a given amount of relocated materials and for a given level of the decay power is analysed for different corium configurations just to point out the consequences on the vessel wall. Penetrations in the lower head are not considered, but they have been intensively investigated by the experimental program CORVIS described in section 2. All the analyses are carried out neglecting the presence of a gap between the corium crust and the vessel and assuming perfect contact. Neglecting the gap is considered to be conservative because it represents a heat resistance between the corium and the vessel as shown in section 2. Furthermore, the residual water circulating through the gap may represent an additional and very effective heat sink that could prevent the thermal attack of the vessel wall. Indications of this effect were found for the TMI accident.

For the necessary fluid-dynamics calculations the conservation equations of mass, momentum and energy have been discretised by a finite element method and solved numerically. For more details on the methodologies used refer to Caroli (1997), Caroli and Magnaud (1997), Caroli and Milillo (1998), Milillio and Caroli (1998). Other investigations are published by Nourgaliev (1997), for instance.

1.1.3 Main results

The pure natural convection analyses have shown the presence of a stable stratification in the lower part of the pool with a quasi isothermal upper pool region, see Fig. 1-1 and 1-2. This behaviour persists for a large range of the Rayleigh number. A strong variation of the heat flux has been observed along the hemispherical pool boundary. The heat flux maximum is located in the upper part of the boundary. Increasing the Rayleigh number the heat flux peak increases and moves toward the equatorial region, see Fig. 1-6.

The coupled analyses of the molten pool and vessel wall give interesting information on the influence that the corium configuration has on the vessel wall. For the same level of decay power in the relocated material (13 MW) and with external water cooling of the lower head we observe a partial melting of the vessel whose extension is strictly related with the corium configuration. In Figs. 1-3 to 1-5 the typical pool and vessel behaviour at the end of the thermal transient is described for four different configurations. From these results the following general conclusion can be drawn:

- The homogeneous pool shows the highest safety margin. In this configuration the molten pool is completely bounded by a corium crust that avoids direct contact with the vessel. The corium crust, thick at the pole and thin near the equator, undergoes a strong variation of the cross heat fluxes along the pool boundary, see Fig. 1-3 and 1-4 (above). The vessel temperature is characterised by an external surface at low temperature (lower than 500 K) and an inner surface that reaches the melting point in a limited section.
- The same decay power distributed in the oxide layer of a stratified pool with a 20 cm thick metal layer, entail a different vessel behaviour, see Fig. 1-3 and 1-4 (below). In this case the behaviour of the oxide layer is similar to the homogeneous pool both in terms of the corium crust and of the convective cells. However, a thermal attack of the vessel is observed in front of the metal layer where a large eddy develops. The vessel temperature is always very low at the external surface where the cooling efficiency is very good, but very high temperature gradients establish across the residual vessel thickness.
- Increasing the metal layer thickness to 40 cm the convection shows qualitatively the same behaviour but no melting of the vessel wall is observed, see Fig. 1-5 (above).
- The heat flux at the external surface of the vessel in case of homogeneous pool shows a regular distribution with a flat maximum. For stratified pools it shows two narrow peaks, one close to the oxide layer and one close to the metal layer, see Fig. 1-7. Depending on the metal layer thickness the highest peak is localised in front of the oxide layer (case of the thick metal layer) or in front of the metal layer (case of the thin metal layer). In both cases the heat flux peaks are higher than for homogeneous pool.
- The presence of a residual power in the metal layer accentuates all the phenomena associated with the layer, see Fig. 1-5 (below). The safety margin is reduced additionally.

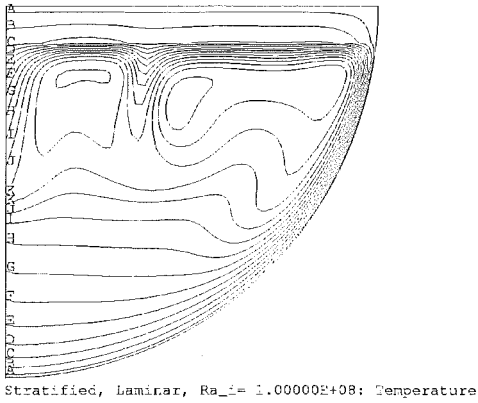
1.1.4 Conclusions

The capability of the vessel to withstand the attack depends, of course, on the amount of relocated material and residual power but it is strongly influenced by the configuration assumed by the corium. If a corium stratification cannot be excluded, safety assessments of the molten pool configuration should account for the consequences that the metal layer has on the vessel behaviour. In the present research a focusing effect has been observed for stratified pool configurations with the thermal attack of the vessel wall preferentially localised in front of the metal layer. This effect increases with a reducing metal layer thickness but the behaviour of very thin metal layer is not yet known and here further investigations are strongly recommended.

Flooding of the pit, no matter how the corium configuration looks like, helps to avoid melt through of the vessel but it induces very strong temperature gradients through the vessel wall. The mechanical behaviour of the vessel under this loading condition has been investigated by the FASTHER experiment section 1.3.

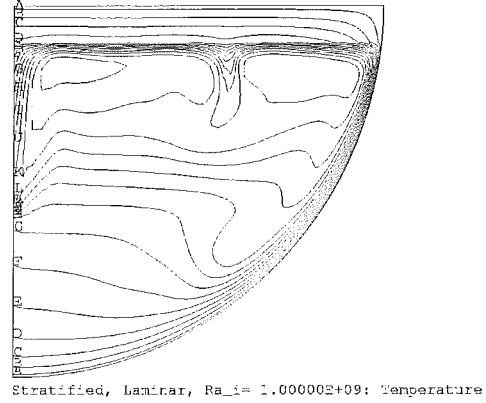
The present research has been developed assuming the absence of a gap between vessel and corium crust. As shown by the CORVIS experiments, section 2, this can be considered as a conservative assumption. Whether a reliable prediction of an isolated gap will ever be possible, is questionable.

RPV under Severe Accident Loading, FINAL REPORT



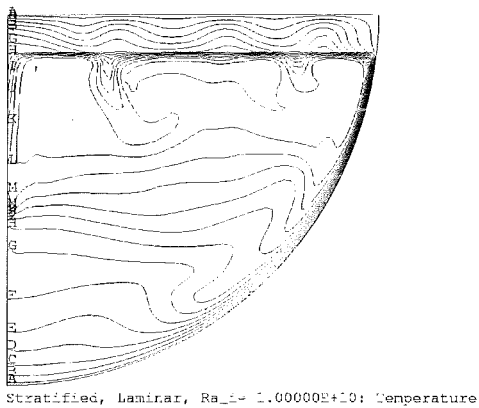
VAL -

A	.25
B	1.76
C	1.11
D	2.22
E	3.33
F	4.44
G	5.55
H	6.66
I	7.77
J	8.88
K	9.99
L	11
M	13



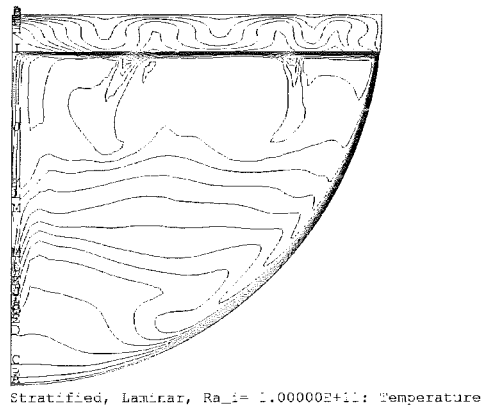
VAL -

A	.36
B	1.76
C	1.11
D	2.22
E	3.33
F	4.44
G	5.55
H	6.66
I	7.77
J	8.88
K	9.99
L	11
M	13



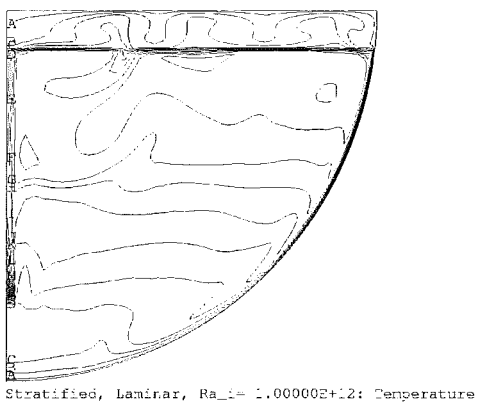
VAL -

A	.47
B	1.11
C	1.11
D	3.33
E	4.44
F	5.55
G	6.66
H	7.77
I	8.88
J	9.99
K	11
L	12
M	13



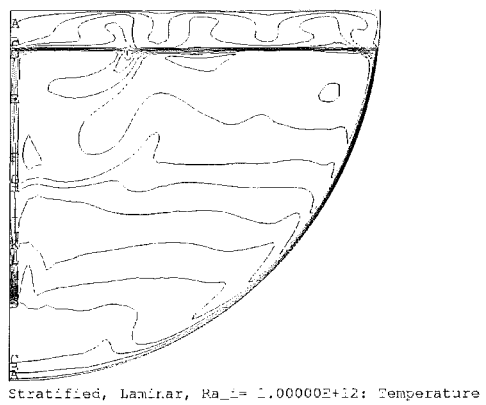
VAL -

A	.63
B	1.11
C	1.11
D	4.44
E	5.55
F	6.66
G	7.77
H	9.99
I	11
J	12
K	13
L	14
M	17



VAL -

A	1.2
B	3.3
C	5.5
D	8.8
E	11
F	13
G	15
H	17
I	20
J	22
K	24
L	27
M	29



VAL -

A	1.2
B	3.3
C	5.5
D	8.8
E	11
F	13
G	15
H	17
I	20
J	22
K	24
L	27
M	29

Fig. 1-1: Temperature distribution (dimensionless) in a stratified molten pool for different Rayleigh numbers

RPV under Severe Accident Loading, FINAL REPORT

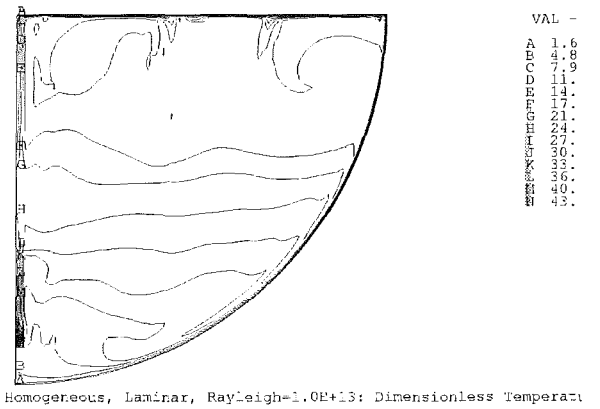
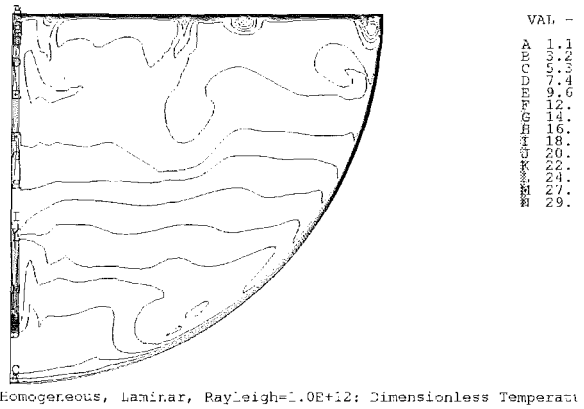
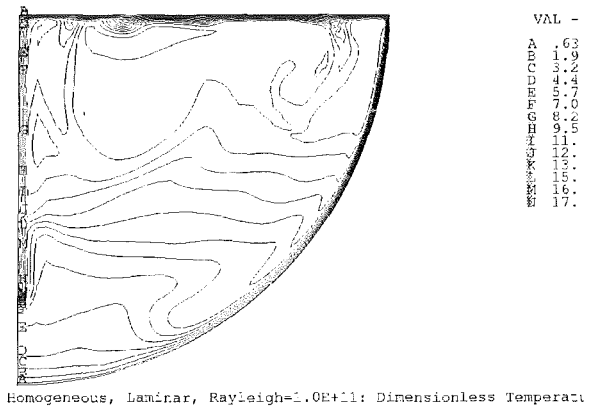
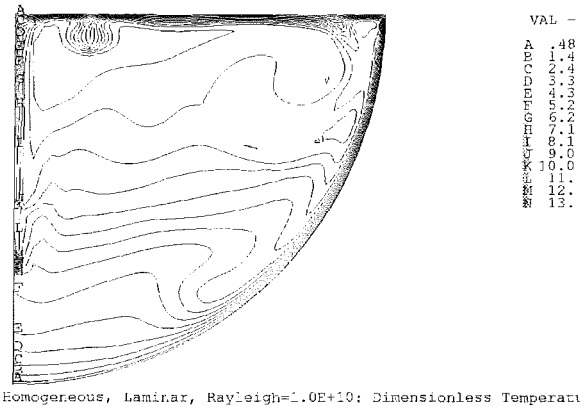
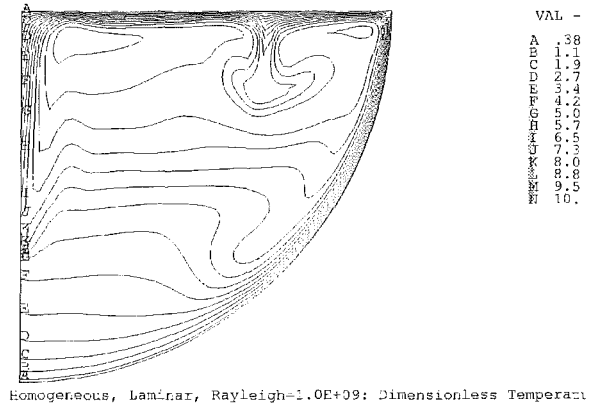
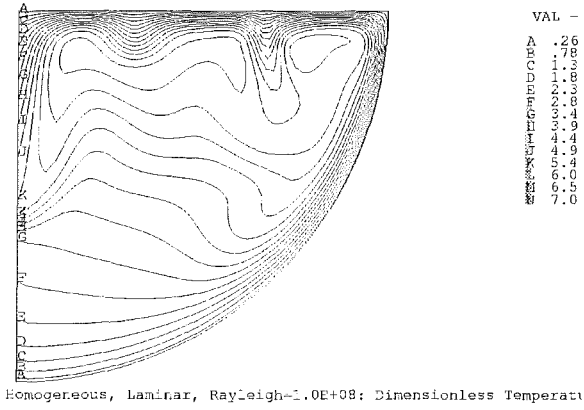


Fig. 1-2: Temperature distribution (dimensionless) in a homogeneous molten pool for different Rayleigh numbers

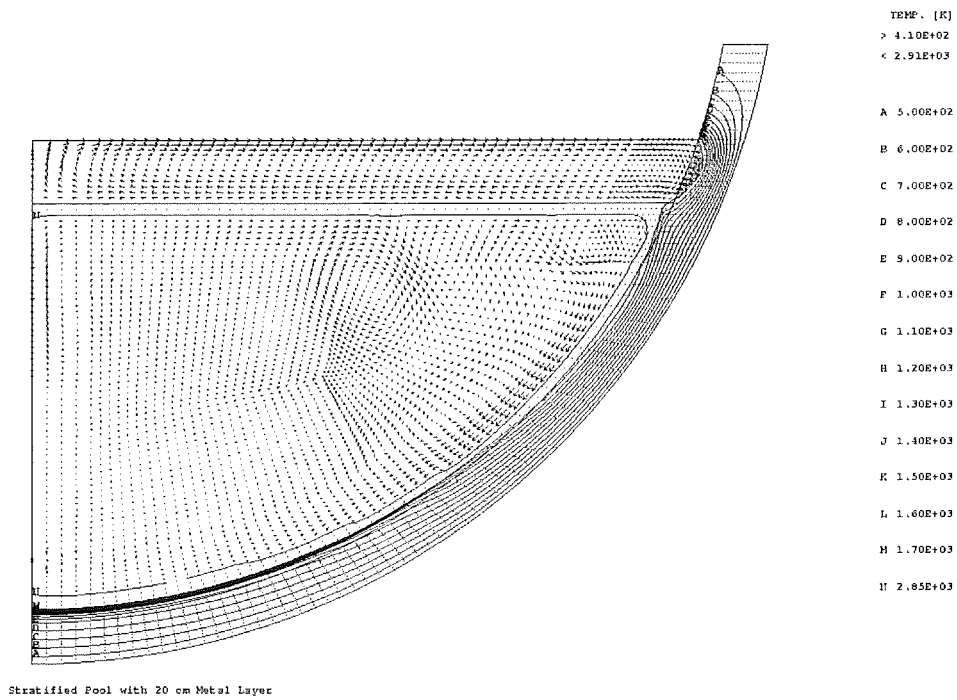
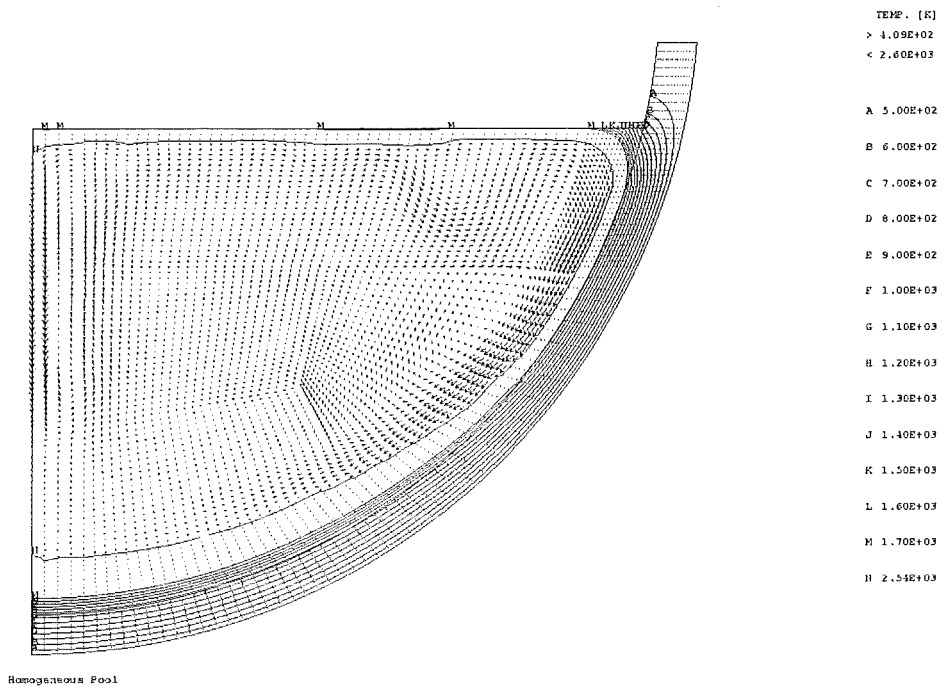


Fig. 1-3: Velocity and temperature fields in a molten pool for a given amount of relocated material and residual power. Homogeneous configuration (above) and stratified configuration with a 20 cm metal layer without residual power in this layer (below).

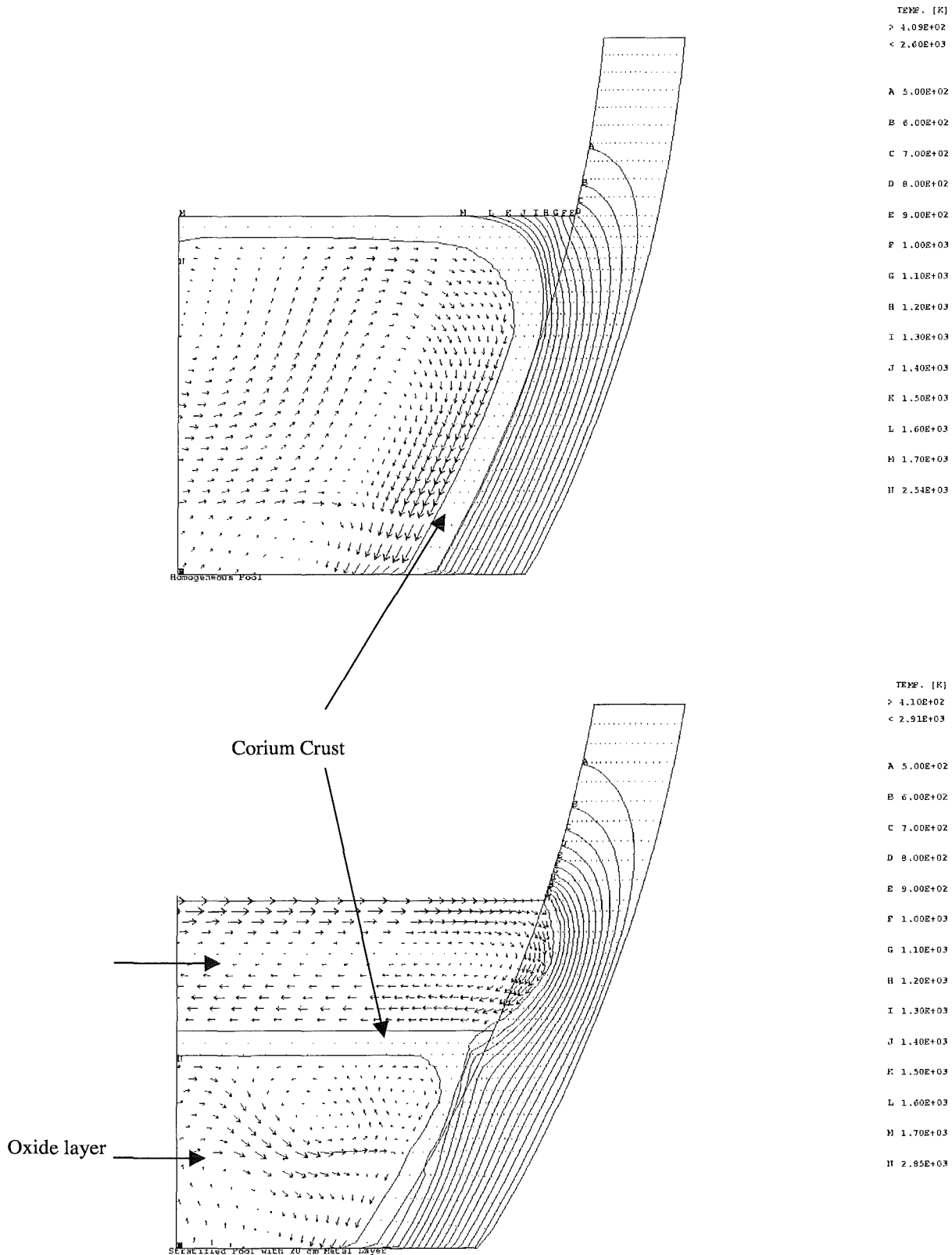


Fig. 1-4: Magnified sections of Fig. 1-3

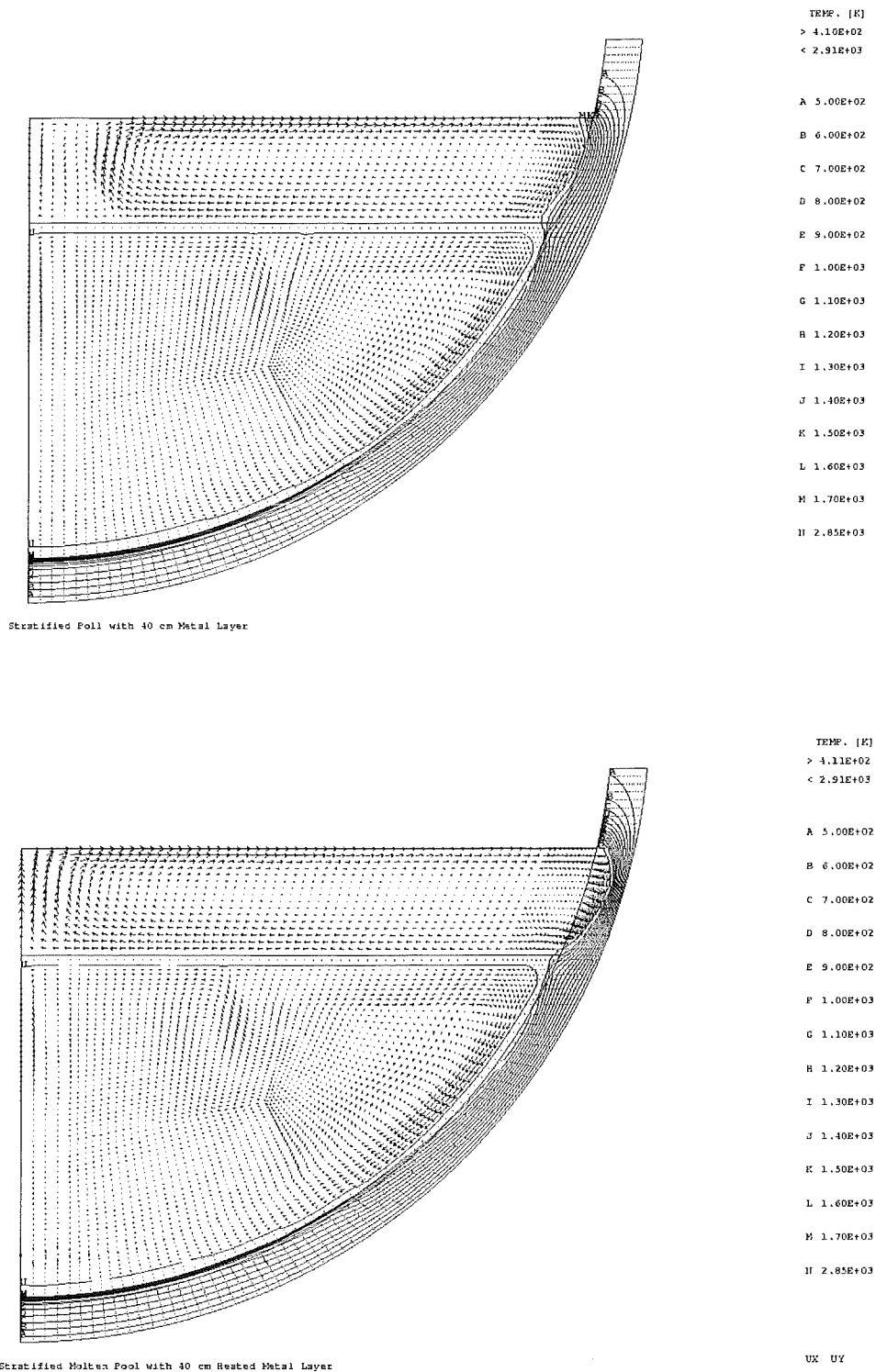


Fig. 1-5: Velocity and temperature fields in a molten pool for a given amount of relocated material and residual power. Stratified configuration with a 40 cm metal layer without residual power in the layer (above) and with residual power (below).

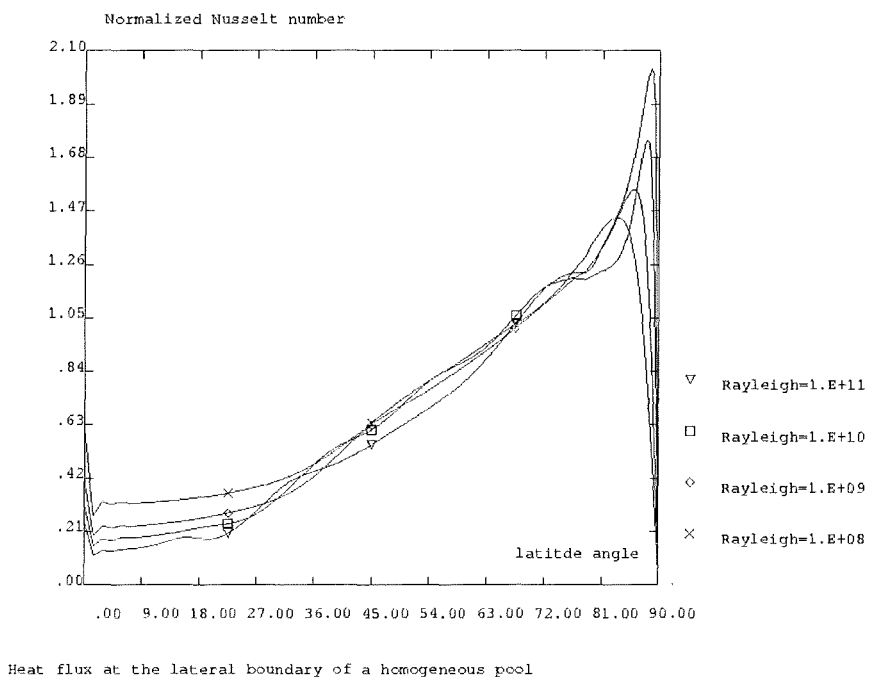


Fig. 1-6: Normalised Nusselt number along the lateral boundary of a homogeneous molten pool for different Rayleigh number.

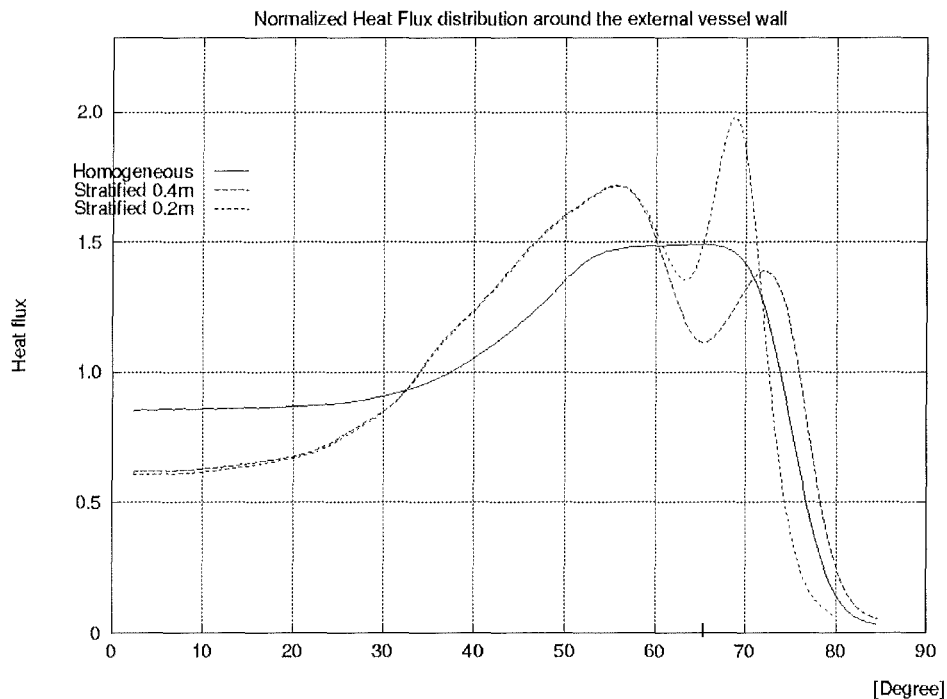


Fig. 1-7: Heat flux from the vessel to the cooling water in correspondence of different corium configurations.

1.2 Creep experiment RUPTHER

1.2.1 Objectives

The structural integrity of the RPV lower head in presence of molten core material has been investigated in the TMI post analysis and in the RPV project of the previous EU program. These two studies clearly showed that further investigations are required including

- more information on the mechanical properties of the steel at high temperature,
- more sophisticate mechanical models and failure criteria,
- intermediate scale experiments for validation of the simulation tools.

The first point has been partly addressed in the RPV project of the previous EU program and is further investigated here in section 5.1. The two others are addressed in this and the following sections 1.3 to 1.5. The intermediate scale experiments are RUPTHER and FASTHER.

1.2.2 Experimental set-up for RUPTHER

RUPTHER is a simple analytical experiment in which a thin shell tube is subjected to internal pressure and thermal loading with an axial temperature gradient. The maximum temperature is very high, 1000 °C in the present experiment. The test performed within the RPVSA frame is called RUPTHER #9.

The complete experimental set-up is presented in Fig. 1-8. A cooled induction heating coil is used which has the following design characteristics:

- 2 parallel loops made of 10 mm square copper tubing;
- 180 mm internal diameter;
- 20 mm distance between the 2 induction loops;
- 45.5 mm initial test piece clearance.

The thermocouple equipped tube is located in a vessel filled with argon gas. The vessel is an airtight cylinder with an internal diameter of 588 mm and a height of 950 mm. The vessel wall and the door are cooled by internal water circulation. An axial displacement sensor and a water leak detector are fixed at the lower flange of the vessel.

The vessel is equipped with 5 windows;

- the laser measuring uses the 2 windows at the east-west axis,
- the infra-red camera is located behind the south-east window,
- the pyrometer is located behind the south-west window,
- the north door window is used for direct observation. The photographs are taken through this window.

The tube position in the heating coil can be adjusted with a mechanical system located at the top of the upper flange of the vessel. Two sensors are used to measure the north-east and north-west displacement during the adjustment of the tube position.

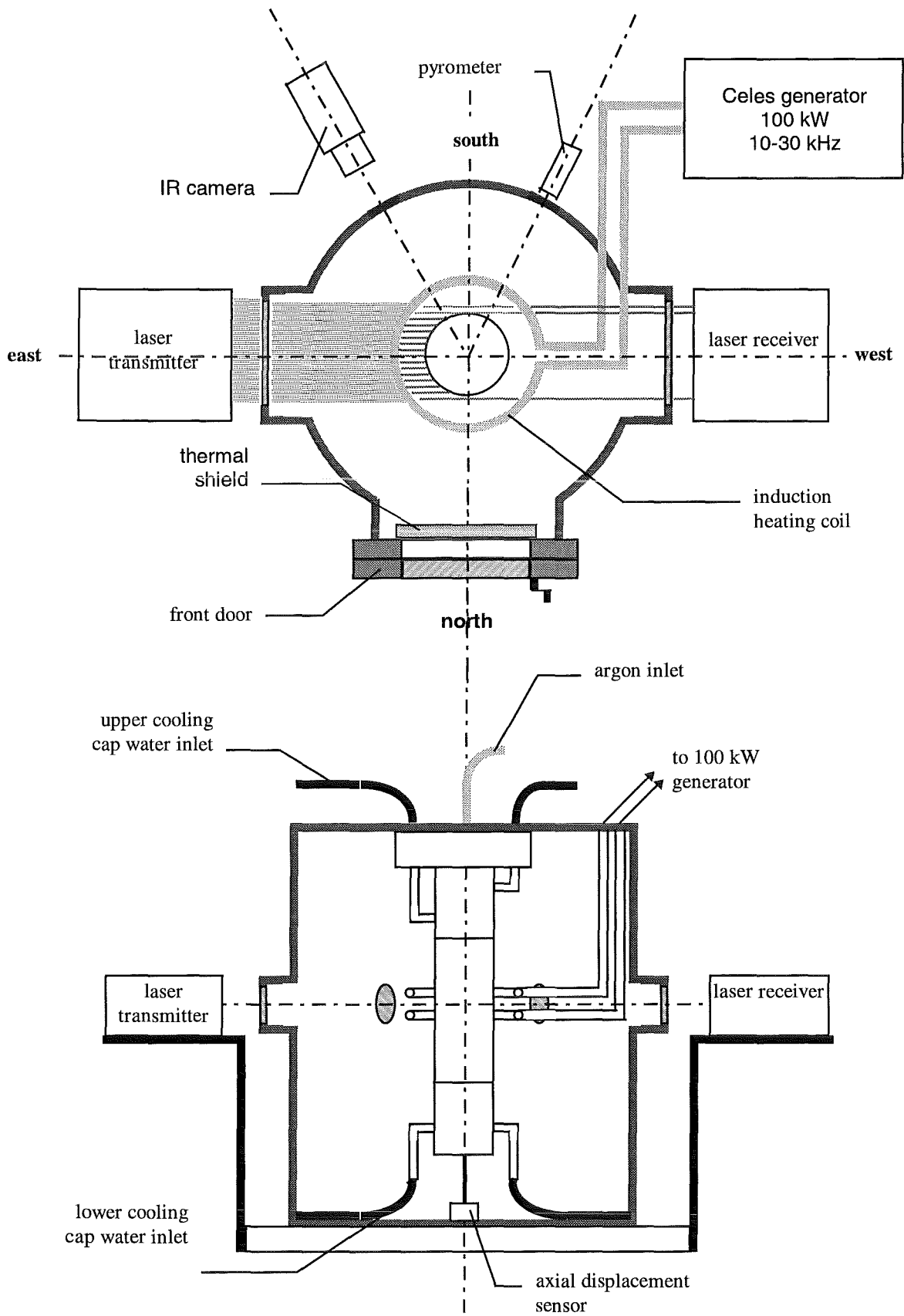


Fig. 1-8 : Schematic representation of RUPTHER device.

1.2.3 Test conditions

The test piece was first heated to a maximum temperature of 1000°C in the hottest mid plane of the tube and then subjected to a linear pressure increase up to 6.5 bars.

This was done as follows :

1. temperature increase with a rate of 50°C/min up to 100°C;
2. temperature increase with a rate of 100°C/min up to 1000°C;
3. thermal centring adjustment of the tube position in the induction coil;
4. temperature held at 1000°C until the end of the test;
5. pressure increase with a maximum rate of 0.5 bar/min up to 6.5 bars;
6. pressure held at 6.5 bars until rupture occurred.

The process is illustrated in Fig. 1-9.

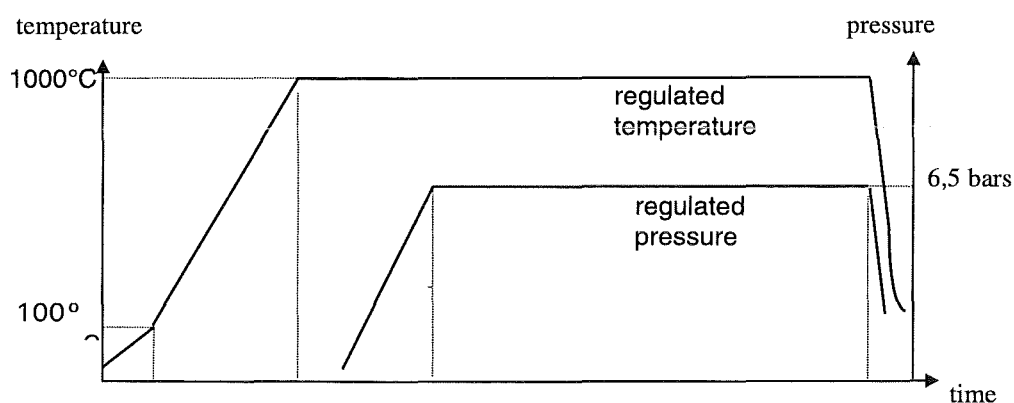


Fig. 1-9: Loading diagram.

1.2.4 Temperature control

The induction coil power was controlled using an Eurotherm 903P programmable regulator which was monitoring the maximum temperature measured by 8 thermocouples fixed at the mid-height circumference (hottest mid plane of the tube).

If the temperature regulation is monitoring the signal of a single thermocouple, both thermal and mechanical instabilities appear: temperature and deformation at the opposite point cannot be controlled, and they give rise to a very quick instability.

In this test, the temperature regulator was monitoring the maximum temperature measured by the 8 thermocouples fixed at the mid-height circumference. Using this system, the temperature cannot exceed the specified value.

However, while the temperature increases at the beginning of the test, the temperature regulator is monitoring the temperature measured by the thermocouple #110 (45°) in order to avoid perturbations. When the tube is well adjusted in the heating coil, the maximum temperature regulation system is triggered from the computer.

1.2.5 Tube response during the test

- from the beginning of data acquisition to 9025 seconds

This preparation phase corresponds to the creations of vacuum and the argon filling in the vessel.

from 9025 to 11345 seconds

During the temperature increase and the recentring of the test piece, the thermocouple #110 (45°) was used for the temperature regulator.

The temperature increase up to 1000°C was accompanied by a 0.6 mm diameter expansion, Fig. 1-10. Most of the deformation was located on the north edge of the tube. The axial displacement was about 2 mm. Only one thermocouple measured a temperature over 1000°C during this period (tc112, 135°).

After re-centring of the test piece in the coil, the maximum temperature regulation system was triggered, the thermocouple 112 monitored the temperature regulator.

- from 11345 to 12400 seconds

The pressure increase caused a low increase of the diameter.

- from 12400 to 82825 seconds

When the internal pressure reached 6.5 bars, a continuous deformation of the tube was observed, Fig. 1-10. Most of this deformation was located on the north edge of the tube (the hottest edge). The temperatures are shown in Fig. 1-11.

From 12400 to 35700 seconds, the maximum temperature was recorded by the thermocouple 112. The temperatures of the thermocouples 115, 116 and 113 (-90°, -135° and 180°, north-west edge of the test piece) increased. At the same time, the other temperatures decreased. At 35700 seconds, the thermocouples 112, 113 and 116 measured the same temperature of 1000°C.

From 35700 to 50450 seconds, the thermocouple 116 (-135°) controlled the temperature regulator. All the temperatures decreased, but at the end of this period the temperatures increased and the thermocouple 112 reached 1000°C. At 50450 seconds a sudden decrease of the temperature measured by the thermocouple 116 was observed: the thermocouple tip had been pulled away due to large deformation of the north edge of the test piece.

From 50450 to 81890 seconds, all the temperatures decreased (except thermocouple 112). The tip of the thermocouple 113 (180°) was pulled away at 66000 seconds. So, there were no indications about the temperature in the zone of maximum deformation. At 81890 seconds, the tip of the thermocouple 113 came very near the test piece wall because of the deformation increase. But, one cannot be sure of the contact quality between thermocouple tip and test piece wall.

From 81890 seconds to the rupture (82825 seconds), the thermocouple 113 monitored the temperature regulator. But one does not know whether the temperature measured by the thermocouple 113 was the real temperature on the test piece surface.

Rupture instant (82825 seconds)

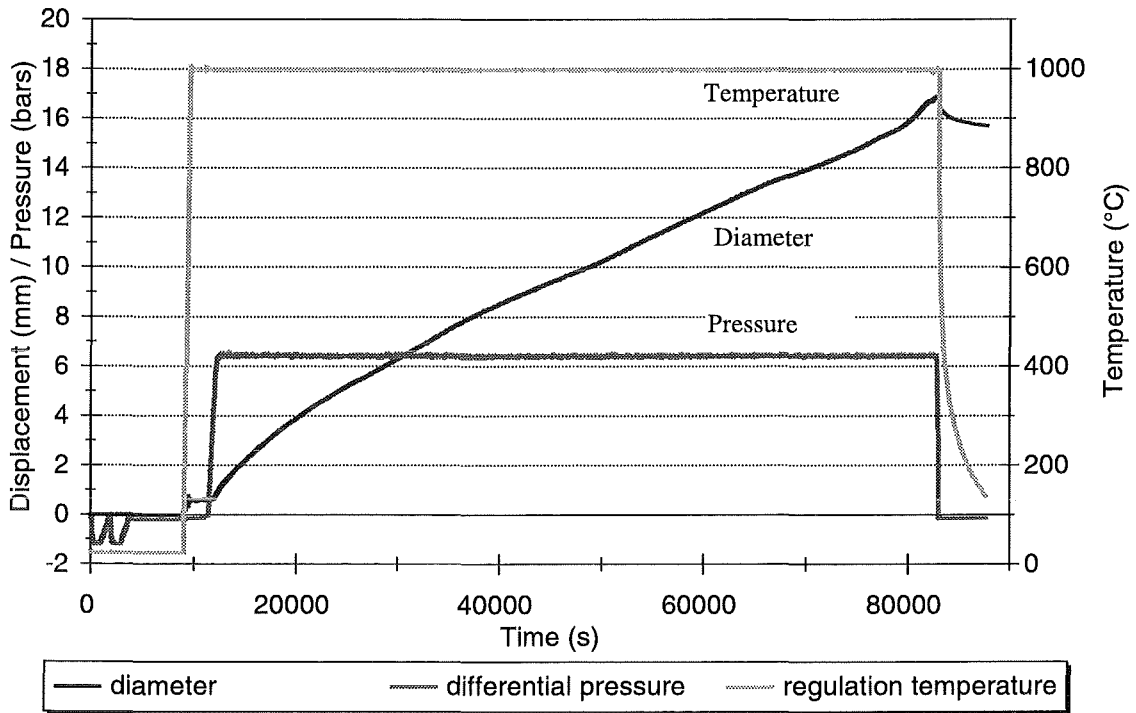
The diameter increase reached 17 mm and the axial displacement was about 2 mm. There was a quick pressure decrease in the test piece and a simultaneous pressure increase in the vessel from 0.07 bar up to 0.4 bar.

- From rupture to the end of data acquisition

Heating and pressure feed were stopped immediately and rapid natural cooling caused the diameter to decrease by 1.3 mm and the axial displacement to decrease by 1.6 mm.

Rupther: test #9

Diameter, temperature and pressure



Rupther: test #9

Rectified laser measures, displacement

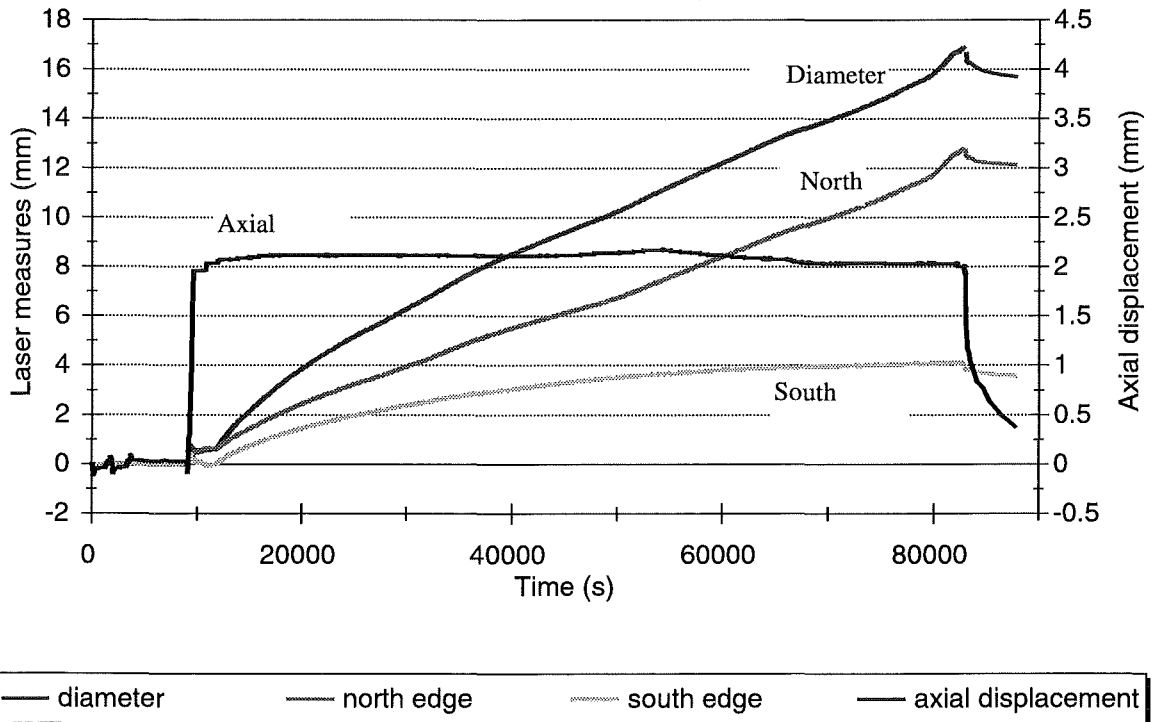
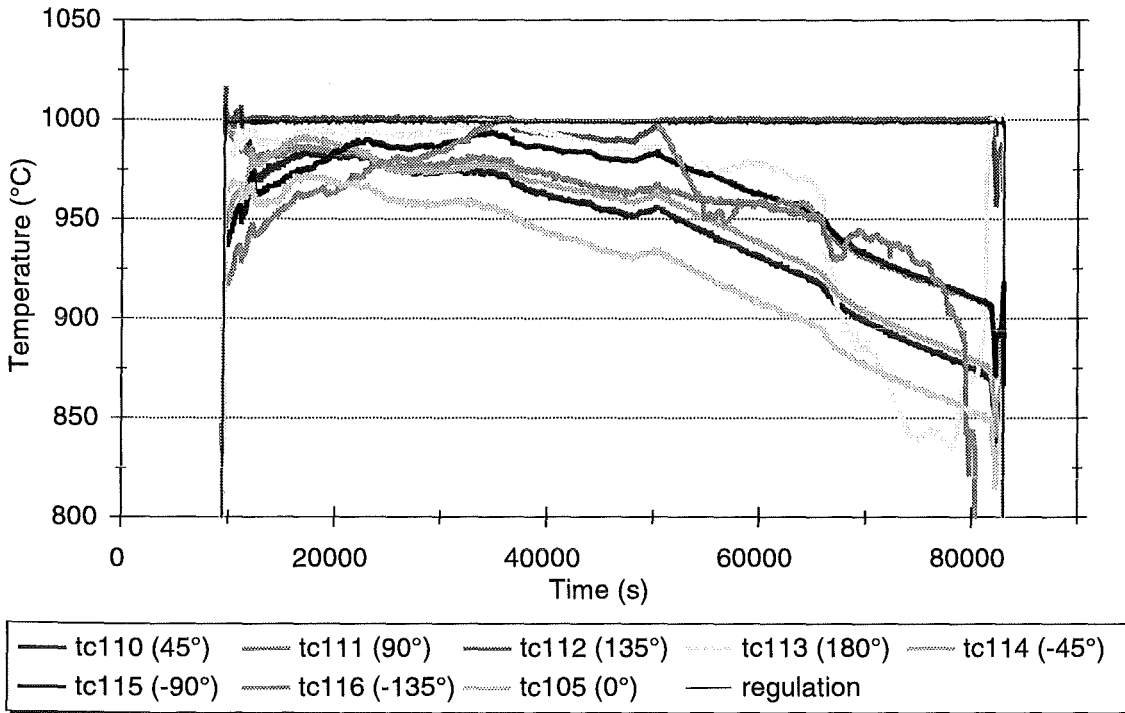


Fig. 1-10: Laser measurements, loading and axial displacement

Rupther: test #9
Temperatures on level 140



Rupther: test #9
Regulation system checking

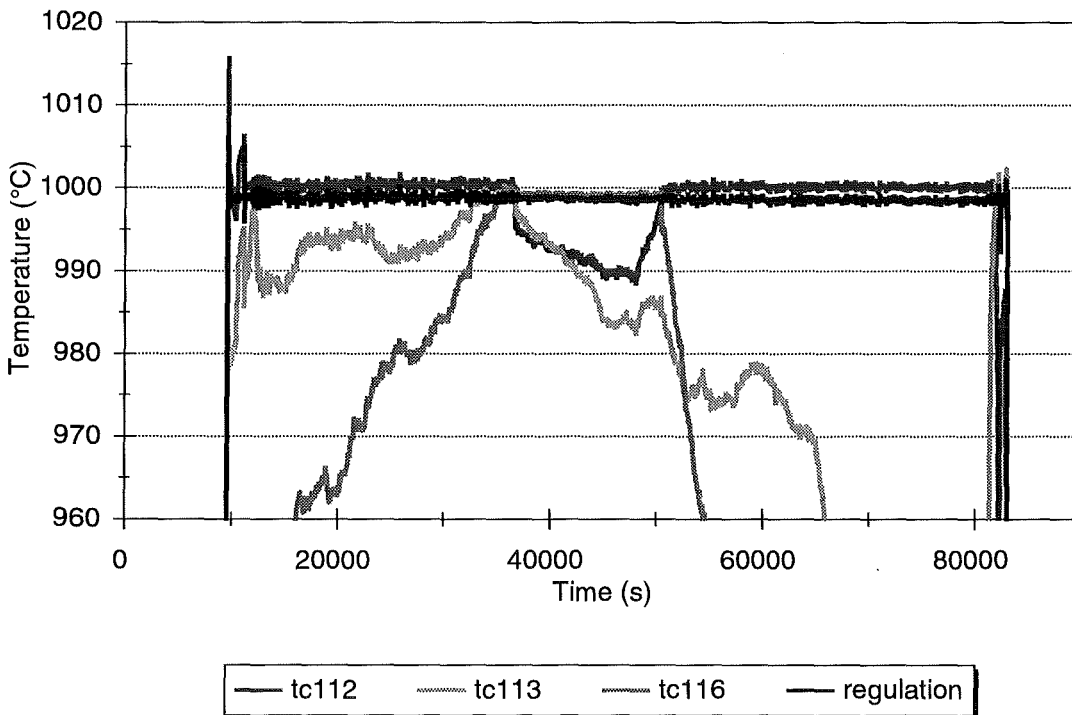


Fig. 1-11: Temperature histories at the circumference of the test piece

1.2.6 Conclusions from RUPATHER test #9

The experiment worked properly until 10 hours 50 min, but then one thermocouple went out. So, the exact temperature in one region of the circumference is unknown after that time. At 15 hours 10 min, another thermocouple went out. Due to this problem, the regulation (maximum of circumferential temperatures) did not take into account these two points and after 19 hours 50 min, the failure occurred between these points. Concerning the other aspects, the experiment was successful and the tube shows a clear ballooning without oxidation. Nevertheless, due to these thermocouple problems, the test would have been difficult to interpret as the maximum temperature is missing in the experimental records. For more details on the experiment refer to Mongabure (1998).

For interpretation as a benchmark it was decided to submit another RUPATHER test performed earlier. It was RUPATHER #4 with a maximum temperature of about 700°C and a pressure of 33 bars.

1.3 Validation of computational models (RUPATHER benchmark)

1.3.1 Introduction

The benchmark consists in the interpretation of the results obtained for the RUPATHER test #4. In this report, not all the conditions of RUPATHER #4 are reported. For more details concerning this experiment, refer to Sainte Catherine and Cotoni (1997). This test was planned with a maximal temperature of 700°C and with an internal pressure of 3.3 MPa. Failure occurred 7h16 after the beginning of temperature increase. The tube was clearly ballooned with slight surface oxidation.

1.3.2 Table of participants and main options of the FE codes used

Table 1-1 summarises the main options adopted by the participants in the RUPATHER benchmark. It has been performed by 7 participants from 4 countries and 6 companies (EDF, ENEA, FRAMATOME, FZK, PSI, CEA).

The individual reports are as follows for each participation (see References) :

- Bandhari (1997) for FRAMATOME in France,
- Duijvestijn (1997) for PSI in Switzerland,
- Dupas (1998) for EDF in France,
- Miliozzi (1997) for ENEA in Italy,
- Nicolas (1997) for CEA/LAMS in France,
- Lämmer, Ritter and Tsakmakis (1998) for FZK in Germany,
- Cotoni and Sainte Catherine (1997) (1) for CEA/LISN in France.

All the results of the different participants are marked by an identification number used in the following part of this report (e.g. participant #3). Of course, the corresponding key is not corresponding to the previous list of participants.

Table 1-1: Participants in the RUPATHER benchmark and main features of the codes applied

Participant #	1	2	3	4	5	6	7
F.E. code	ADINA	ASTER	CASTEM 2000	CASTEM 2000	CASTEM 2000	SYSTUS	ABAQUS
Elements 2D	9 nodes (2*50)	QUA8 (3*50)	QUA8 (2*41)	QUA8 (2*41)	QUA8 (2*50)	QUA8R (2*41)	QUA8 R (95)
F.E. options 2D	large strains	small displacements	large strains	large displacements	large strains	large strains	large strains
Elements 3D	27-nodes (436)	-	CU20R (8) (2*12*16)	CU20 (2*13*16)	-	-	-
F.E. options 3D	large strains	-	large displacements	large displacements	-	-	-
Creep Law	Norton (Graham-Walles)	Lemaitre-Chaboche with damage	Norton-Bailey	Lemaitre-Chaboche with damage	Norton-Bailey	Norton-Bailey	FZK model
Parameters identification	Levenberg- Marquart	(from CEA)	Ident1D	Ident1D, Ajust (Castem 2000)	Ajust (Castem 2000)	(from CEA)	Neural networks
Updating of pressure vector	OK	OK	OK	OK	OK	OK	OK

* Free participation from REVISA partners.

1.3.3 Predicted uniaxial creep curves at 700°C

In order to check the quality of material parameters identification, the participants were requested to calculate the uniaxial creep curves at 700°C, for initial stress levels of 70 and 90 MPa (experimental creep loads). These two load levels are near the equivalent Von Mises stress at the hottest point in the RUPTHER experiment. The Figs. 1-12 and 1-13 display in a comparative way the calculated curves from the participants.

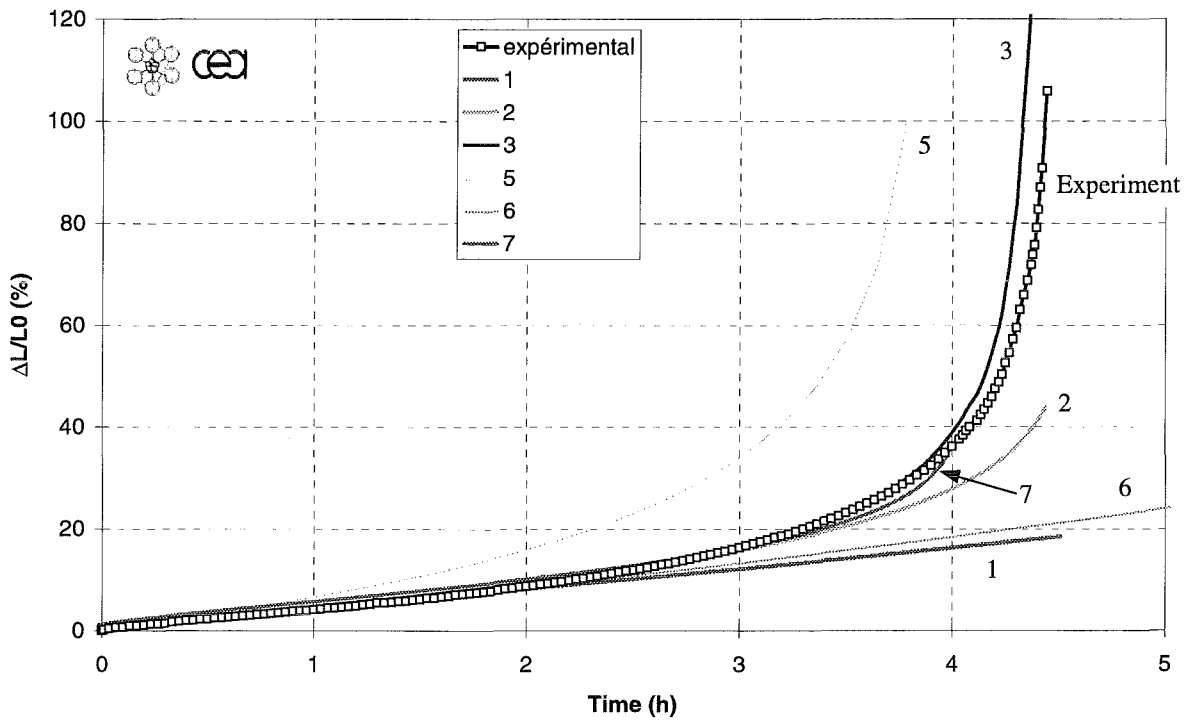


Fig. 1-12: Comparison of experimental and calculated creep curves at 700C and 70MPa

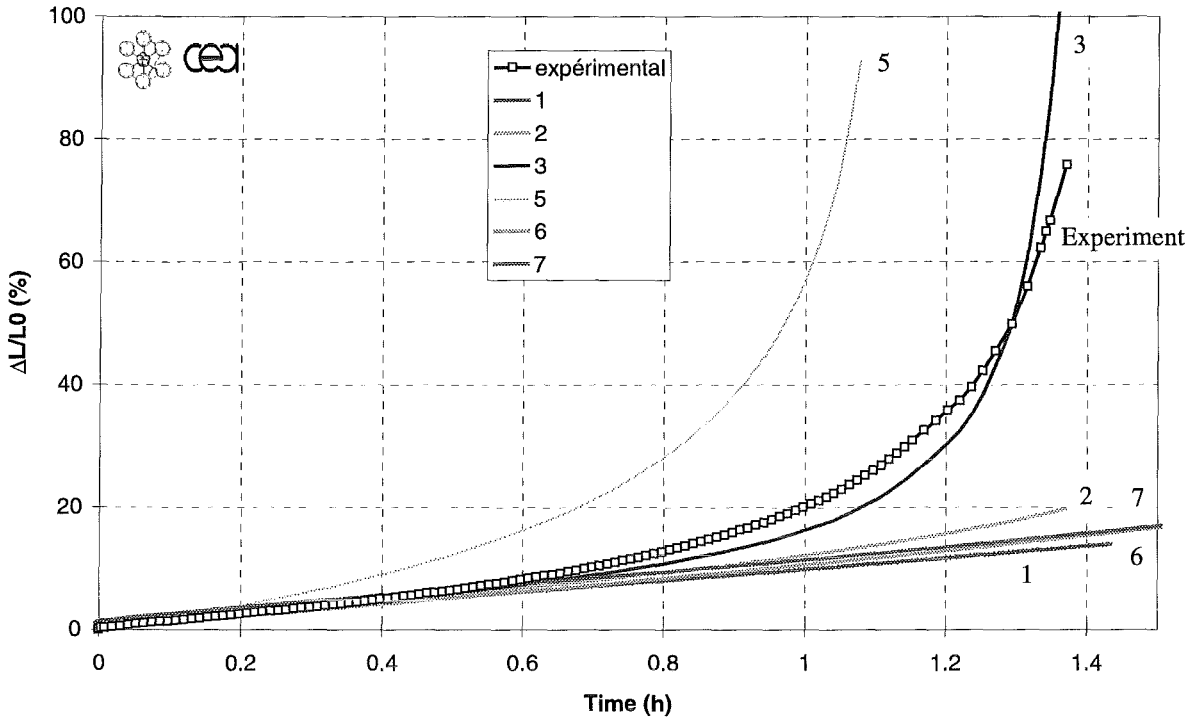


Fig. 1-13: Comparison of experimental and calculated creep curves at 700C and 90MPa

Participant #3 exhibits the best agreement with experimental results but he makes use of the Norton Bailey law which is normally unable to describe the third creep stage. This agreement is due to the fact that he takes into account the stress updating and all the creep curves for its identification task. One can also notice that participants #1 and #6 are predicting linear evolution during these time ranges.

1.3.4 Thermal loading

The axial temperature field has been taken into account by all the participants as specified below. The maximum temperature was normalised and then multiplied by the evolution of the maximum temperature versus time. Its general shape is given in the Fig. 1-14 and a corresponding polynomial approximation is given by:

$$T = -1.8081 \cdot 10^{-6} z^4 + 5.8953 \cdot 10^{-4} z^3 - 6.0013 \cdot 10^{-2} z^2 - 1.2556 z + 686.19$$

The different participants did not use the same thermal loading history. They used different results from the measurement carried out on the tube. One can distinguish four cases as shown in Fig. 1-15.

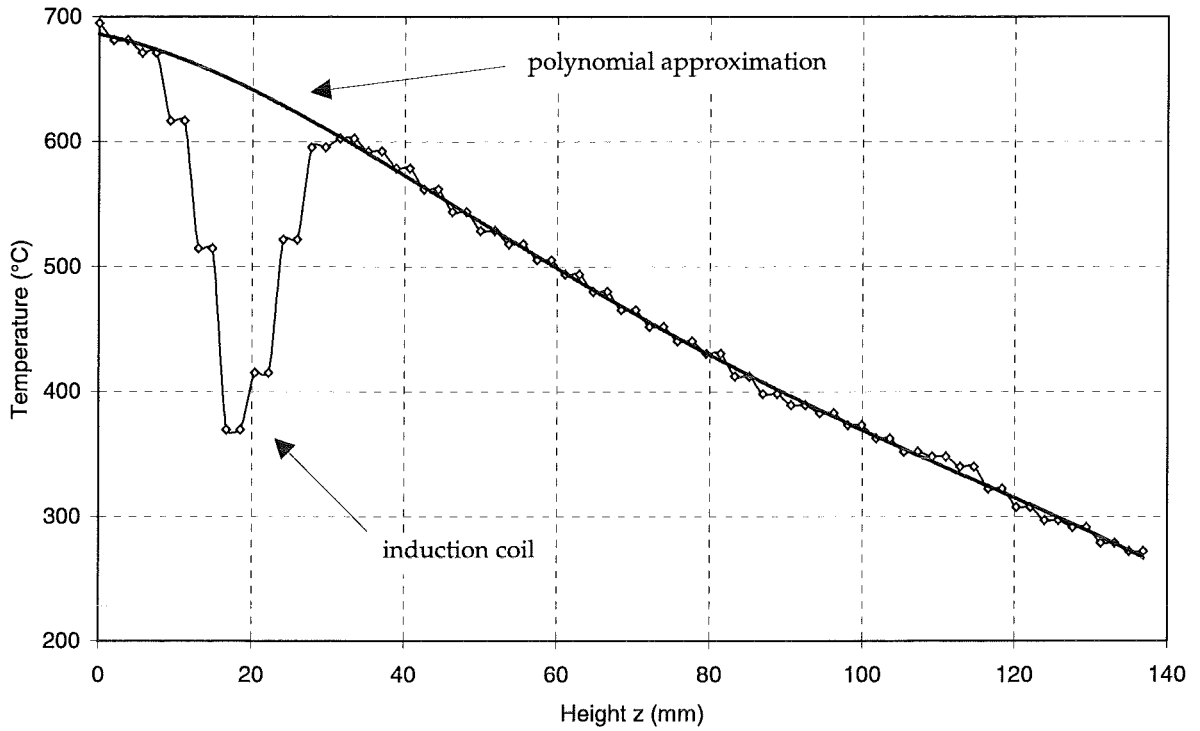


Fig. 1-14: General shape of the axial thermal gradient ($z=0$ for the maximum temperature).

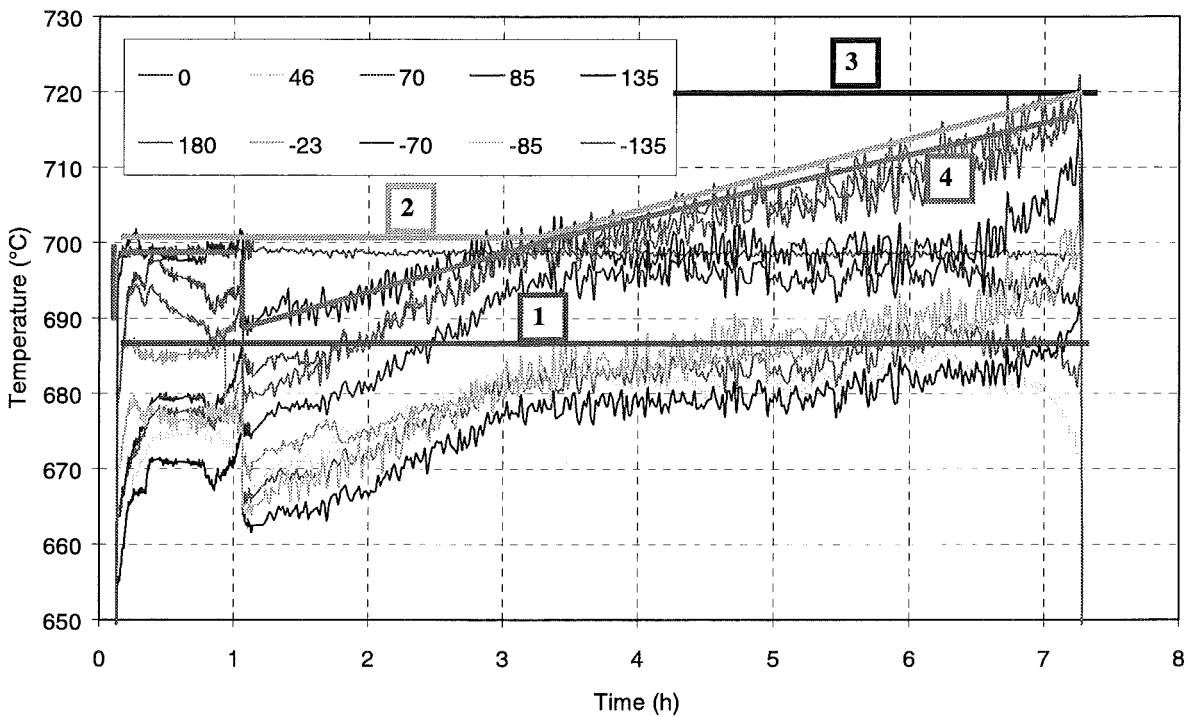


Fig. 1-15: Experimental temperatures on RUPATHER #4 tube's circumference

Case 1 : (Participant #3 and #7) The temperature is constant during all the loading time and equal to the target value (700°C).

Case 2 : (Participant #2) The temperature is the maximum of the recorded temperatures along the hottest circumference.

Case 3 : (Participant #4 and #5) The maximum temperature is constant during the test and equal to the maximum value (720°C) recorded at the end of the test at the failure point.

Case 4 : (Participant #1 and #5) The temperature of the thermocouples close to the failure point is taken into account.

For 3D computations, 3 participants (#1, #2 and #6) used the experimental signals at each angle position and performed linear interpolation between them.

1.3.5 Diametral deformation

The calculated curves of diametral deformation versus time by the different partners and the experimental one for the RUPATHER tube in its hottest middle plane are given in Fig. 1-16. The maximum diametral deformation is reported as $\Delta D/D_0$ where D_0 is the initial diameter of the tube (89 mm) and ΔD the variation during the test.

As it can be observed on the graph, the initial deformation is due to the thermal expansion of the material due to temperature increase. The calculated curves are not identical for all the participants. Three types of curve can be separated. The first set (participant#2 (2D ivit)) exhibits an increase rate which is larger than from the experimental results. For the second set (participants #1 (axi and 3D), #4 and #5), the calculated curves are in good agreement with the experiment. For the third set (participants #2 (2D ipar and 3D ipar), #3, #6 (axi and 3D) and #7) the diametral deformation is less than the experimental result.

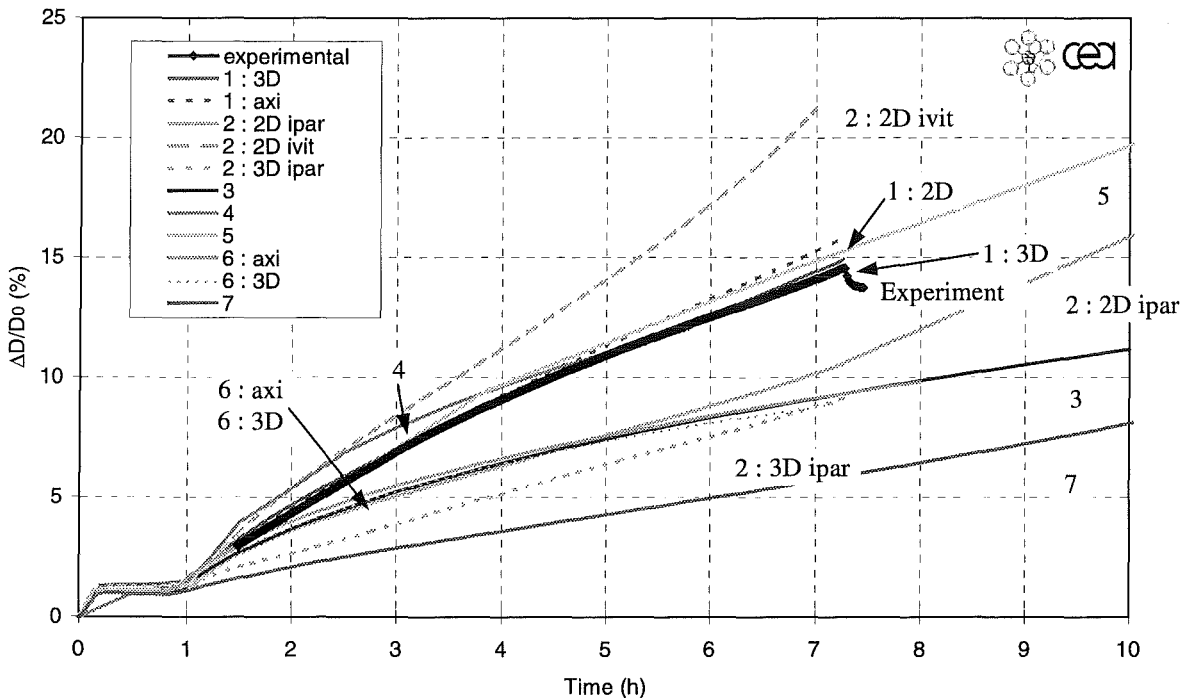


Fig. 1-16: Calculated diametral deformation at the hottest point of the RUPATHER tube, comparison of experimental and calculated curves.

1.3.6 Damage evolution

The different participants have used different failure criteria based on maximum strain, on time cumulating damage (Robinson) or more physically based criteria such as the Kachanov law with uncoupled (i.e. post-proceed) or coupled models. The total set of predicted results for the damage evolution is given in the Fig. 1-17. One can easily see that approximately all possibilities are covered from an almost non damaged structure ($D < 0.1$) at 7h16 to a highly damaged one ($0.1 < D < 0.9$) and to failure which is predicted to occur before 7h16.

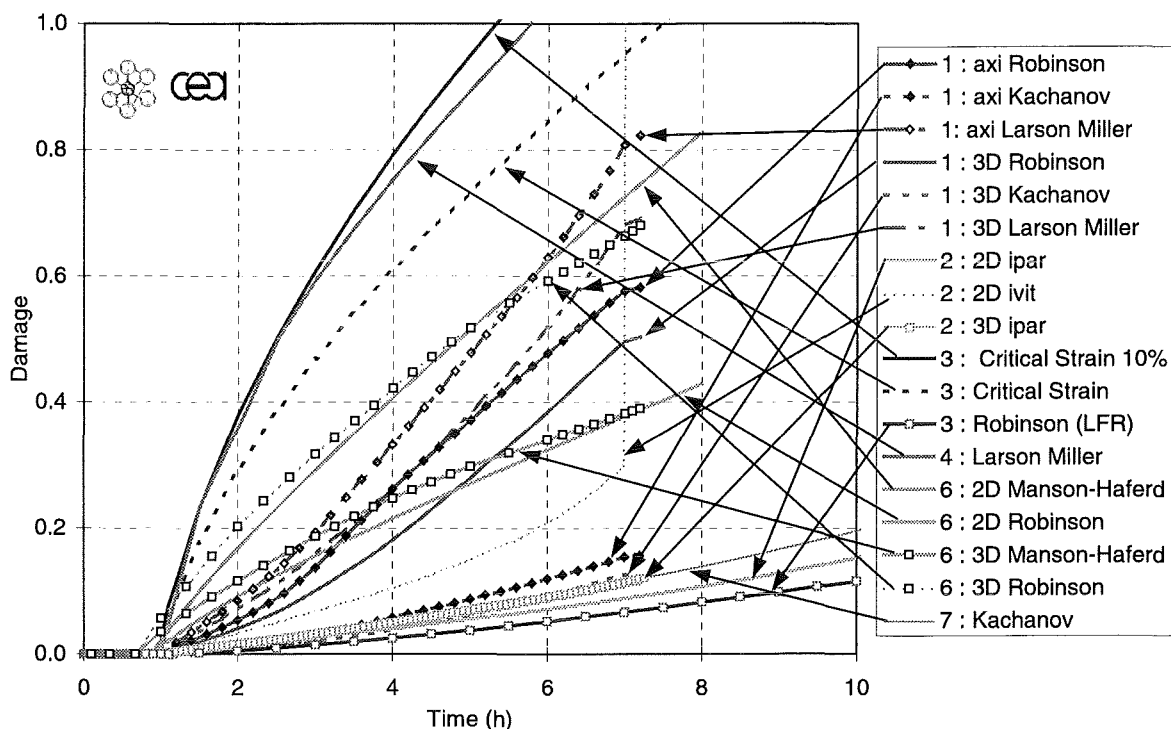


Fig. 1-17: Calculated curves of damage evolution.

In order to be able to allow a more intensive discussion, the results are separated in different graphs according to the damage rule.

Strain criterion:

For participant #3, the first criterion is based on the ratio between the equivalent plastic strain and a rupture strain set equal to 10% as a hypothesis. As an extension of this criteria the rupture strain is assumed to be variable with the temperature and equal to the strain at the end of the secondary stage.

For participant #5, the failure is obtained when the deformation of the tube $\Delta D/D_0$ exceeds 18%.

Fig. 1-18 presents a comparison of these methods. The failure criterion based on critical strain as a function of temperature and equal to the end of the secondary creep stage gives the best results (7.4 hours).

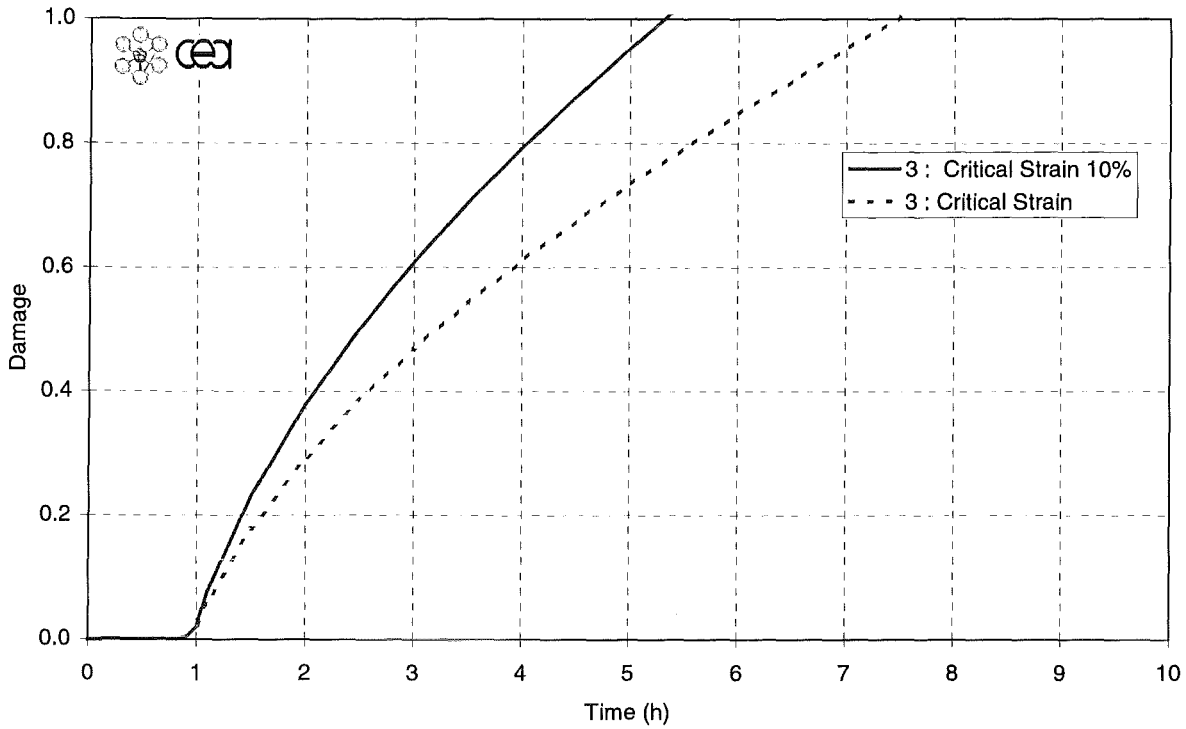


Fig. 1-18: Calculated curves of damage evolution (strain criteria)

Time cumulating rule: (for the explanation of the symbols refer to the detailed reports)

Participants #1, #3 and #6 used Robinson's damage rule. It is based on a linear time damage accumulation. It does not give a physical estimation of the damage value, but it is very useful in simplified methods as it gives an estimate of the remaining life duration. It is defined as :

$$D = \int_0^t \frac{dt}{t_r(\sigma_{VM})}$$

$$t_r(\sigma_{VM}) = \frac{1}{r+1} \left(\frac{\sigma_{VM}}{A} \right)^{-r}$$

The failure criterion based on the Larson-Miller approach was used by participants # 1 and #4. It is also based on a linear time damage accumulation. This approach is well known to over-estimate the damage . It considers that stress remains constant during the creep test, which is not realistic in our case. It is defined as :

$$D = \int_0^t \frac{dt}{t_r(\sigma_{VM})}$$

$t_r(\sigma_{VM})$ is extracted from the Larson-Miller equations :

$$LMP = \frac{T(^{\circ}K)}{1000} \cdot (C + \log(t_r))$$

$$\log(\sigma_{VM}) = A - B \cdot LMP$$

Participant #6 used the Manson-Haferd creep failure method which was developed following the Larson-Miller method where t_r is determined by the following relations:

$$MHP = \frac{\log(t_r - A)}{T - B}$$

$$MHP = C_1 + C_2 * \log(\sigma) + C_3 * \log^2(\sigma)$$

Fig. 1-19 presents a comparison of the results obtained with these methods. The predicted damage at 7h16 where the tube failed was between 0.4 and 0.82. Only participant #4 found a damage greater than 1, which means that he got a conservative estimate (5h47).

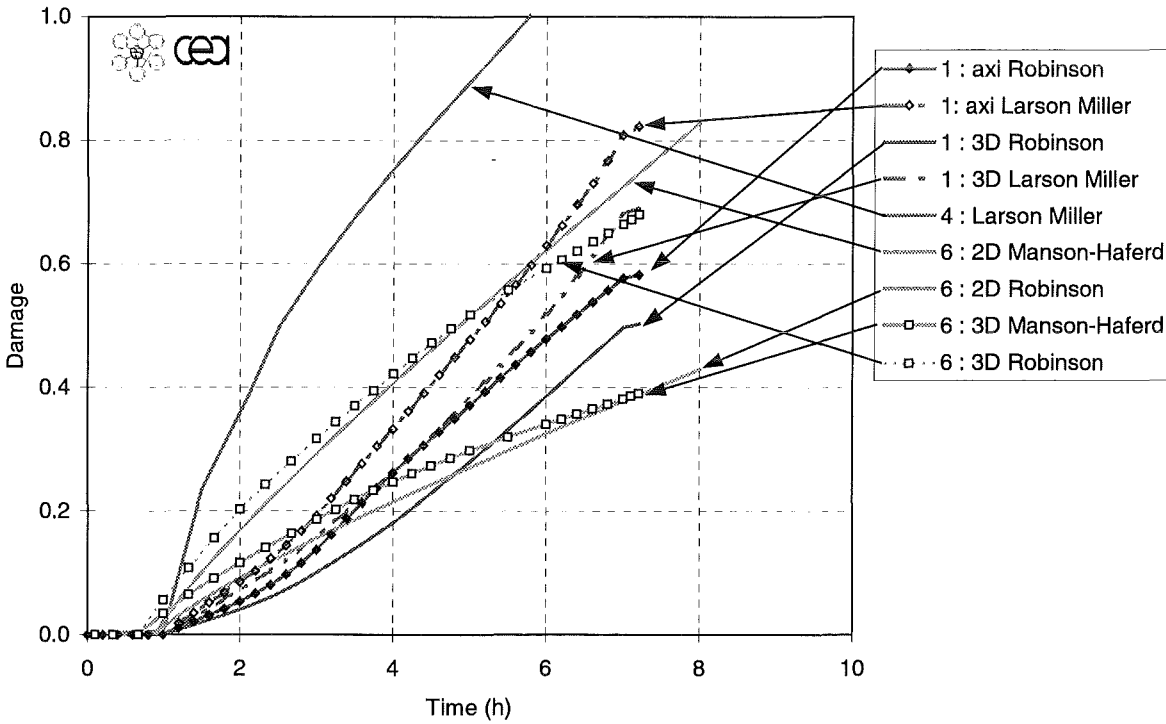


Fig. 1-19: Calculated curves of damage evolution (time cumulating rule)

Nonlinear rule:

Participant #1 used the failure criterion given by a damage value computed by Kachanov's law. It is more physically based than the Robinson's damage rule. It normally gives a more realistic evolution of physical damage (cavities proportion), but it is very nonlinear.

Kachanov's law is expressed by :

$$\dot{D} = \left(\frac{\sigma_{VM}}{A \cdot (1 - D)} \right)^r$$

Fig. 1-20 presents the results obtained by this method. The cavities proportion remains quite low (less than 20%), but the Kachanov law is known to yield abrupt increases. Thus, no extrapolation is possible.

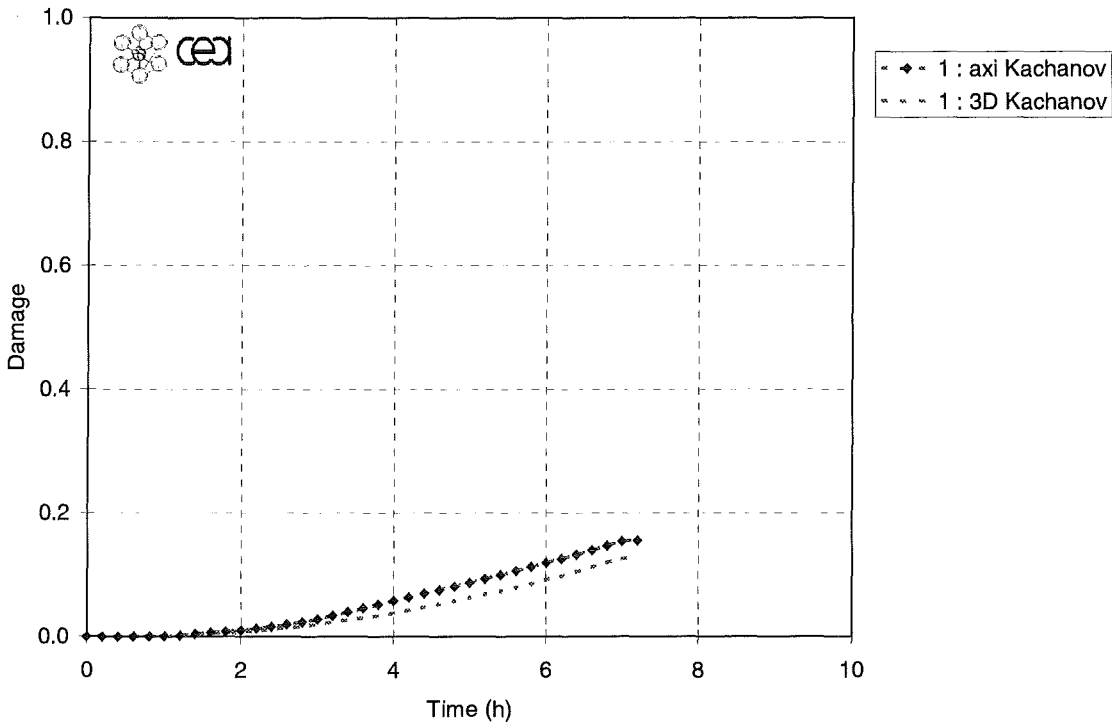


Fig. 1-20: Calculated curves of damage evolution (nonlinear rule in post processing)

Nonlinear rule coupled with the constitutive equation:

Participants #2 and #7 used the Kachanov's law coupled with the constitutive equations. The creep damage evolution law is given in 1D formulation by :

$$\dot{\epsilon}_p = \frac{1}{(1-D)^{N+1}} \cdot \left(\frac{\sigma}{K \cdot \epsilon_p^{1/M}} \right)^N$$

$$\dot{D} = \left(\frac{\sigma}{A \cdot (1-D)} \right)^r$$

Fig. 1-21 presents the results obtained by this method. Only participant #2 (option ivit) obtained a realistic result (D=1 at 7h00), but with a very abrupt increase from 0.3 to 1.0. This results is the best estimate of the experimental failure time.

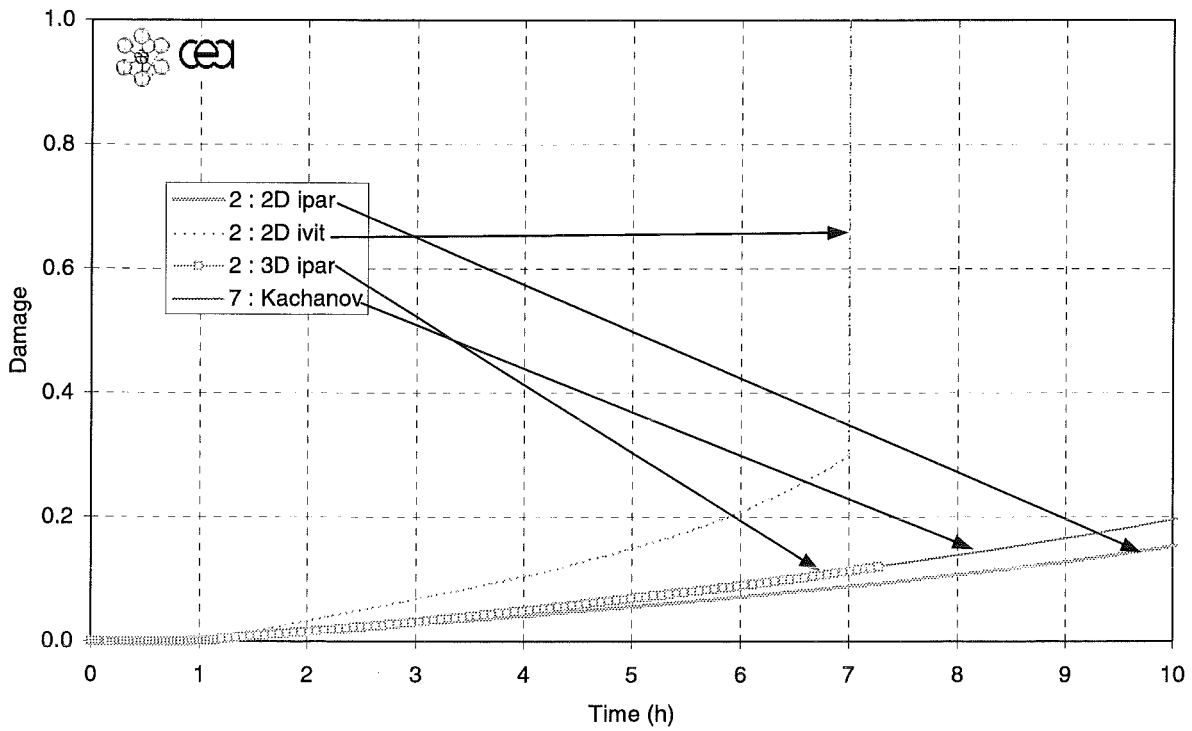


Fig. 1-21: Calculated curves of damage evolution (nonlinear rule coupled with the constitutive equations)

1.3.7 Comparison and discussion of the results

As indicated before, depending on the FE calculation and the adopted failure criteria, the failure time of the RUPTHER tube is estimated between 5.3 hours and 16.8 hours for an experimental result equal to 7h16.

Table 2: Damage law and predicted failure time.
 (Post : calculation of damage is not coupled with the constitutive equation)
 (Coupled : calculation of damage is coupled with the constitutive equation)

Participant	Damage law	Damage at Experimental Failure Time (7h10)	Calculated Failure Time	Localisation of Failure (mid plane for every participants except as indicated)
1	Robinson (post) Kachanov (post) Larson Miller (post)	0.58 (2D), 0.50 (3D) 0.156 (2D), 0.128 (3D) 0.82 (2D), 0.70 (3D)	11h45 (2D) - -	mid plane, outer side
2	Kachanov (coupled)	0.105 (2D ipar) 1.0 (2D ivit) 0.09 (3D)	12.8h 7h -	mid plane, outer side
3	Critical strain 10% (rate1) Critical Strain (rate2) Robinson (LFR)	1.26 0.98 0.07	5.3h 7.4h >>10h	mid plane, outer side
4	Larson Miller	1.0	5h47	mid plane, outer side
5	Excessive strain	-	8.95h	mid plane, -
6	Manson-Haferd (MHP) Robinson	0.39 (2D), 0.45 (3D) 0.75 (2D), 0.68 (3D)	-	mid plane, inner side center midpoint
7	Kachanov (coupled)	0.12	16.8h	mid plane, inner side

The different failure criteria can be evaluated as follows:

- strain criteria : they can give good results for a critical strain as a function of temperature and equal to the value at the end of the secondary stage of the creep curves. The application is very simple.
- Time cumulation rule: it gives an estimation of life fraction and is already very useful, as extrapolations of results are possible. Depending on the calculation hypothesis, the life fraction estimated by the participants was over 50%. Only the estimation carried out with Larson-Miller performed by participant #4 was conservative. This approach is more useful in an engineering sense but it is more expensive as additional parameters are required.
- Nonlinear rule: Kachanov law is more physical founded as it normally gives the cavities proportion. But, as a consequence, the evolution is very nonlinear and no extrapolation can be made. The estimated damage value at the experimental failure time was lower than 20%.
- Nonlinear rule coupled with the constitutive equations : physical damage evolution can be taken into account in the constitutive equations in order to describe the induced softening of the material. The predicted evolutions are much more non linear, but can give a good description of the process. In the particular case of this benchmark, the best failure time prediction (7h00) was performed with this model.

The results of this benchmark and of the preceding one clearly show that the main discrepancies for the global mechanical behaviour come from

- the identification of material constitutive equations parameters,
- the large or small strain hypothesis,
- the updating or non-updating of the pressure vector with respect to the deformed mesh,
- the particular temperature history selected.

Concerning the predicted failure time and the damage evolution, the discrepancies between the participants are much larger. It comes from the fact that very different failure criteria were used.

1.4 Creep experiment FASTHER

1.4.1 Test conditions

FASTHER (FAilure under Strong THERmal gradient) is a simple analytical experiment in which a thick tube ($\varnothing_{\text{int}}=30$ et $\varnothing_{\text{ext}}=70$ mm) is submitted to a high thermal radial gradient (about 1000°C) produced by external induction heating and by internal cooling with water circulation. The height of the heated zone is about 70 mm. The mechanical loading is an imposed displacement with a 2500 kN servo-hydraulic machine.

The external diameter of the central part of the tube is 70 mm. Its total length is 270 mm, but the central part with the homogeneous section has a length of 154 mm. Its wall thickness is 20 mm. The corresponding block has been extracted from a RPV at the level of the nozzles. The tube axis is oriented in the radial direction of the vessel. The material is a carbon manganese ferritic low alloy steel corresponding to 16MND5 in the French designation system (eq. A508 1.3).

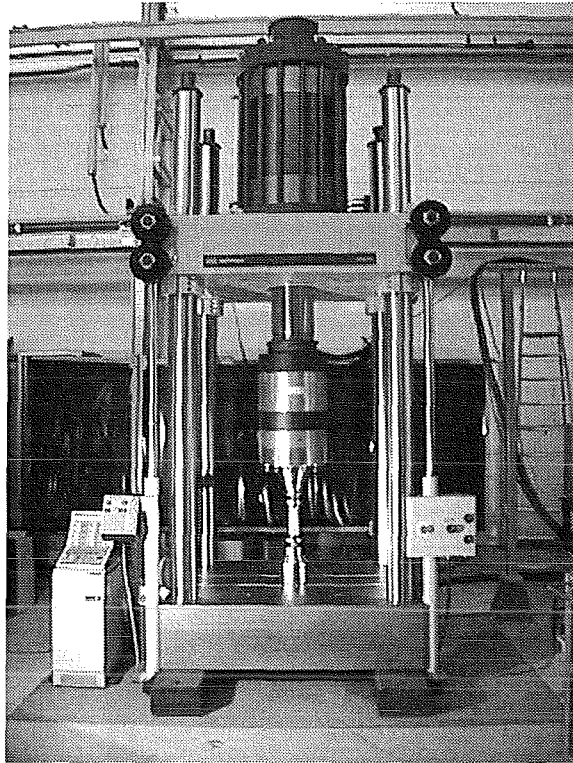


Fig. 1-21: Overview of FASTHER tube as installed on 250 t servo-hydraulic machine.

1.4.2 Experimental facility and instrumentation

The FASTHER tube is submitted to imposed displacement while being heated by four turns of an induction coil in its central section on a limited height. The test takes place in air without any gas protection. So, oxidation occurs during the test, but due the short period involved, it has no influence on the mechanical behaviour.

The instrumentation include 4 main features :

- Load is measured by the load cell of the servo-hydraulic machine,
- Displacement is measured by the LVDT and by a system of 2 alumina rods intercepting scanning lasers,
- Temperatures are measured with more than 20 thermocouples, while a general map is acquired by an infrared camera facing 0° axial line,
- Diametral deformation in the central section is measured with a laser scanning shadow technique.

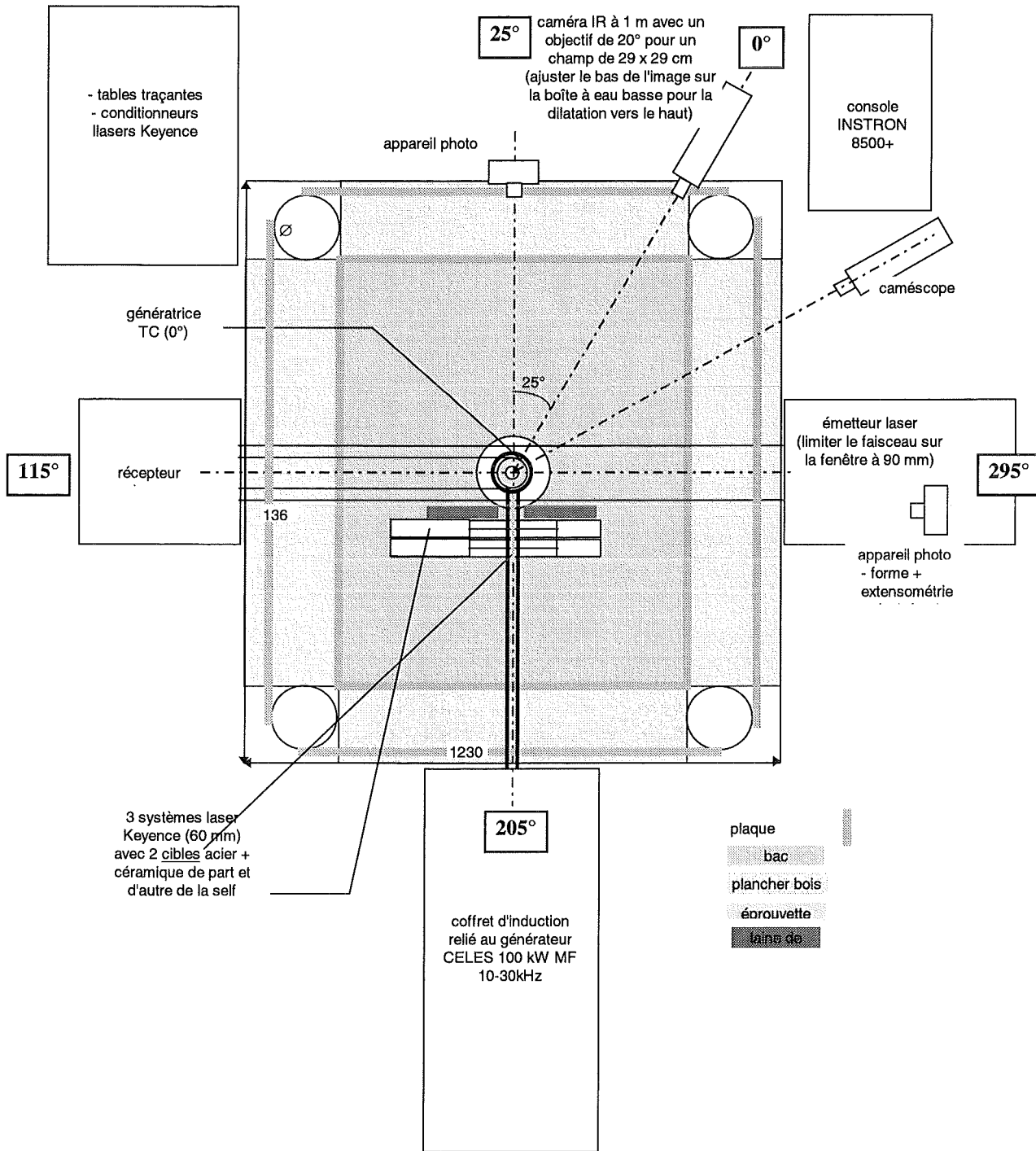


Fig.1-22: Schematic upper view of FASTHER experimental facility.

Four thermocouples are located at the mid-height plane (80 mm), recording the temperatures around the tube. They are placed at : 0°, 90°, 180° and 270°. Two other circumferences at 67 and 87 mm height are instrumented in the same way. Furthermore, an axial line located at 0° is more intensively instrumented. This 0° line will be used for the regulation which is based on the maximum temperature observed along this line. Two thermocouples are located inside the tube in order to measure the radial gradient during the test (TC 117 at 80,0° and TC 118 at 80,90°). These thermocouples are in front of the external thermocouples TC 107 and TC 108.

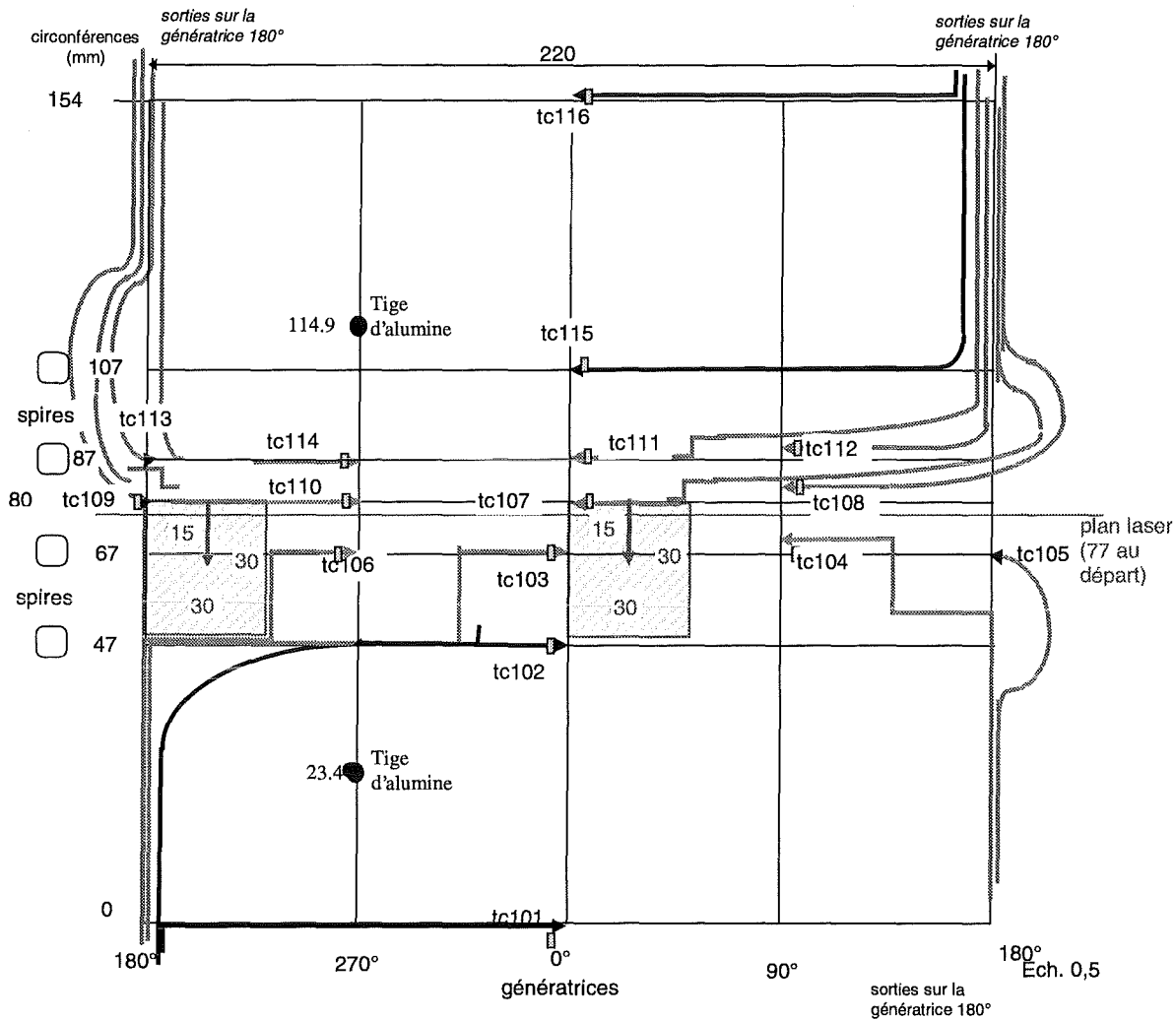


Fig. 1-23: Thermocouple positions at the FASTHER tube.

1.4.3 Results

During the temperature increase, the machine was set in the load control mode with a 0 kN level in order to allow free thermal expansion. After the thermal field stabilisation, the servo-hydraulic machine was turned to the displacement control mode and a ramp rate of 1.0 mm/min was imposed until failure occurred. The deformation essentially occurred in the middle part located inside the induction coil because the end parts of the tube are water cooled.

Thermal loading:

The evolution of temperatures with time does not show a really simple pattern. It is not axisymmetric, nor symmetric between the lower and the upper part and does not remain constant with time. The complete evolution of the temperatures versus time are given in Fig. 1-24.

The values given by the thermocouples have an accuracy of $\pm 2\%$. The records given here are raw signals, no treatment has been performed. So, some perturbations are sometimes clearly visible such as transients peaks on thermocouple signals.

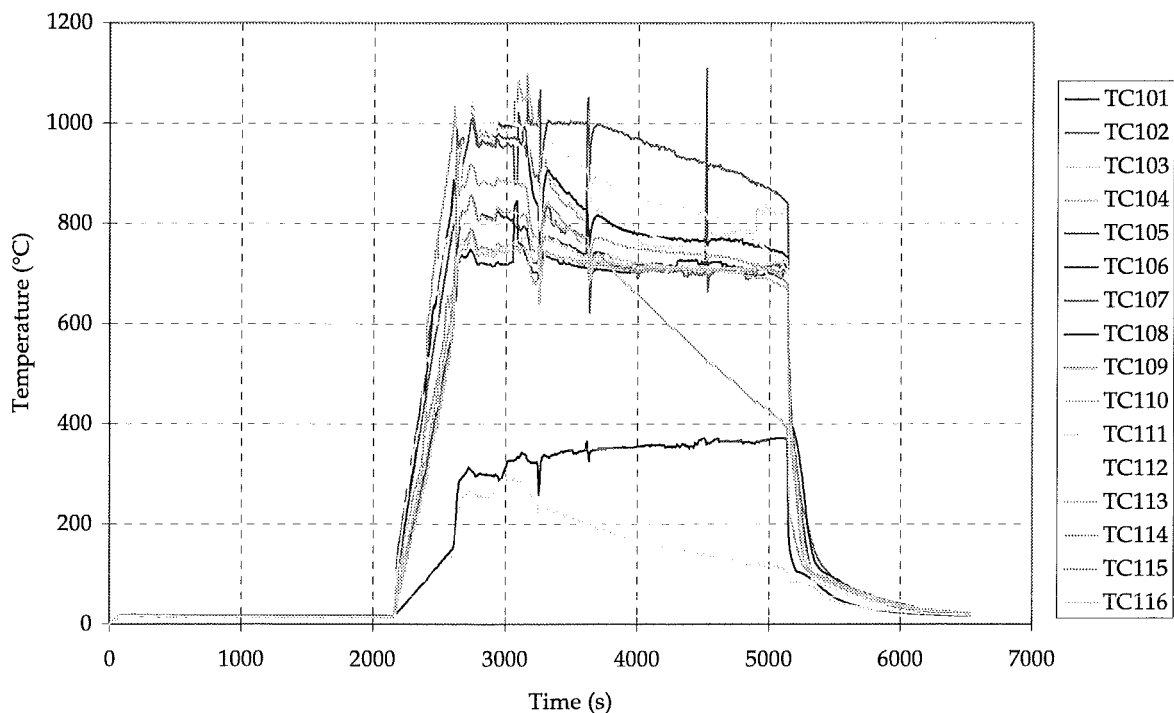


Fig. 1-24: Whole set of experimental temperatures at the external skin of the FASTHER tube.

Axial thermal field observed with infrared camera:

The axial temperature profile has been also measured with the infrared camera during the experiment. This IR camera is in 0° direction, so its results can be compared with the vertical line having the largest number of thermocouples. Furthermore, the 0° line is used to adjust the emissivity which is not constant during all the test as the surface is continuously in evolution.

These measurements can be used as a basis for the structural mechanics calculation. Thus, thermal computations are not required. Unfortunately, due to oxidation problems and disturbing inductions in thermocouples, a good agreement between thermocouples signals and the IR profiles was not achieved. So, a compromise must be done in order to obtain the thermal field. Fig. 1-25 gives an example of the axial thermal field shape at a particular time step. The corresponding six degree polynomial approximation is also given. Six temperature fields like this one were delivered to the benchmark participants.

Mechanical loading:

The mechanical loading was a displacement ramp at a rate of 1 mm/min imposed by the hydraulic jack. The corresponding loading diagram is given in the Fig. 1-26.

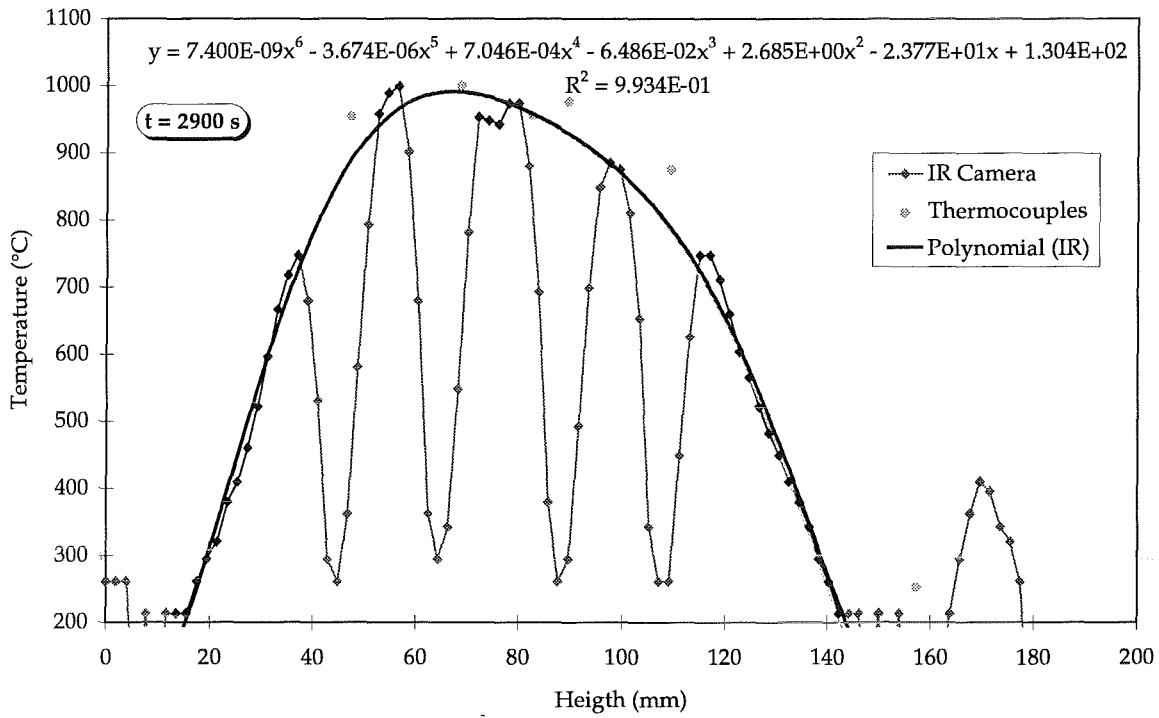


Fig. 1-25: Shape of the axial thermal field at 0° direction at 2900 s.

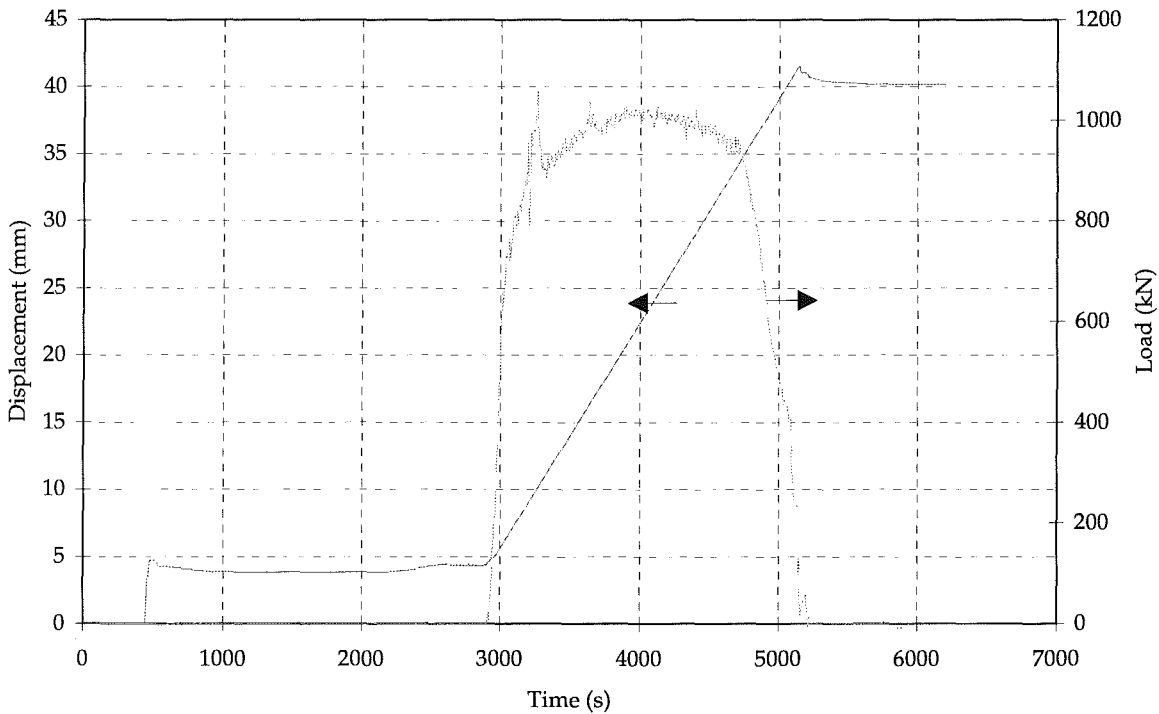


Fig. 1-26: Imposed displacement by the hydraulic jack and corresponding load during the FASTHER test.

Tube deformation and final crack:

There was no detection of the failure initiation and the crack propagation. The FASTHER tube first exhibited a necking similar to the deformation observed on tensile specimens. This necking is clearly marked and not so diffuse as those observed for specimens tested at high temperature. Failure occurred suddenly, the first indication was given by a water leak in the specimen near the induction coil. After cooling, a crack of 12.7 mm was observable in the necking region between 61.5° and 90° with an inclination of around 12.7° from the horizontal. The nearest thermocouple is TC104. The crack tip positions are located at a height of 70.3 and 73.1 mm. Figs. 1-27 and 1-28 show photographs of the tube.

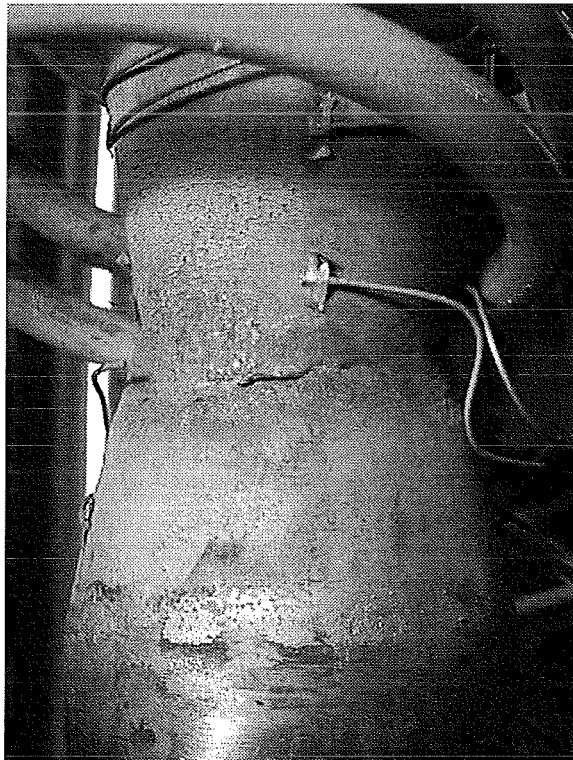
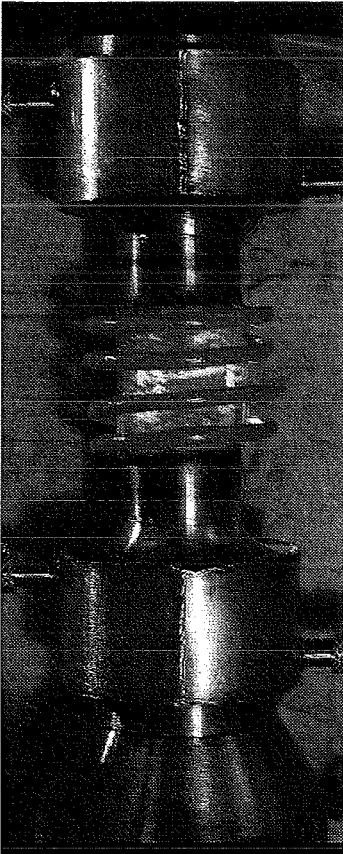


Fig. 1-27: FASTHER tube during and after test.

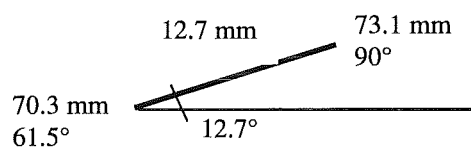
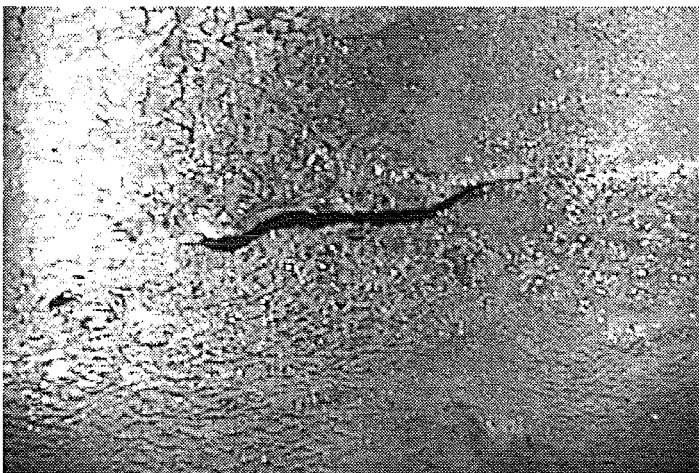


Fig. 1-28: Crack shape, dimension, position and orientation.

A scanning laser was also used for the measurement of the tube diameter evolution during the test. It was initially located at a height of 77 mm. But, due to oxidation problems during the test, the laser measurements were disturbed. The first increase in diameter between 2000 and 3000 s is related to the thermal expansion. After 3000 s, the general diameter decrease is due to contraction and necking of the tube.

1.5 Validation of computational models (FASTHER benchmark)

1.5.1 Introduction

A specification report (Sainte Catherine and Champain (1998)) corresponding to the interpretation benchmark of FASTHER test has been distributed to the interested participants.

Only four participants from four companies and three different countries contributed to this task. All used isoparametric quadratic 8 nodes elements with large displacement or large strain options and a pressure vector updating with the deformed mesh. Different types of constitutive equations were used ranging from simple elastic-plastic relations up to viscoplastic or unified thermoviscoplastic formulations. Furthermore, the determination of material parameters was performed independently by three different participants starting from the raw characterisation curves, Tab. 1-3 gives an overview.

All computations are 2D axisymmetric. Only one 3D attempt was presented by PSI. Estimation of failure time and location was only performed by 3 participants.

Table 1-3: Finite Element Main Options

#	F.E. code	Elements	F.E. options (large/small displacement...)	Creep law	Parameters identification
1	CASTEM 2000	QUA8	Large Strain	Elastic Plastic	True Stress Strain Curves
2	ABAQUS	QUA8	Large Strain	Thermoviscoplastic	Neural Network
3	CASTEM 2000	QUA8	Large Disp.	Norton-Bailey	AJUSTE
4	SYSTUS	QUA8	Large Strain	Elastic Plastic + Norton-Bailey	from CEA

1.5.2 Thermal loading

As only 2D axisymmetric computations were performed the thermal field was supposed to be perfectly axisymmetric which, of course, was not the case in the experiment (see earlier description of the experiment). Furthermore, only an approximate profile of the temperature through the thickness of the tube was given. In reality it is governed by a logarithm curve for which an analytical estimation is given by Carslaw and Jager (1959), page 189.

Participant #1 performed four different 2D computations in order to evaluate the influence of certain thermal field parameters on the global mechanical response of the tube. First he considered two cases corresponding to the cold (270°) or hot (0°) longitudes. Then he considered an induction skin effect of 3 mm thickness. Furthermore, the nonlinear analytical approximation of the temperature through the thickness of the tube was used.

Participant #2 imposed the axial temperature profile at 2900s. For the time evolution of the maximum temperature on the external side, he followed a thermocouple signal.

Participant #3 used the axial thermal profile at 5100 s. He considered only the maximum temperature of 910°C (non-normalised polynomial approximation) which was assumed to be constant during all the loading sequence. The thermal field through thickness is not well estimated as the linear approximation was adopted.

Participant #4 used the axial temperature distribution at 2900 s and a maximum temperature of 991°C. The thermal field through, the thickness is not well estimated as the linear approximation was adopted.

1.5.3 Global mechanical behaviour

The global mechanical behaviour of the tube is well quantified by two curves. The first one is the load versus elongation, Fig. 1-29, and the second one is the load versus diametrical contraction, Fig. 1-30. The main advantage of these curves is that they can be easily compared with experimental results, where the load is measured by the load cell of the servo-hydraulic machine. For the elongation, the pertinent value is the measurement between the two alumina rods. In comparing this measurements with computations, one must keep in mind that the calculated elongation is a function of both, the load and the applied thermal field. Concerning the diametrical contraction, the major drawback is that the measurement is performed at a constant height of 77 mm which is not always easy to extract from computations.

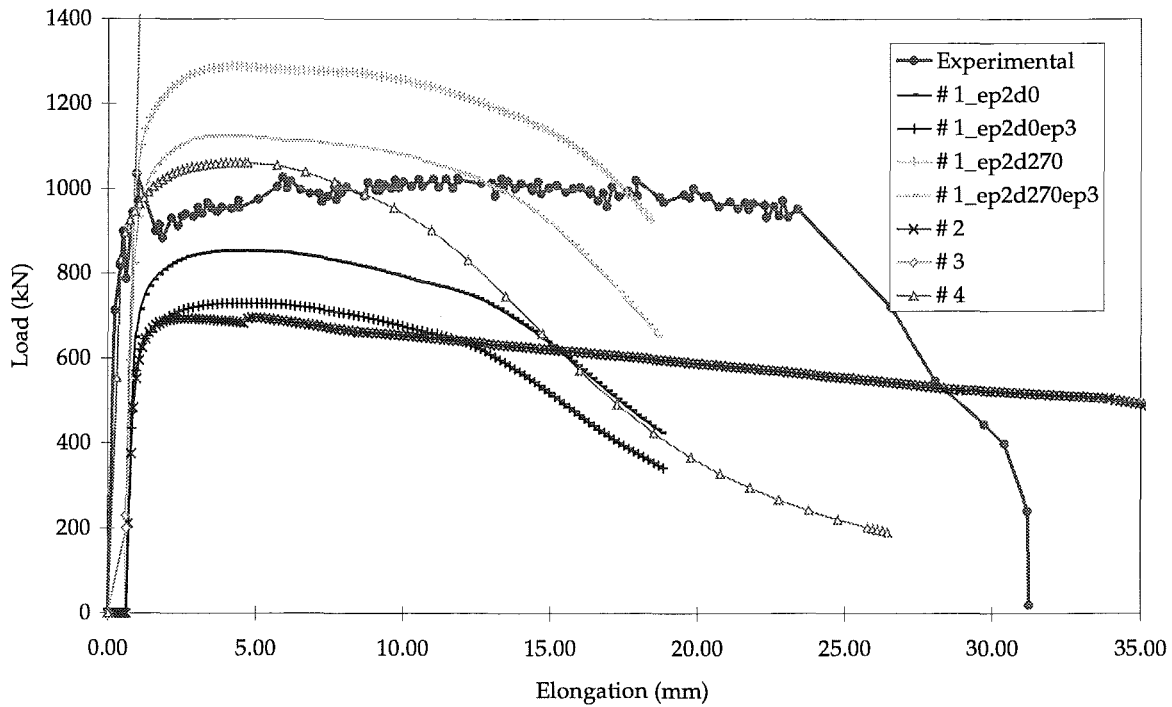


Fig. 1-29: Comparison of experimental and calculated load versus elongation.

For participant #1, no computation is perfectly corresponding to the experimental curve. The induction skin effect can play an important role, but 3 mm thickness seems to be too large. Necking (here assumed to be at maximum load) is occurring earlier in the computation than in the experiment. Furthermore, the experimental elongation seems to be higher than the calculated one for all cases irrespectively to the FE hypotheses. An interpretation possibility is that the internal cracking of the tube is affecting the elongation.

For participant #2, the calculated maximum load is clearly underestimating the experimental value. This can be explained partly by the fact that only the target value of 1000°C was taken into account and not the true experimental temperatures which are lower. After the maximum load the load carrying capacity is decreasing very slowly while the elongation increases. This can be partly explained by the fact that no damage criterion is used in this computation, but it does not explain why the necking is so weak.

Participant #3 predicts an approximately linear elastic global behaviour of the tube. This is due to the fact that he used an elastic-viscoplastic constitutive equation. But, as the internal skin of the tube remains cold, it remains elastic and influences the global mechanical behaviour significantly. So, one can say that these constitutive equations are inadequate for the description of this type of problem (mechanical loading of a structure with high thermal gradients through thickness).

Participant #4 prediction is very close to the maximum load. It is mainly due to the fact that the constitutive equation used is combining elastic, plastic and viscoplastic behaviour of the material. Nevertheless, the necking is occurring much earlier than in other computations.

The same trends are observable for the curves of the load versus the diametrical contraction. Nevertheless, one can notice that the diametrical contraction is quite well described by participants #1, #2 and #4.

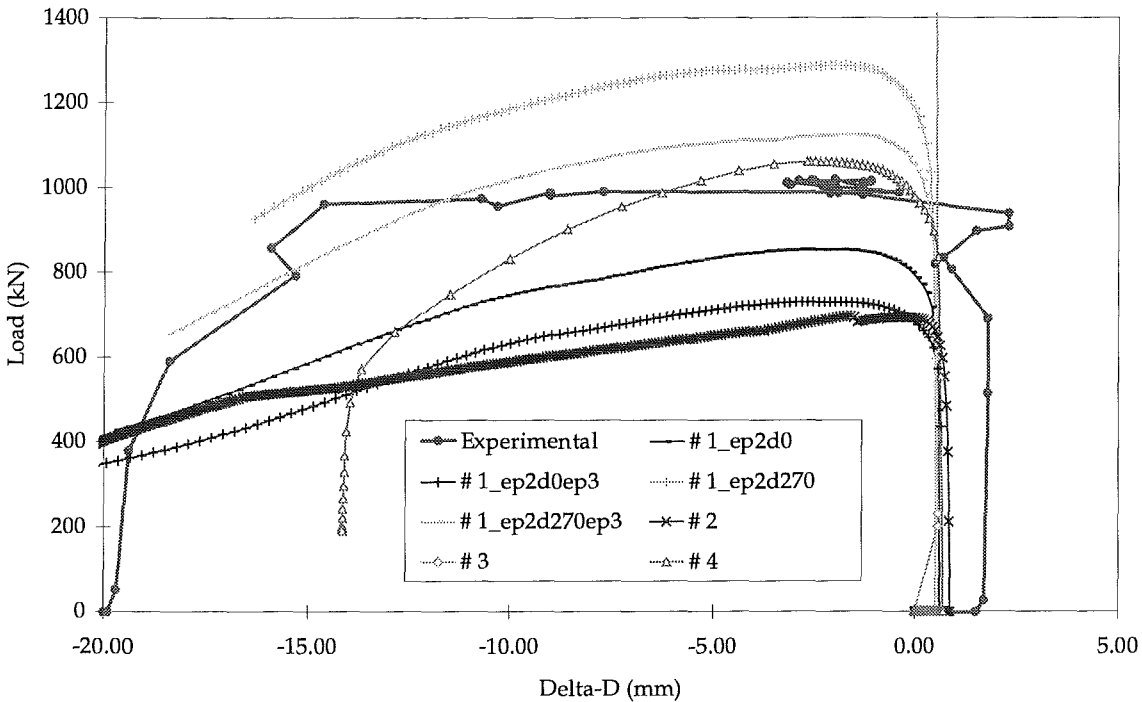


Fig. 1-30: Comparison of experimental and calculated load versus diametrical contraction.

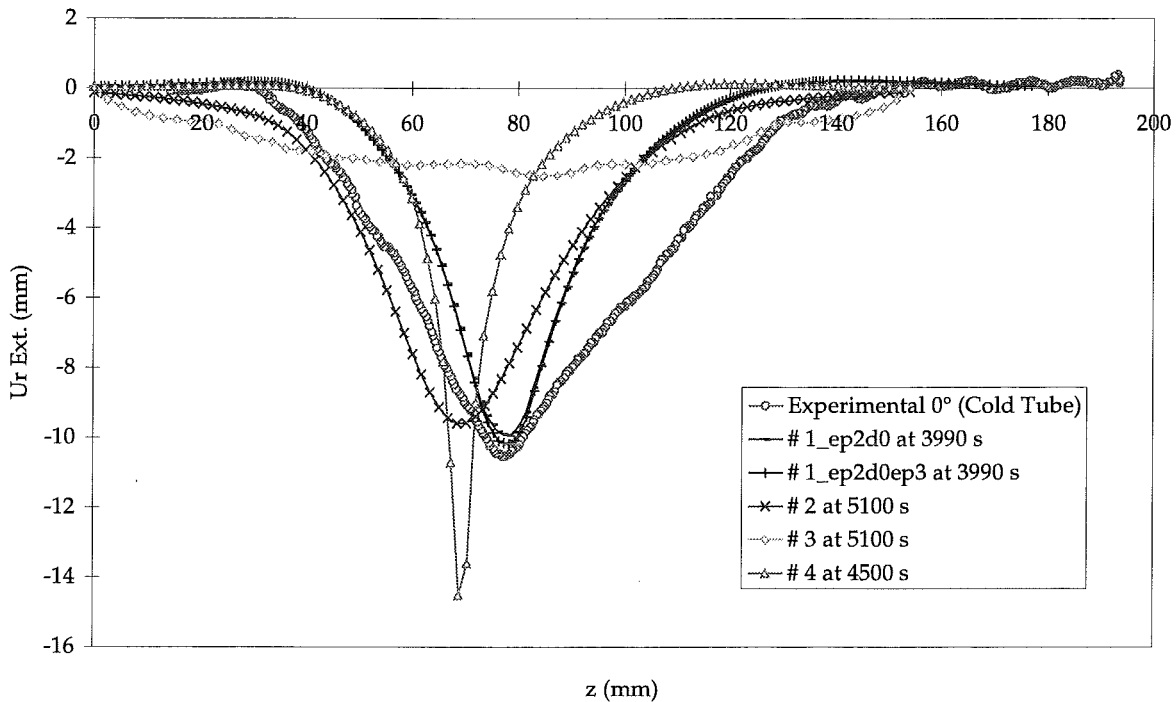


Fig. 1-31: Comparison of experimental and calculated radial displacement of the external line versus the tube height.

The radial displacements along the axis for the external line at the end of computation indicate that a necking is occurring on the external side. Furthermore, the localisation are not at the same height. The experimental external profile measured at the cold tube after test completion is wider than the calculated one, but it is centred at the same height (77 mm) which is corresponding to the diametrical measurement. It is not purely by chance as it is the center of the induction coil.

The comparison between the results of the different participants is not so easy as the final times are not the same. But, one can notice that only participant #1 reported values of z higher than the initial tube length (154 mm). This is due to the fact that most finite element codes deliver results versus the initial co-ordinates and not versus the updated one considering the deformation. By taking this into account, the maximum of necking predicted by participants #2 and #4 coincide with the experimental observation.

1.5.4 Prediction of failure initiation

As already mentioned, very few participants predicted the failure time and the failure location. As participant #3 used a viscoplastic constitutive equation, he also used a Robinson damage criteria. He found that the maximum damaged area is located on the external side. This is not in agreement with experimental observations revealing many cracks on the inner side.

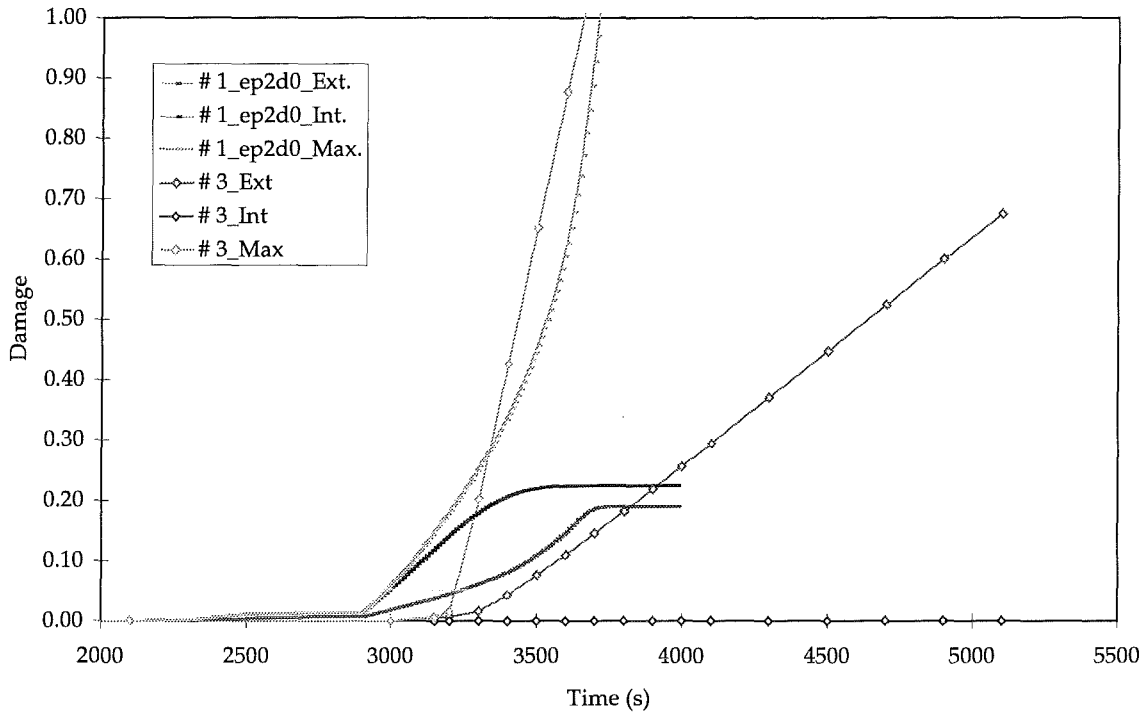


Fig. 1-32: Predicted damage at different tube location.

For participant #1, it is interesting to notice that a small amount of damage is already predicted during the heating phase for the cool part of the tube. But, the predicted damage really begins to increase when the tube is submitted to the mechanical loading sequence. Damage is much higher on the cooled side. The maximum is located at $(r,z) = (15.0,66.79)$ mm for the time 4000 s. The corresponding isovalues of damage are given in Fig. 1-33.

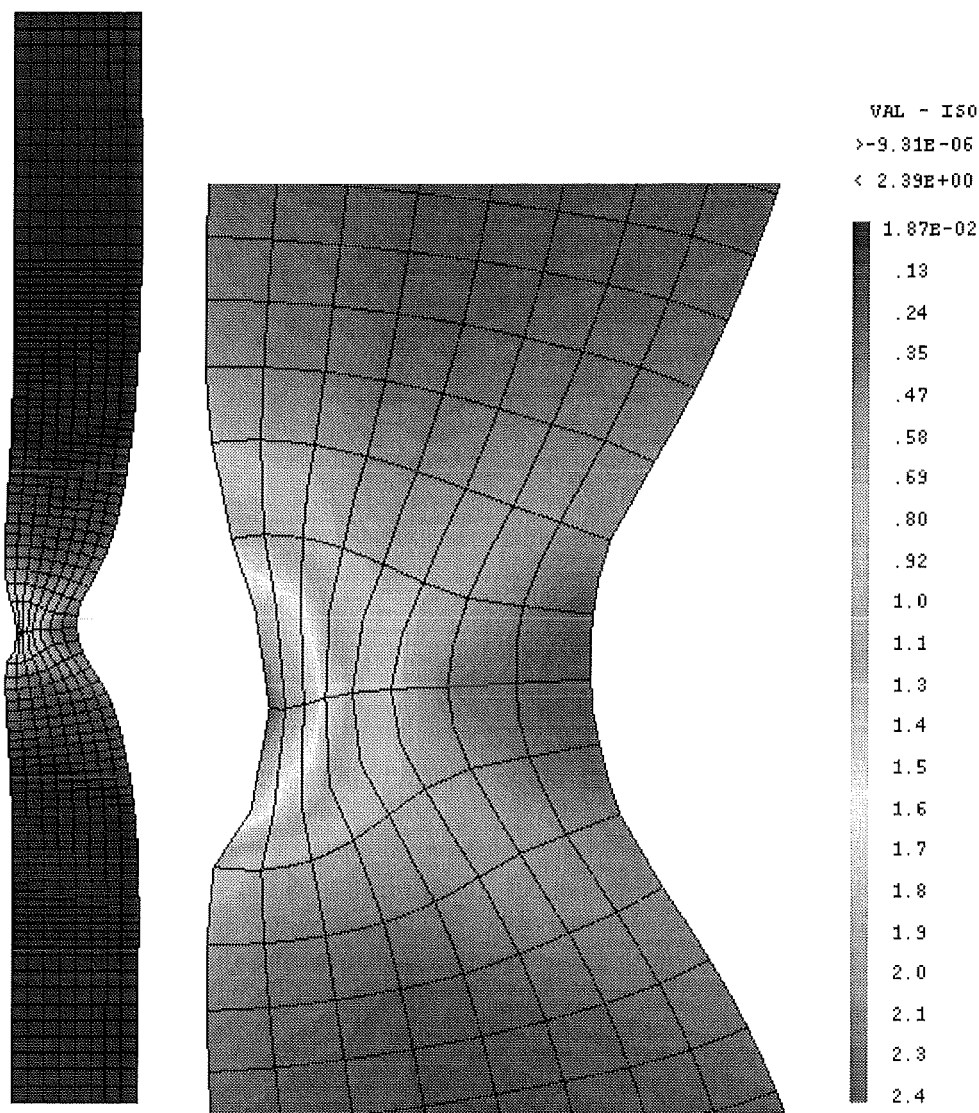


Fig. 1-33: Isovalues of plastic Damage for the particular case calculated by participant #1 (ep2d0 at 4000 s).

All the predicted failure times are considerably lower than the experimental failure time which was considered to be around 5000 s (Sainte Catherine and Champain (1998)). But this was based on the detection of a water leak indicating the presence of a through thickness crack. The post test observation of the tube clearly showed that a large number of cracks are present on the inner side of the tube. So, the initiation of the first crack was probably quite earlier than 5000 s. Unfortunately, it was not possible to determine this time. The failure initiation seems to occur earlier for the hottest longitude region. The through thickness crack was observed between angles 61.5° and 90° which belong to the hottest area.

The experimental elongation seems to be higher than the calculated one for all cases irrespectively to the FE hypotheses. An interpretation possibility is that the internal cracking of the tube is affecting the elongation.

1.5.5 Conclusions from the FASTHER benchmark

From the results obtained, we can make the following observations :

- Purely viscoplastic modelling is inadequate as the internal skin remains elastic. An elastic-plastic or unified modelling is more appropriate.
- Thermal loading already gives rise to yielding of the tube.
- Load evolution and its maximum are largely dependant on the thermal field. The non-axisymmetry of the thermal field and the unknown induction skin thickness give rise to the main uncertainties in the FE simulations.
- The reduction of diameter on the external side is well predicted. Furthermore, the global shape of the tube during the necking is quite well modelled.
- Failure initiation is predicted to occur on the internal skin at a time very close to the experimental maximum load. This is quite coherent with the large number of cracks observed on the inner side of the tube after the test.
- Maximum damage is predicted at the internal skin (cold side), but for the hottest longitude and the crack causing the leakage was experimentally observed to occur in the hottest region.

Improvements are proposed in three main directions :

- Experimental improvement for a better control of the thermal field and use of a vessel in order to perform creep tests under controlled atmosphere,
- Full 3D finite element computation,
- Use of a non-unified elastic-plastic-viscous constitutive equation.

2. Lower head melt-through failure caused by the attack of molten core material

J. Birchley, G. Duijvestijn, H. Hirschmann, P. Hosemann, B. Jäckel, D. Kalkhof, PSI, Switzerland

2.1 Melt-through experiments CORVIS

One of the objectives of the research on nuclear safety is to evaluate the behaviour of the reactor pressure vessel (RPV) under thermal and mechanical loading in case of a severe accident. Failure mechanisms had previously been studied by means of computational models, as part of a post-TMI research programme initiated by the USNRC. From these studies a general methodology was formulated, the modes of failure identified and the timings estimated (Rempe, 1993). Missing at the time, however, were experimental data to validate the models. The research project CORVIS (Corium Reactor Vessel Interaction Studies) was conducted at PSI to investigate the potential failure of the RPV lower head when attacked by molten corium during a core melt accident. The experiments were performed using models of RPV lower head penetration tubes of reactor-typical designs, at atmospheric pressure. The corium substitute was an alumina/iron thermite melt of which the oxidic and/or the metallic part could be applied. The decay heat was simulated by a sustained heating of the corium substitute with a submerged electric arc. Heating up of the steel structures, melting, structural deformations and thermal effects of oxide crusts were observed. Temperature measurements were obtained from thermocouples on the outer surface of the test plate, within the test plate, at the inner surface in contact with the melt, and on penetration tubes. Infra-red thermography provided detailed on-line spatial resolution of the temperatures, externally. The facility configuration is shown in Fig. 2-1

Test vessels of differing size were used during the program, with the largest scale experiments performed on a vessel of an internal diameter of 740 mm. The models of the RPV wall (vessel bottom) were plates manufactured from reactor steel with a thickness of 100 mm, tube penetrations inserted in the plate were of scale 1:1 compared to reactor design. A mass of 450 kg of oxide melt was used, and the specific power of the arc heater was ≥ 250 W/kg of melt. Thus the dimensions of the test components are representative for a commercial RPV. The overall length scale is large enough to qualitatively capture the transport phenomena, or at least, large compared with the scale of the processes at the interface between the melt and the test components. Computational modelling supplements the measurements to provide a deeper understanding of the physical processes underlying the observations, and hence apply the knowledge to a wider range of conditions, for example high pressure.

A long series of tests was performed since February 1993 through September 1996:

- 16 experiments to develop and qualify the experimental technique (93/2-96/3),
- 1 large scale test on a lower head without penetrations (93/6),
- 2 large scale tests on a lower head with a BWR drain line according to the specifications by General Electric (94/12-96/5),
- 1 large scale test on a PWR lower head with instrument tube penetrations according to specifications by Westinghouse (96/9).

The experimental results, and analyses from the earlier part of the programme, 1993 to 1995, are reported by Brosi (1997). Details of the experiments performed during 1996, together with technical details and analytical results are given by Hirschmann (1997).

Three experiments were carried out in 1996. They are part of the RPVSA project.

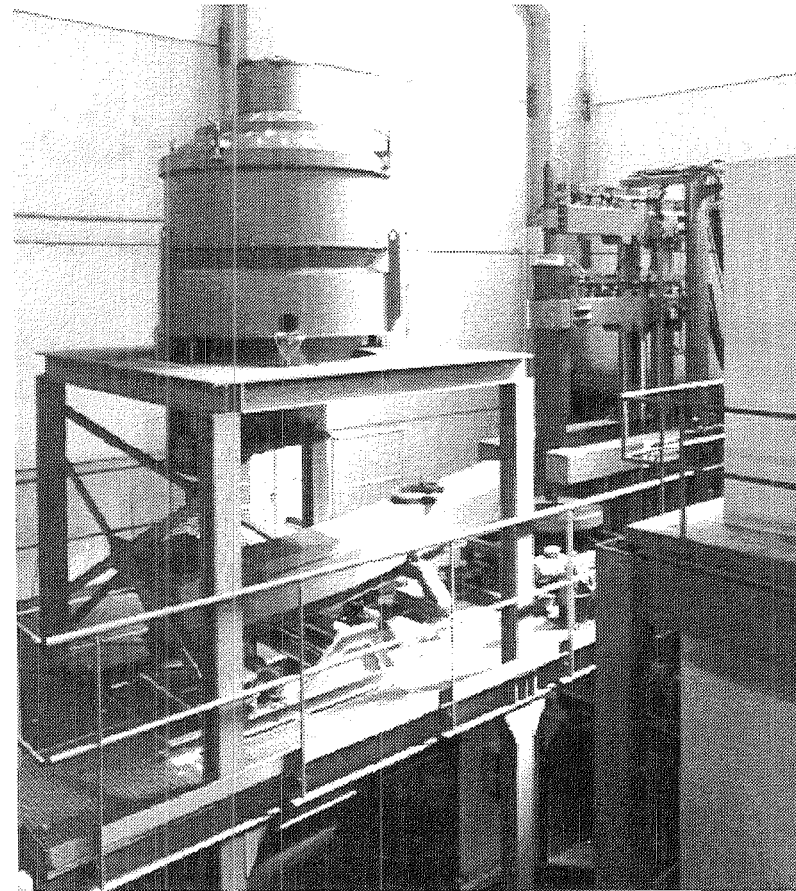
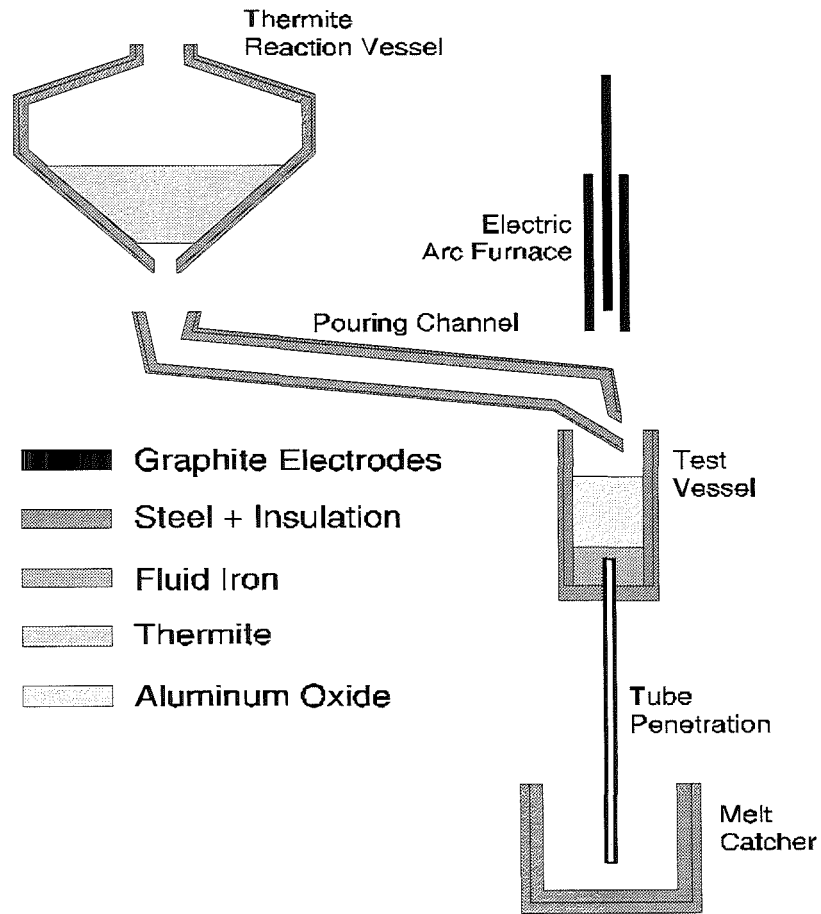


Fig. 2-1: CORVIS Experimental Facility

2.1.1 Experiment 01/11 (March 28, 1996)

Experiment 01/11 was the first test of a sustained heating in a melt of pure aluminium oxide. Since the oxidic melt imposes a much smaller heat load on the structures than the metallic melt, the sustained heat input now assumes a greater importance. Experience from earlier tests had shown that only about half of the heater power is delivered to the melt. Therefore the electric arc heater was upgraded to provide the required power. An average total electric power of 200 kW was achieved, corresponding to a specific power to the melt of about 250 W/kg, compared with a typical specific decay heat power for a molten reactor core (2 hours after shut down) of 150 W/kg. The test plate did not carry penetrations, so that the melt could not flow out immediately after pouring, and the temperatures in the test plate could be studied for a melt which was almost stagnant in the vessel except for flow induced by the heat input. A temperature measurement in the melt with molybdenum shielded high temperature thermocouples was possible during the first 100 s although the thermocouples were in contact with remnants of molten thermite iron. Thus, at least the initial temperature of the melt could be measured. Some localised melting of the test plate occurred during the start of the test due to impingement by a jet of molten material. Fig. 2-2 shows the region scooped out to maximum depth of 2 cm, and the layer of resolidified material separated from the unmelted steel by a narrow gap. The leading edge of the jet was found to have contained some residual thermite iron in addition to the main mass of ceramic.

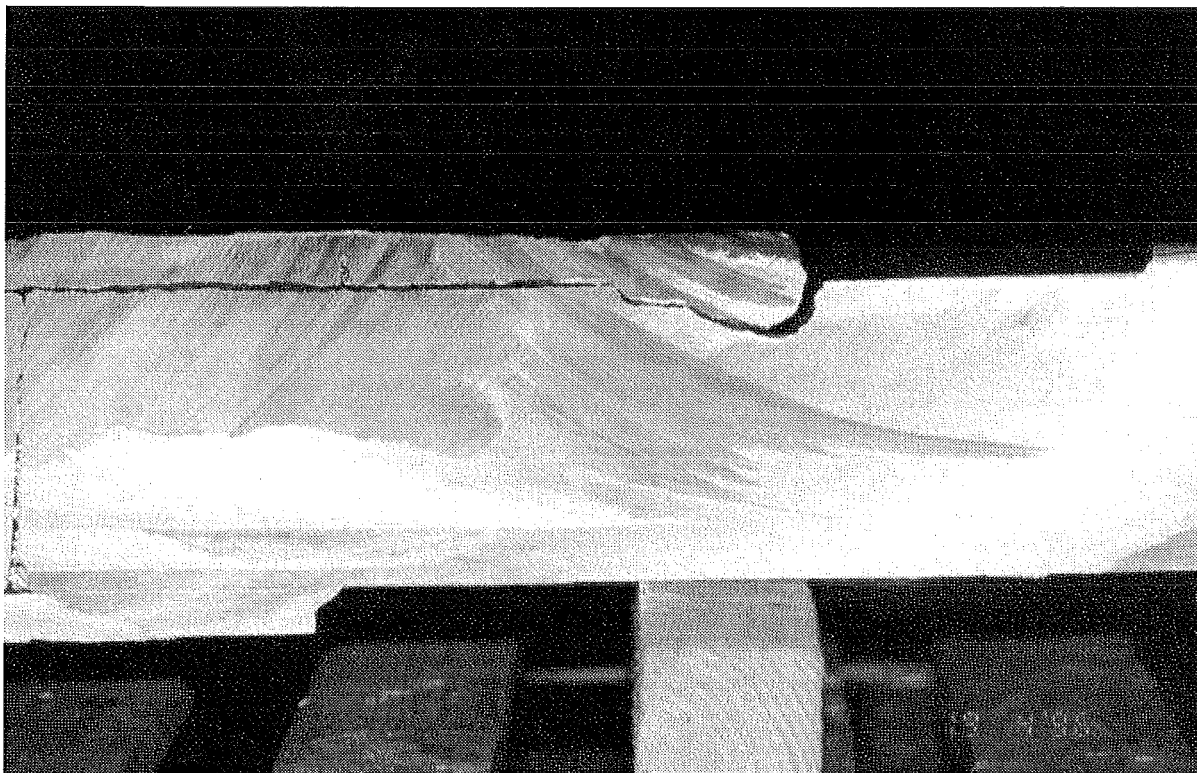


Fig.2-2: Zone of jet impingement: gap between test plate and mass of solidified thermite iron and steel ablated from plate (01/11)

It cannot be concluded definitely whether a jet of pure oxide would similarly have eroded the test plate. There was no further melting of the test plate, after jet impingement. Molten material near the wall solidified rapidly to form a crust, which limited the heating of the test plate and retained most of the heat within the molten region and inhibited further solidification until the power was turned off. Partial remelting of the crust may have occurred after 2500 s.

Later examination revealed two regions of solid alumina, indicated in Fig. 2-3 by the region occupied by the crust (red alumina) where rapid solidification occurred, and the grey alumina zone of slow solidification. The temperatures on the outer surface of the plate reached a maximum of 1100 °C, compared with >2000 °C in the melt, as the heat flux was reduced due to the insulating effect of a layer of solidified melt. The thermal response is shown in Fig. 2-4.

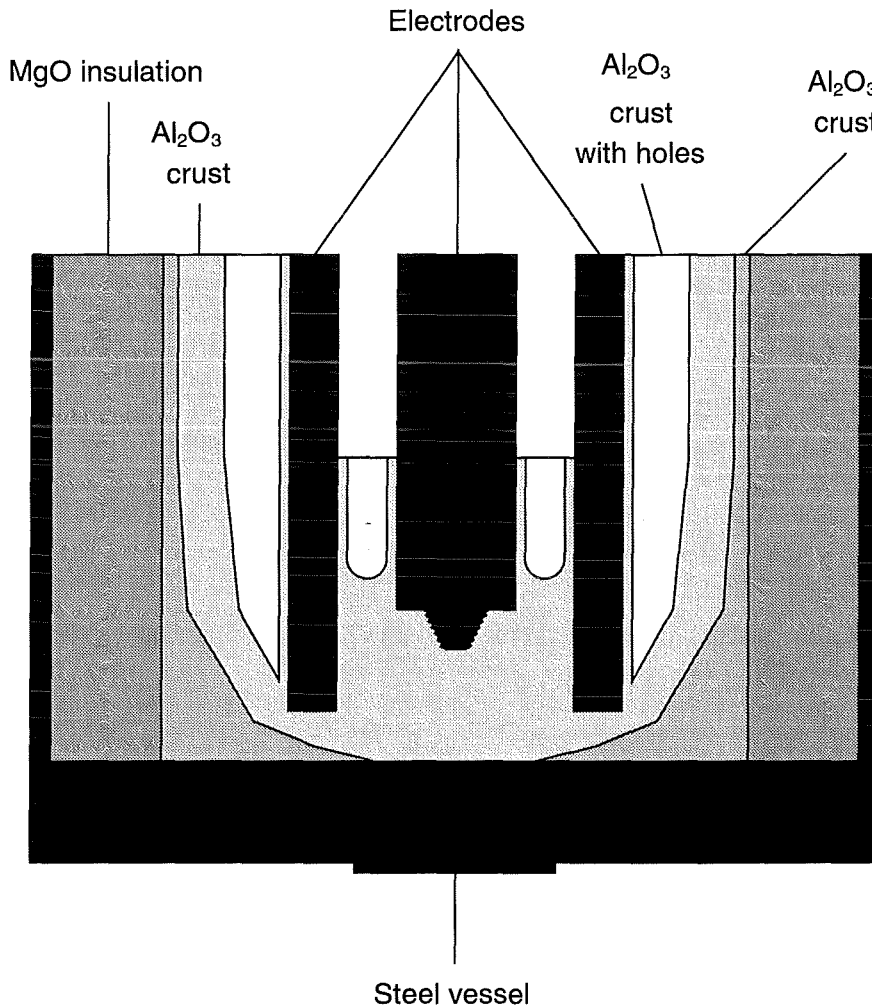


Fig. 2-3: Regions of rapid solidification (crust) and slow solidification of alumina

The experiment demonstrated that a ceramic melt tends to solidify and form a crust which inhibits melting of the steel structure.

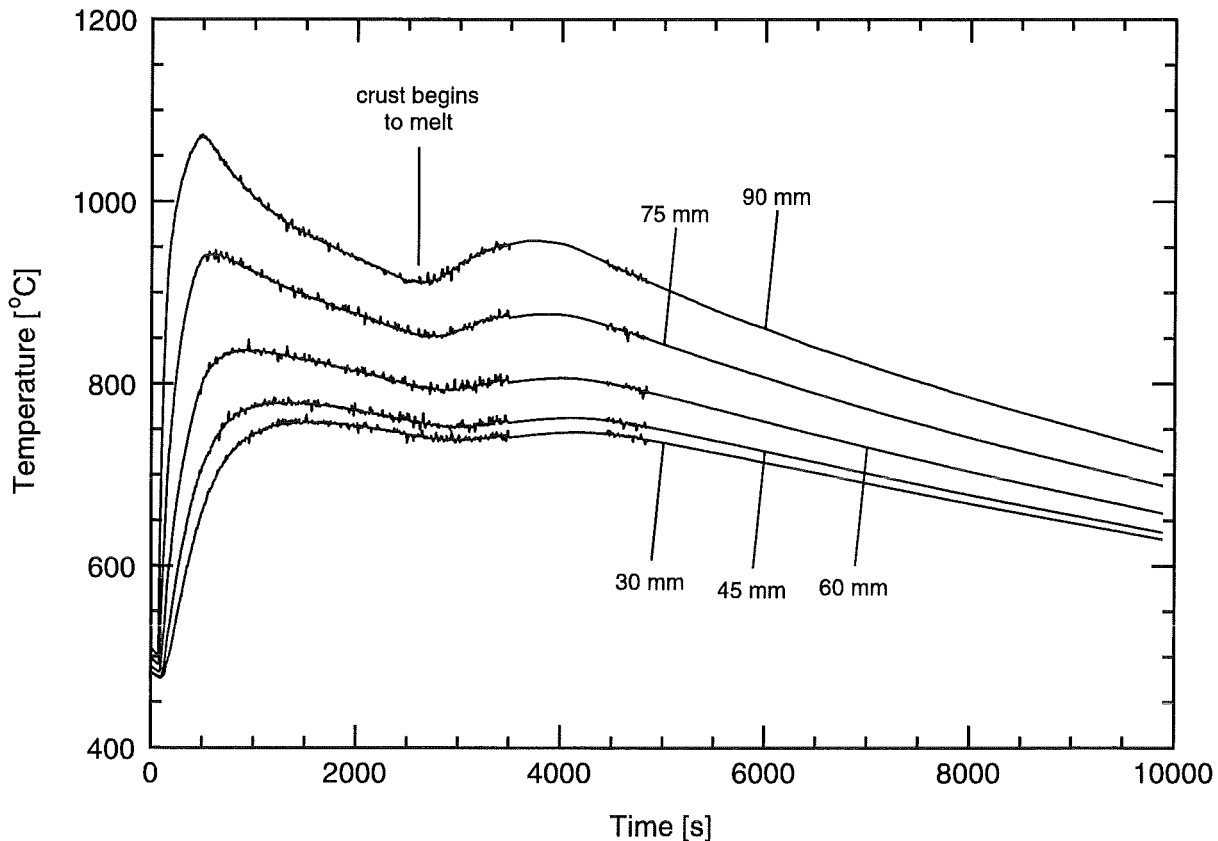


Fig. 2-4: Temperature histories at different depths of the test plate at a radial distance of 200 mm (01/11)

2.1.2 Experiment 03/2 (May 30, 1996)

In an earlier experiment 03/1, a straight (vertical) model of a BWR drain line had been subjected to an attack by metallic melt. Experiment 03/2 complemented the investigation of the drain line behaviour by studying its response to attack by an almost pure oxidic melt. The drain line tube was formed with realistic bends according to the design of the General Electric BWR at Mühleberg, Switzerland. The curved parts of the drain line had been expected to be weak points at which, in the absence of water, the tube could melt through immediately upon contact with the melt.

The oxide melt of initial temperature of 2245 °C - 2270 °C was poured into the experimental vessel and impinged onto the test plate. There was, again, a small quantity of thermite iron but less than in experiment 01/11 and distributed within the oxide instead of concentrated at the leading edge. The test plate was locally eroded to just a few millimetres, in contrast to 01/11.

The melt flowed into the drain line and filled it completely along its 7 m length. The melt flow was stopped by the steel plug at the end of the tube extension. Otherwise, the melt would have penetrated further. **For a real core melt accident it was concluded that the melt would penetrate the entire length of that section of the drain line which does not contain any residual water.** The drain line was not sheared off or melted through. Geometric distortions and plastic elongation by 50 mm of the tube extension were observed after the experiment. Fig. 2-5 shows the thermal behaviour of the drain line. During the first 200 s, temperature maxima between 1050 °C and 800 °C were measured on the outside surface of the drain line tube, depending on the distance from the test plate. The highest surface temperature of 1050 °C was temporarily reached on the tube near to the welding between tube

and nozzle. It is interesting to note that the temperatures in the drain line reached maximum values in the first few minutes after filling with melt, and then decreased due to ambient losses while thermally isolated from the source of heat in the bulk melt. Significantly, the flowing oxide melt caused no erosion at the nozzle or in the drain line.

At the same early time, the drain line nozzle and the central region of the test plate were also heated up by the melt, but the outside surface temperatures did not exceed 800 °C. Later on, during the period of sustained melt heating, a hot zone developed around the welding nozzle with (outside) surface temperatures up to 1100 °C. After 5000 s of heating temperatures of 1450 °C were measured in the test plate at a level of 90 mm above the lower plate surface (i.e. 10 mm below the upper plate surface). Fig. 2-6 shows the temperatures in the test plate. As had occurred in experiment 01/11, a temperature "plateau" was observed during the time between melt pouring and 2000 s, which was explained by a transient build-up of a thermally insulating oxide crust on the plate. Again, there were signs that the crust had started to remelt due to the sustained heat input, but nevertheless melting of the steel plate was prevented. **These temperatures may be used for stress analyses of the lower head.**

Some distortion of the test plate occurred, as seen from the measurement of displacement shown in Fig. 2-7. The early, non-monotonic behaviour is attributed to thermal stresses due to large, but decreasing temperature gradients. The longer term behaviour is more uniform and indicates small but potentially significant creep deformation, even at this low mechanical loading. Despite small displacements the test section did not fail. **It is clear however, that the drain line would have been torn off at higher internal pressure, due to accumulation of creep damage. Ablation of the drain line by the flowing oxide melt was negligible.**

2.1.3 Experiment 04/1 (September 19, 1996)

The test section was a model of a PWR lower head of Westinghouse design. The test plate carried 5 penetrations with long tube extensions at the lower side, representing the guide tubes for the movable neutron flux detectors. The construction of the penetrations were the same as those of the PWR at Beznau, Switzerland. One of the tubes (I) was closed; the other four (II, III, IV, V) were open. A pure oxide melt of 450 kg was used.

As in 03/2 minor and localised erosion of the test plate was observed, though it was insignificant in terms of structural impact. A small amount of oxide melt entered the 4 open tubes and penetrated to distances up to 4 m. After the experiment, the melt line in the tube extensions was found to be broken in several pieces. The central (closed) tube contained no oxide but only remnants of the metal plug. The transient temperatures on the surface of the tube extension reached maxima between 200 °C and 400 °C, depending on the distance from the test plate, and then slowly decreased. The surface temperatures on the closed tube and on one of the open tubes are shown in Figs. 2-8. After 1000 s of sustained heating, a hot area developed around the test plate centre with maximum temperatures of 1100 °C at the outer surface. The hot area spread to most of the test plate by the end of the period of sustained heating at 5200 s. The temperature histories on the outer surface of the test plate, and through the test plate are shown in Figs. 2-9 and 2-10, respectively. Near the test plate upper surface the temperatures exceeded the melting temperature of steel up to a depth of 20 mm, and reached a maximum of 1500 °C at 3000 s. It is interesting to note that the temperatures were stable about 1000 to 2000 s, but then increased again, apparently as the crust began to remelt. There is indication from post-test inspection that the crust completely remelted at the location of steel melting.

Above the test plate, the penetrations were melted off up to remnant lengths of 40-60 mm. These remnants had probably been enclosed in an oxide crust for a long time.

Remnants of the melted penetrations accumulated at the centre became welded to the test plate. Fig. 2-11a shows the original configuration of the four open and the central, closed penetration tubes (and also the melt thermocouples), to be contrasted with the photographs of the post-test remnants and the cake of refrozen inconel from the melted tubes, shown in Fig. 2-11b. The oxide prevented melting of the plate surface except in this small area. The test section did not fail, nor were there any permanent deformations of the tubes below the test plate. In particular, the penetrations did not slip out of their seats in the test plate.

The results demonstrate that the oxide crust shields the structure from the thermal attack. Melting occurs only after remelting of the oxide crust. The measured temperatures and the other observations provide data to support development and qualification for analyses of the lower head behaviour.

2.1.4 Summary of major findings

Unlike superheated metallic melt, oxidic melt readily solidifies on contact with steel structures to form a crust. The solid crust has an insulating effect which reduces the heat load to the structure, limits the structural temperature and the extent of any melting. The insulating effect is enhanced if a gap develops between crust and structure.

Quite small amounts, 5 percent of the melt mass, of superheated metallic melt can cause significant erosion of the steel by jet impingement, particularly if concentrated at the leading edge of the jet. Any erosion caused by a jet of oxidic melt containing a small fraction of distributed metallic is insignificant.

The crust and gap behaviour is controlled, apparently, by the interaction of heat input and transfer mechanisms, and deformation. Under sustained heat input to the melt, the structural temperatures continue to rise slowly. Eventually remelting of the crust and melting of the structure can occur.

The molten ceramic material readily flows into penetration tubes that are open within the vessel and can occupy a considerable length of the tubes. Initial crust formation on the inside of the tube may cause the melt to retain its heat and remain in a molten state long enough for it to penetrate a long way. There is no indication of penetration tube or weld failure due to contact with ceramic melt in CORVIS, at the low internal pressure.

Despite the tendency for a crust to form on steel structures, penetration tubes within the reactor vessel are melted where they extend beyond the crust into the molten region, allowing the melt to enter tubes which are otherwise closed.

Large thermal stresses develop in thick structures, evidenced by distortion of the test plate. Some creep behaviour may occur following sustained heating, even under low mechanical load.

The CORVIS results provide data to support analytical models which can be applied to a wider range of conditions. In particular, with the aid of material data obtained via other programs, it will be possible to make assessments of failure at high pressure.

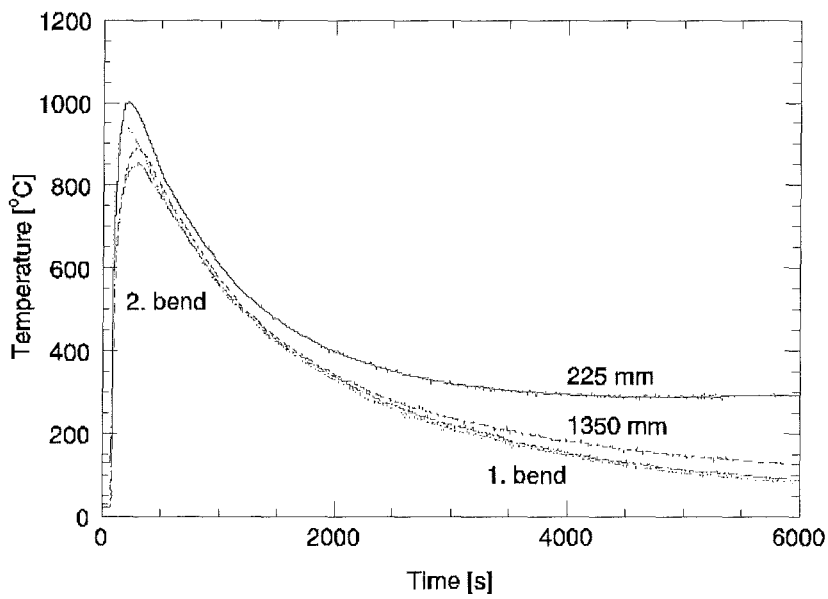
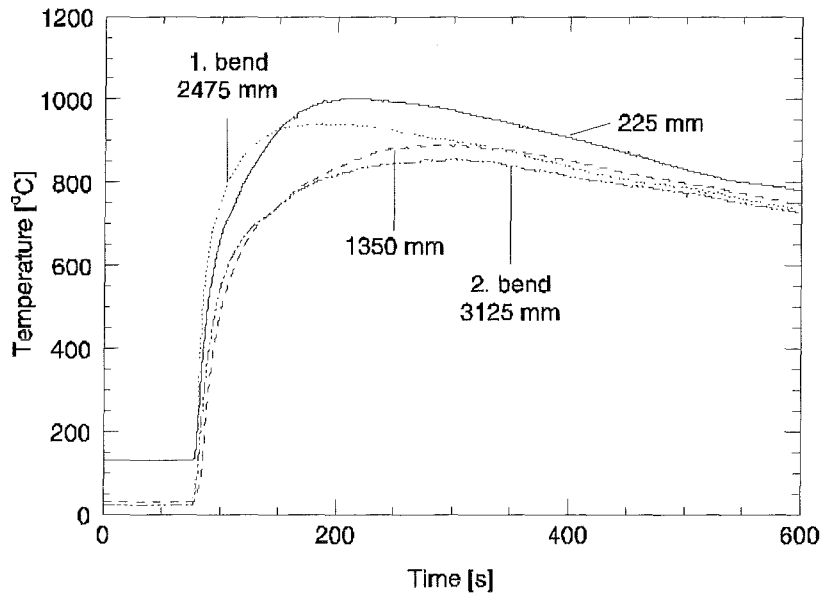


Fig. 2-5: Temperature histories at 4 locations on the drain line (03/2)

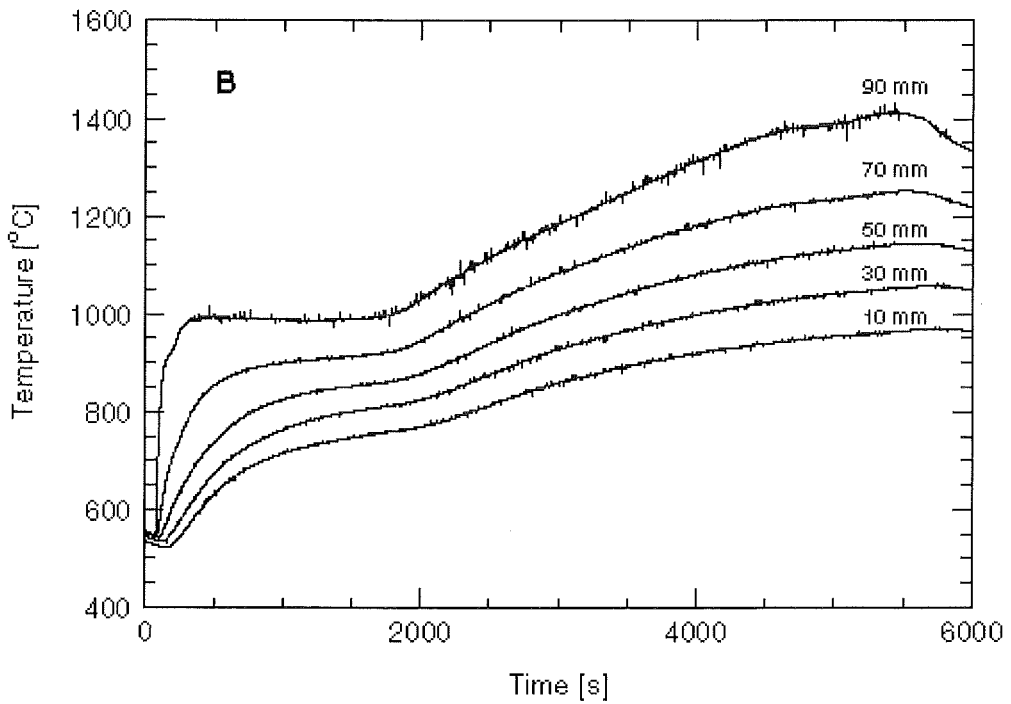
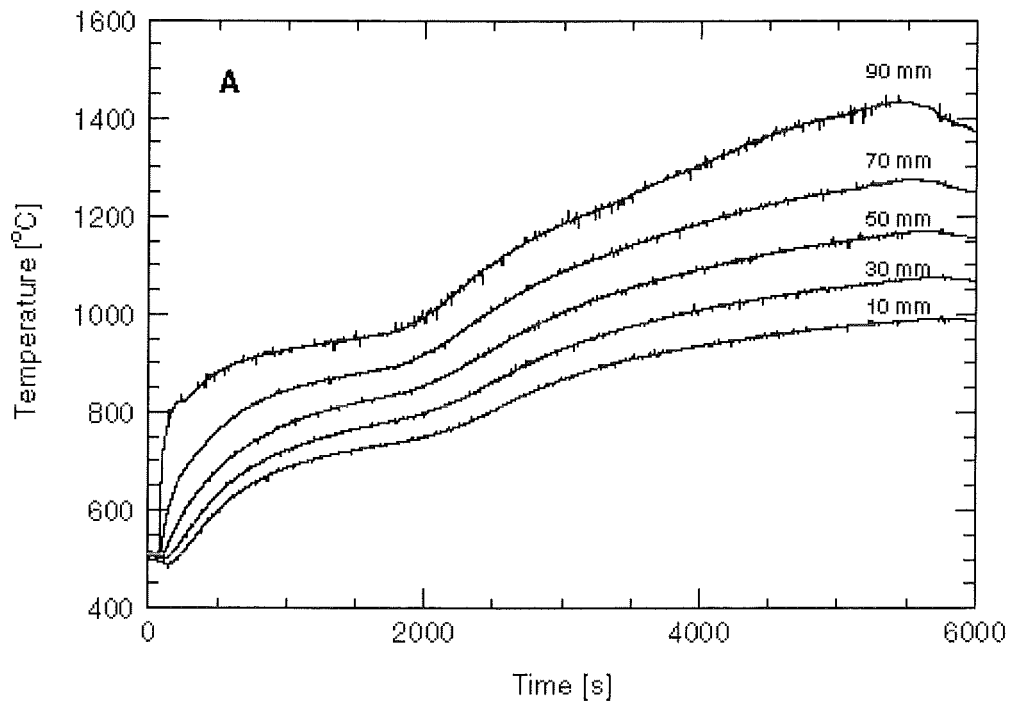


Fig. 2-6: Temperatures at different depths within test plate (distance from lower surface) – figure B is on side of melt pouring (03/2)

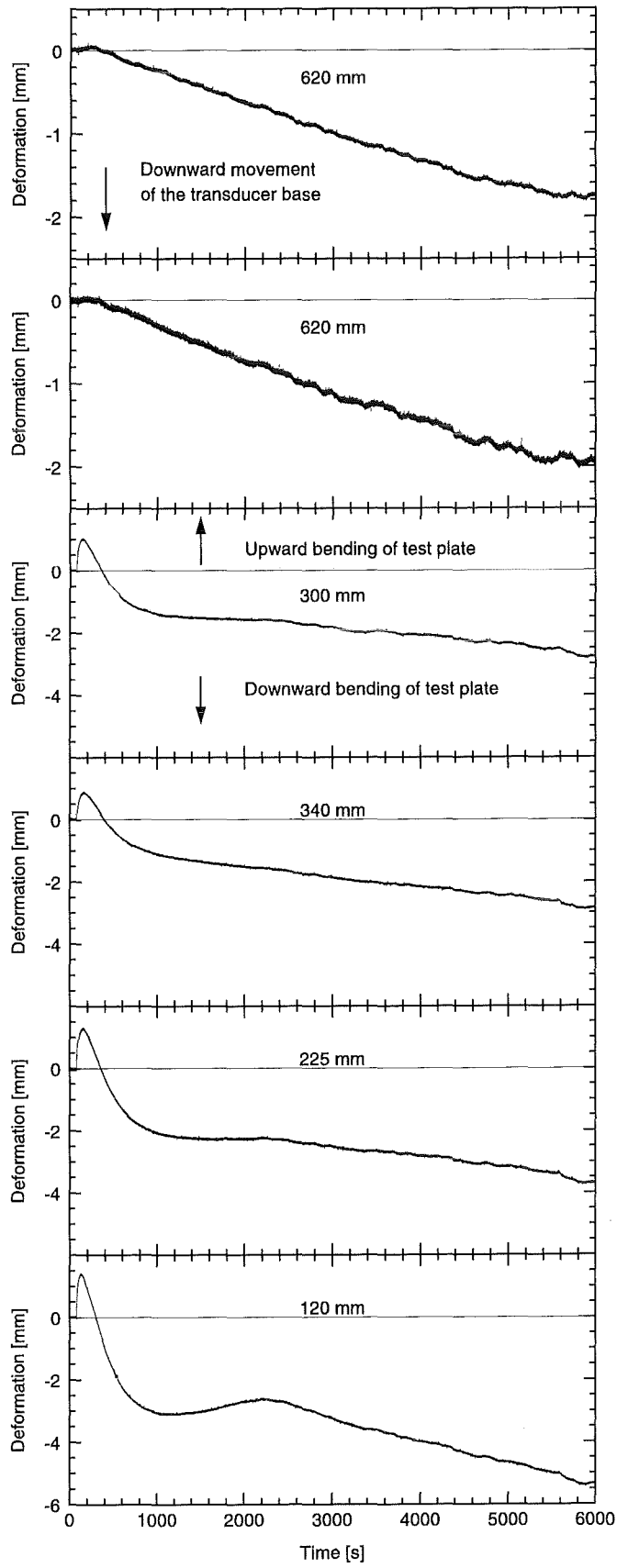


Fig. 2-7: Vertical displacement of the test plate at different radial positions (03/2)

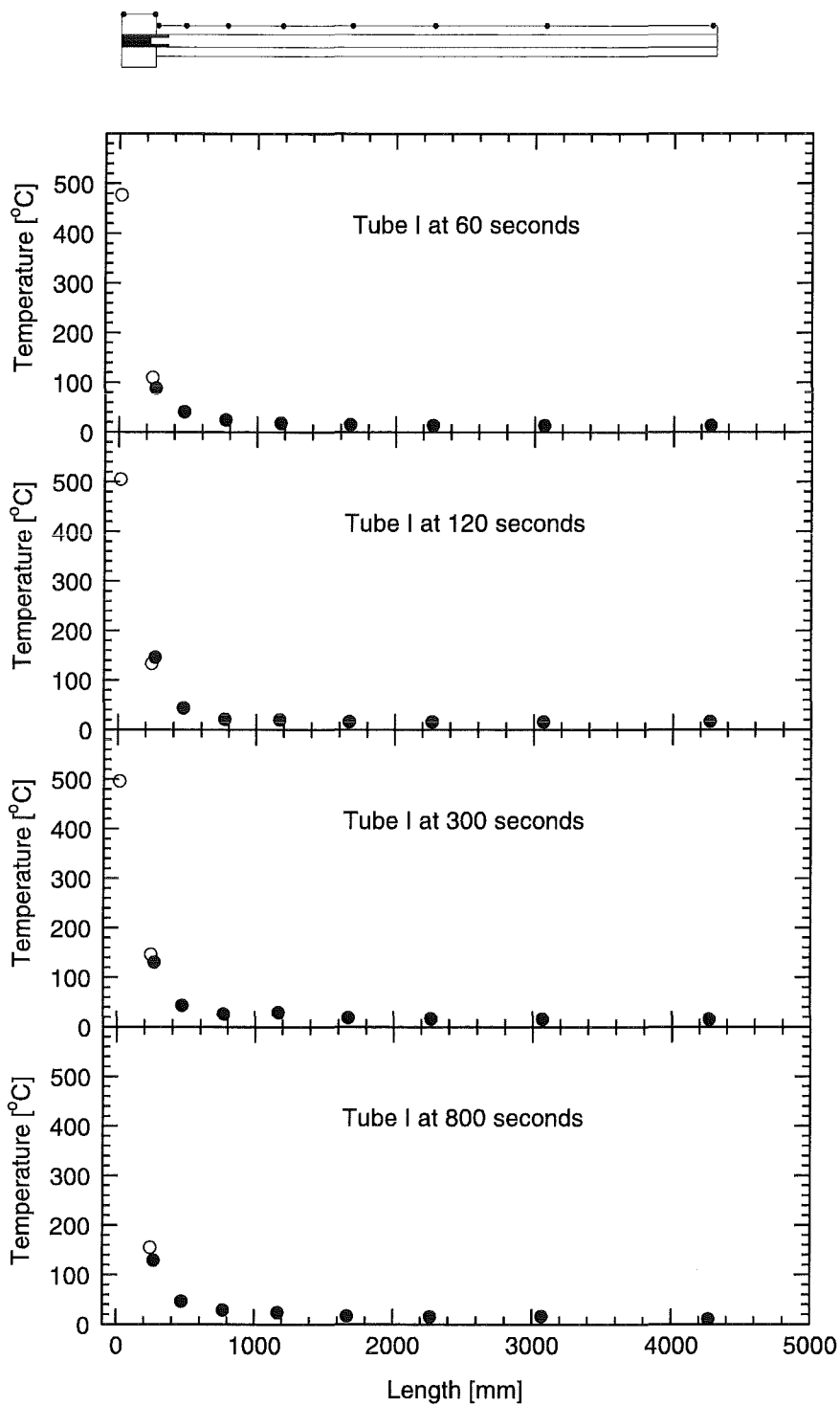


Fig. 2-8: Temperatures on instrumentation tubes I and II at 4 different times – schematic indicates locations of alumina plugs and thermocouples: (tube II curves show thermography measurements) (04/1)
 a) Tube I

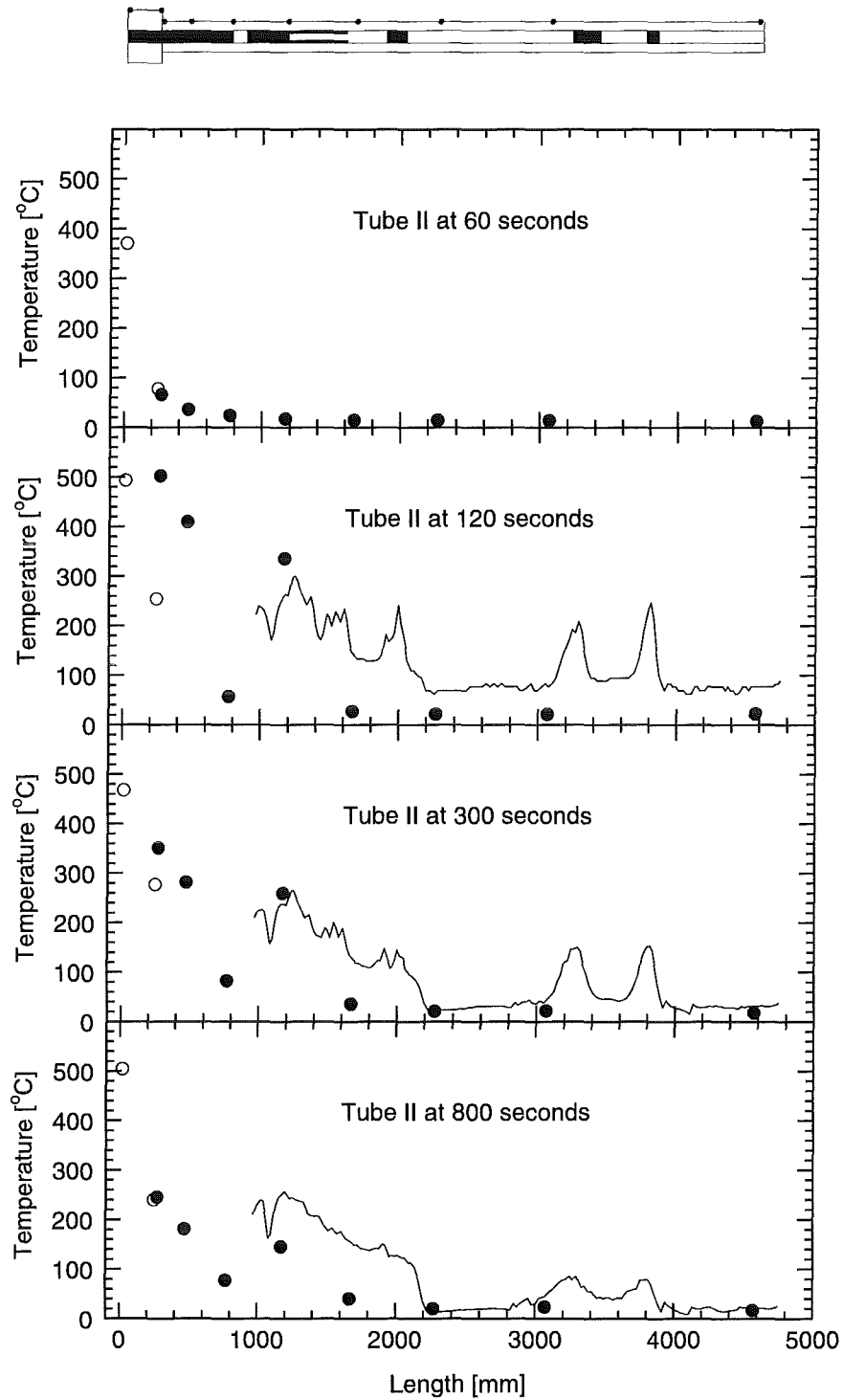


Fig. 2-8: Temperatures on instrumentation tubes I and II at 4 different times
 – schematic indicates locations of alumina plugs and theormocouples: (tube II
 curves show thermography measurements) (04/1)
 b) Tube II

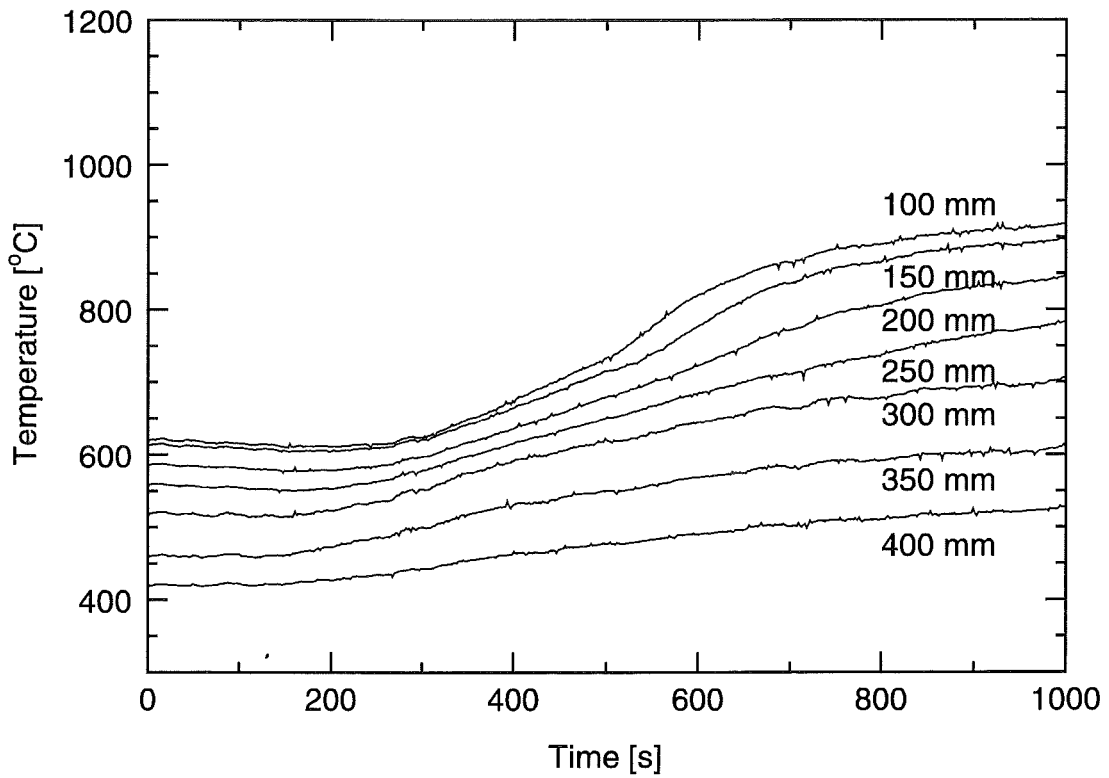
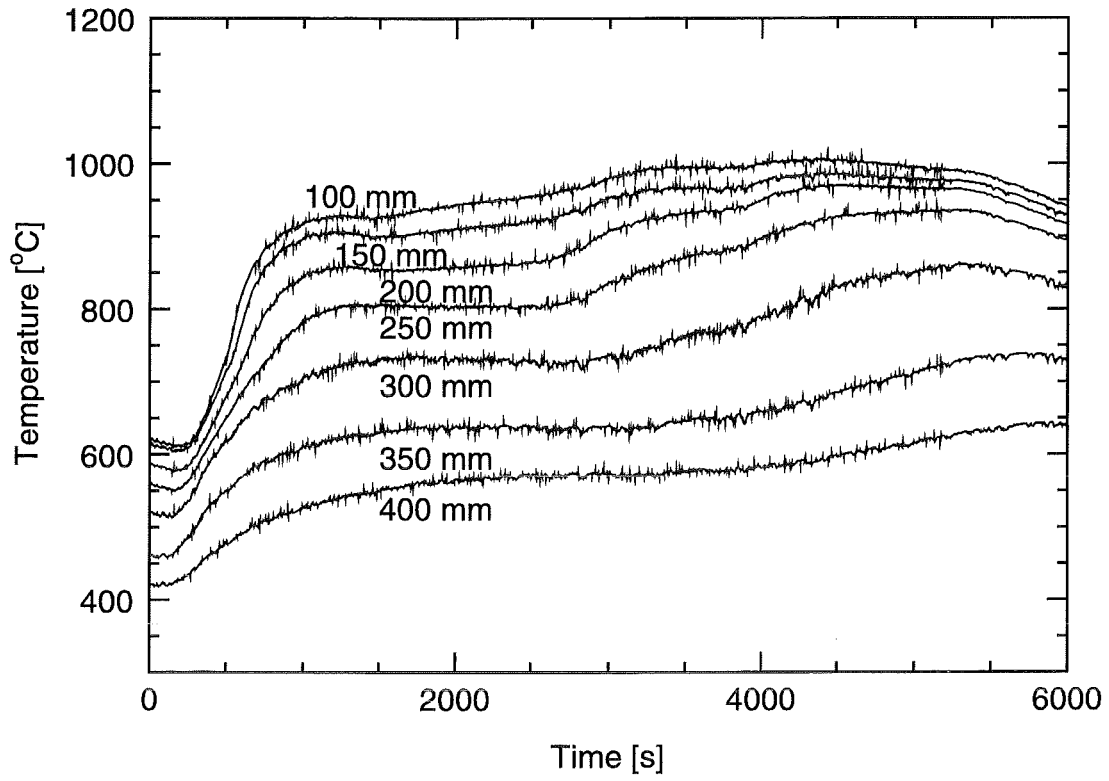


Fig. 2-9: Temperatures on test plate lower surface at different radial locations (04/1)

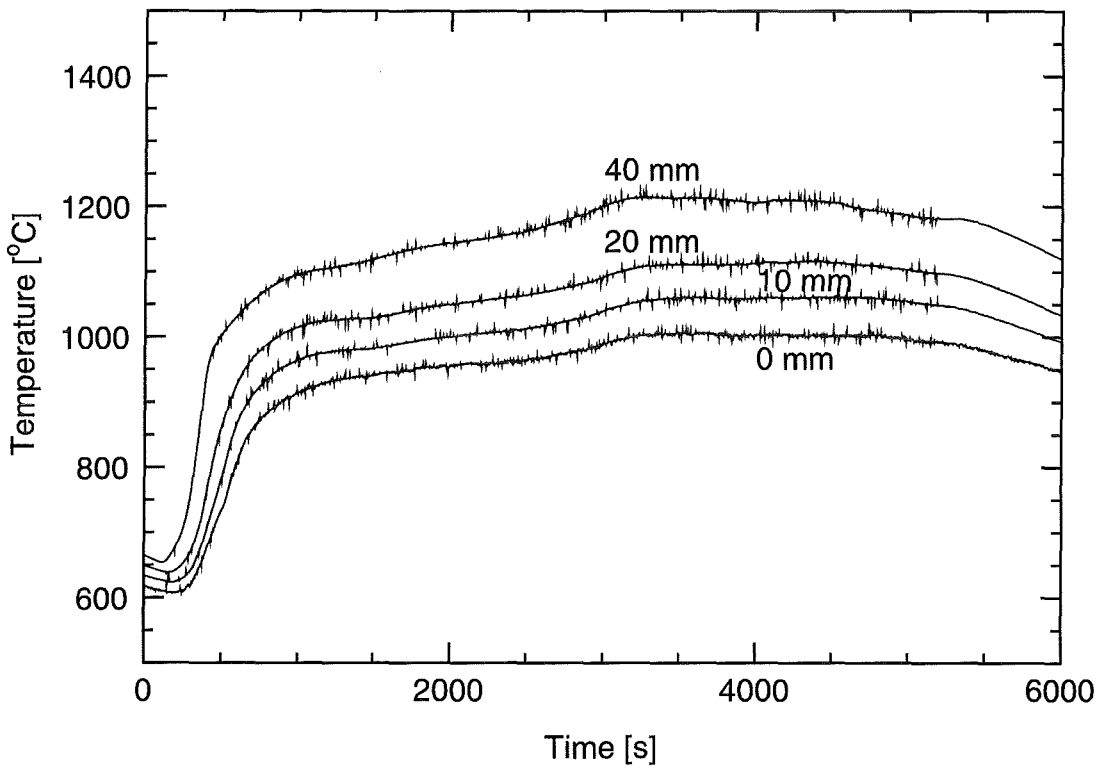
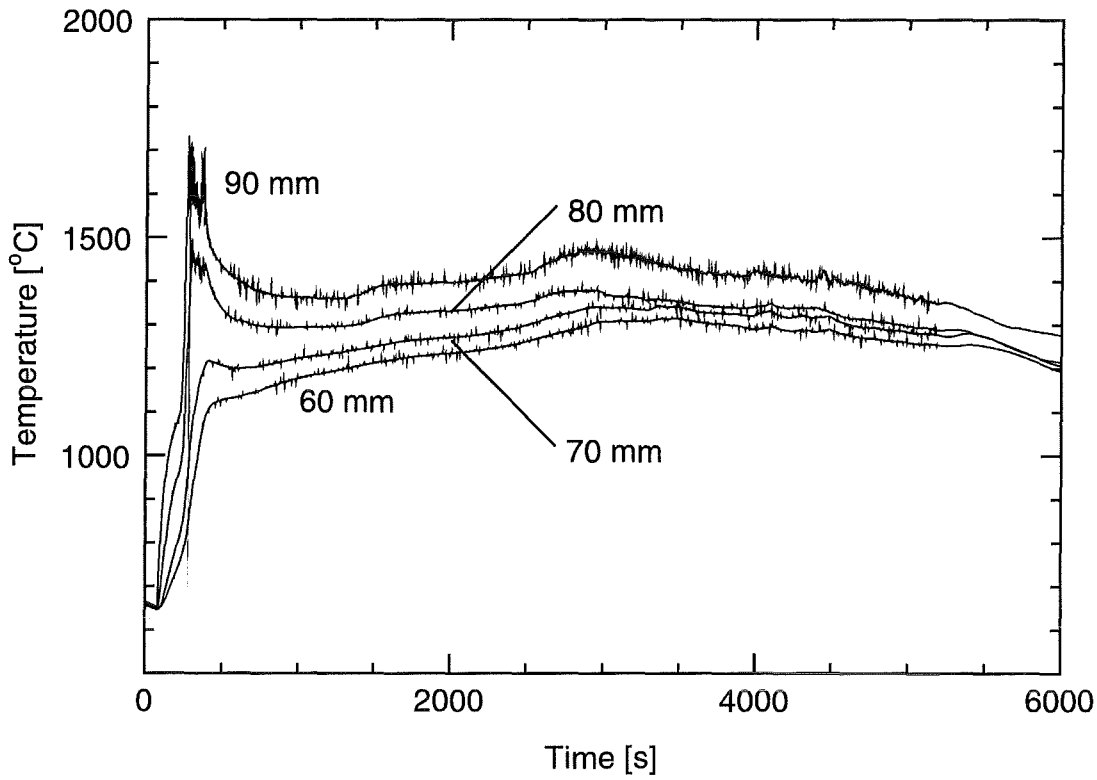


Fig. 2-10: Temperatures at different depths within test plate (distance from lower surface) close to central penetration (04/1)

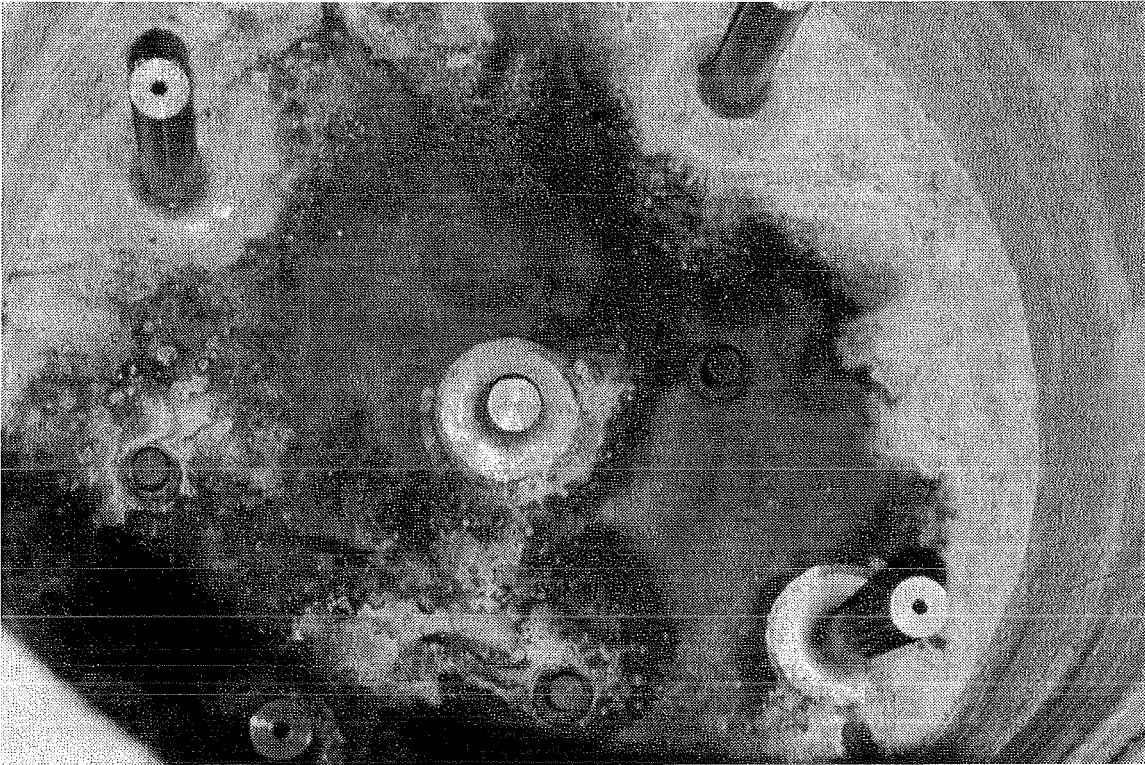


Fig. 2-11a: Penetrations inside test vessel of lengths 50 mm (central: I) and 305 mm (outer: II, III, IV, V) and 3 thermocouple welding areas (04/1)



Fig. 2-11b: Test plate upper surface after removal of oxide: penetration remnants and solidified inconel cake (04/1)

2.2 Validation of computational models

Analyses of the CORVIS experiments were performed in order to interpret the data in terms of the processes which govern the thermal attack and possible melt-through of the lower head, and to validate models to be applied to plant accident situations. The analyses focussed mainly on the following aspects of the behaviour: the thermal transport within the molten pool and to the structure, the freezing of the molten material as it cools, the formation and remelting of a solid crust, the thermal resistance between the solid crust and the lower head structure, the melt behaviour in penetration tubes and the thermal and mechanical response of the heated, ablated structure. The main tool was the ADINA finite-element set of computer codes which provide for computational fluid dynamic (CFD), heat conduction, and structural analyses.

2.2.1 Thermal transport within the molten pool

Detailed CFD calculations with ADINA demonstrated strong convection effects in the region above the bottom of the heating element, which transported a sizeable fraction of the heat to the side walls and to the top. In contrast, the fluid below the heating element was comparatively stagnant, and thermally stratified. This result is corroborated by the CORVIS experimental data and results of small scale CORVIS-counterpart experiments performed at FZK, for which CFD calculations demonstrate good agreement for both the flow and temperature distribution. Fig. 2-12 shows the good agreement for the temperature evolution in CORVIS 1/6 obtained using a CFD model and with a conduction model in which a large multiplier (λ) is applied to the thermal conductivity if the material is molten. **The insights gained from the detailed calculations make it possible to define a simple engineering model for the thermal transport, based on enhanced heat conduction in the molten regions.**

2.2.2 Crust formation by freezing of ceramic melt

Post-test analyses of CORVIS experiments involving ceramic melts shows that the material froze readily on the lower plate, as heat was conducted through the metal faster than it was being transported through the melt. Also, there was found a higher concentration of dissolved material in the lowest layers of the solidified melt, indicative of mainly stratified, stagnant conditions. Fig.2-13 compares the calculated development of the solidified region with the results deduced from post-test examination for CORVIS 1/11. The crust behaviour was found to be crucial to the melting, or not melting, of the structures. In none of the experiments involving ceramic melt did any structural melting occur. The external temperature typically stabilized when ambient losses matched the heat delivered.

2.2.3 Freezing of ceramic melt in penetration tubes

In CORVIS 3/2 and 4/1, ceramic melt penetrated some distance into instrumentation tubes before freezing, but did not ablate the tube wall. Table 2-1 compares the observed distance of penetration with predictions from three models which assume, respectively, bulk freezing, laminar flow conduction freezing, and turbulent flow conduction freezing. The result for the metallic melt is shown for comparison. The penetration distance was typically larger

than predicted, indicating that additional processes, not yet understood, control the heat transport.

Table 2-1: Penetration distance (m) in CORVIS experiments
Melt-through of penetration line by metallic melt

	Bulk freezing	Turbulent flow	Laminar flow	Experiment
Metallic melt Drain line	1.01	1.72	252.6	>4.0
Ceramic melt Drain line	1.43	2.58	22.7	>7.0
Ceramic melt Instrumentation tube	0.14	0.15	0.79	ca. 3.5

In contrast with ceramic melt, a highly superheated metallic melt resulted in heat fluxes from the melt that were much higher than could be conducted away through the wall, and significant structural melting occurred. The melting was augmented by the erosive effect of the flowing melt, which removed the newly melted (and not superheated) structural steel and brought additional superheated material to the melting location. In the case of metallic melt flowing through a BWR drainline, CORVIS 3/1, the initial contact temperature was below the melting point, hence a metallic crust formed at first. After a very short period, the large heat flux from the flowing melt quickly remelted the crust and then melted the inside of the drain line itself. The weakening of the drainline by heating and ablation resulted in deformation and failure of the component just below the attachment weld to the lower plate, after about 6 seconds. **The calculations correctly reproduced the temperature histories, including the time to remelt the initial crust, and the time and location of the failure, as seen by the comparison of temperatures shown in Fig. 2-14. Thus the applied calculational methods could be validated.**

2.2.4 Gap between crust and structure

The build-up of a crust strongly inhibited the heat flux from a ceramic melt. Not only does the lower conductivity of the solid crust reduce the heat transfer, but the imperfect contact or gap between the crust and the structure presents an additional thermal barrier. Analysis of CORVIS 1/11 shows that a narrow gap first formed, but the thermal resistance increased further, apparently due to thermal deformation caused by the large temperature gradients. The gap effect later decreased as the temperature profile became less steep. Fig. 2-15 compares the structure temperature assuming a time-dependent gap resistance with the experimental results. The non-monotonic thimble response of the lower plate could only be explained in terms of a time-varying gap resistance. **The effect of (thermally or mechanically) induced deformation on opening of a gap has important implications for the heat flux to the vessel wall, particularly if liquid water is present in which case additional cooling of the structure is possible.**

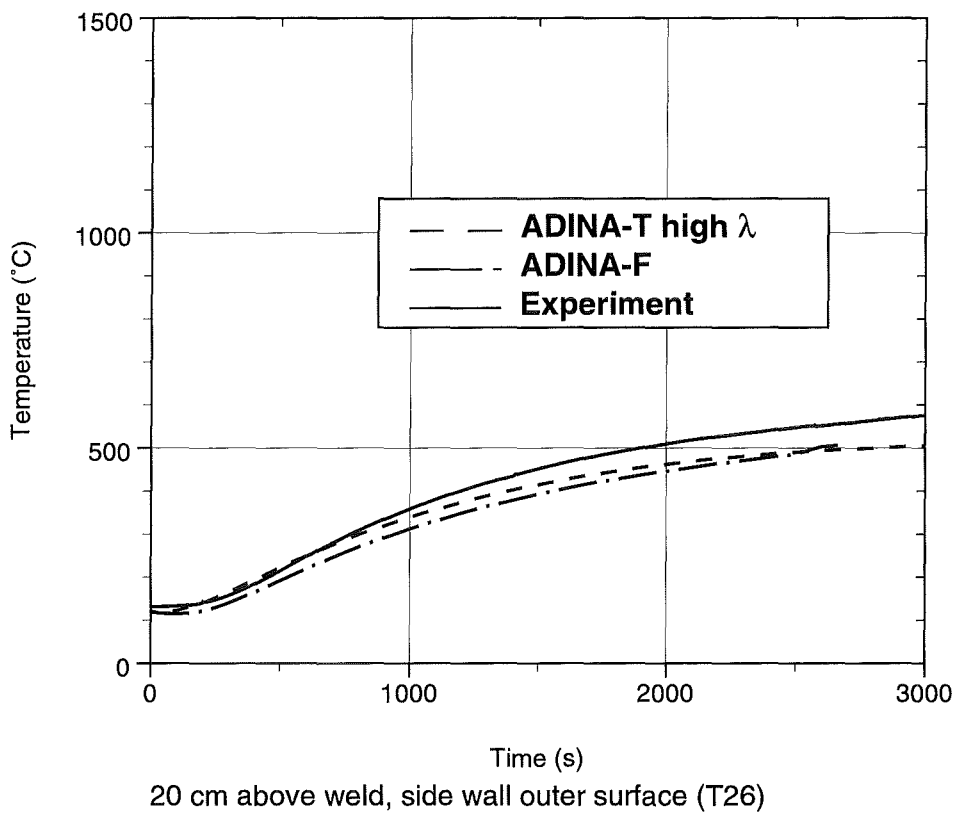
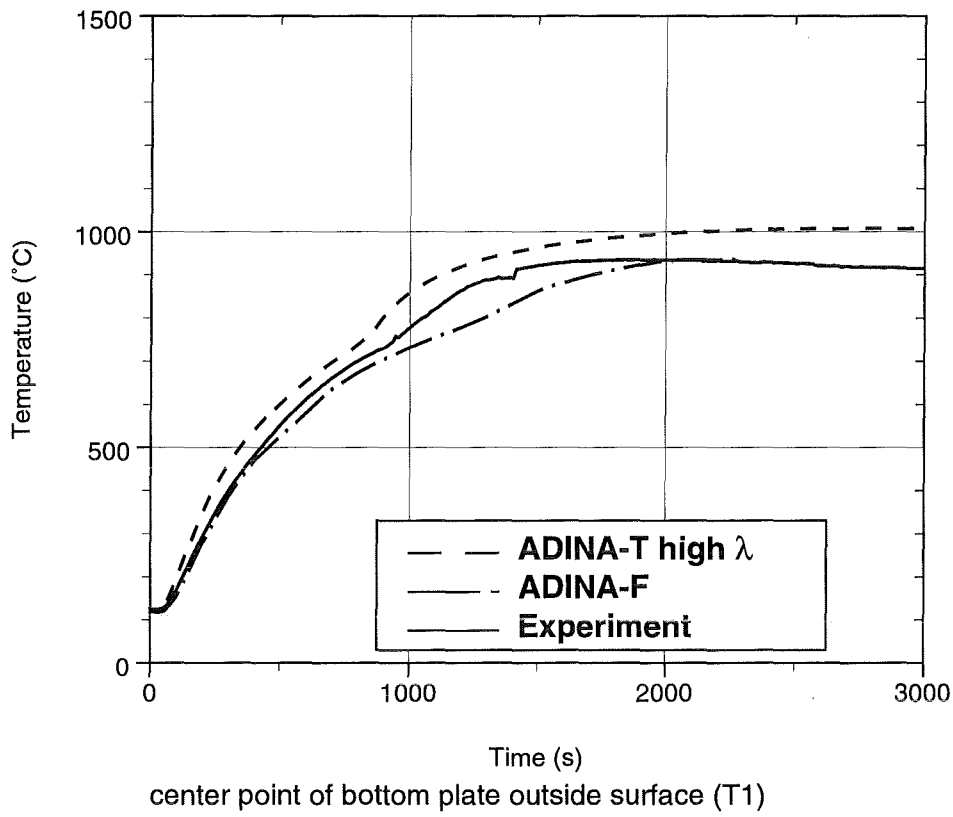


Fig. 2-12: CORVIS 01/6 temperature histories

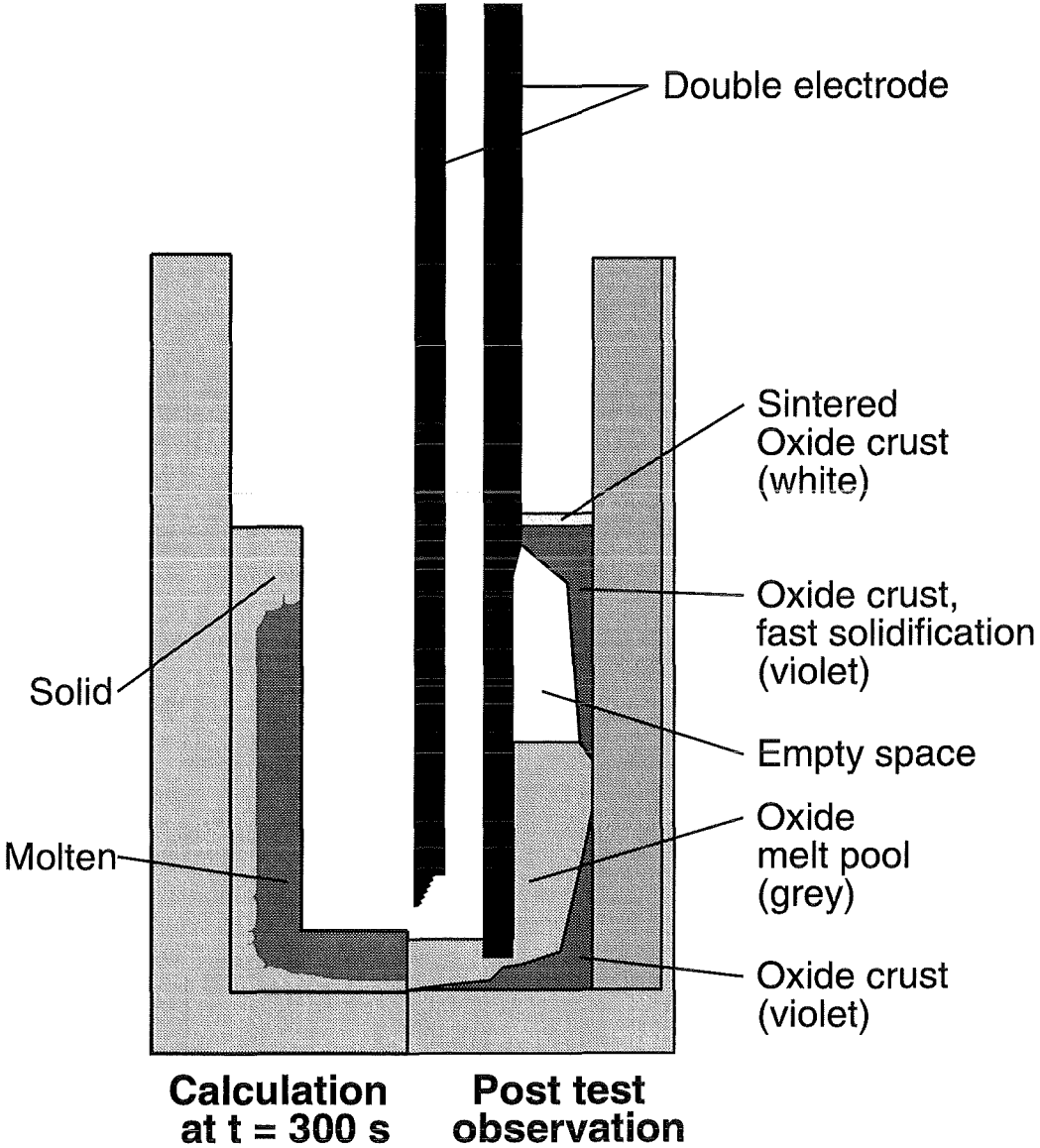


Fig. 2-13: CORVIS 01/11 melt solidification

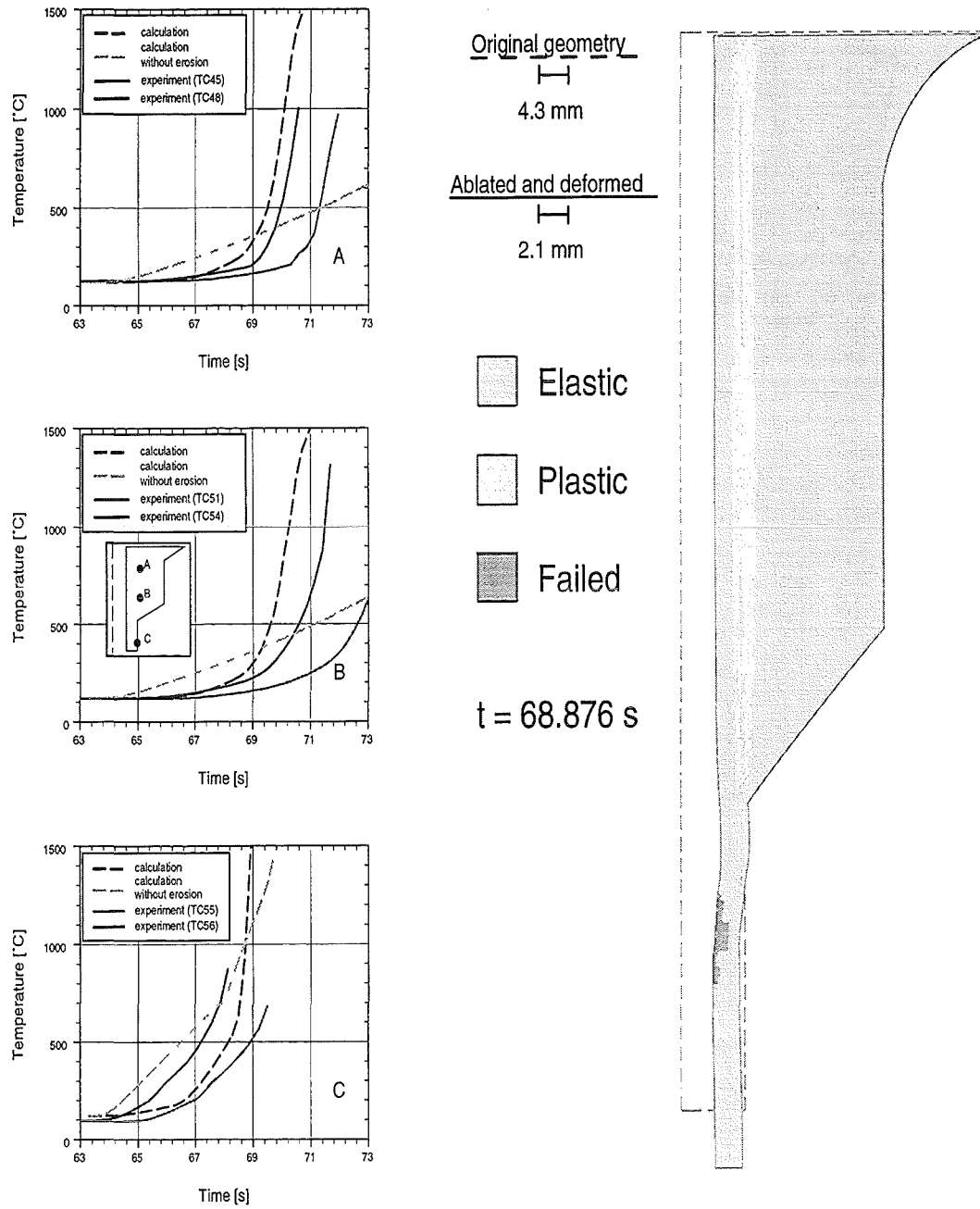


Fig. 2-14: CORVIS 03/1 drain line heat-up and failure

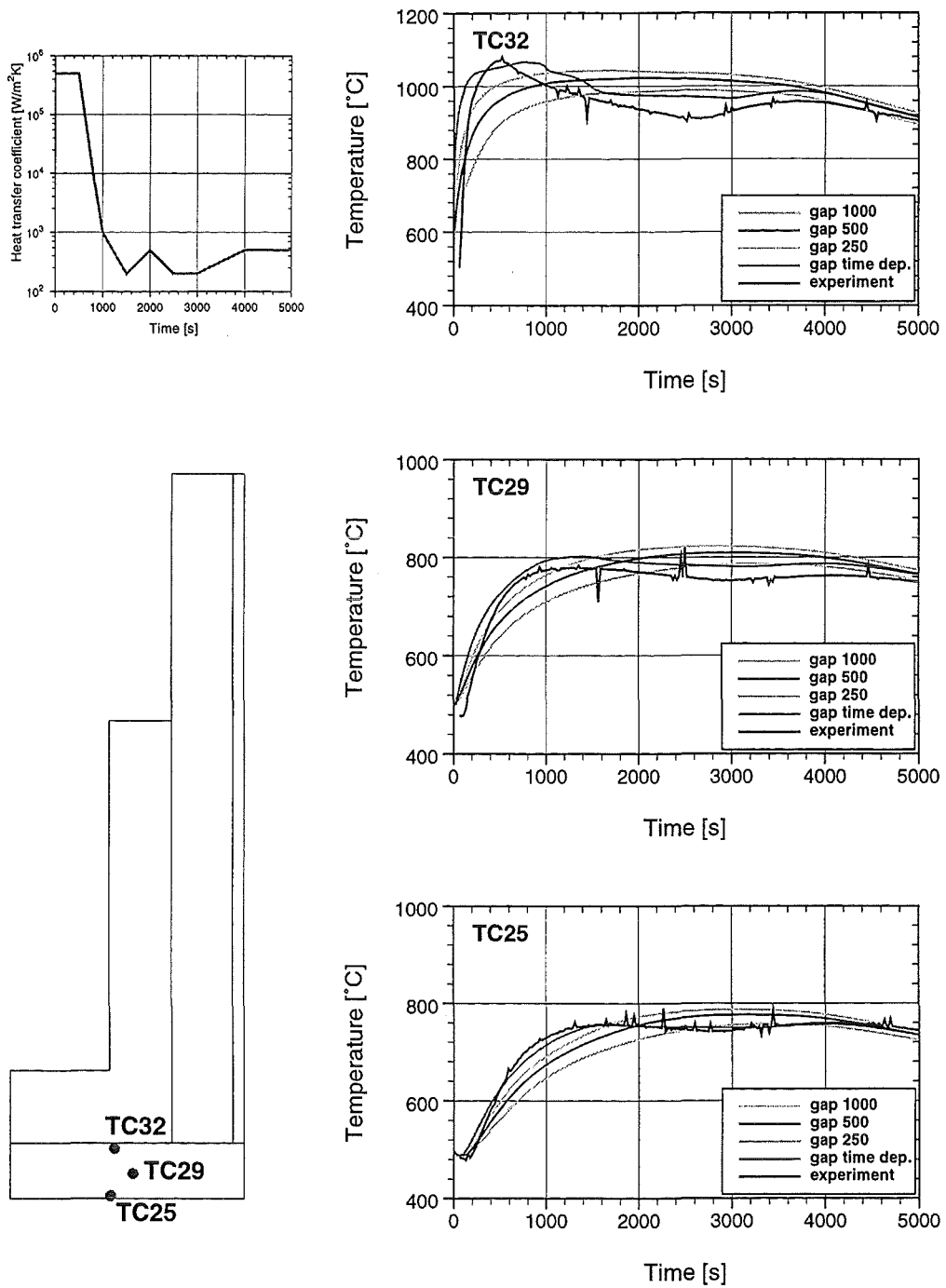


Fig. 2-15: CORVIS 01/11 effect of gap on temperatures

3. Lower head region loaded by dynamic pressure during a postulated steam explosion

B. Dolensky, B. Göller, G. Hailfinger, R. Krieg, E. Stratmanns, G. Vorberg,
FZK, Germany
(no financial support by the EU for this work)

It is assumed that during an in-vessel steam explosion steam, water, and corium is hurled against the lower face of the core support plate. Thus the core support plate is accelerated upwards. If the loading exceeds a certain threshold, the core barrel will be plastically compressed.

Two effects are of interest:

- The lower head response; will it fail under the dynamic loading?
- The behavior of the core support plate and the corium on top of this plate; how much energy will be converted to kinetic energy of an upward moving corium slug?

The overriding investigation strategy suggests concentration on the second problem. A first discussion of this problem was carried out in [1]. Information about dispersion effects which may reduce the kinetic energy and the compactness of the corium slug may be found in the basic literature and for instance in [2]. However, because of the very special conditions during the slug acceleration, further more specific investigations are required.

3.1 Preparation of the experiments BERDA II to investigate the acceleration of an upward moving corium slug

With the BERDA I experiments described in section 4, the admissible kinetic slug energy is determined such that the vessel head will not be endangered by the slug impact. In these tests only the slug impact and the energy dispersion by the upper internal structures is considered.

The BERDA II experiments will additionally take into account the whole acceleration phase, including the acceleration of the lower core support plate where the molten corium is located on. The experiment set-up is shown in Fig. 3-1.

A hammer will hit a model of the core support plate and accelerate the plate and the liquid metal on top of it. The core support plate will simultaneously be decelerated by compression of the core barrel whereas the liquid metal is hurled against the vessel head.

Aim of the experiments is to find the admissible mechanical energy input into the lower core support plate and to determine dispersion effects that will reduce the kinetic energy of the slug. Therefore not only the upper internal structures are modelled but also the lower core support plate and the core barrel. The heavy reflector is not explicitly modelled but taken into account with its mass.

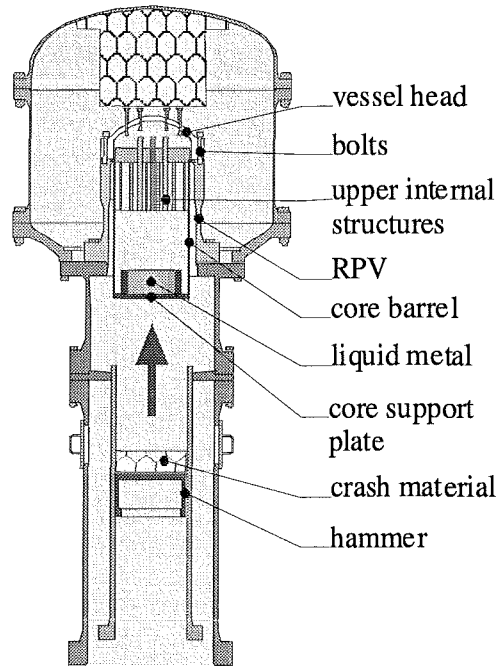


Fig. 3-1: Experimental set-up BERDA II

Different dissipation effects will be examined (Fig.3-2):

- (a) The vertical slug dispersion that will lead to a less compact slug.
- (b) The radial slug dispersion caused by the high radial forces due to the acceleration. Thus the upward slug acceleration will be reduced.
- (c) The energy dispersion due to deformation of the core barrel.
- (d) The effect of water that penetrates the holes of the support plate and may also lead to a more dispersed slug.

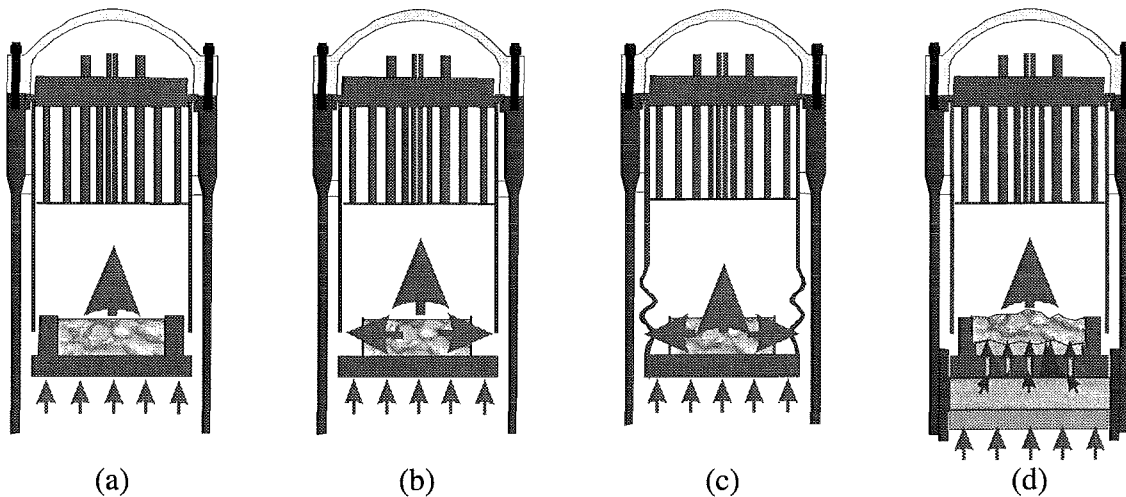


Fig. 3-2: The different set-ups of the BERDA II experiments for different dispersion effects

With the first set-up (a) it will be examined whether there will occur any dispersion in vertical direction. The surrounding structure of the liquid metal is modelled in a way that it will not fail during the acceleration process. The results of the experiment will be compared with a corresponding BERDA I-test.

The second set-up (b) will provide some information about the radial expansion of the slug during the acceleration phase. Only a thin 'crucible' simulating the crust of the corium

will keep the liquid metal. Due to the high pressure in the liquid metal caused during its acceleration the crucible will fail and the liquid metal will spread. Calculation with the FEM code ABAQUS showed that the radial forces of the spreading corium might be able to deform the core barrel. This deformation can even lead to a blockage of the down-comer (Fig. 3-3), a condition very important for the steam explosion and thus for the pressure release from the lower head.

With the third set-up (c) additionally to the vertical and radial dispersion of the liquid metal the deformation of the core barrel is taken into account. In comparison to (a) and (b) the core support plate is directly fixed at the core barrel, whereas in the previous cases a loose connection is chosen to admit a higher (conservative) velocity of the core support plate before being decelerated by the core barrel.

In the fourth set-up (d) it is assumed that a water layer above the explosion centre of the steam explosion might penetrate the holes of the lower core support plate and lead to an additional acceleration of the liquid metal on the one hand and to some dispersion on the other hand. In a first step this experiment might be done in a smaller scale (length scale 1:40) to investigate the fluid dynamics of this problem (which conditions will lead to an instability of the heavier phase, i.e. the liquid metal).

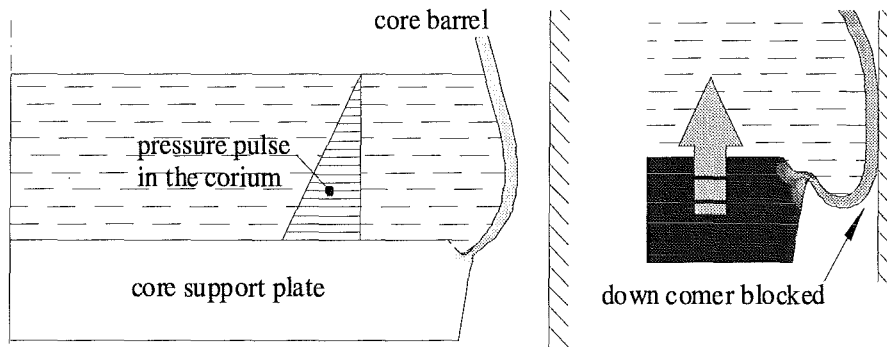


Fig. 3-3: Core barrel widening due to the pressure pulse in the corium (left hand side) and the superimposed upward movement of the core support plate (right hand side)

In the experiments the input momentum (mass and velocity of the impacting mass on the lower core support plate) and the velocity of the lower core support plate are measured as well as the forces i.e. the strains in the bolts and the head deformation after the test. With these measurements the velocity of the resulting liquid metal slug can be calculated and therefore its momentum can be compared with the input momentum.

The mean slug velocity can be calculated as follows:

$$\bar{v}_{\text{slug}} = \frac{m_h (v_{h,0} - v_{\text{csp}}) - m_{\text{csp}} v_{\text{csp}}}{m_{\text{slug}}}$$

respectively

$$\bar{v}_{\text{slug}} = \frac{m_h v_{h,0} - \int F_b dt}{m_{\text{slug}}},$$

where

\bar{v}_{slug} = mean slug velocity,

m_{slug} = mass of the liquid metal,

m_{csp} = mass of the impacting mass,

- $v_{h,0}$ = initial velocity of the impacting mass,
- v_{csp} = velocity of the lower core support plate,
- m_{csp} = mass of the lower core support plate,
- F_b = forces in the bolts.

The first equation gives the mean slug velocity for the experimental set-ups (a), (b) and (d). With the second equation the mean slug velocity for the experiment (c) can be calculated. There the integral of the forces in the bolts has to be taken over a time period until the lower core support plate has come to rest.

The experimental facility is designed and the components have been ordered. The measurement techniques are chosen. The tests are scheduled to start in 1999. Some calculations have been done in section 3.2 to have a first idea of how much the slug acceleration will be reduced in comparison to the acceleration of the lower core support plate due to the above mentioned effects.

3.2 Analysis of the acceleration of an upward moving corium slug

As mentioned before the upward acceleration of the core support plate may cause a radial dispersion of the corium on top of this plate. Thus the upward acceleration of the corium is non-uniform. In the mean this acceleration is only a fraction χ of the upward acceleration of the core support plate.

The fraction χ has been calculated approximately for different corium configurations using the boundary element code SING [3]. The boundary condition and the discretization by boundary elements for a cylindrical configuration is shown in Fig. 3-4.

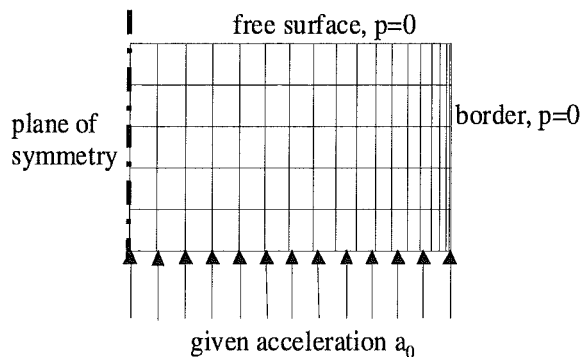


Fig.3-4: Model and boundary conditions for calculations with the code SING

Three cases were studied, each with a mass of 80,000kg of core melt on top of the core support plate, see Fig. 3-5:

1. The core melt has a cylindrical form. The diameter of 3.9m is given by the heavy reflector. Taking into account that also the heavy reflector will be removed radially, the code SING yields $\chi = 0.7$.
2. The core melt has a cylindrical form. The diameter and height more or less correspond to the form of the crucible used in the BERDA I experiments (see section 4) enlarged by the scale factor of 10. The crust around the corium fails during the acceleration and the code SING calculates a fraction $\chi = 0.5$.
3. The core melt has the shape of a truncated cone. Also here, the crust of the core melt is not supposed to prevent radial dispersion and SING gives as result $\chi = 0.4$.

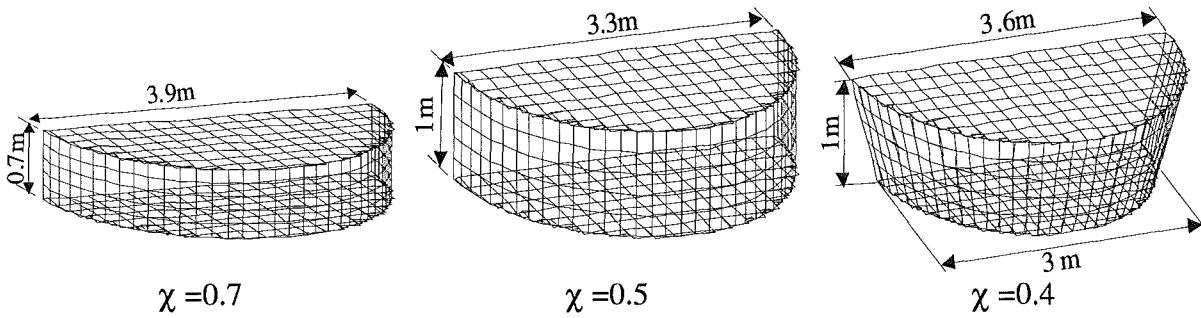


Fig. 3-5: Factor χ calculated by the code SING for different corium configurations

Changes of the geometrical conditions during the dispersion are assumed to be small and the resulting increase of χ was not taken into consideration in these analyses. Also the limitation of the radial dispersion by the wall of the reactor pressure vessel was not taken into account.

Furthermore a formula was developed in order to assess the ratio between the mechanical energy E_{plate} , fed into the upward moving core support plate, and the kinetic energy E_{slug} of the upward moving corium slug. Here, the computation model represented in Fig. 3-6 was used.

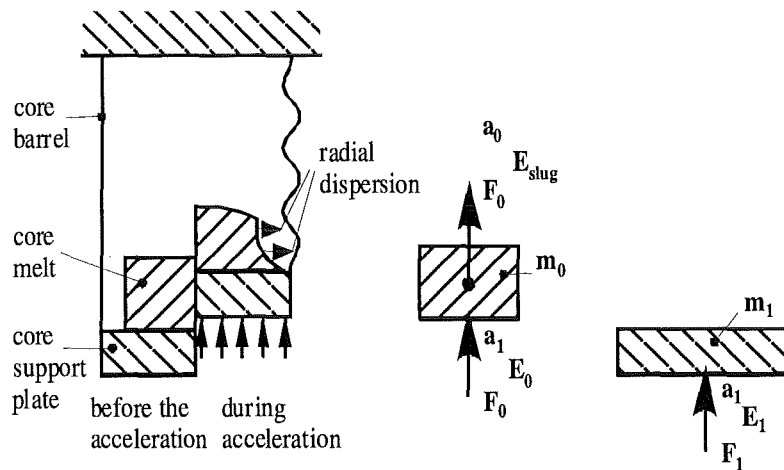


Fig. 3-6: Computing model for the calculation of $E_{\text{plate}}/E_{\text{slug}}$

The kinetic energy E_{slug} of the core melt which is hurled upwards is (Fig. 3-5 a)

$$E_{\text{slug}} = \int F_0 ds_0 = m_0 \int a_0 ds_0$$

with the acceleration force F_0 , the mean acceleration path s_0 , the core melt mass m_0 and the mean acceleration a_0 .

Due to the radial dispersion of the liquid metal the energy input E_0 into the core melt is higher than E_{slug} ,

$$E_0 = \int F_0 ds_1 = m_0 \int a_0 ds_1.$$

Due to equilibrium reasons, the applied force must be equal to the acceleration force F_0 . During the radial dispersion, however, the acceleration path s_1 and the acceleration a_1 on the support surface of the core melt will be larger than the mean acceleration path s_0 and the mean acceleration a_0 in the core melt.

The kinetic energy of the core support plate is

$$E_1 = \int F_1 ds_1 = m_1 \int a_1 ds_1$$

with the acceleration force F_1 required for the plate with the plate mass m_1 .

If the decelerating force from the crashing core barrel and hence the dissipated energy is neglected, the admissible energy input E_{plate} at the core support plate is obtained by

$$E_{\text{plate}} = E_0 + E_1.$$

The terms of E_0 and E_1 have to be determined such that after the acceleration phase the core melt is moved upwards with the admissible kinetic energy of E_{slug} .

In case of unrestricted radial core melt dispersion the acceleration ratio χ

$$\chi = \frac{a_0}{a_1}$$

above all depends on the core melt geometry. If the geometry change during the acceleration is assumed to be small, χ also describes the path ratio

$$\chi = \frac{s_0}{s_1}.$$

Hence, the energies E_0 and E_1 can be expressed as multiples of E_{slug} and the ratio of E_{plate} to E_{slug} can be obtained as

$$E_{\text{plate}}/E_{\text{slug}} = \left(\frac{1}{\chi} + \frac{1}{\chi^2} \frac{m_1}{m_0} \right).$$

The formula says that the ratio $E_{\text{plate}}/E_{\text{slug}}$ increases, if the corium slug becomes slender and if the ratio m_1/m_0 increases.

The application of the formula and important conclusions will be discussed in section 4.

4. Upper head region loaded by a corium slug impact during a postulated steam explosion

B. Dolensky, B. Göller, G. Hailfinger, A. Hirt, G. Hoffmann, O. Jonatzke, T. Jordan, I. Kornelson, R. Krieg, T. Malmberg, G. Messemer, T. Stach, G. Vorberg, FZK, Germany; T. Grunenwald, C. Strub, CEA, France

The main question is:

- What is the admissible kinetic energy E_{slug} of the corium slug such that the upper vessel head does not fail?

Early investigations of this problem were carried out by Lucas, Amarasooriya and Theofanous (1987). Because of the complexity of the liquid slug impact against the upper internal structures and the upper vessel head, the computations were very rough and essential assumptions were needed which have been never checked. The review of other literature revealed that thorough investigation of the liquid-structure impact problem is very rare. One of the most advanced codes applicable to such problems is PLEXUS, Bung (1993). However, it is not validated for the upper head problem and it cannot take into account the upper internal structures. On the other hand, recent studies carried out at FZK, Krieg (1995), indicated that these structures are expected to increase the load carrying capacity of the upper head considerably. Therefore, appropriate investigations are carried out which consider the limitations of computational models.

4.1 Model experiments BERDA I to determine the admissible kinetic energy of the corium slug

The model experiments BERDA I are designed to fulfil essential similarity conditions of the corium slug impact against the vessel head such that the results can be directly converted to reactor dimensions. The upper part of the reactor pressure vessel is simulated by models scaled down 1:10, i.e. length scale $\lambda_l = 10$. In general, for the models the same material is used as for the reactor. Only for some parts of the models softer material is used, in order to simulate high temperature effects.

The experimental set-up is shown in Fig. 4-1. A view of the model head is shown in Fig. 4-2. The corium slug is simulated by liquid metal having about the same density as corium. It is accelerated upward by a pneumatic drive mechanism. In some tests very detailed models of the upper internal structures were used. Since the impact forces may reach up to about 15 MN, the whole set-up is connected to a heavy base plate, which has a mass of about 40 000 kg and is supported by springs.

Due to the different temperatures of the model head (room temperature) and the reactor pressure vessel head (300 – 400 °C), slightly different stress-strain diagrams must be considered. The stresses in the diagram for the pressure vessel head are about λ_σ times the stresses in the diagram for the model head, where the stress scale $\lambda_\sigma < 1$. The influence of the strain rate mentioned below leads to an additional slight reduction of the stress scale. Based on material data obtained in section 5.2 (Table 5-8, strain rate 15/s and Table 5-9, strain rate 1.5/s) a value of $\lambda_\sigma = 0.87$ was chosen.

The different temperatures of the upper internal structures of the model (room temperature) and the upper internal structures of the reactor pressure vessel (600 °C) have a stronger impact on the stress-strain diagrams. Considering the material tests in section 5.2, Fig. 5-18, the strength of the austenitic steel used for the internal structures is reduced to about 50 %. However, this is not reflected by the chosen stress scale. Rather internal structures made of softer brass were employed in some cases. Tests of this material in section

5.2, Fig. 5-34, show that in this way a strength reduction to about 40 % and a considerable ductility reduction can be simulated. In one test, the guide tubes of the control rods even consisted of much softer lead material.

Within the RPVSA project, the BERDA I tests 01 to 17 have been performed. The results are described in the following sub-sections. Information may also be found in Krieg (1997 and 1999), as well as in the special test reports.

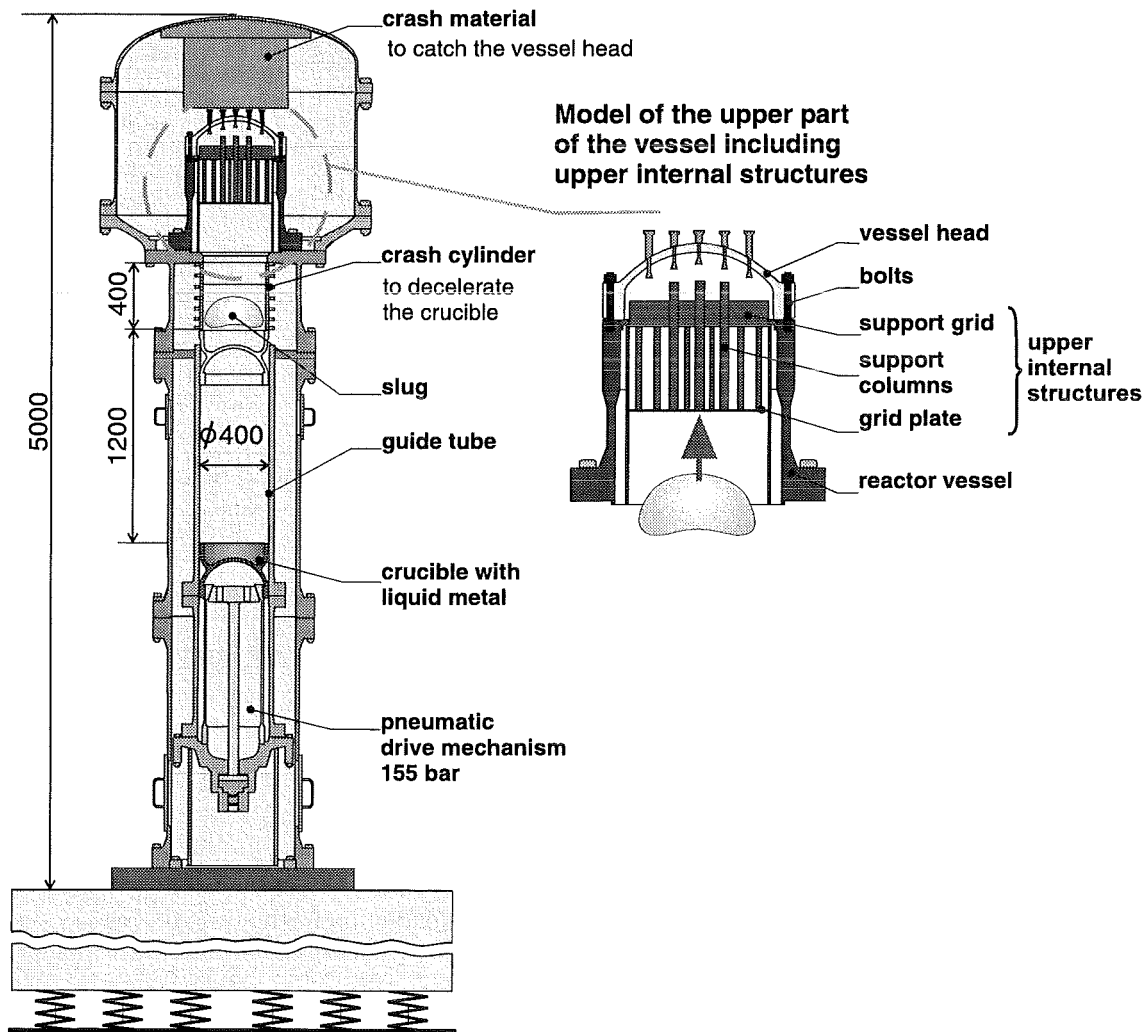


Fig. 4-1: BERDA facility

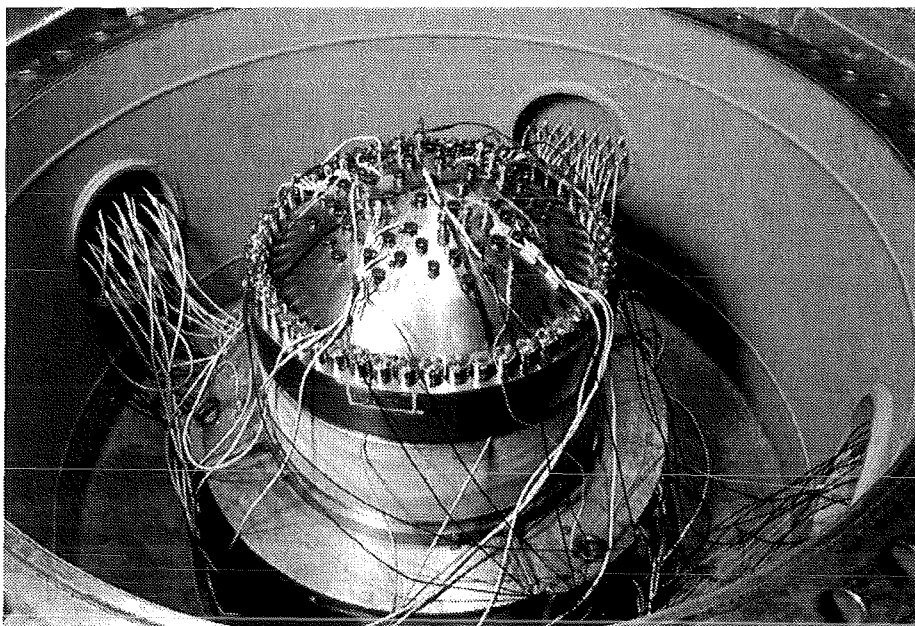


Fig. 4-2: Model head in the BERDA facility with instrumentation

4.1.1 Impact of slugs consisting of lead spheres, upper internal structures neglected, test 01 and 02

In the first and second test lead spheres of 10 mm diameter were accelerated against the head. The total mass of the spheres was 65 kg, the measured impact velocities were 78 m/s and 101 m/s, respectively. For simplicity, there was only one central hole of 12 mm diameter in the heads. The results are shown in Figs. 4-3 to 4-6. In both cases the time integration of the impact force yielding the momentum transferred to the head approaches the initial momentum given by the product of slug mass and slug velocity. This is in line with the principle of momentum conservation, if one considers, that for the impact of lead spheres significant rebound effects do not occur. This is confirmed by the strong plastic deformations of the spheres after the impact. Thus, we have additional evidence that the measurements are correct. The permanent head deformations were 0.3 and 4.4 mm.

4.1.2 Impact of a solid slug, upper internal structures neglected, test 03

For comparison in the third test a steel projectile with a spherical surface was hurled against the head; radius of the spherical surface 160 mm; radius of the inner surface of the head 278 mm. The mass of the projectile was only 26 kg, the measured impact velocity was 101 m/s. Again, there was only one central hole of 12 mm diameter in the head. The results are shown in Figs. 4-7 and 4-8. Consider that for the solid slug the maximum impact force is much higher than for test 02 with lead spheres, although the velocity was the same. Comparison of the momentum transferred during the first force peak with the initial momentum led to a rebound factor of 1.4. The permanent head deformation was 17.8 mm.

4.1.3 Impact of liquid metal slugs, upper internal structures neglected, test 04 to 07 and 09

In order to simulate worst case conditions, rather compact slugs are desired. Therefore, the liquid metal was contained in a very thin-walled crucible, which was carried in a stronger crucible. The thin-walled crucible was not decelerated by the crash tube but it moved on together with the liquid metal till the impact occurred. Thus, the slug mass consisted of the liquid metal of 80 kg plus that of the second crucible and the heater of 2.4 kg.

In test 04 the strong crucible failed during the deceleration by the crash tube. Thus, the impact mass was additionally increased by a crucible fragment of about 2.6 kg. Furthermore, the determination of the impact velocity was very difficult and ambiguous; it was assumed to be 118 m/s. The force history shown in Fig. 4-9 consists of several moderate peaks. We assume that this result was largely influenced by the failed crucible which probably led to enhanced slug dispersion. A picture of the failed crucible is shown in Fig. 4-10.

In test 05 to 07 and 09 the thick-walled crucible remained intact. The impact velocities reached 110 m/s, 107 m/s, and two times 61 m/s, respectively. For tests 05, 06 and 09, heads were used with a pattern of control rod holes similar to that of German PWR of Convoy type; diameter of the central hole 12 mm, of the other holes 10 mm. For test 07 a head was used containing only the central hole. The results are shown in Figs. 4-11 to 4-19. Now, the force histories contain only one major peak. The maxima are much higher, but the impact durations are shorter than obtained for test 04. The rebound factors were between 1.12 and 1.18. In comparison with test 01 and 02, where slugs of lead spheres were used, the impact forces are slightly higher, even if one extrapolates the forces to the same slug masses; the impact durations are about the same. However, in comparison with test 03 with the solid slug the impact forces are much lower. The permanent head deformations were 22.0, 30.8, 10.1 and 3.2 mm. The significant deviation between test 07 and 08 is discussed in section 4.3. In order to give an impression of the head deformations, for test 05 the head before and after the impact is shown in Fig. 4-13.

In test 06 an additional hole was drilled close to the central hole, where the highest strain occurs. Consequently, in this local area a through wall crack developed, as shown in Fig. 4-15. Before the tests the holes were closed by plugs with threads similar to German PWR. During the slug impact of test 05 and 06 many plugs were expelled reaching velocities up to about 80 m/s.

4.1.4 Impact of liquid metal slugs, upper internal structures of original steel considered, test 08, 10, 12 and 15

The details of the liquid metal slugs were the same as before. In all tests heads were used with control rod holes. A model of the upper internal structures is shown in Fig. 4-20. Many details are considered. A model of a guide tube is shown in Fig. 4-21. Even the masses of the rods in the tubes, the stiffening by the rod spacers and the weakening at the feet of the tubes are considered. The impact velocities were 106 m/s, 121 m/s, 131 m/s and 129 m/s, respectively. The results and some information about the upper internal structures are shown in Figs. 4-22 to 4-27. The impact forces are much lower and the impact durations are much longer than in the tests without upper internal structures. The rebound factors were between 1.08 and 1.14. Permanent head deformations did not occur, although in most of the tests the impact velocities were higher than before. In all tests the upper internal structures were heavily deformed. An interesting detail shows Fig. 4-27, where four central squares of the support grid which were not protected by the guide tubes are blown up by the pressure peak of the liquid slug.

4.1.5 Impact of liquid metal slugs, upper internal structures of red brass considered, test 11, 13 and 16

The details of the liquid metal slugs and the model heads were the same as before. The impact velocities were 130 m/s, 128 m/s and about 160 m/s, respectively. However, in test 16 the crucible failed, and therefore, the determination of the velocity of 160 m/s is questionable. Also the geometry of the upper internal structures was the same as before, however, now the material was red brass and for test 16 the material of the control rod guide tubes was lead. The results are shown in Figs. 4-28 to 4-36. The force histories were similar as before, except test 13, where the maximum force occurred as a peak with a very short duration of only about 0.4 ms. Therefore, it is called the peak maximum. The remaining force history reached a smaller maximum called bulk maximum. It turns out that the weaker and more brittle upper internal structures made of red brass have no significant influence on the loads, except the narrow peak discussed above. The rebound factors were 1.26 and 1.28, which is noticeable higher than before. For test 11 and 13 permanent head deformations did not occur, for test 16 it was 6.5 mm. The upper internal structures broke into many pieces. Thus the resulting fragments are very different from the large deformations observed for structures made of steel.

4.1.6 Impact of a liquid metal slug, only an upper support grid of steel considered, test 14

The conditions were similar to those before. The impact velocity was 108 m/s. However, the thickness of the upper support grid had been reduced to 75 % of its nominal value. The results are shown in Figs. 4-37 and 4-38. One can see that the maximum force is about twice the corresponding value obtained with the complete upper internal structures, but it is still considerably lower than the values without any upper internal structures. The permanent head deformation was 0.5 mm.

4.1.7 Impact of liquid metal slugs, only upper support grids of red brass considered, test 17

Again, the conditions were similar to those before. The impact velocity was 126 m/s. The results are shown in Figs. 4-39 and 4-40. The maximum force occurred as a peak like observed for test 13. However, despite of this high force the permanent head deformation reached only 9.6 mm. This confirms that peak maxima of very short durations (about 0.5 ms) have not the same effect as the other maxima with longer durations (about 1.0 ms).

4.1.8 Major findings from the BERDA I tests

A survey of the results is shown in Fig. 4-41. To have a better basis for comparisons, the maximum impact forces are linearly converted to a reference slug mass of 80 kg. The main findings are:

- As expected, the impact force of a liquid is much smaller than that of a respective solid (compare test 03 with tests 05 and 06.) The reduction factor amounts to 3 – 4.
- As also expected, the internal structures cause a further considerable reduction in the impact force (compare tests 05 – 07 and 09 with tests 08 and 10 – 17). For moderate velocities that do not cause plastic head deformations the reduction factor amounts to about 7, if the complete upper internal structures are considered. The reduction factor is assessed to be between 3 and 4, if only the upper support grid is available.
- During the slug impact the upper internal structures were heavily deformed and damaged. However, a careful examination of the resulting wreckage revealed that only a mechanical

energy of about 0.05 MJ had been dissipated in these structures. The mechanical energy dissipated in other structural components can be assumed to be even smaller (since there was no permanent head deformation). However, the kinetic slug energy was between 0.5 and 0.7 MJ before the impact. Thus it can be concluded that the major part of this energy had been dissipated by the irregular flow of the liquid after the impact.

- The material properties of the internal structures do not have very significant influence on the head load (the results obtained for steel and brass structures nearly correspond to each other). Nor does the number of fractures have very strong influence. This behaviour can be understood, since the major part of the kinetic slug energy is dissipated in the liquid. This result is of great advantage for the application to the reactor. Detailed knowledge of the temperature of the internal structures during the steam explosion and the resulting material properties as well as on the extent of radiation-induced embrittlement is not required.
- As evident from test 17, the previous assumption of the reactor pressure vessel head always failing earlier than the head bolts under overload conditions could not be confirmed.
- For the verification of the results, the major characteristics were determined in a redundant manner. The momentum obtained from the force measured as a function of time was compared with the momentum of the liquid slug prior to the impact. It was concluded that major measurement errors hardly exceed about 10 %. Visual control of the contour of the incident liquid slug turned out to be impossible. However, calculations carried out under section 4.3. suggest that e.g. in test 07 the slug had a rather compact form, while in test 09 the form was less compact.

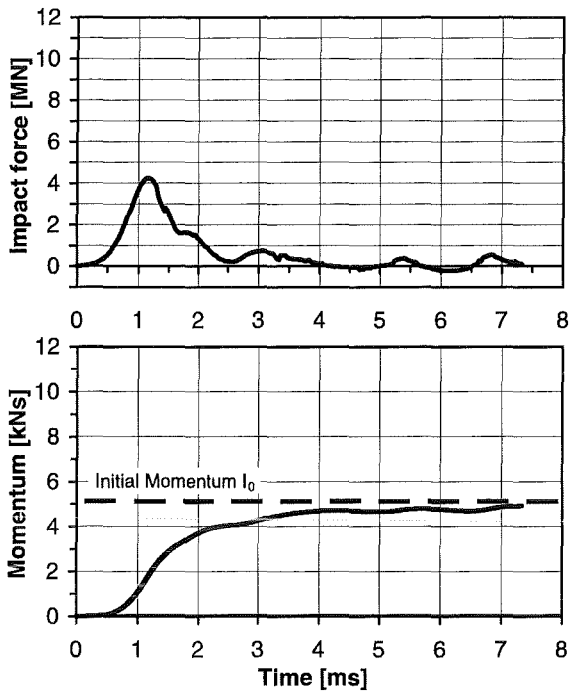


Fig. 4-3: Test01, lead spheres, 65 kg, 78 m/s, upper internal structures neglected.

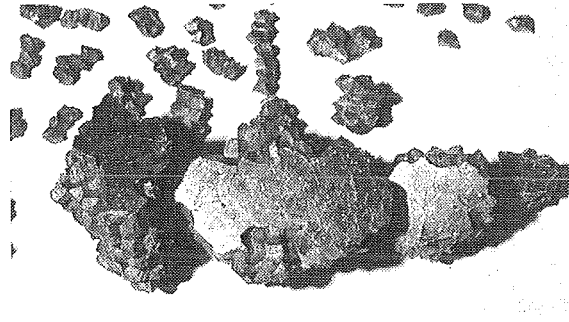


Fig. 4-4: Test01, plastic deformations of the lead spheres after the impact.

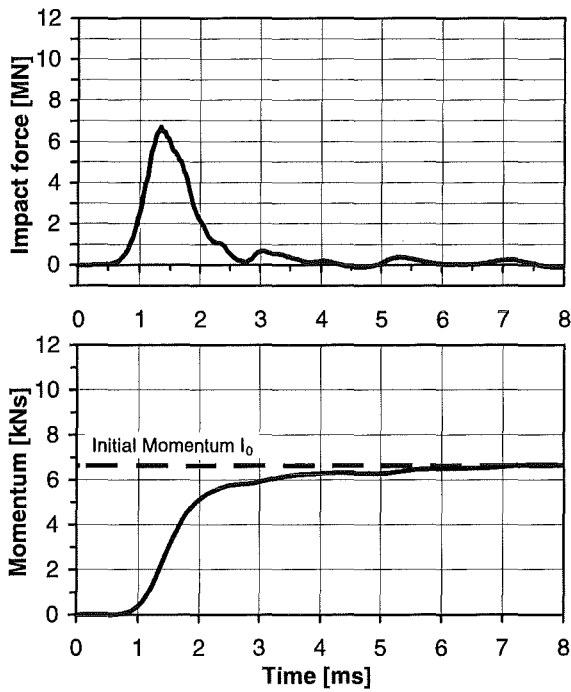


Fig. 4-5: Test02, lead spheres, 65 kg, 101 m/s, upper internal structures neglected.



Fig. 4-6: Test02, plastic deformations of the lead spheres after the impact.

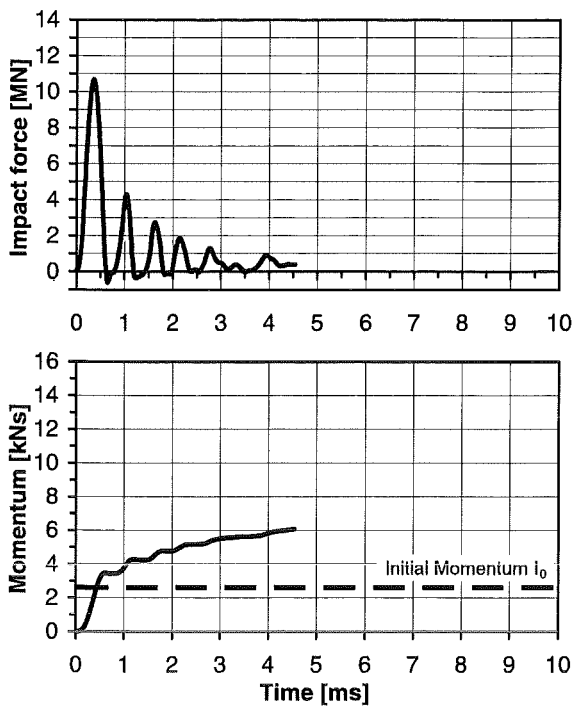


Fig. 4-7: Test03, solid slug, 26 kg, 101 m/s, upper internal structures neglected.

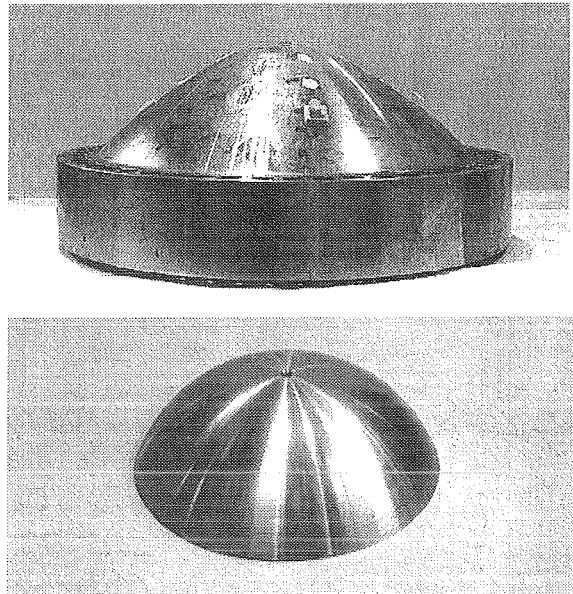


Fig. 4-8: Test03, solid slug and deformed model head after the impact.

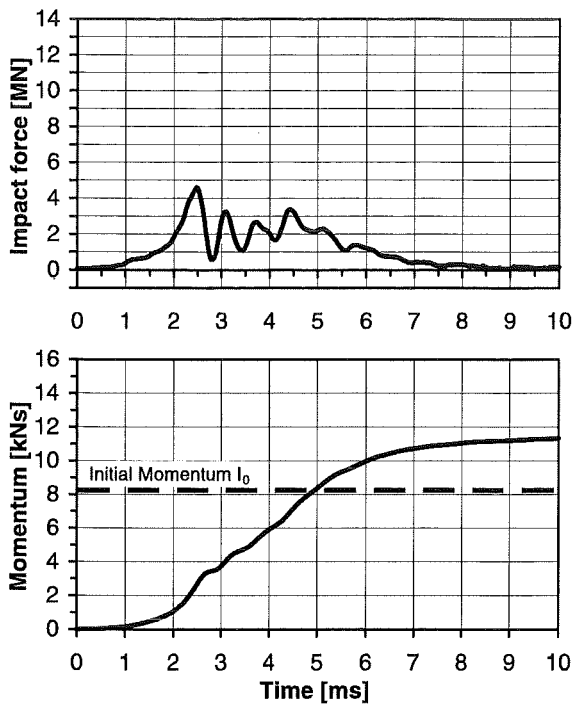


Fig. 4-9: Test04, liquid metal, 80 kg, 118 m/s, upper internal structures neglected.

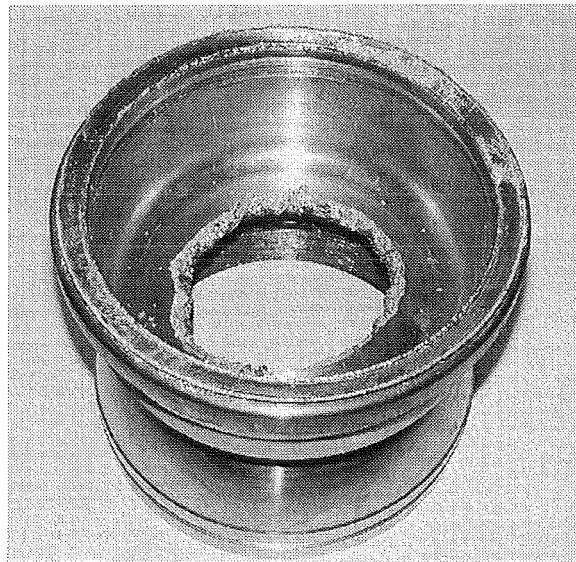


Fig. 4-10: Test04, broken crucible after the impact.

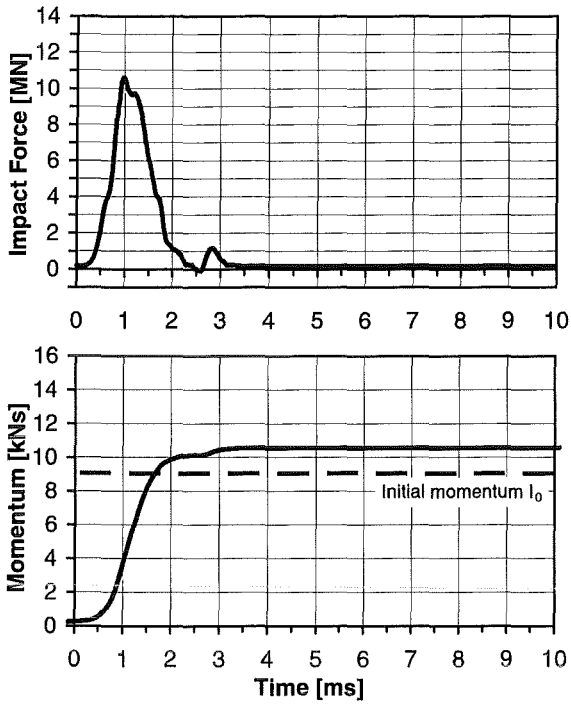


Fig. 4-11: Test05, liquid metal, 80 kg, 110 m/s, upper internal structures neglected.

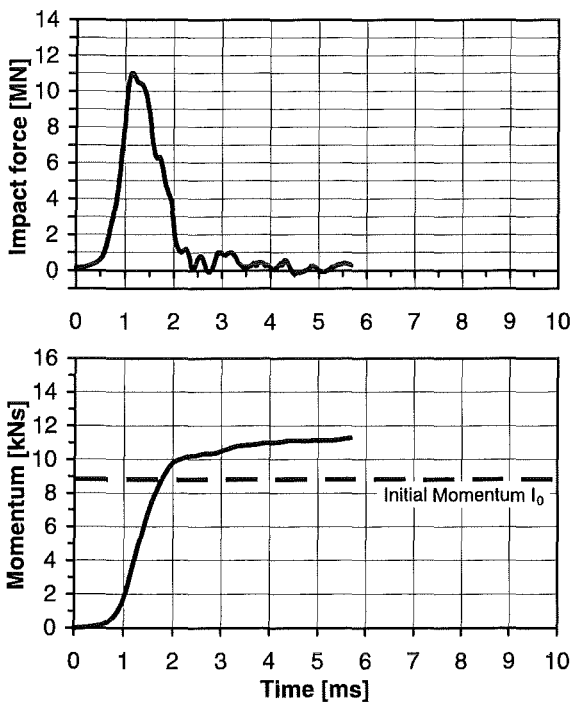


Fig. 4-14: Test06, liquid metal, 80 kg, 107 m/s, upper internal structures neglected.

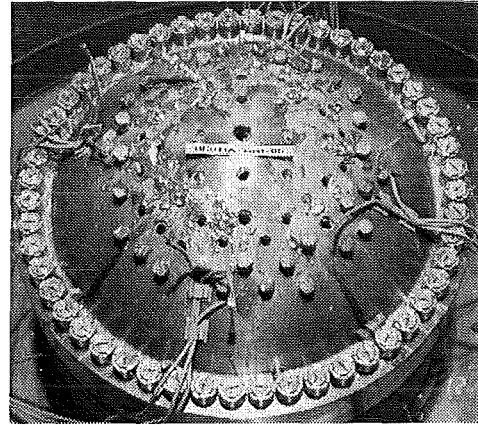


Fig. 4-12: Test05, the holes in the head were increased and many plugs which had closed the holes were expelled.

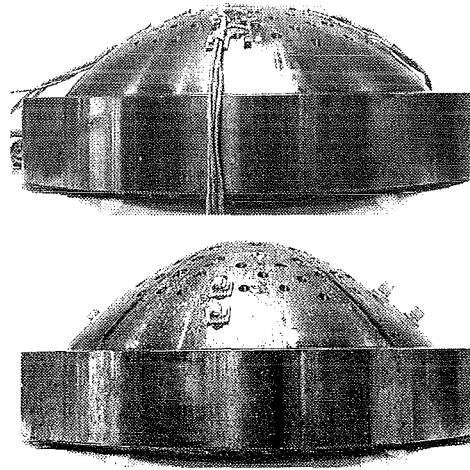


Fig. 4-13: Test05, shape of the head before and after the impact.

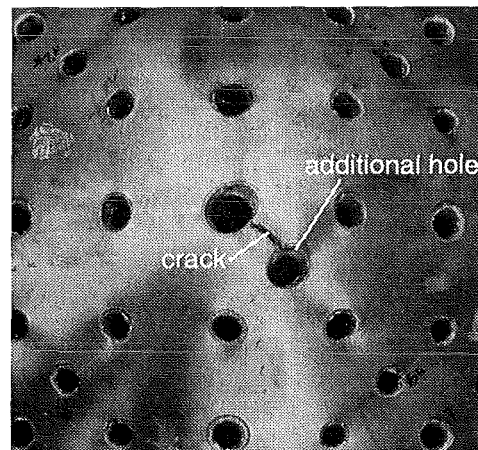


Fig. 4-15: Test06, During the head deformation a crack developed.

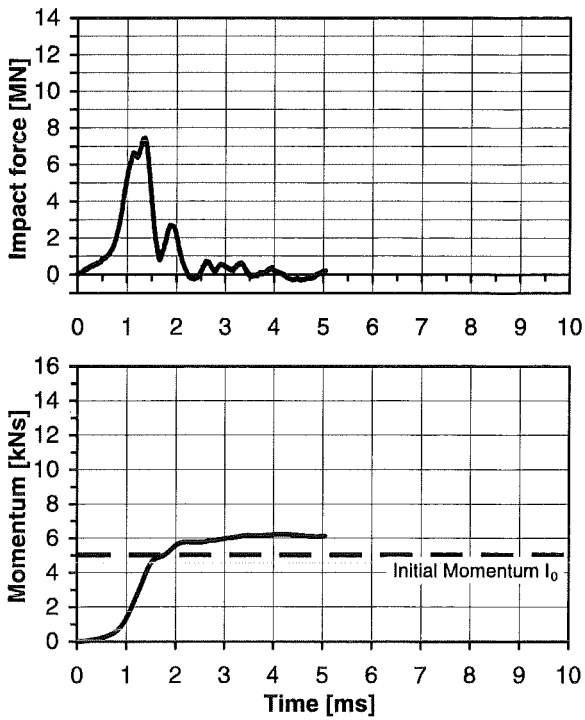


Fig. 4-16: Test07, liquid slug, 80 kg, 61 m/s, upper internal structures neglected.

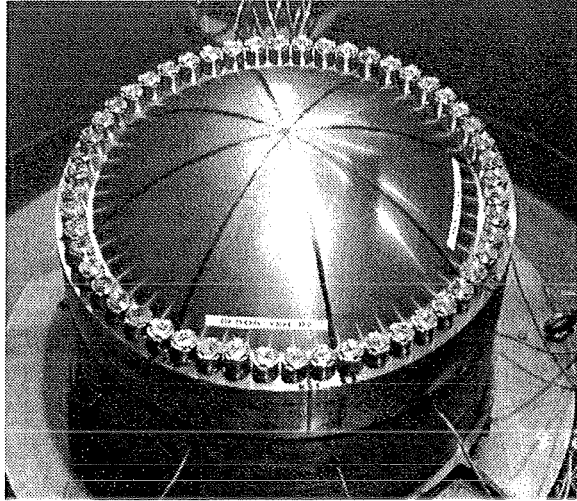


Fig. 4-17: Test07, model head after the impact.

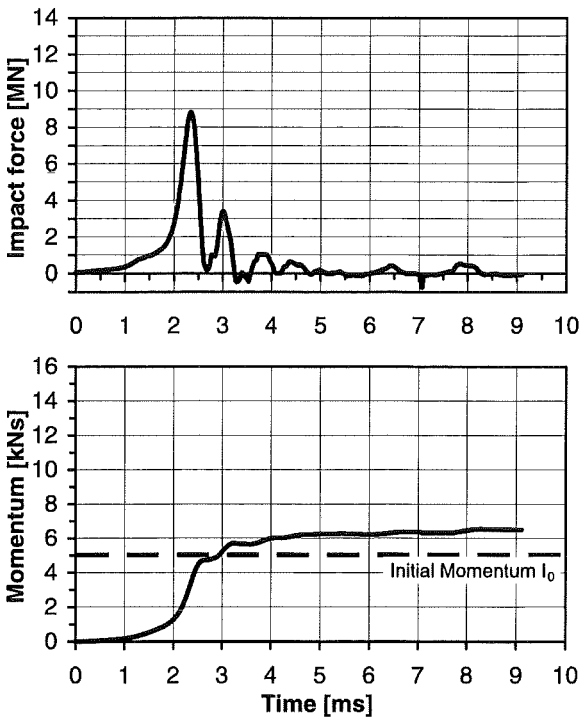


Fig. 4-18: Test09, liquid metal, 80 kg, 61 m/s, upper internal structures neglected.

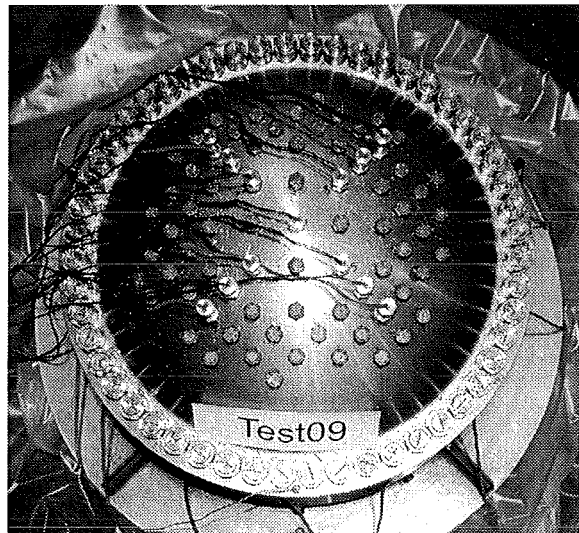


Fig. 4-19: Test09, model head after the impact.

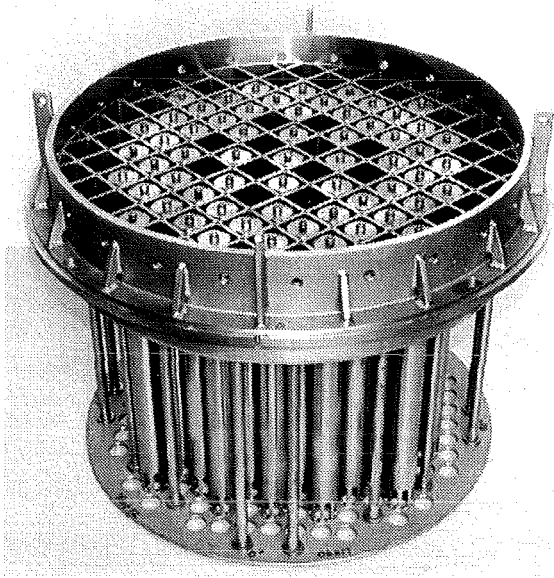


Fig. 4-20: Model of the upper internal structures.

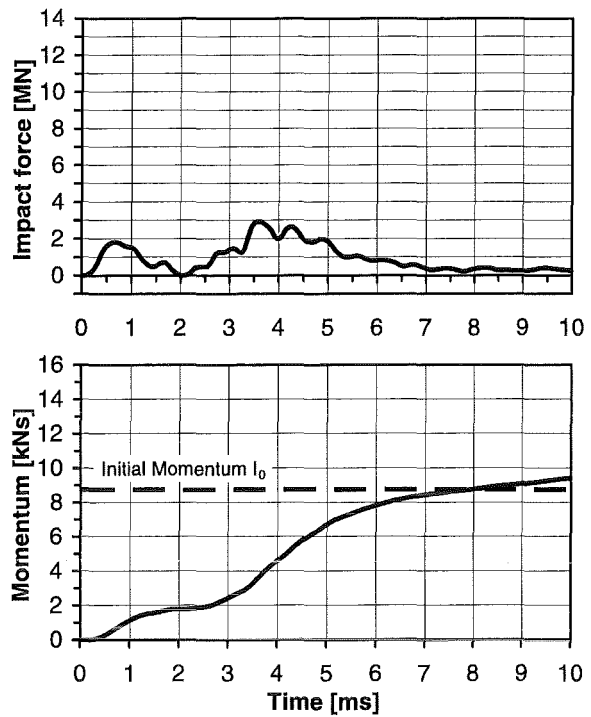


Fig. 4-22: Test08, liquid slug, 80 kg, 106 m/s, upper internal structures of steel.

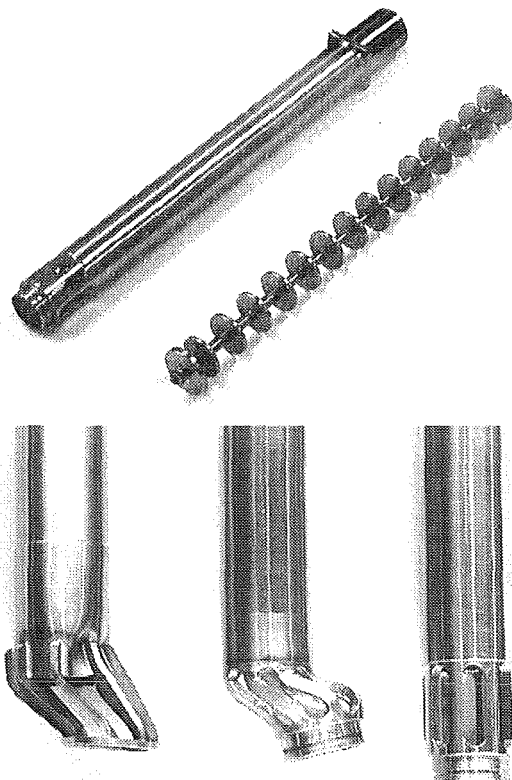


Fig. 4-21: Model of a guide tube with simulation of many details.

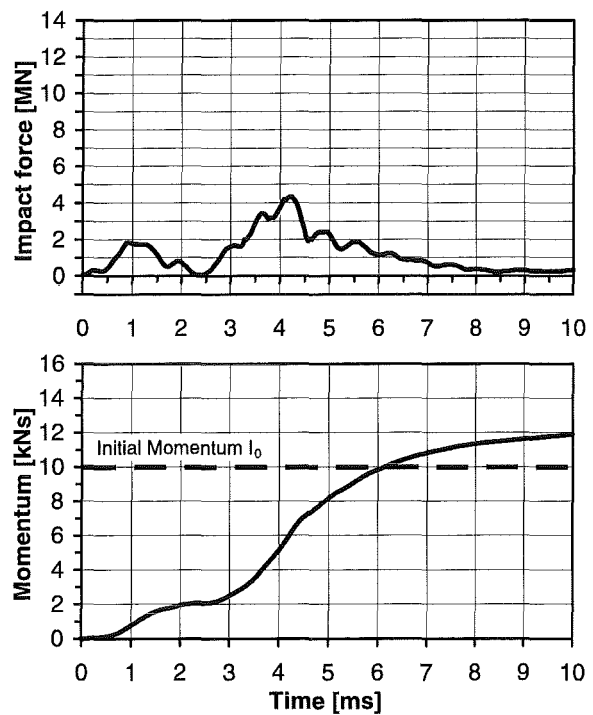


Fig. 4-23: Test10, liquid metal, 80 kg, 121 m/s, upper internal structures of steel.

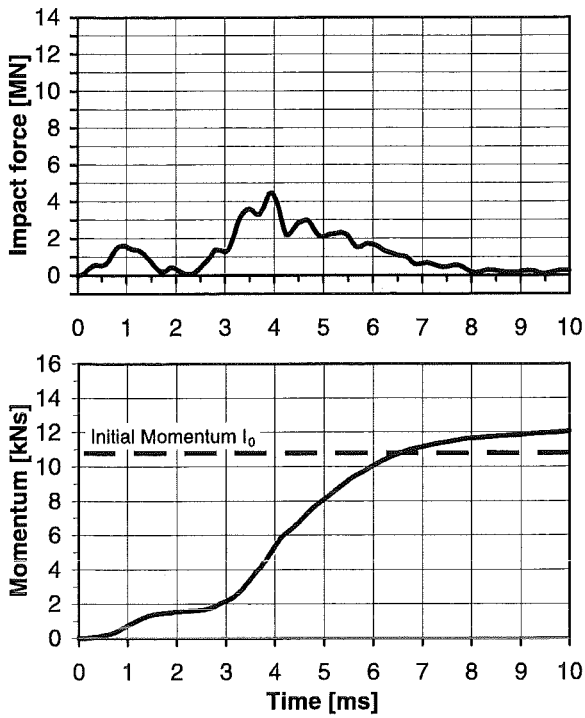


Fig. 4-24: Test12, liquid slug, 80 kg, 131 m/s, upper internal structures of steel.

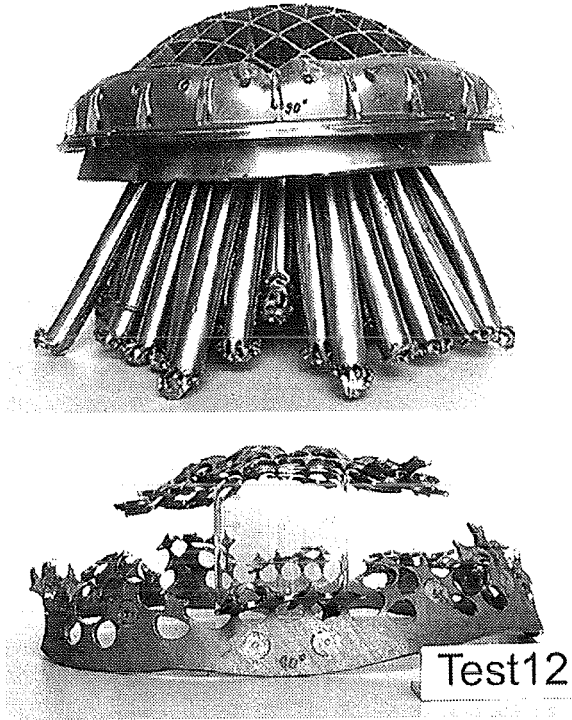


Fig. 4-25: Test12, upper internal structures of steel after the impact.

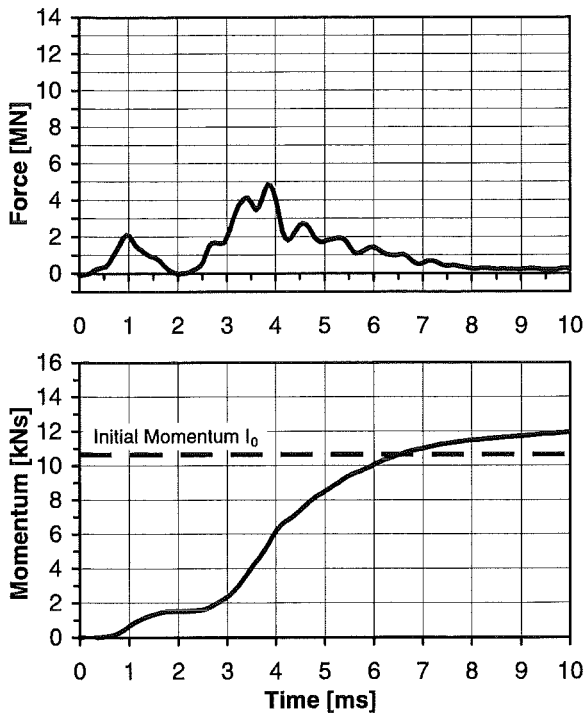


Fig. 4-26: Test15, liquid metal, 80 kg, 129 m/s, upper internal structures of steel.

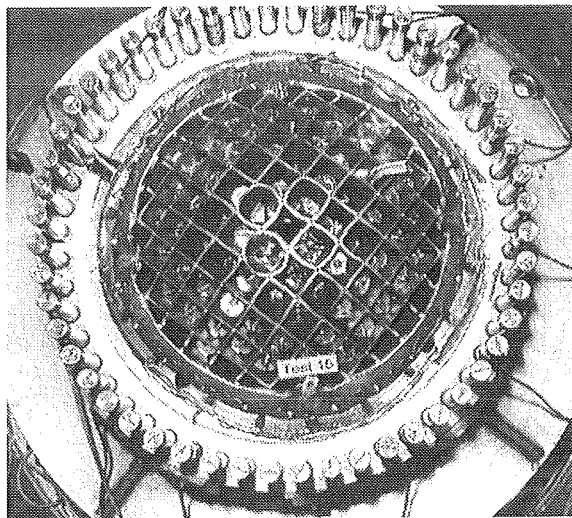


Fig. 4-27: Test15, upper internal structures of steel after the impact.

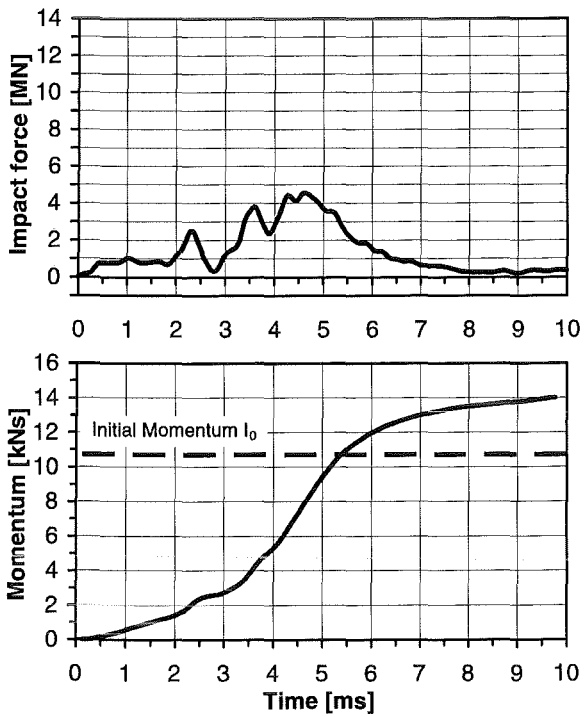


Fig. 4-28: Test11, liquid slug, 80 kg, 130 m/s, upper internal structures of brass.

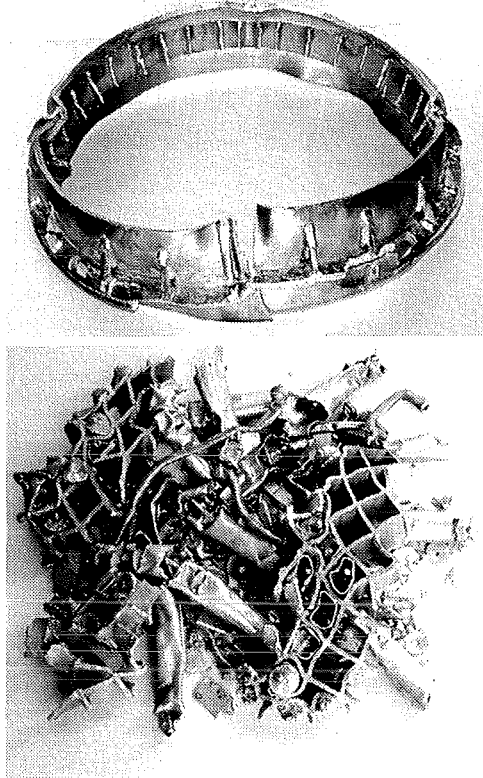


Fig. 4-29: Test11, parts of upper internal structures of brass after the slug impact.

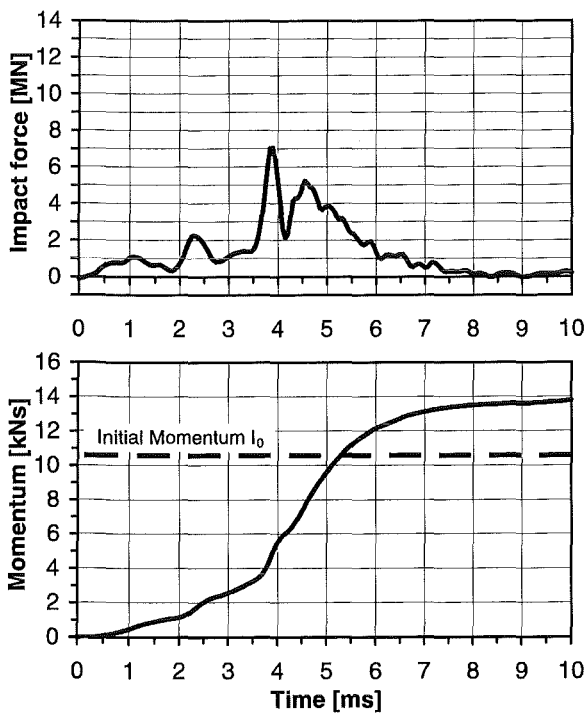


Fig. 4-30: Test13, liquid slug, 80 kg, 128 m/s, upper internal structures of brass.

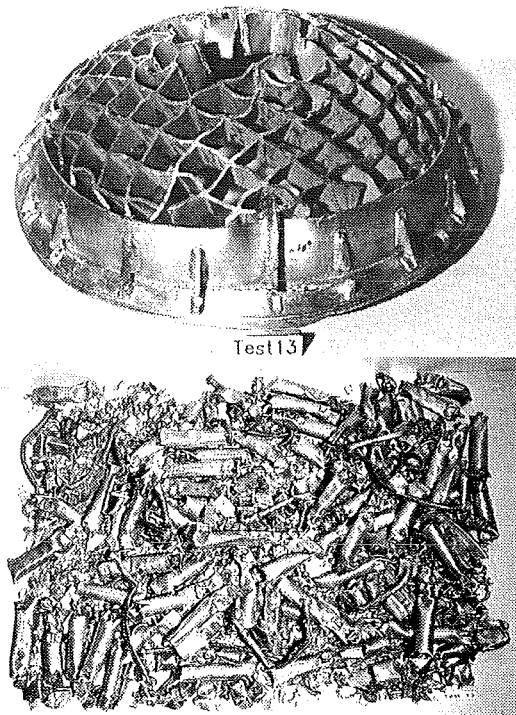


Fig. 4-31: Test13, upper internal structures of brass after the slug impact.

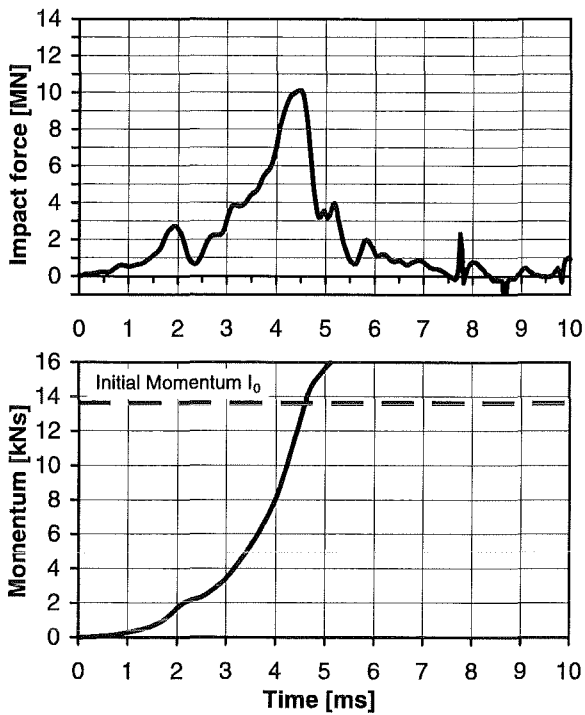


Fig. 4-32: Test16, liquid slug, 80 kg, 160 m/s (estimated), upper internal structures of brass and lead .

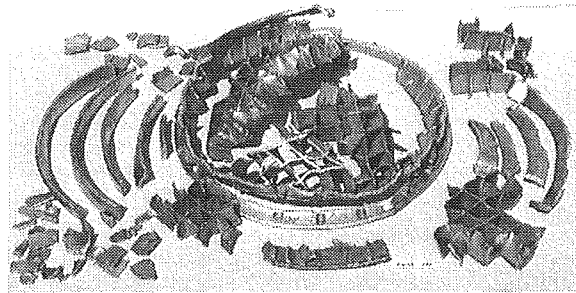


Fig. 4-34: Test16, upper support grid of brass after the slug impact

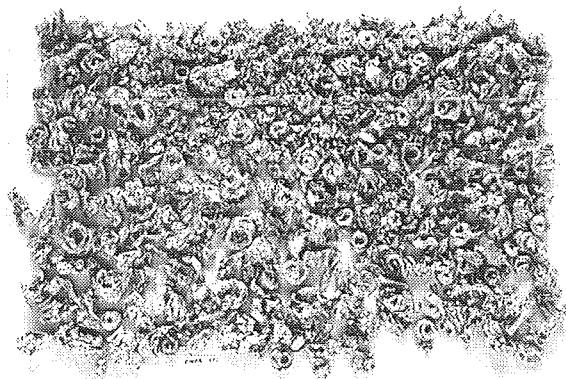


Fig. 4-35: Test16, guide tubes of lead after the slug impact

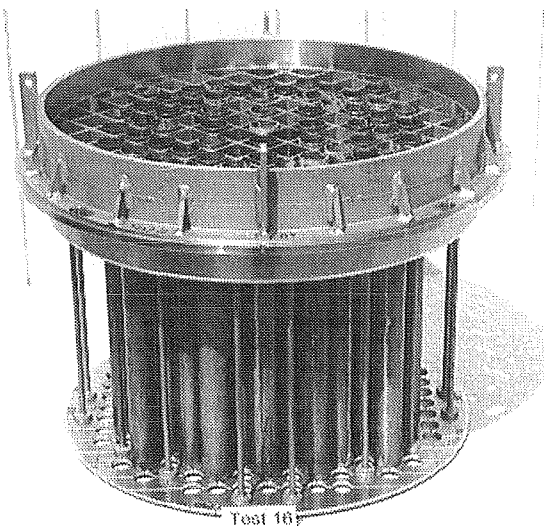


Fig. 4-33: Test16, model of the upper internal structures of brass (upper support grid) and lead (guide tubes).

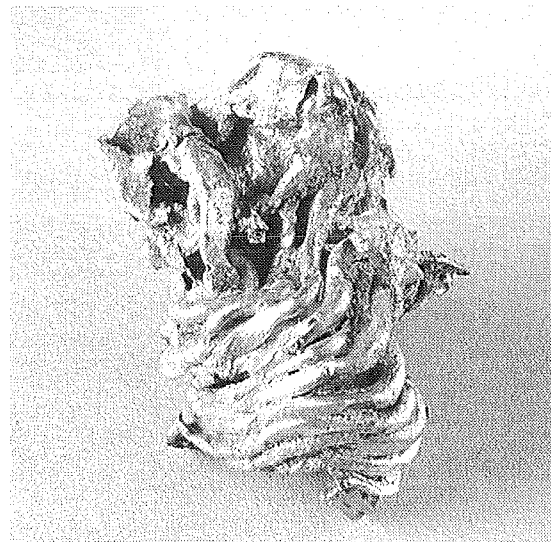


Fig. 4-36: Test16, a single deformed guide tube of lead

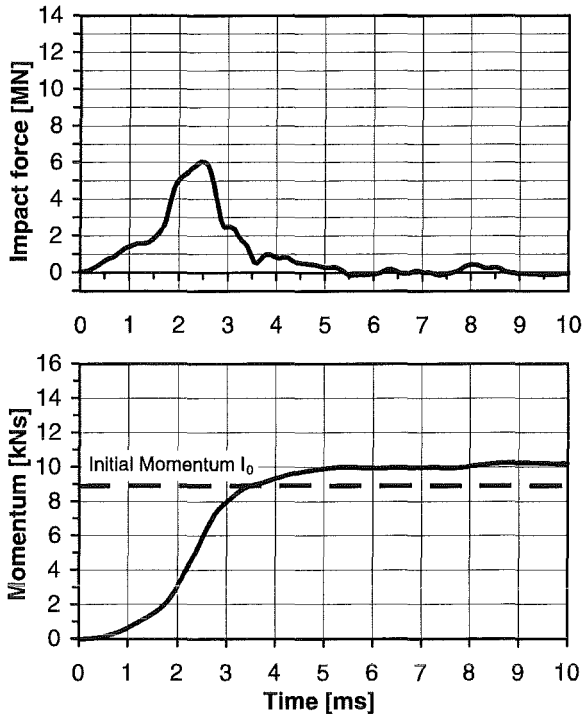


Fig. 4-37: Test14, liquid slug, 80 kg, 108 m/s, only upper support grid of steel.

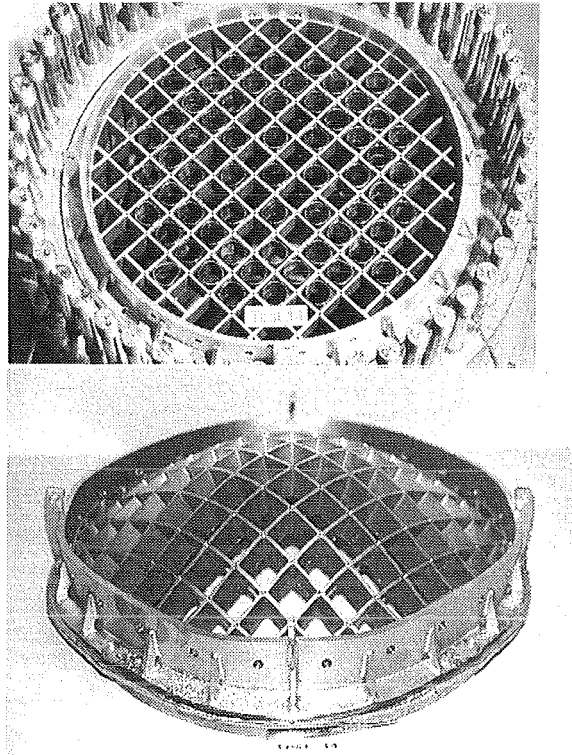


Fig. 4-38: Test14, upper support grid of steel before and after the slug impact.

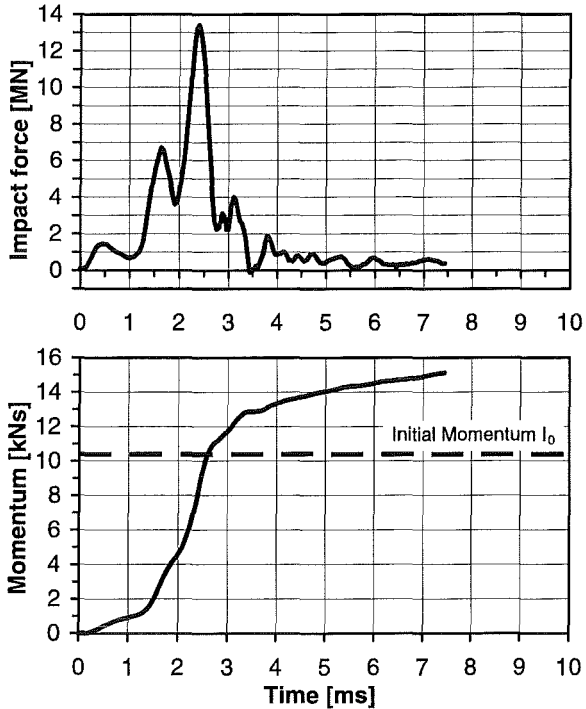


Fig. 4-39: Test17, liquid slug, 80 kg, 126 m/s, only upper support grid of brass.

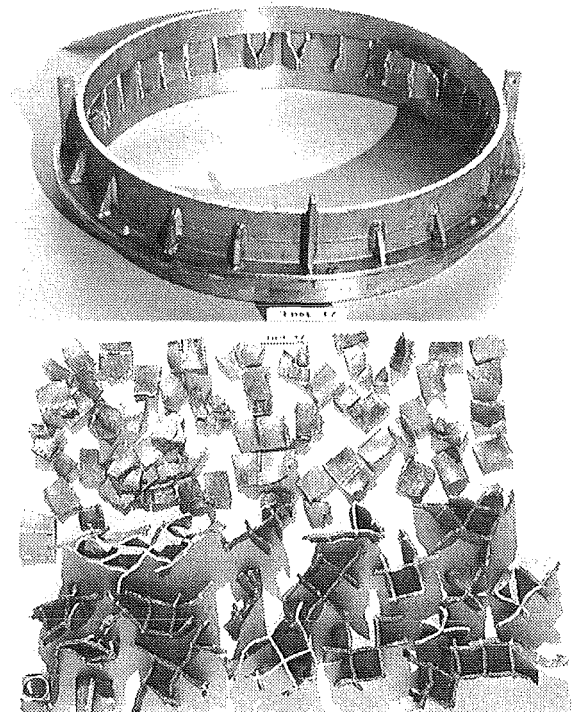


Fig. 4-40: Test17, upper support grid of brass after the slug impact.

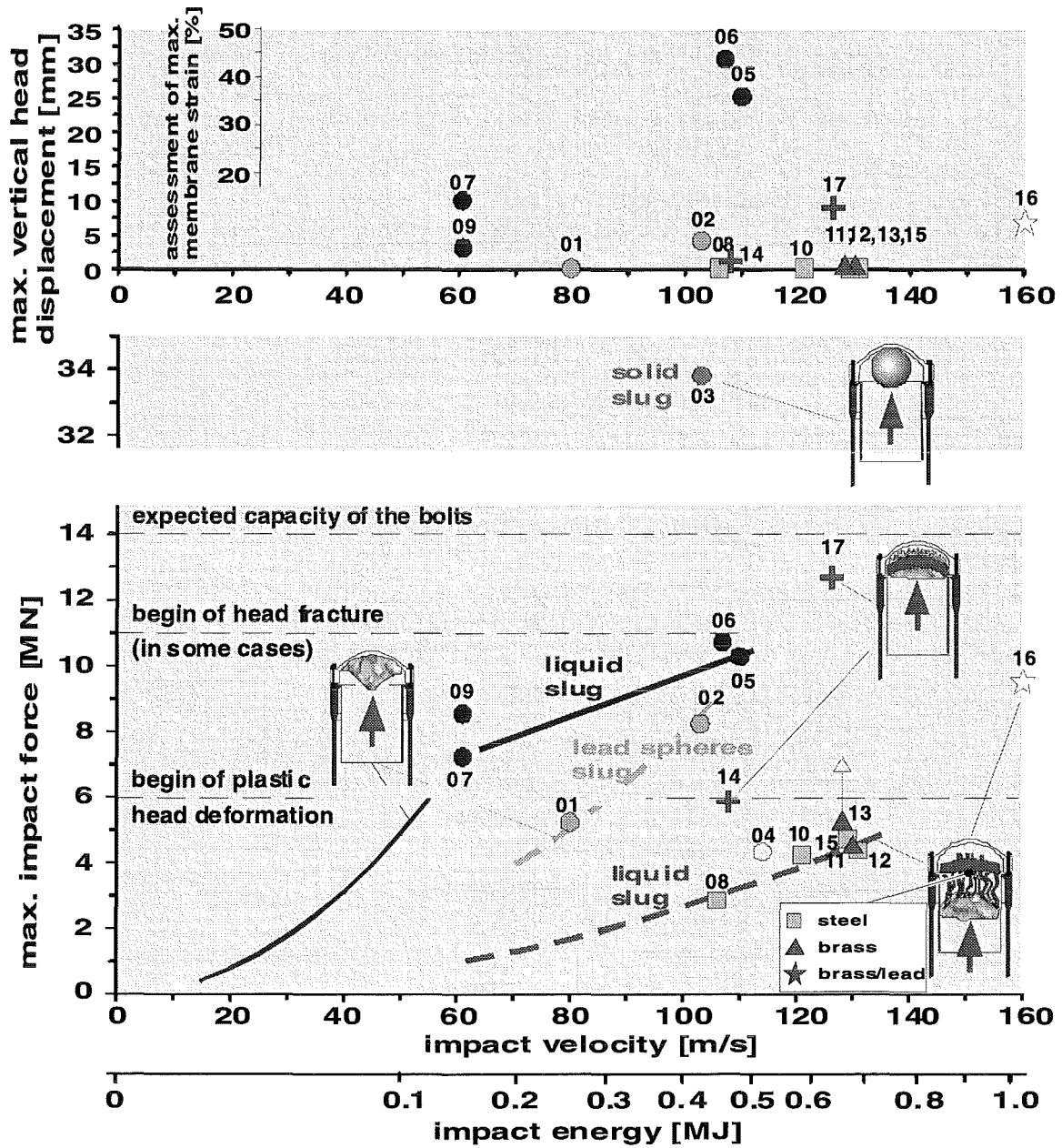


Fig. 4-41: Results of model experiments BERDA I, slug impact against a PWR vessel head during a steam explosion, forces linearly converted to a reference mass of 80 kg

4.2 Simplified slug impact experiments

4.2.1 Similarity experiments FLIPPER

In order to check the similarity for liquid-structure-impact problems, the experiments FLIPPER were performed, Stach (1997). Tests under simplified conditions were carried out on three different scales. The experimental arrangement and the results are shown in Fig. 4-42.

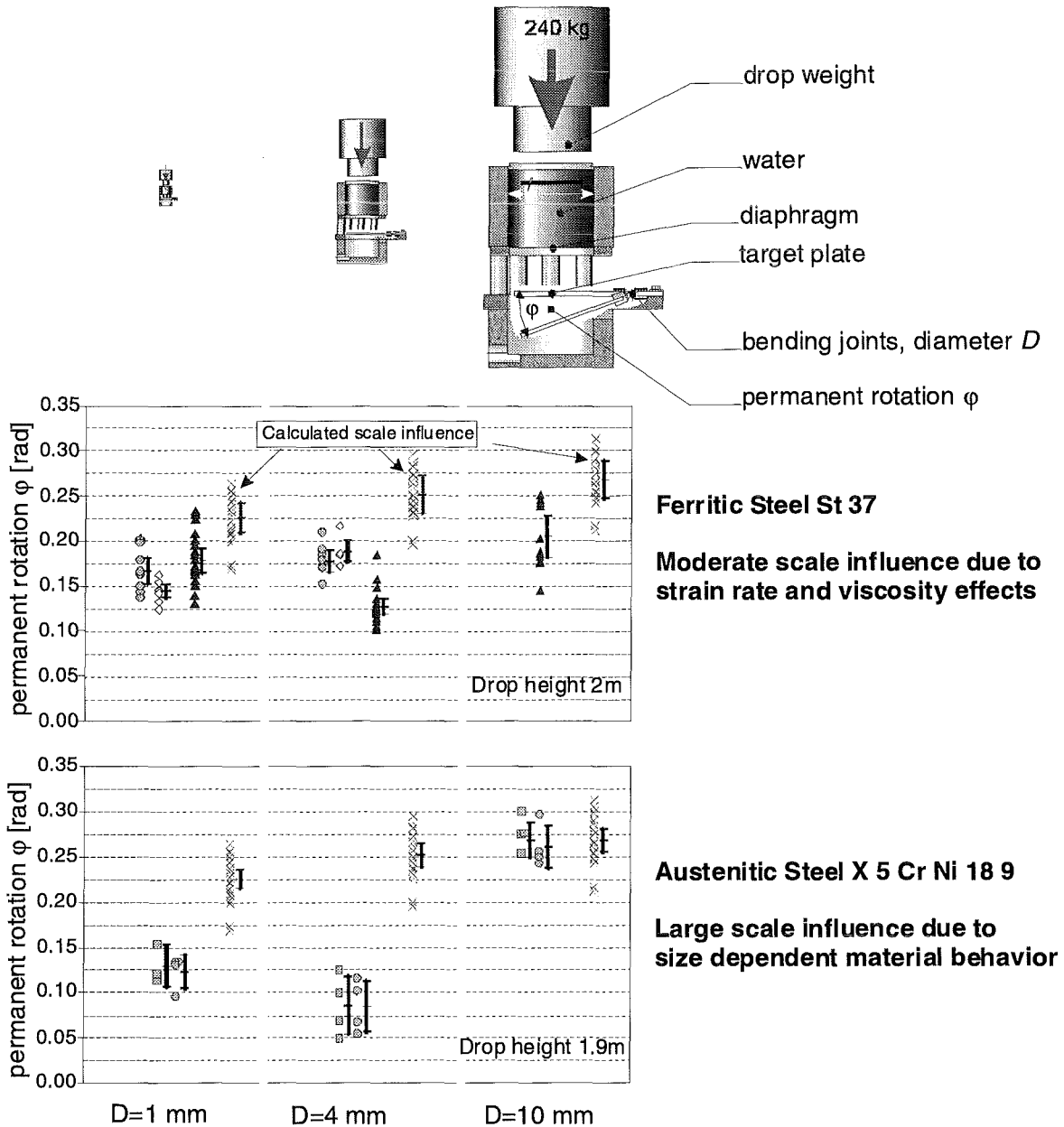


Fig. 4-42: Similarity experiments FLIPPER, size effect for liquid impact on deformable structures

For ferritic steel, indications regarding a slight size effect on the structural deformation represented by the permanent rotation were found. It may be explained by the known strain rate effect on the stress-strain diagram (section 5.1) and can be taken into account by the respective reduction of the stress scale λ_{σ} .

For austenitic steel a pronounced size effect was observed. As suggested by further indications, this is to be attributed to a size effect on the material behaviour. For the given reactor problem, this effect does not cause major problems, as austenitic steel is only used extensively for internal structures. However, according to BERDA I results, the influence of the material properties of the upper internal structures on the head load is rather small.

4.2.2 Impact tests SKIPPY

In order to investigate the effect of the slug material characteristics on the impact force, the SKIPPY 1 tests were carried out.

The test rig is shown in Fig. 4-43. It consists in a vertical tube, which guides the slug during the initial dropping time. The slug diameter is 0.04 m, the length is 0.2 m. The slug geometry is controlled by a thin paper wrapping, whose contribution is neglected during the impact. This means that the paper wrapping should easily explode when the slug reaches the circular steel target at the bottom of the test rig. This target is equipped with 3 force transducers in order to measure the impact force. The dropping height is 0.8 m, leading to a velocity of about 4 m/s.

The impact forces provided by the slug dropping on a target was measured for different slug material:

- Water slug
- Glass spheres (3mm diameter)
- Mixed glass spheres and water.
- Sand.

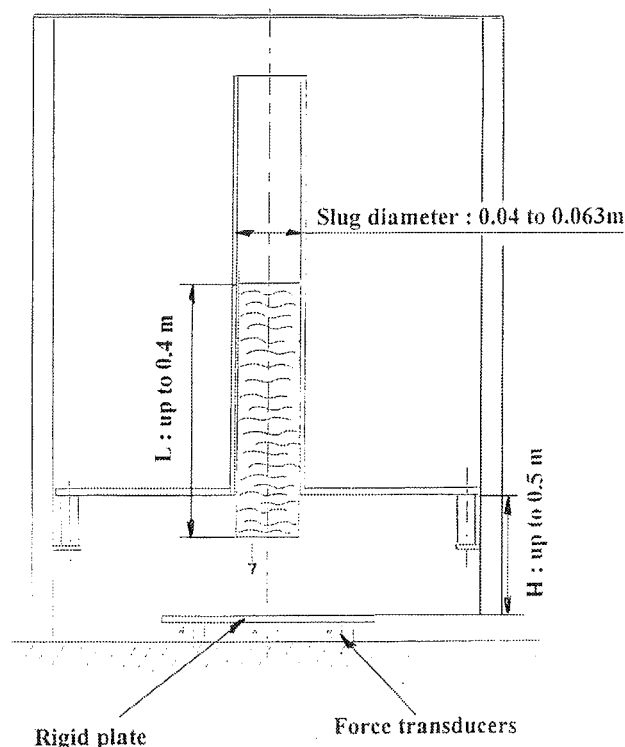


Fig. 4-43: Skippy 1 test rig.

Typical test results are shown in Figs. 4-44 and 4-45 for impacts with a water slug and a sand slug.

The instrumented steel plate had two first vibration modes at 800 and 2350 Hz. Unfortunately, the plate thickness, and stiffness, could not be increased very much because a higher specimen to plate mass ratio would have led to a bad signal sensibility.

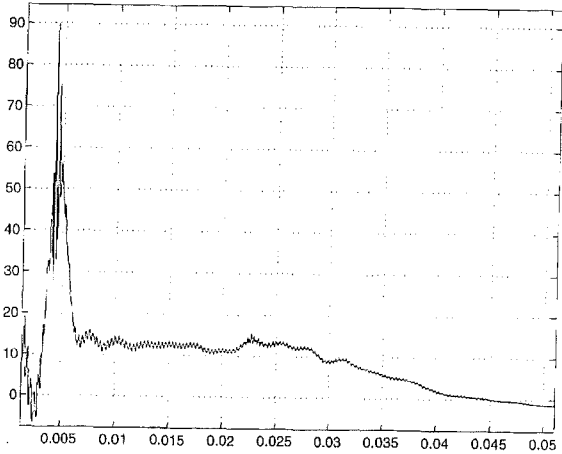


Fig. 4-44: Force time history for a water slug.

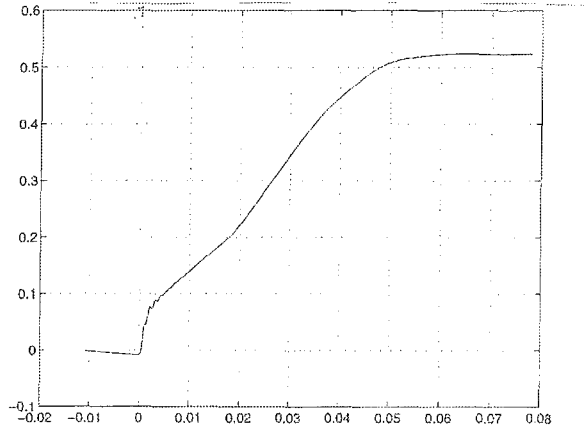


Fig. 4-45: Impulsion transmitted by a water slug.

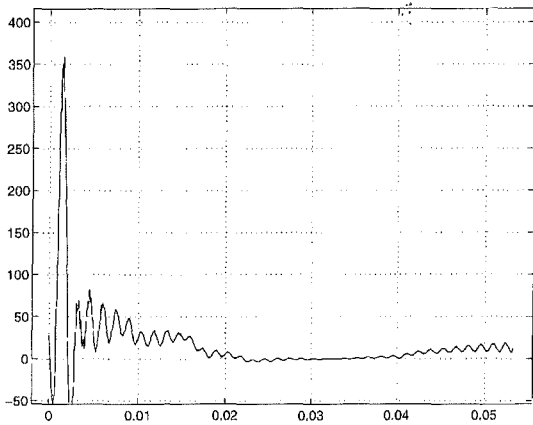


Fig. 4-46 : Force time history for a granulous slug (sand)

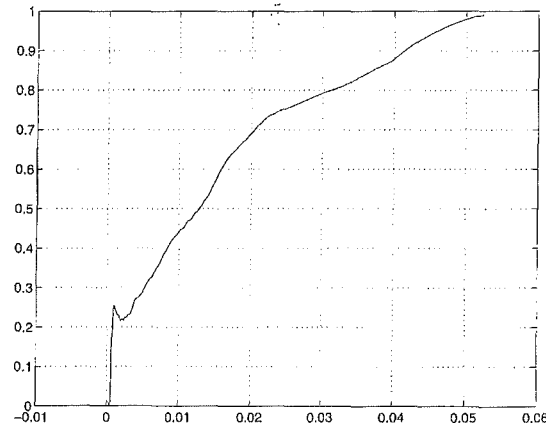


Fig. 4-47 : Impulsion for a granulous slug (sand)

It should be pointed out that, because of the short duration of the impulsion at the first impact step, the modal response of the plate is excited. Thus the desired force measurement is disturbed by the plate vibration. Filtering is necessary to eliminate undesired frequencies from the signals. The modal analysis of the plate gives an appropriate filtering criteria. The signals presented in Figs. 4-46 and 4-47 are filtered with a butterworth low pass filter at a frequency of 700 Hz.

Theoretically, the peak force duration is proportional to the wave travel time in the slug, which can be compared to a compression wave propagation in a rigid bar. The amplitude is

related to the sound velocity in the media. The second phase duration is connected to initial impact velocity and length of the slug. The amplitude of this second phase is one order of magnitude lower than the first one.

The conclusions from this preliminary tests Skippy 1 are:

- In fact, the measured maxima of the force is lower than the theoretical prediction. It is also shown that the measured duration of the initial peak is about ten times higher than the wave travelling time through the slug.
- The ratio of the transferred momentum to the initial momentum was calculated. This ratio is higher for liquid slugs (about 90 %) than for granulous slugs (70 to 80 %). But in the case of granulous slug, more of the momentum is transmitted in the first step of the impact.

It was decided that slugs of granulous material will be tested with the new test rig SKIPPY 2 with an improved instrumentation.

The Skippy 2 tests are performed on the dropping tower ORION at CEA Saclay. Therefore, the tested specimen may have a bigger size and the instrumentation is improved.

The test rig is shown in Fig. 4-48.

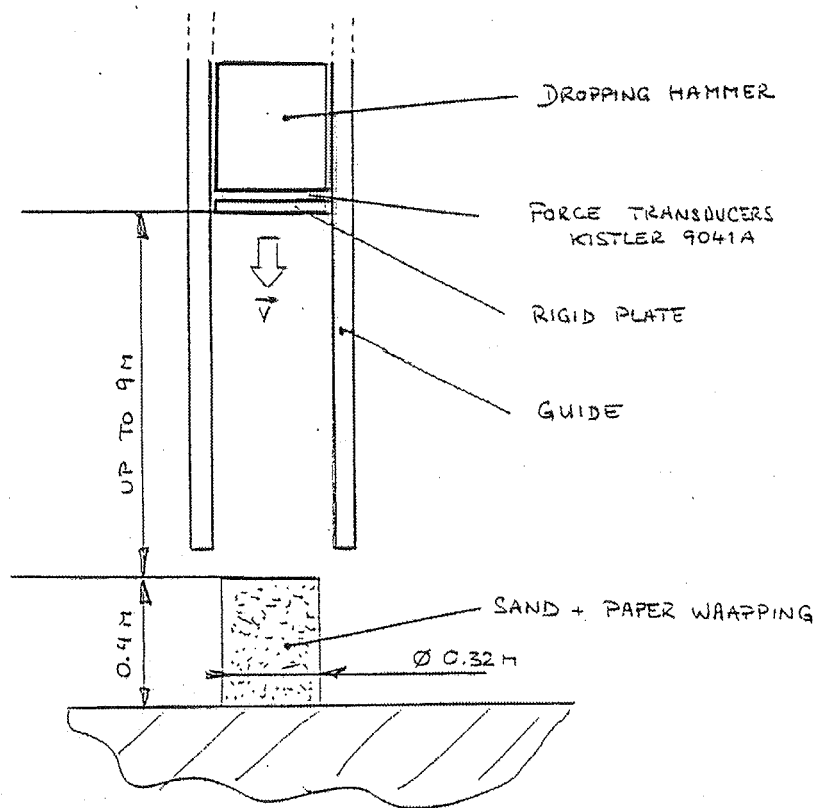


Fig. 4-48: The Skippy 2 test rig

The geometry is controlled by a paper wrapping around a cylindrical sand slug. The diameter of the slug was 0.32 m, the height 0.4 m. The specific mass of the sand is 1554 kg/m³. Thus, the tested mass was about 50 kg. The granulous specimen was impacted by a rigid dropping hammer of 70 kg. The dropping height was 5 m, leading to an impact speed of about 10 m/s. The paper wrapping was wetted before the test to decrease its

contribution during the impact. It was experimentally verified that one can neglect it. The instrumentation was composed by three force transducers mounted on a rigid plate on the bottom of the projectile. This plate impacts the sand slug and the force time history is directly measured.

The results of the tests are shown in Figs. 4-49 by the dashed curves. The force time history shows a first peak whose amplitude is about 100 kN during 5 ms. The second phase amplitude is about 10 times lower than the first one.

The displacement signal versus time is obtained with a camera. This optical device follows a high contrasted (black/white) target mounted on the projectile. Velocity is obtained by post processing (integration) an appropriate acceleration signal.

Calculation of SKIPPY 2 tests with the SPH method :

The SPH ("Smooth Particles Hydrodynamic") was originally developed to model bird strike on plane turbofan blades. It is an alternative to the NABOR method discussed in the next section. The SPH method has been implemented in the transient nonlinear finite element code PLEXUS.

The SKIPPY 2 tests were calculated with the PLEXUS code in order to check if the particle method is an appropriate tool to describe granulous slug impacts. The slug is modelled using spherical particles. Each particle is interacting with its neighbourhood.

The Figs. 4-50 show the deformed slug at $t = 1, 10$ and 40 ms. A high speed movie of the experiment is in good qualitative agreement with the calculated shapes.

The Figs. 4-49 a and b show the calculated force time-history (solid line) compared to the measured one (dashed line). Fig.4-49 b is a zoom of the first peak force.

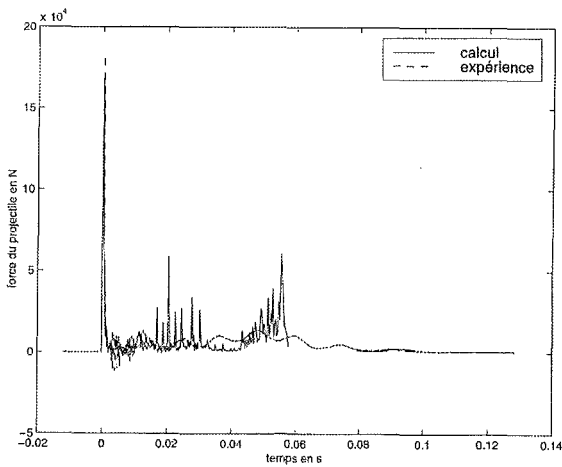


Fig. 4-49a: Force time history comparison between SPH calculation and experimental result.

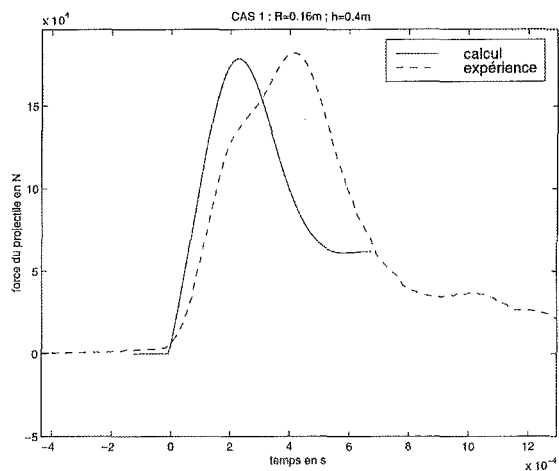


Fig. 4-49b: Force time history comparison between SPH calculation and experimental result. Temporal zoom of the first peak.

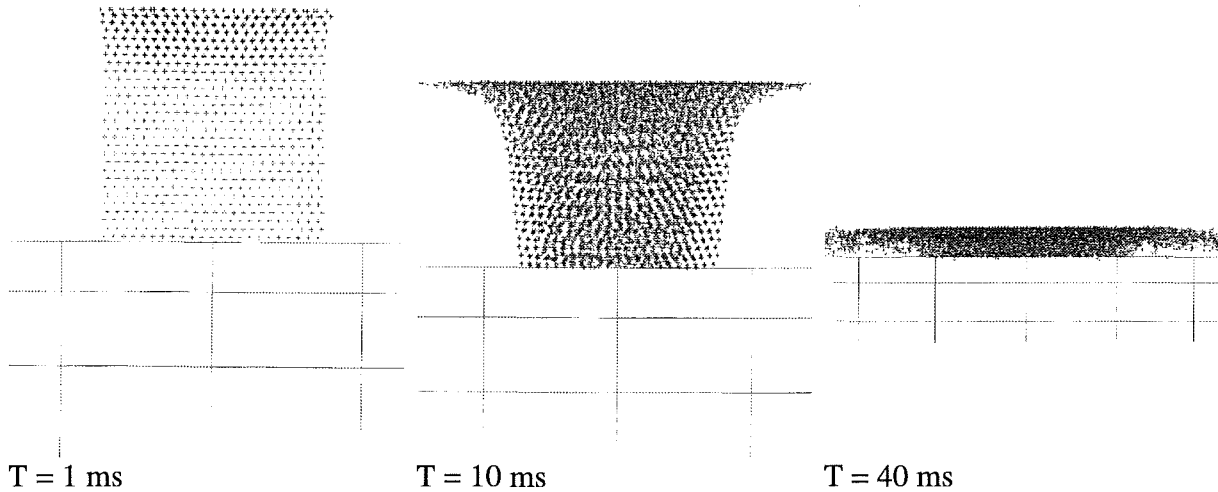


Fig. 4-50: Deformed shape of the slug obtained by the SPH calculation

The Fig. 4-51 shows the momentum transmitted to the instrumented projectile target.

One can see a good agreement between experimental data and calculation. Thus, one can conclude that SPH modelling is an appropriate tool to describe granulous slug impact behaviour at low velocity impact.

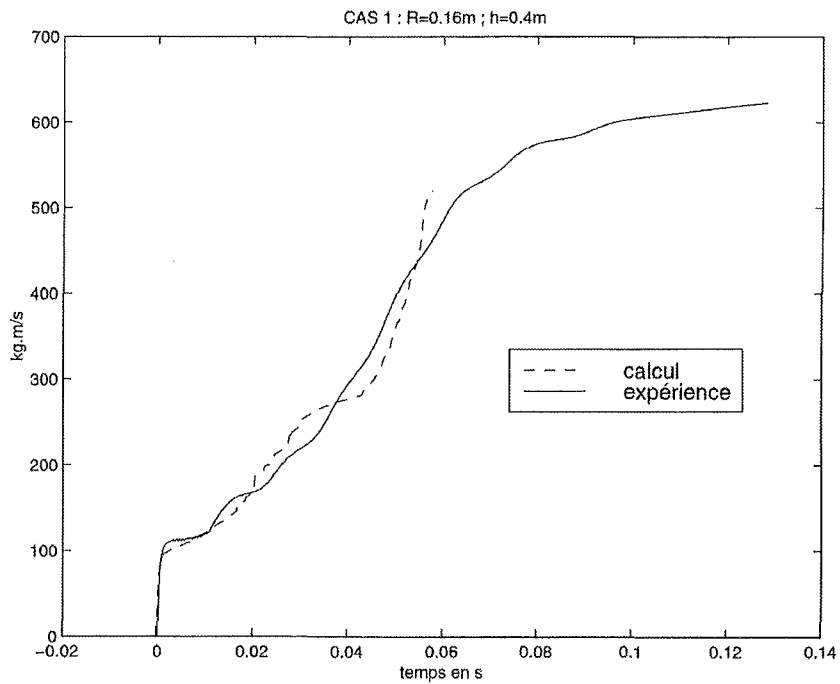


Fig.4-51: Transmitted momentum to the projectile target. Comparison between calculation (dashed line) and experiment (solid line).

4.3 Analysis of slug impact and slug penetration

4.3.1 Introduction

Parallel to the liquid slug impact experiments in the BERDA facility theoretical investigations were performed in order to improve the understanding of experimental findings and to test appropriate calculational tools. The classical fluid dynamic codes have large problems to describe serious distortion or even splashing of a liquid slug impacting on a structure undergoing large deformations. The calculational model has to solve simultaneously the coupled fluid dynamics and structural mechanics problem, as yielding of the structures influences the impact pressures and vice versa.

The new particle model for a fluid developed by CEA for the finite element code PLEXUS, Bung (1993), promised to overcome these difficulties. The method allows to discretize the liquid slug by an assemblage of discrete particles. In each time step a particle interacts with different other particles or with the boundaries. The density of a particle is only a function of the average distance between a particle and its neighbours. Pressure is related to density by the constitutive law for a perfect fluid. The forces between the particles are related to the pressure based on geometrical considerations. The occurrence of slug distortion or even splashing will not present a serious problem for this new "NABOR" method. Thus, it was attractive for both CEA and FZK to use the new method for calculations of the liquid slug impact experiments in the BERDA facility. However, there are still basic questions concerning the particle methods. Some are addressed by the special experiment FLIP designed at FZK. In addition to the NABOR method CEA developed the "smooth particle hydrodynamics" (SPH) method to overcome some of the problems, Letellier (1996). The SPH method was used for the SKIPPY calculations presented earlier.

In order to study in a more general sense the significance of the involved physical phenomena, the special code SIMSIC, Hirt (1997), was developed. In contrast to the PLEXUS model which is based on first principles and allows rather high space and time resolutions, for SIMSIC some of its parameters have to be adjusted to meet experimental results and then extrapolations and parameter variations can be performed easily.

Furthermore, structural mechanics calculations for the pressure vessel head were performed, in order to find out key effects which might explain a large deviation in the head deformations of two tests with the same impact velocities, Dolensky (1998).

4.3.2 Calculations for BERDA test 07 with the particle model in PLEXUS

The NABOR particle model in PLEXUS was used to perform coupled slug impact calculations for BERDA test 07, Strub (1998). Fig. 4-52 shows the discretization used. The head was modelled by 810 triangular thin shell elements DKT3, which allow for elastic-plastic membrane and bending deformation. The head was fixed by 54 bolts clamped at their lower end; their cross-section was modified appropriately, in order to account for the 52 bolts in reality. Non-linear material properties were considered for head and bolts. The slug was discretized by 1203 particles in a hexagonal arrangement. Fig. 4-53 shows the calculated paths of the particles during 2.5 ms of the impact. Fig. 4-54 shows the calculated forces and deformations compared with the measurements. The forces agree reasonably well in a conservative sense: if the oscillations are disregarded the maxima are rather close; the transferred momentum exceeds the measurement by about 25 %. However, the calculated deformations deviate considerably by a factor of three from the measurements.

Intensive discussions finally led to a refinement of the slug discretisation using 12425 particles (instead of 1203). Fig. 4-55 shows the new results, Strub (1998). The forces are only slightly changed, mainly because of a reduction of the oscillations which leaves maxima

closer to the experiment. The transferred momentum did not change significantly and still exceeds the measurement by 25 %. However, the head deformation increases considerably from 2 to 11 mm and thus nearly meets the experimental value. Summarizing, the calculation with 12425 particles agrees well with the measurements.

This result suggests that the numerical idealisation must have met the experimental conditions quite well, i.e. the real slug in the test 07 must have been rather compact. For test 09 with the same parameters the forces were nearly the same, however, the head deformation was only about one third of the deformation of test 07. Consequently, in this case, the impacting slug has to be considered as rather dispersed. Thus, if one would like to analyse test 09 a new more appropriate model for the dispersed slug would be required.

However, one important question is still open. Fig. 4-56 shows bolt forces and head deformations calculated for BERDA test 07 varying the numbers of particles for the liquid slug systematically from about 1200 to nearly 20000. A tendency for a convergence of the results can hardly be seen.

4.3.3 FLIP: Fluid impact experiment under well known boundary conditions

Some calculations were performed with PLEXUS for idealised impacts on rigid surfaces which yielded surprising results. In order to study such impacts experimentally, a small facility FLIP was designed at FZK, in which impacts between a liquid and a solid body having a well defined contact area can be investigated. Fig. 4-57 shows a sketch of the apparatus. The water slug is initially in rest. It has a rigid bottom, rigid side walls, and a free surface. The impact area of the slug and its opposite end is made from thin diaphragms. The solid impact body, which is initially in contact with one diaphragm of the water slug, is suddenly accelerated by the impacting pendulum. The displacement of the water is filmed by a high speed camera.

First experimental results for an impact with a velocity of 4.5 m/s are discussed. Fig. 4-58 shows the shape of the water slug 2.8 ms after impact begin, redrawn from the high speed film, and compared with a corresponding calculational result using the NABOR particle model in PLEXUS. It can be seen that in the calculations the water particles move faster than the impacting mass, as there occurs a gap between both. Furthermore, the particles at the surface have a tangential velocity component. This is physically not reasonable, as there is no pressure gradient along a free fluid surface. These findings indicate, that the particle model in PLEXUS describes the impact too hard. It ought to be checked whether the description of the particle behaviour at a free surface could be improved; presumably, the intensity of the slug rebound would then be mitigated.

4.3.4 Application of the special code SIMSIC

In order to study in a more general sense the impact of molten core material upon the upper internal structures and upon the vessel head, the special code SIMSIC was developed, Dolensky (1997). Since the complex geometry prevents a detailed description, only the essential physical effects are considered. The involved structures and the slug are described by separate models. Based on the balance of momentum in integral form a model is derived for the motion of the slug and for the involved fluid forces. The models for the deforming structures are based on simplified assumptions for the dynamic relations between force and deformations. The different models are coupled by the interacting forces and the compatibility condition for the displacements. Fig. 4-59 gives an impression of the model. For the calculations the code needs some input parameters gained in BERDA I and FLIPPER

experiments. Then SIMSIC can be used to study the significance of the different involved physical phenomena and to do extrapolations.

Fig. 4-60 shows results of a study concerning the influence of the elastic-plastic yielding of the head material for different impact velocities, Dolensky (1997). It can be seen that plastic deformation of the vessel head leads to a significant reduction of the bolt forces.

A variation of some boundary conditions suggests that an increasing slug mass (with the same other boundary conditions) leads to enlarged loading of the head, whereas the influence of the slug shape is negligible especially when the upper internal structures are considered. Significant plastic deformations of the head appear only at very high slug velocities (150 ... 170 m/s). Further, the calculations show that the damping effect of the internal structures is mainly based on their mass and geometry and less on their deformation characteristics, Hirt (1997).

4.3.5 Structural mechanics calculations for interpretation of BERDA tests 07 and 09

Tests 07 and 09 were both performed with an impact velocity of 61 m/s for a slug mass of 82.5 kg. Fig. 4-61 shows the bolt forces measured during the test and the head deformations measured after the test. The bolt forces agree reasonably well, while the head deformations deviate by a factor of three. In order to solve this seemingly contradiction, uncoupled calculations with the finite element program ABAQUS were performed for a series of prescribed pressure pulse loadings, Dolensky (1998). The aim was to find two simple pressure pulses for the head yielding forces and deformations similar to the experimental findings.

Fig. 4-62 shows those calculated results which agreed most favourably with the experiments. The corresponding loading for test 07 is a longer pressure pulse on a rather small head area, and for test 09 a shorter pressure pulse on a rather large head area. The momenta of the two loadings corresponded to the initial slug momenta used in the experiments.

Studying the calculational results more thoroughly yielded that the head deformations are very sensitive to the size of the loaded area for these loading conditions. Fig. 4-63 summarizes some decoupled calculations with prescribed pressure pulses having the same force resultant, but acting on head areas of different sizes. The loading conditions simulating impact in BERDA test 09 leads to deformations with small strains just above the yield point. The loading for test 07 yields deformations with large strains significantly beyond the yield point of the head material. Consequently, the deviations of the head deformations in tests 07 and 09 can be explained by different slug impact conditions causing more or less excess of the yield point of the head material. Repetition of BERDA tests with these impact conditions should lead to a large scatter in the head deformations with bolt forces agreeing reasonably well.

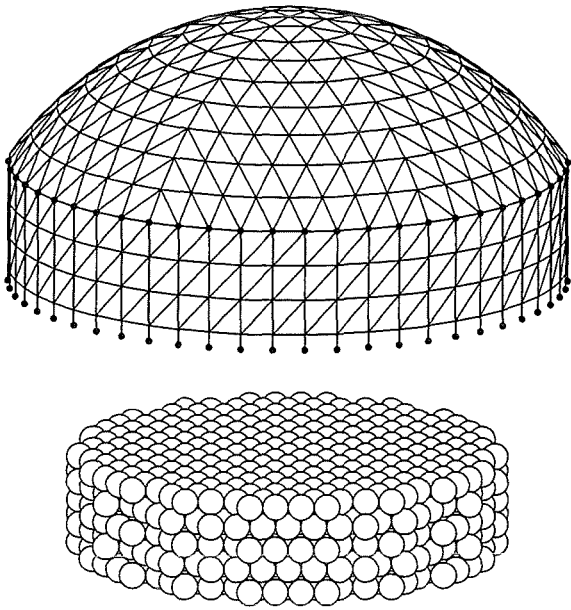


Fig. 4-52: Discretization of the liquid slug impact problem using the particle model in PLEXUS (810 shell elements, 54 bolts, 1203 slug particles).

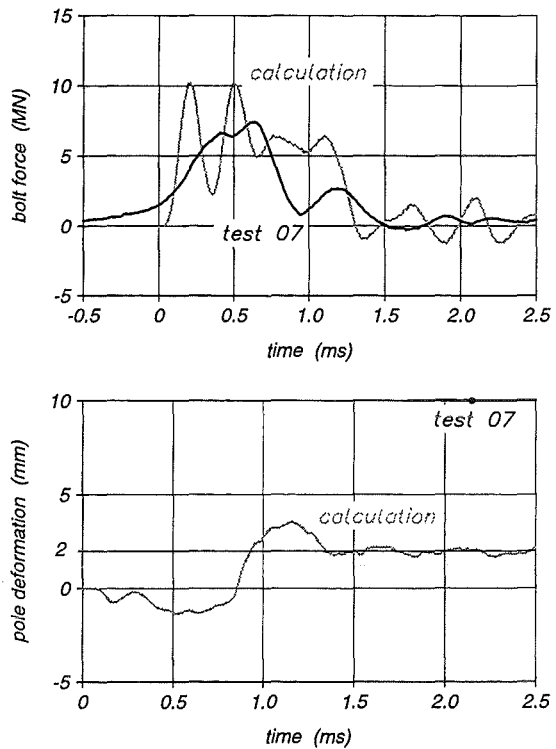


Fig. 4-54: Comparison of results from BERDA test 07 with PLEXUS calculations using 1203 particles for the slug discretization.

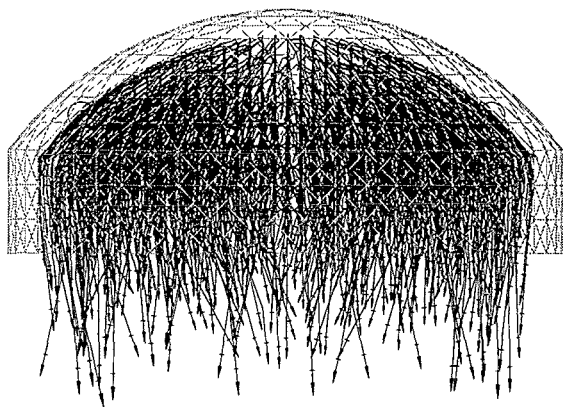


Fig. 4-53: Paths of the particles during an impact.

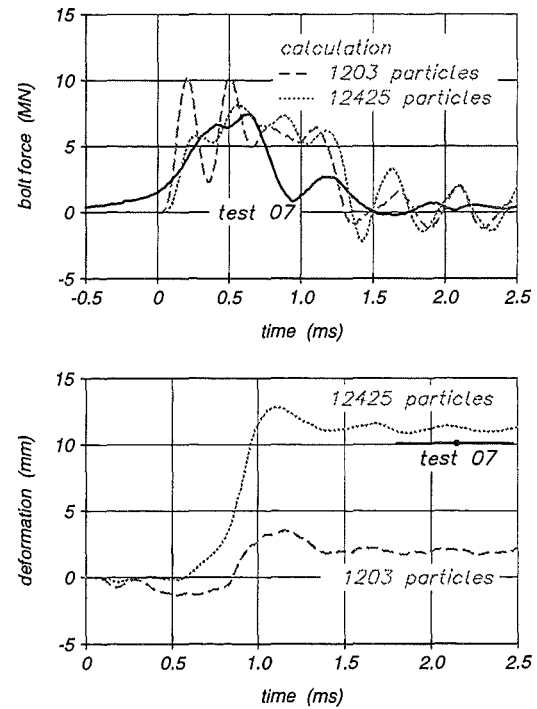


Fig. 4-55: Comparison of results from BERDA test 07 with PLEXUS calculations using 1203 and 12425 particles for the slug discretisation, resp.

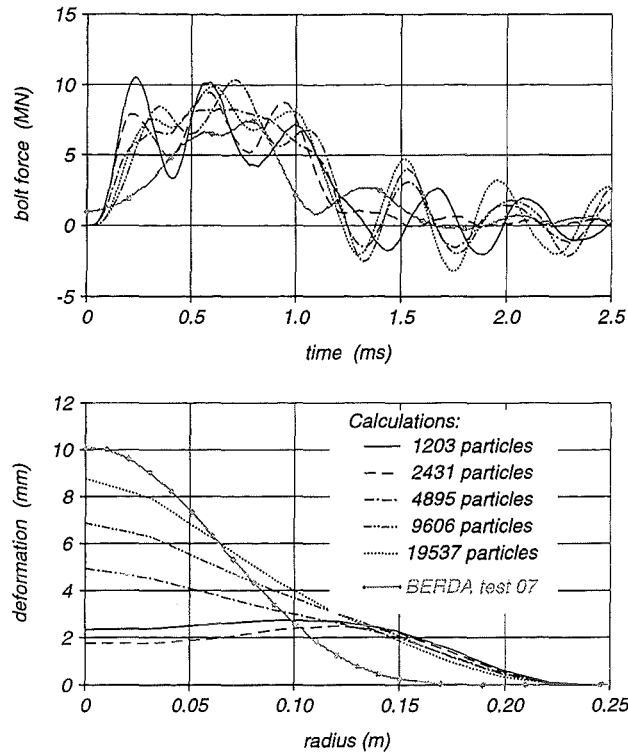


Fig. 4-56: Bolt forces and head deformations calculated with PLEXUS using different numbers of particles for the slug discretisation.

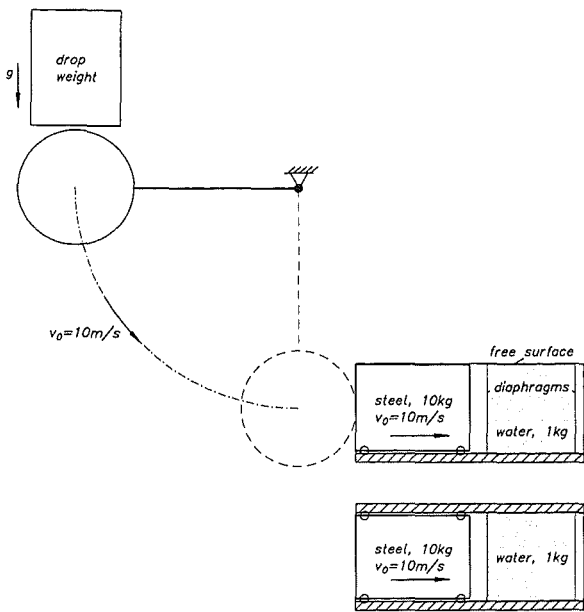


Fig. 4-57: Sketch of the FLIP apparatus for investigation of impact of a rigid mass on a plane fluid surface.

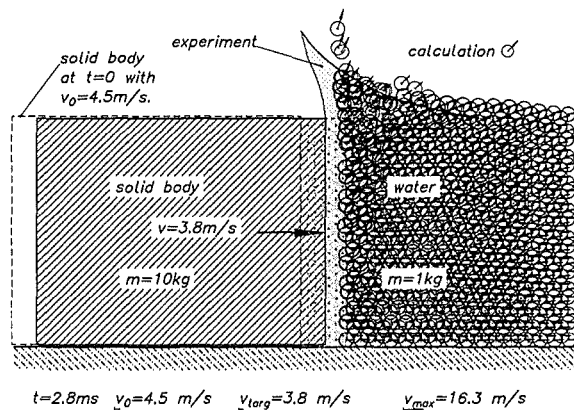


Fig. 4-58: Comparison of observed and calculated slug shape at 2.8 ms after impact begin in the FLIP set

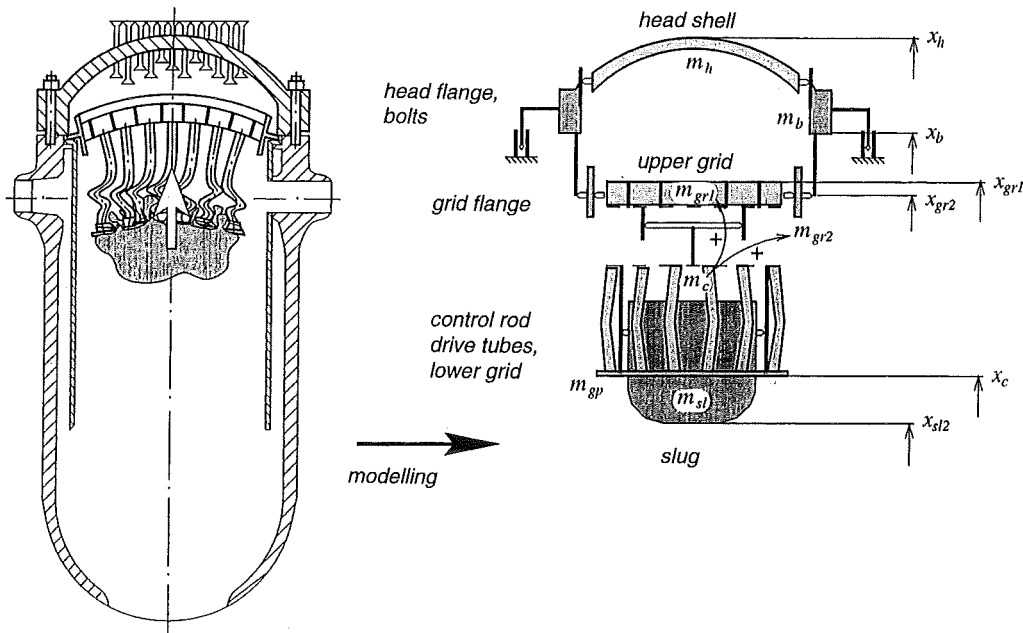


Fig. 4-59: Modelling of the liquid slug impact problem in the special code SIMSIC.

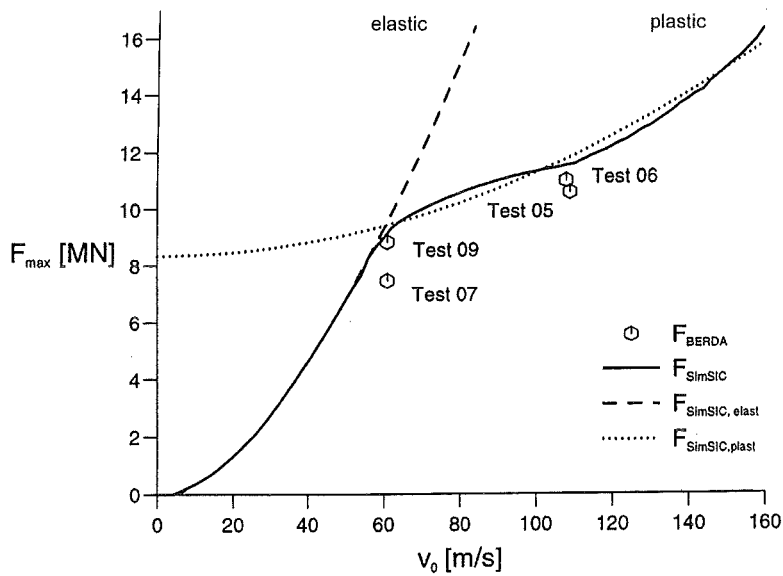


Fig. 4-60: Maximum bolt forces for slug impacts without internal structures calculated with SIMSIC for different impact velocities. Values from four BERDA experiments included.

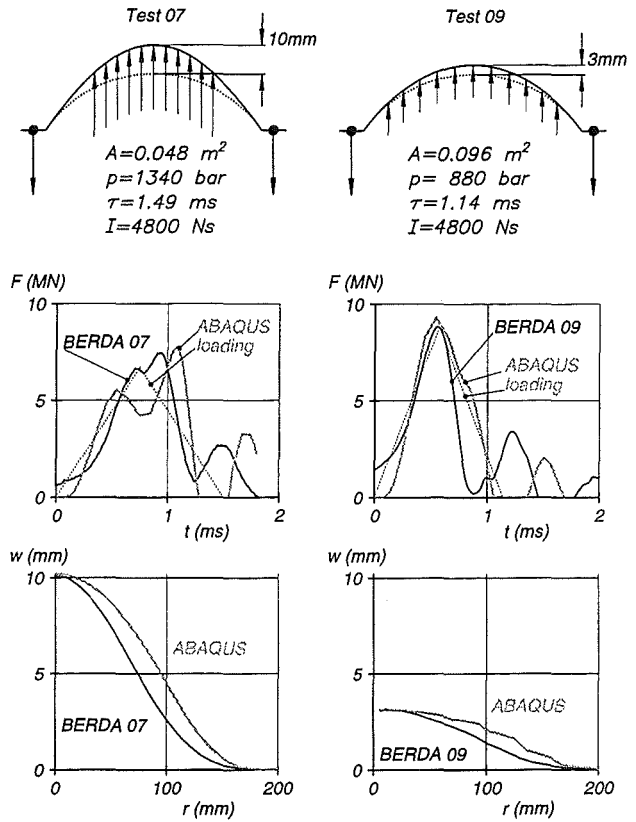
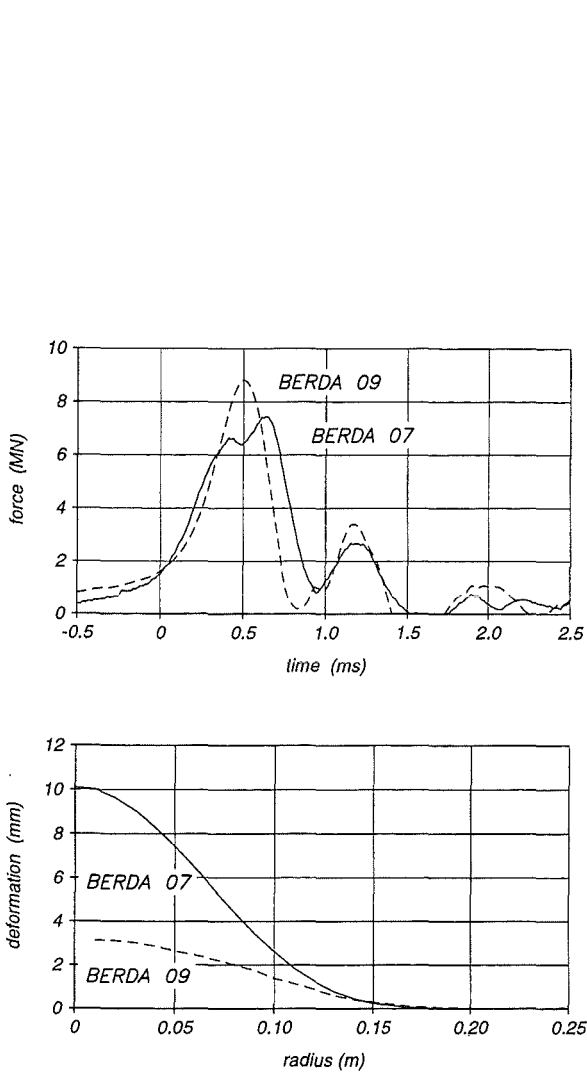


Fig. 4-62: ABAQUS calculations with two different prescribed pressure pulses for interpretation of the seemingly conflicting results of BERDA tests 07 and 09.

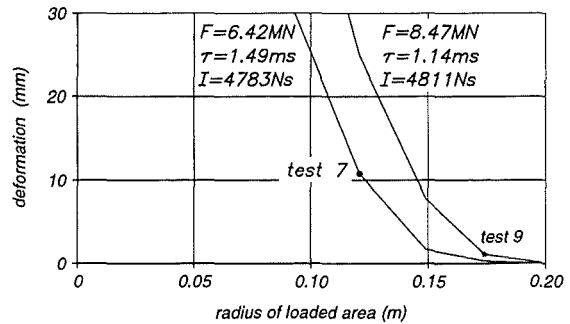


Fig. 4-63: Deformation of a vessel head loaded by two dynamic force pulses, distributed on areas of different size.

4.4 Conversion of results from the BERDA scale to the reactor scale

The conversion was accomplished using similarity theory. By means of the conventional basic equations (equilibrium conditions, time-independent elastic-plastic material behavior, etc), the scales below were derived from the length scale $\lambda_\ell = 10$ and the stress scale $\lambda_\sigma = 0.87$:

displacement scale	=	λ_ℓ	=	10
strain scale	=	1		
time scale	=	$\lambda_\ell / \sqrt{\lambda_\sigma}$	=	10.7
velocity scale	=	$\sqrt{\lambda_\sigma}$	=	0.93
force scale	=	$\lambda_\ell^2 \lambda_\sigma$	=	87
energy scale	=	$\lambda_\ell^3 \lambda_\sigma$	=	870

Of course, the basic equations and assumptions only allow an approximate description of the processes. Consequently, the above scales are also approximate. To determine the resulting deviations by way of example, the similarity experiments FLIPPER were performed as described in section 4.2. It turned out that for ferritic steel, which is used for the pressure vessel head, the similarity theory is acceptable.

The scales also apply to non-linear processes. However, material damage and fracture processes could not be taken into account, as adequate theoretical models do not exist. Therefore, the conversions are only performed for those model experiments BERDA I, where it is quite certain that the plastic head deformations do not cause significant damage and fracture even for reactor dimensions.

As findings regarding component fracture as a function of the component size are hardly available, only small plastic deformations are admitted at the moment. Thus from Fig. 4-41 the following can be concluded:

- In case A, where all upper internal structures are molten, the admissible kinetic slug energy is 0.12 MJ for the BERDA scale, corresponding to $E_{\text{slug}} = 0.1$ GJ for the reactor.
- In case B, where only the upper support grid is available, the admissible kinetic slug energy is 0.45 MJ for the BERDA scale, corresponding to $E_{\text{slug}} = 0.4$ GJ for the reactor.
- In case C, where all the upper internal structures are available, the admissible kinetic slug energy is 0.9 MJ for the BERDA scale, corresponding to $E_{\text{slug}} = 0.8$ GJ for the reactor.

From section 4.1 and 5.1 it can be concluded that in cases B and C the temperature of the upper internal structures should not be much higher than 600 °C.

Now based on the predicted core melt progress and the resulting temperature distribution (EU projects COBE and MVI) the appropriate cases A, B, C can be selected and based on the predicted corium ejection and its kinetic energy caused by a postulated steam explosion (EU project MFCI) it can be determined whether a failure of the upper head can be ruled out.

Furthermore, applying the formula developed in section 3.2, the admissible mechanical energy E_{plate} fed into the upward moving core support plate can be determined. For different cases a, b, c, d of the shape of the corium on top of the core plate, the results are shown in Fig. 4-64.

Now a comparison with the mechanical energy release from a postulated steam explosion is sufficient to determine whether a failure of the upper head can be ruled out. This is quite helpful in the current situation, where the steam explosion problem is not yet completely understood.

For example, if only the upper grid plate is left (case B) and if the most unfavorable corium distribution on top of the core support plate is assumed (case b), the admissible mechanical energy release from a steam explosion is at least 1.0 GJ. On the other hand, very rough and pessimistic assessments of the steam explosion are likely to suggest a thermal energy of the explosion of less than 3 GJ and a mechanical efficiency of less than 30 %, leading to a mechanical energy release of less than 0.9 GJ. This would mean that the upper head integrity is assured.

It should be mentioned, however, that the admissible values assessed in Fig. 4-64 still need confirmation by the experiments BERDA II. It should also be pointed out that recently investigations have been started to find out whether higher plastic head deformations can be allowed. Depending on the results, the admissible impact force and the admissible kinetic slug energies may possibly be increased.

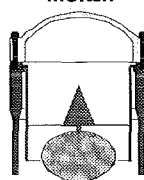
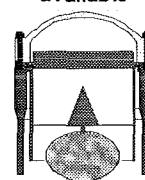
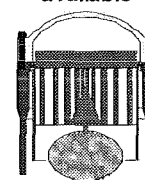
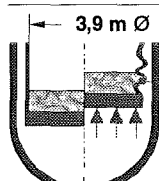
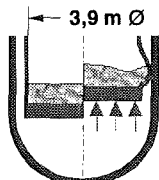
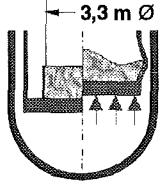
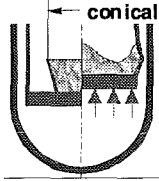
	A Upper int. struct. molten	B Only upper grid available	C Upper int. struct. available
upper line: mass of the heavy reflector <u>not</u> considered			
lower line: half of the mass of the heavy reflector added to the mass of the support plate	$E_{slug} = 0,1 \text{ GJ}$	$E_{slug} = 0,4 \text{ GJ}$	$E_{slug} = 0,8 \text{ GJ}$
a  concertina mode $\chi=1,0$	$E_{plate} = 0,15 \text{ GJ}$ 0,20	Because of high E_{slug} concertina mode not expected	
b  radial expansion $\chi=0,7$	Because of small E_{slug} rad. expansion not expected	$E_{plate} = 1,0 \text{ GJ}$ 1,4	2,0 2,8
c  $\chi=0,5$	0,4 0,6	1,6 2,4	3,2 4,8
d  $\chi=0,4$	0,5 0,8	2,2 3,5	4,4 7,0

Fig. 4-64: Calculated admissible mechanical energy input E_{plate}

5. Material properties for the lower and the upper head problem

G. Breitbach, P. Ennis, KFA, Jülich; G. Solomos, K. Labibes, JRC, Ispra

At the lower head large temperatures may occur during a core melt-down accident. In section 1 corresponding constitutive equations and failure criteria have been investigated. In this part of the project the data base for the mechanical deformation behaviour of the pressure vessel steel 20 MnMoNi 5 5 in the temperature range 700 to 1000°C has been improved. For comparison purposes, some tests were also carried out on the steel 16MnD5. Standard uni-axial tensile and tube tests were carried out and the results evaluated with special reference to the ferrite-austenite transformation which occurs in the steels of interest at temperatures around 750°C.

At the upper head and the upper internal structures high dynamic loads may occur caused by a postulated in-vessel steam explosion. In section 4 these loads are investigated by model experiments or reduced size causing increased strain rates. Furthermore, the models are at room temperatures. Consequently, information about the size effect, the strain rate effect, and the temperature effect on the relevant material properties is needed. Corresponding tests and their results on the pressure vessel steel 20 MnMoNi 5 5, as well as on the steels for the bolts and the upper internal structures are described. Also tests with red brass used as simulation material for the upper internal structures are included.

5.1 Creep tests

5.1.1 Uni-axial tests

The test matrix for the uni-axial creep rupture testing of the steels is shown in Table 5-1. The stresses for the respective temperatures were selected to allow an iso-stress evaluation of the test results. The specimen geometry is shown in Fig. 5-1 and the tests according to DIN 50110 were carried out in constant load, single-specimen test machines with continuous strain measurement during the tests. To avoid excessive oxidation of these low alloy steels at the high test temperatures, the tests were carried out in a helium atmosphere. Because of the high ductility of the steels not all tests were taken to rupture. Many specimens became too long for a constant temperature along the gauge length to be guaranteed and the specimens were removed before fracture occurred. The evaluation of the test results was based on the time to reach 1, 5 and 15% creep strain and on the secondary creep rate which was determined from the creep (strain-time) curves. In the range of test temperatures the low alloy steels undergo a phase transformation from ferritic (body-centred cubic structure) to austenitic (face-centred cubic structure) which involves a volume change of around 1% and a change in the deformation characteristics. This effect will be discussed in the interpretation of the experimental results.

The creep curves measured for the steel 20 MnMoNi 5 5 are shown in Fig. 5-2. From the creep curves, the times to creep strains of 1, 5 and 15% and the secondary creep rate (the linear portion of the curves) were obtained.

The times to 5 and 15% creep strain to achieve various temperatures and stresses for the 20 MnMoNi 5 5 specimens are plotted in Fig. 5-3. It can be seen that there is a discontinuity in the behaviour at a test temperature of 800°C, the creep strength at 800°C being higher than that measured at 750°C. The secondary (minimum) creep rates are shown in Fig. 5-4, and again there is a discontinuity at 800°C, the creep rates measured at 800°C being lower than those at 750°C for the same stresses.

The reason for the discontinuity is the transformation of the low temperature ferrite phase to the high temperature austenite phase. For 20 MnMoNi 5 5, the temperature range over which this transformation occurs is 690 – 825°C. It appears that at test temperatures up to 750°C, the deformation is dominated by the low temperature ferrite phase and at 800°C and above by the high temperature austenitic phase. Microstructural studies of specimens which had been heat treated at various temperatures showed that after 4 h at 800°C the structure was nearly all martensitic indicating that the ferrite to austenite transformation was near 100%. Specimens heat treated at 730°C showed large proportions of ferrite still present in the structure, see Fig. 5-5.

Table 5-1: Creep testing parameters for 20 MnMoNi 5 5 (CYZ) and 16 MnD 5 (FSY)

specimen number	temperature °C	stress MPa	status
CYZ201	700	80	test completed
CYZ202	700	60	test completed
CYZ203	700	40	test completed
CYZ204	730	60	test completed
CYZ205	730	40	test completed
CYZ206	730	30	test completed
CYZ207	750	40	test completed
CYZ208	750	30	test completed
CYZ209	750	20	test completed
CYZ210	800	30	test completed
CYZ212	800	20	test completed
CYZ213	850	20	test completed
CYZ215	850	15	test completed
CYZ218	900	15	test completed
CYZ216	900	10	test completed
CYZ219	950	15	test completed
CYZ220	950	10	test completed
CYZ103	977	10	test completed
FSY002	750	20	test completed
FSY003	800	30	test completed
FSY004	800	20	test completed
FSY005	850	20	test completed
FSY006	850	15	test completed

In the temperature range of the transformation, some creep tests were carried out on the French steel 16MnD5. The creep curves are shown in Fig. 5-6 and in Fig. 5-7. The steels 20 MnMoNi 5 5 and 16MnD5 are compared on the basis of the time to 15% creep strain and the secondary creep rate. It can be seen that the discontinuity in the creep behaviour occurs at a higher temperature for 16MnD5 than for 20 MnMoNi 5 5, the change being first seen in 16MnD5 at 850°C. A large difference in the creep strength of the steels was therefore obtained at 800°C. This is to be expected from the chemical composition difference between the two steels, especially the carbon content. At test temperatures of 750 and 850°C, the creep strengths of the two steels were similar.

5.1.2 Tube tests

For each steel, two internal pressure tests with tubes at 1000°C were carried out. The specimen geometry is shown in Fig. 5-8. The tubes were heated to 1000°C and subjected to 25 and 30 bar internal pressure. The test atmosphere was argon to prevent excessive oxidation of the steels during testing. The increase in diameter of the tubes was measured at the mid-point of the hot zone with four extensometers located around the tube. All specimens were tested to failure, that is, until a leak appeared and the tube de-pressurized. Fig. 5-9 shows the appearance of a failed tube specimen and indicates extensive creep deformation.

In comparison to the RUPATHER tests of section 1 with tubes of varying temperatures in axial direction, the tube tests reported here with constant temperatures are simpler to interpret. Therefore, some questions which are difficult to answer by the RUPATHER tests may successfully be tackled using the results of the tube tests.

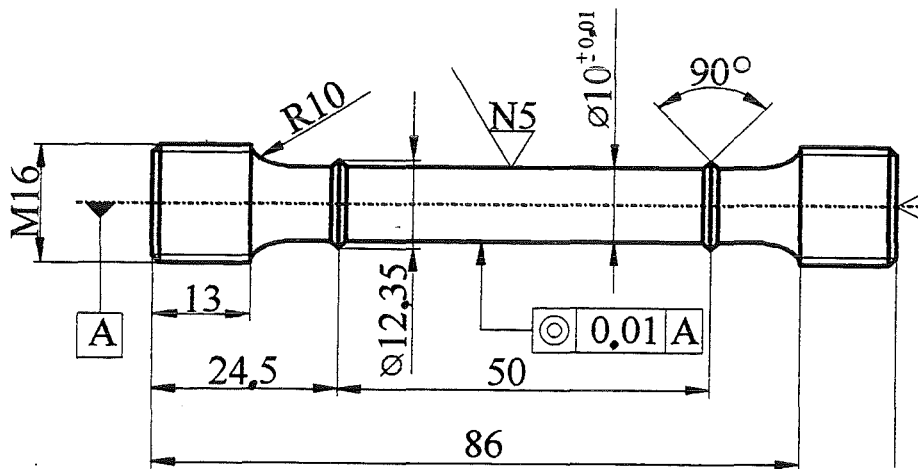


Fig. 5-1: Uni-axial creep test specimen geometry

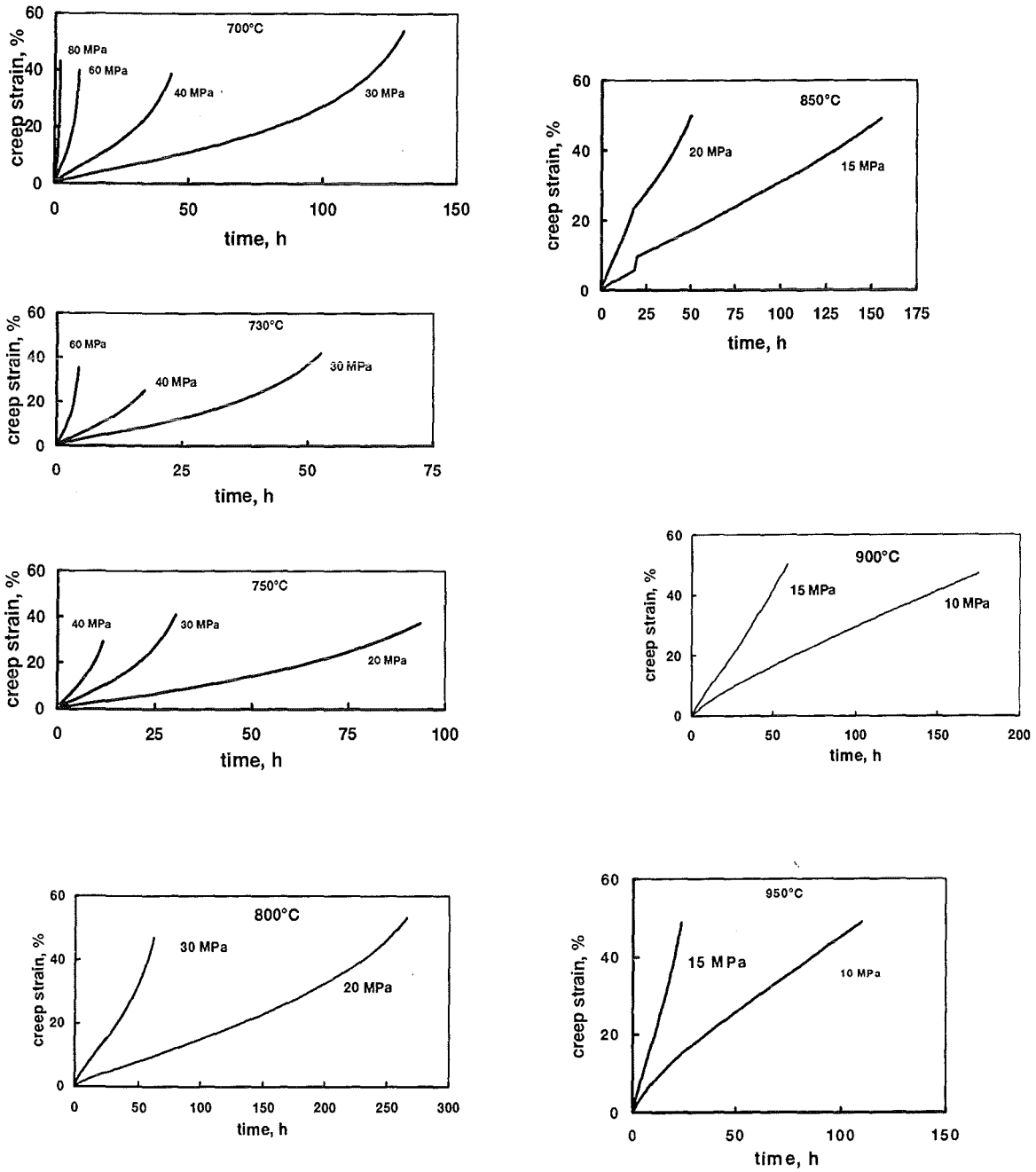


Fig. 5-2: Creep curves for 20 MnMoNi 5 5

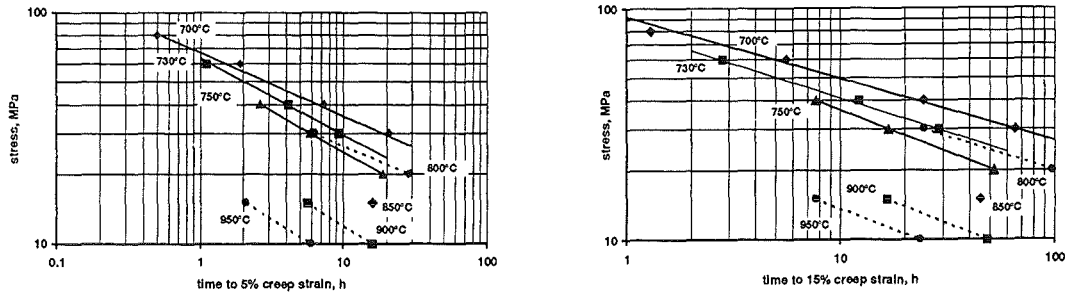


Fig. 5-3: Times to reach creep strains of 5 and 15 %

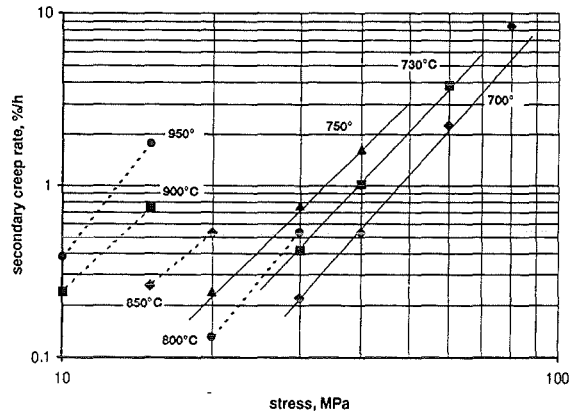


Fig. 5-4: Secondary creep rate of 20 MnMoNi 5 5 as a function of stress

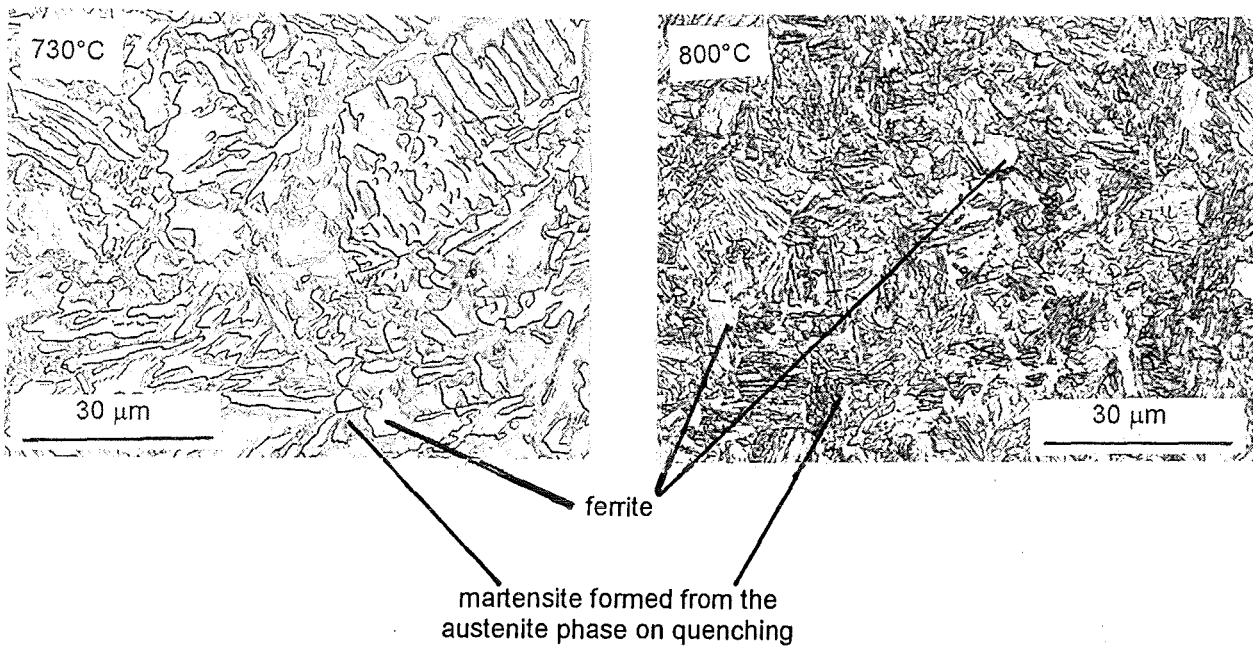


Fig. 5-5: Microstructures of 20 MnMoNi 5 5 after heat treatment at 730 and 800 °C showing the progress of the α - γ transformation

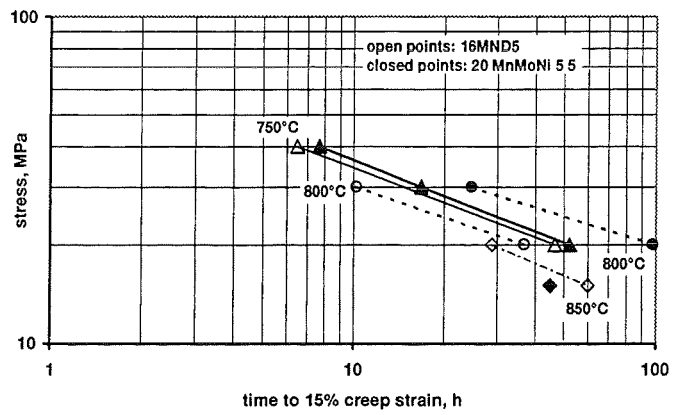
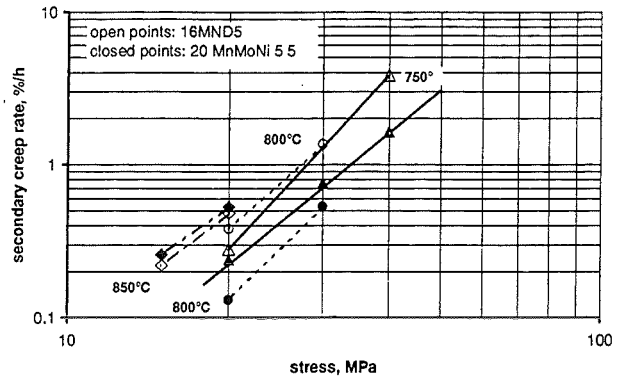
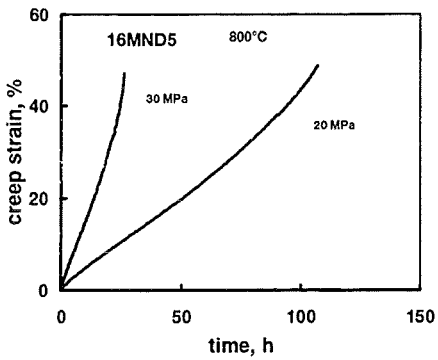
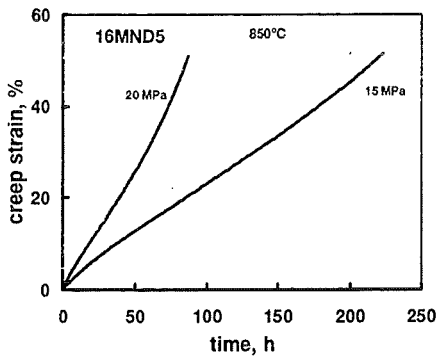
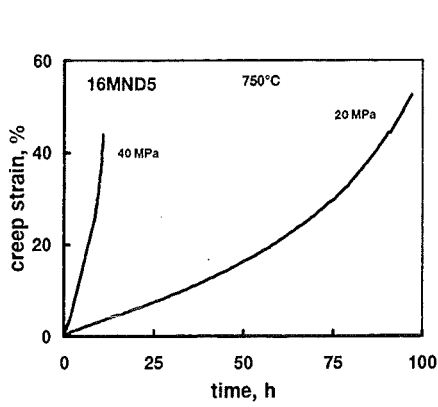


Fig. 5-7: Comparison of the creep properties of 20 MnMoNi 5 5 and 16MND5

Fig. 5-6: Creep curves for 16;ND5 at 750, 800 and 850 °C

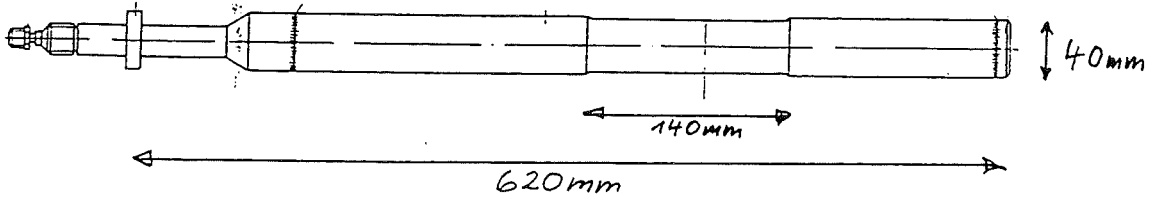


Fig. 5-8: Specimen for tube tests; wall thickness in the gauge length 3 or 4 mm

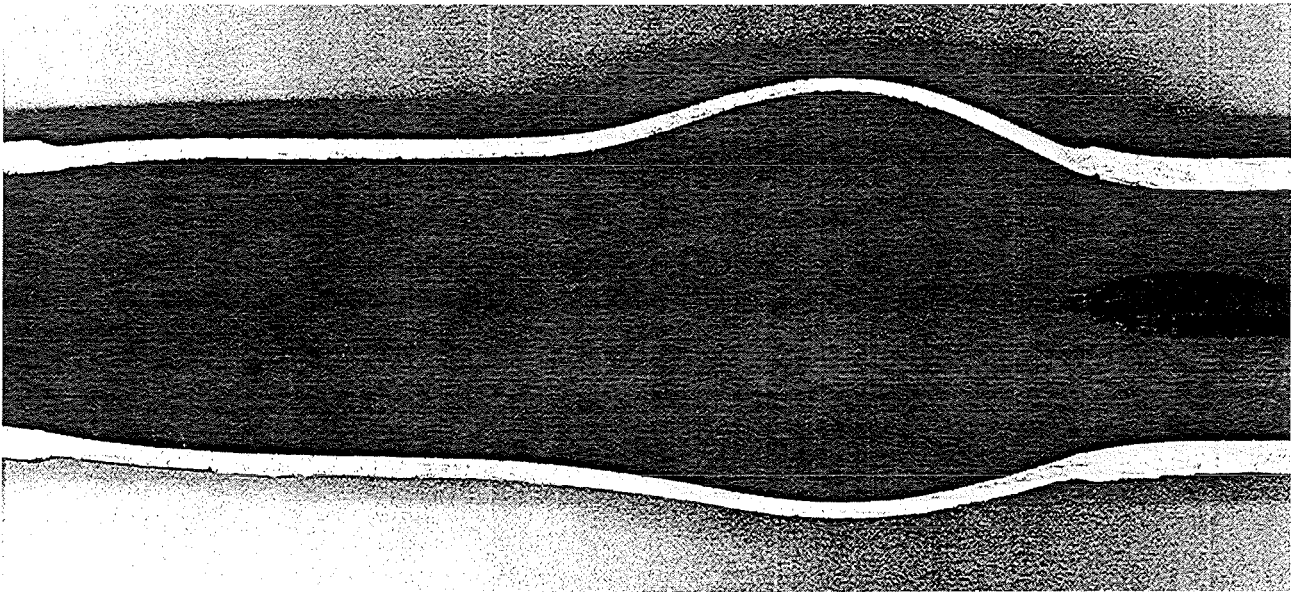


Fig. 5-9: Typical failed tube specimen

5.2 Dynamic tests

5.2.1 Objectives

The impact problems investigated by the BERDA and FLIPPER experiments require a correct knowledge of the material behavior, both under experimental and reactor conditions, in order to transfer the experimental results to the real problem. Accompanying investigations are thus needed to make sure that the essential effects are adequately simulated: *temperature effects, strain rate effects, and size effects*. This research area has been given early attention and dealt with in the past, Moor (1918), Wood (1943), Miklowitz (1948 and 1950), Richards (1958), Malmberg (1995). Previous studies are however not complete in the dynamic regime and they do not adequately include nuclear vessel steels.

The JRC-LDTF sector has been assigned to carry out mainly the dynamic tests for material characterization, employing principally the Large Dynamic Test Facility (LDTF), which allows the testing of large specimens under well-defined strain rates. A test program has been defined of the materials used for the pressure vessel and its internal structures. These include: ferritic steel 20MnMoNi55 (vessel head), austenitic steel X6CrNiNb1810 (Upper Internal Structure), ferritic steel 26NiCr Mo146 (bolting), bronze G-CuSn12 (simulation of UIS in BERDA). Specimens have been tested at room and higher temperatures, and at strain rates ranging from quasi-static (10^{-3} /sec) to dynamic (200/sec) conditions. Uniaxial tensile cylindrical specimens of diameters ranging from 3mm to 30mm have been constructed for studying size effects. Of the results obtained, those of the bronze G-CuSn12 have been reported in a previous publication, Solomos (1998), and they are only briefly summarised. It is finally mentioned that fruitful interaction and coordination of the activities with the project partner PSI (Paul Scherrer Institut, CH) has taken place during the course of this work, as well as with FZK.

5.2.2 Experimental apparatuses

Tensile tests at several strain rates have been carried out by means of different machines. For the small 3mm-diameter specimens the following devices have been used: a screw tensometer for 10^{-3} /s, a hydro-pneumatic machine for 10^{-1} /s and 10/s, and a Hopkinson bar for 200/s. For the large 30mm-diameter specimens the devices have correspondingly been: a servo-hydraulic universal testing machine for 10^{-3} /s and 10^{-1} /s (provided by PSI), and a Hopkinson bar (LDTF) for 10/s and 200/s. The parameters recorded per test are explained in section 5.2.4. It is to be emphasized that identical data analysis procedures have been applied to all tests.

Particular attention has been paid into producing fully comparable results in the dynamic regime for small and large specimens. Thus the modified split Hopkinson bar for the small diameter specimens (3mm) has been redesigned and upgraded. Its new configuration allows the dynamic testing of ductile RPV steels at strain rates even below 200/s. The large modified split Hopkinson bar (LDTF) has been upgraded, too. A second transmitter bar of $\varnothing 72$ mm and 100m length has been installed aiming at adapting the LDTF to accommodate the 30mm diameter steel specimens and thus rendering it the world's biggest Hopkinson bar. A new opto-electronic instrument (by TSI-ZIMMER) has also been employed, allowing direct displacement measurements on the specimens at high strain-rates over a wide displacement range (1mm-100mm) with sufficient resolution (0.9 μ m-200 μ m).

Temperature tests have been conducted by using in-house made and commercial ovens with resistance heating and by taking special care of cooling down the Hopkinson bar ends in order to avoid any alteration in the wave propagation parameters.

5.2.3 Specimens

Material procurement has been handled by the FZK and some initial delay has been experienced in this activity. The two experimental partners, JRC-LDTF and PSI-LSU, have agreed to have part of their specimens made by one external machine shop, in order to achieve maximum uniformity in fabrication conditions.

The actual experiments performed are shown in the test matrix of Table 5-2. The shape of the Ø3mm specimens is sketched in Fig. 5-10. It is noted that these specimens are particularly adapted for dynamic testing at the Hopkinson bar, and are not standard type tensile specimens. The Ø30mm diameter specimens are geometrically similar to the one shown.

Table 5-2: Tensile uniaxial experiments performed within RPVSA.

Material	Test Temperature	Strain Rate (s ⁻¹)	Smooth Specimens Size (mm Ø)	
			3	30
Ferritic Steel 20 Mn Mo Ni 55 (vessel head)	R.T.+ 400°C	10 ⁻³	4 + 3	3
		10 ⁻¹	4 + 3	2
		10	4 + 3	1
		200	4 + 3	4
Austenitic Steel X6 Cr Ni Nb 1810 (UIS)	R.T.+ 600°C	10 ⁻³	4 + 3	3
		10 ⁻¹	3 + 3	2
		10	3 + 3	1
		200	4 + 3	4
Ferritic Steel 26 Ni Cr Mo 146 (bolting)	R.T.	10 ⁻³	4	
		10 ⁻¹	3	
		10	3	
		200	4	
Brass (simulation of UIS in BERDA)	R.T.	10 ⁻³	4	
		10 ⁻¹	4	
		10	4	
		200	4	

In this Table the entries at the right hand column describe the numbers of tests for the particular parameter set.

In the Tables of the following sections, the specimens are identified as follows:

- h1a.. : smooth specimen of diameter 3 mm of austenitic steel X6CrNiNb1810,
- h3a.. : smooth specimen of diameter 30mm of austenitic steel X6CrNiNb1810,
- h10.. : smooth specimen of diameter 3 mm of ferritic steel 20MnMoNi55,
- h30.. : smooth specimen of diameter 30mm of ferritic steel 20MnMoNi55,
- b... : smooth specimen of diameter 3 mm of ferritic steel 26NiCr Mo146.

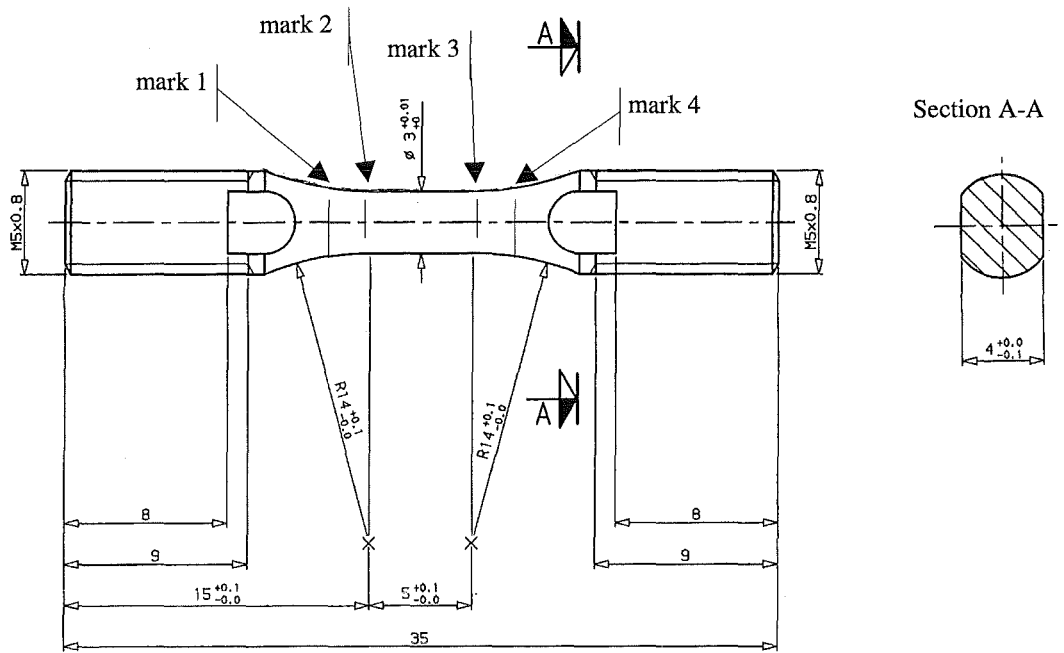


Fig. 5-10: Geometry of the $\varnothing 3\text{mm}$ cylindrical tensile specimen.

5.2.4 Data elaboration

(a) As mentioned above, uniaxial tests at high strain rate were performed on a modified Hopkinson bar device, Albertini (1977), shown schematically in Fig. 5-11. It consists of two half-bars, called incident and output bar respectively, with the specimen introduced in between. Its function is based on storing elastic energy in a pre-stressed bar loading device, which is the solid continuation of the incident bar of the machine. By releasing this energy (rupturing the blocking brittle intermediate piece), a tension wave with small rise-time is transmitted along the incident bar and loads the specimen to fracture. The tension wave thus generated and propagated along the bar fulfils the requirements for being an uniaxial elastic plane stress wave because the pulse wave length is long compared to the bar diameter, and the pulse amplitude does not exceed the yield strength of the bar.

The pulse propagates along the incident bar with the velocity C_0 of the elastic wave and its shape remains constant according to the theory of one-dimensional elastic wave propagation in circular rods, Lindholm (1971). When the incident pulse (ϵ_I) reaches the specimen, part of it (ϵ_R) is reflected by the specimen whereas another part (ϵ_T) passes through the specimen propagating into the output bar. The relative amplitudes of the incident, reflected and transmitted pulse, depend on the mechanical properties of the specimen.

Since the incident pulse is long compared to the time of crossing of the specimen, numerous reflections of elasto-plastic waves take place inside the short specimen length, leading quickly to the creation of a uniform stress and strain state inside the specimen gauge length.

Strain gauges mounted on the incident and output bars of the device, at equal distances from the specimen, are used for the measurement of the elastic deformation (as a function of time) created on both half-bars by the incident/reflected and transmitted pulses, respectively. Using the theory of elastic wave propagation in bars, Lindholm (1971), and the well substantiated assumption of specimen equilibrium attainment, the engineering stress σ_E , strain rate $\dot{\epsilon}_E$, and strain ϵ_E of the specimen can be calculated:

$$\sigma_E(t) = E_b \varepsilon_T(t) \frac{A_b}{A_o} \quad (1)$$

$$\dot{\varepsilon}_E(t) = \frac{2C_o}{L_c} \varepsilon_R(t) \quad (2)$$

$$\varepsilon'_E(t) = \frac{2C_o}{L_c} \int_0^t \varepsilon_R(z) dz \quad (3)$$

where, L_c = corrected gauge length of the specimen (see below), A_b = cross-sectional area of output and input bars, A_o = initial cross-sectional area of the specimen gauge length portion, E_b =elastic modulus of the bars, $C_o = (E_b/\rho)^{1/2}$ = elastic bar wave speed, ρ = bar density.

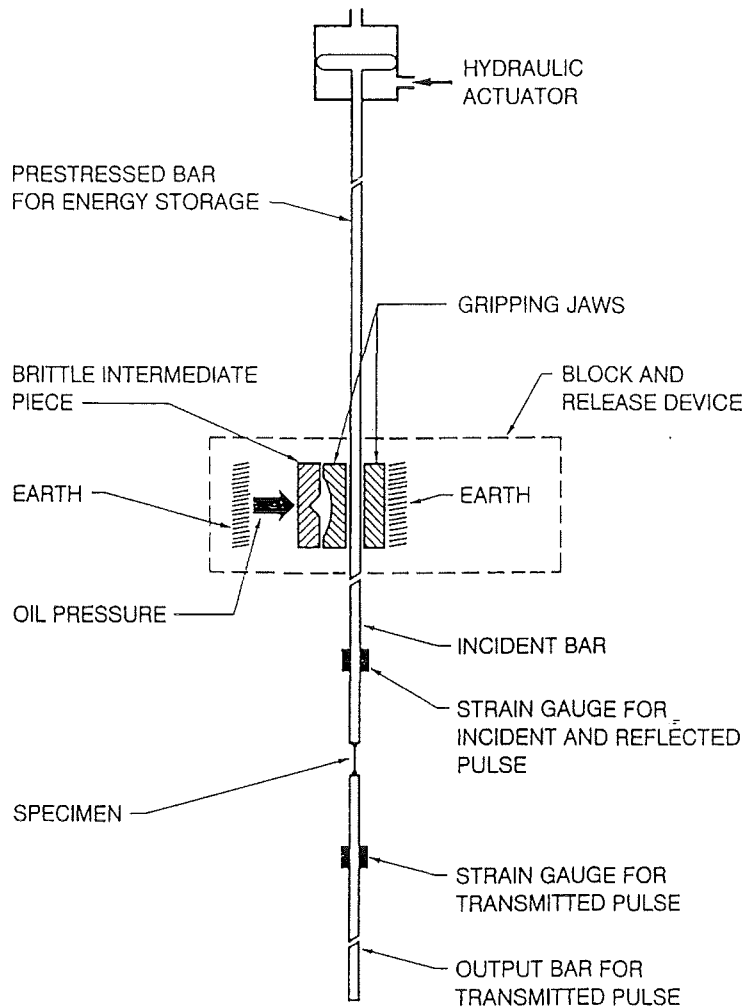


Fig. 5-11: The JRC modified tension Hopkinson bar.

For the *quasi-static* and *medium strain rate* tests load P measurements are made with calibrated strain gauges attached to one of the elastic bars holding the specimen, and displacement measurements $\Delta\ell$ are obtained with a displacement transducer. The engineering stress and strain are calculated by the following simple relationships:

$$\sigma_E = \frac{P}{A_o}, \quad \varepsilon_E = \frac{\Delta\ell}{L_c} \quad (4)$$

The above-described parameters and data acquisition procedures are applied both to the 3mm- and to the 30mm-diameter specimens. The machines are only different, as mentioned in section 5.2.2. In this respect, it is also worth providing some further information about the LDTF. The prestressed energy storage bar consists of 32 steel cables of 100m length and $\sim 3200\text{mm}^2$ total cross-sectional area. The incidence and transmitter bars are solid bars of 72mm diameter, with the length of the transmitter bar being 100m. A rectangular stress pulse of maximum amplitude $\sim 2.5\text{MN}$ and of duration 40ms can be potentially generated. Thus, with a maximum stroke of $\sim 750\text{mm}$ this machine can bring to fracture very big specimens and components of ductile materials.

(b) For all tests a few elongation measurements have been made directly on the initial gage length L_o , which is usually made to coincide with the distance between the specimen two inner marks, Fig. 5-10. What is always measured and recorded is the relative displacement (Δl) of the specimen two extremes (gripping bar ends, or machine cross-head displacement). Consequently, the gauge length L_o is corrected to take into account the contribution to the measured elongation of the two deformable fillets of the tensile specimen, Nicholas (1981). This correction is carried out by measuring the deformation of the length between the two inner marks (L_o) and between the two outer marks (L) with the use of a microscope. Considering that the volume of the gauge part of the specimen remains constant during the experiment, the corrected gauge length L_c is calculated through the following formula, Albertini (1985), Kaneko (1977):

$$L_c = L_o \frac{\Delta L_f}{\Delta L_{of}} \quad (5)$$

where, L_c = corrected specimen gauge length, ΔL_{of} = elongation at fracture over the central gauge length L_o , and ΔL_f = elongation at fracture over the length L .

(c) Stress-strain diagrams obtained with the different experimental set-ups (tensometer, hydro-pneumatic apparatus, Hopkinson bar, servo-hydraulic machine, LDTF) have been re-adjusted by imposing a correct Young modulus. This correction is necessary because the experimental elastic modulus determined from these tests is not accurate:

- at high strain rates the specimen takes a certain finite time to achieve equilibrium along its gauge length;
- in the case of the tests at low and medium strain rates the experimental elastic modulus may be affected by the deformation of the dynamometric elastic bars.

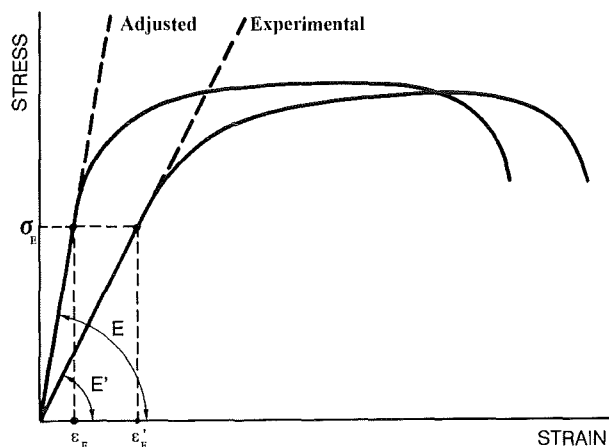


Fig. 5-12: Correction of Young's modulus.

The correction procedure is schematically shown in Fig. 5-12, and is based on the simple relation $\sigma_E = E \varepsilon_E = E' \varepsilon_E'$ for the elastic regime. The corrected final engineering strain values are given by the formula:

$$\varepsilon_E = \varepsilon_E' - \left(\frac{\sigma_E}{E'} - \frac{\sigma_E}{E} \right) \quad (6)$$

(d) The formulae used for the conversion from engineering to true values are:

$$\sigma_{TRUE} = (1 + \varepsilon_E) \sigma_E \quad (7)$$

$$\varepsilon_{TRUE} = \ln(1 + \varepsilon_E) \quad (8)$$

Clearly, the true stress-strain flow curves thus produced must be regarded as meaningful up to the point of maximum stress at the corresponding engineering diagrams; beyond this point, one has to take into consideration the phenomenon of necking and its associated triaxiality. For the majority of the tests the diameter and the meridional radius of curvature at the reduced section after fracture have been measured, and subsequently the last point of the true stress-strain diagram has been reconstructed by using the correction formula for the stress, Bridgman (1952)

$$\sigma_{T,max} = \frac{\sigma_{av}}{\left(1 + 2\frac{R}{a}\right) \ln\left(1 + \frac{a}{2R}\right)} \quad (9)$$

where, a = minimum section radius, R =profile radius at neck, and $\sigma_{av} = P_f/(\pi a^2)$ the average stress (P_f =fracture force). The corresponding strain is calculated by the equation

$$\varepsilon_{T,max} = 2 \ln\left(\frac{D_0}{2a}\right) \quad (10)$$

where, D_0 = initial diameter of the cross-section. Finally, a straight line is drawn in the true stress-strain curves between the last valid point produced by eqs.(7) and (8) and the above determined fracture point.

(e) The procedure followed for the measurement of the meridional radius of curvature (R) at the minimum diameter of the neck is as follows. The fractured specimen is at best reconstructed by bringing together its two broken parts. An acquisition camera, equipped with the proper lens, is utilized and an image of the specimen is taken and stored in a PC. A second image of the specimen is taken after it has been rotated about its longitudinal axis by 90° . The specimen is then removed and a ruler (with millimeter divisions) is positioned at its exact place; an image of it is taken and stored in the PC, too.

Next an image analysis program is invoked. The image of the ruler is brought to the monitor screen and by measuring the number of pixels between two known-distance points on the ruler, the correspondence *pixels-length* is established. Obviously, this correspondence varies among different series of measurements or different specimen sizes etc.

The first image of the reconstructed specimen is then brought to the screen; an adjustable diameter circle is generated and carefully approached to the minimum diameter area. When a satisfactory tangency condition of this circle with the specimen image outline is obtained, Fig. 5-13, the diameter of the circle is measured (in terms of pixels, which is immediately expressed in millimetres). Another circle is generated and approached to the other side of the specimen, etc. Thus two values of the radius of curvature are produced. The 90° -image of the specimen is next similarly analysed and two more radius values are obtained. The radius of curvature used in the calculations is the average of the above four

values. Clearly, the whole procedure is operator dependent and for this reason the same person has always been engaged in these measurements. It is estimated that an error of $\pm 15\%$ should be allowed for in the reported values.

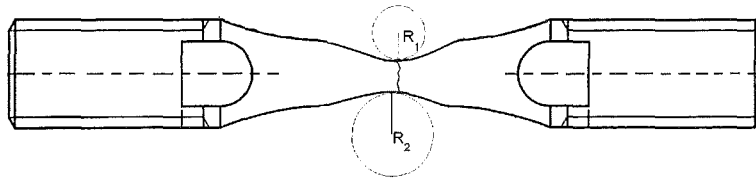


Fig. 5-13: Sketch indicating the procedure for measuring the meridional radius of curvature at the neck.

5.2.5 Recorded and calculated data

The test results per material examined are presented in the next three sections. Only engineering stress-strain curves are included, the true stress-strain curves being reported by Solomos (1999). In order to render the inter-comparison graphs clear and easily legible, individual specimens have not been identified in them. Apart from the complete stress-strain curves, a series of additional parameters has been determined and reported in graphical or tabular form. They comprise stress and strain characteristic values and geometrical features of the specimens, as listed below. In general engineering quantities are implied, unless otherwise explicitly stated.

$\sigma_{0.2}$ or $\{\sigma_{\text{upper}}, \sigma_{\text{lower}}\}$: yield stress
$\sigma_{1\%}$: 0.01 strain flow stress
$\sigma_{5\%}$: 0.05 strain flow stress
σ_u	: ultimate tensile stress
ϵ_u	: uniform strain
σ_f	: fracture stress (from σ - ϵ curve)
ϵ_f	: fracture strain (from σ - ϵ curve)
$\epsilon_{\text{fr}} = \Delta L_o / L_o$: fracture strain (from post-fracture inspection of the specimen)
$\sigma_{T,\text{max}}$: corrected fracture true stress, eq.(9)
$\epsilon_{T,\text{max}}$: fracture true strain, eq.(10)
W_u	: specific work up to uniform strain, $W_u = \int_0^{\epsilon_u} \sigma d\epsilon$
W_f	: specific work up to fracture, $W_f = \int_0^{\epsilon_f} \sigma d\epsilon$
$(W_f - W_u) / W_f$, W_u / W_f : work parameters	
D_o	: initial specimen diameter
D_f	: minimum specimen diameter after fracture
$\psi = 100(D_o^2 - D_f^2) / D_o^2$: area reduction parameter

$R=R_{c,av}$: meridional radius of curvature at minimum diameter of neck (average of the four values $R_{0,1}$, $R_{0,2}$, $R_{90,1}$, $R_{90,2}$)
 R/D_0 : normalized radius of curvature.

5.2.6 Experimental results - austenitic steel X6CrNiNb1810 (1.4550)

This is the actual material of the Upper Internal Structure (UIS), also employed in the BERDA experiment. The specimens have been constructed from material delivered to the FZK in four plates of dimensions 1000x300x70(mm) coming from the same heat. The chemical composition, as indicated by the supplier in the acceptance sheet, is as shown in Table 5-3.

However, PSI, charged with the plates' cutting and the construction of the specimens, has conducted and completed a limited scope quality control, mainly concentrating on chemical composition, grain size determination and hardness tests. Inhomogeneities, which are typical to austenitic steels, have been encountered, Krompholz (1998). Brinell-hardness values across the thickness of the plates have also been found lower than those on the surface along the longitudinal direction. Because of this, it has been recommended by PSI to perform tensile tests, at least at R.T., for the determination of the scatter-band of the respective tensile data.

Table 5-3: Chemical composition of austenitic steel X6CrNiNb1810.

C %	Si %	Mn %	P %	S %	Cr %	Ni %	Mo %	Co %	Nb %	Nb/C
0.025	0.32	1.70	0.028	0.002	18.00	10.36	-	0.08	0.43	17.2

Experiments have been performed with $\varnothing 3$ and $\varnothing 30$ cylindrical specimens at room temperature and at 600°C and at the target strain rates of Table 5-2 (produced strain rates by the machines have been slightly different). All corresponding stress-strain curves (both engineering and true) have been obtained. For the reasons explained before, the Young modulus of these curves has been adjusted to 200GPa for R.T. and to 165GPa for 600°C, respectively, Stainless steels, quality specifications, DIN 17440 (1972).

Characteristic values of tests and specimens are reported in Tables 5-4 to 5-6, and a series of full stress-strain curves are also included. The main conclusions from these tests are summarised below, where it has been attempted to group them under three categories: strain rate effects, temperature effects and size effects. Clearly, a multitude of graphs with combinations of these effects can also be produced.

Strain rate effects, specimens $\varnothing 3$ at R.T. and at 600°C

Fig. 5-14 shows the complete set of σ - ϵ curves at R.T. It can be seen that strain rate hardening effects appear overall. With increasing strain rate the tensile strength shows a small increase, Fig. 5-15. In the same figure, the yield stress presents a small but constant increase with strain rate. As noticed also in Fig. 5-14, for the 200/s strain rate an instability (upper and lower yield points) appears.

As reported in Table 5-4, the $\sigma_{1\%}$ and $\sigma_{5\%}$ stresses exhibit a constant small increasing tendency with strain rate. Both the uniform and the fracture strains decrease substantially with increasing strain rates, and the material seems to become less ductile.

The area reduction parameter ψ is monotonically decreasing with strain rate, and the normalized radius of curvature R/D_0 remains almost invariant. The work parameter W_u/W_f shows a small initial decrease with strain rate, and a sudden jump upwards at 200/s.

Table 5-4: Test characteristic values of $\varnothing 3$ mm specimens of austenitic steel X6CrNiNb1810 at R.T. and at several strain rates.

Strain rate Specimen	$\sigma_{0.2}$ $\sigma_{\text{upp}} / \sigma_{\text{low}}$	$\sigma_{1\%}$	$\sigma_{5\%}$	σ_u	ϵ_u	σ_f	ϵ_f	$\sigma_{T,\text{max}} / \epsilon_{T,\text{max}}$	W_u	W_f	$W_f - W_u / W_f$	W_u / W_f	ψ %	R/D _o
	MPa	MPa	MPa	MPa		MPa		MPa /	MPa	MPa				
0.002/s														
h1a05	250	288	353	614	0.65	-	-	- / 1.88	334.2	-	-	-	84.8	0.19
h1a06	266	284	353	612	0.68	450	0.90	3667 / 1.86	355.5	481.5	0.26	0.74	84.4	0.18
h1a07	282	302	369	615	0.64	436	0.87	4350 / 1.87	332.6	466.5	0.29	0.71	84.6	0.19
h1a24	293	316	379	610	0.65	-	-	- / 1.92	342.0	-	-	-	85.3	0.19
0.15/s														
h1a29	272	303	380	574	0.46	374	0.65	2280 / 1.55	229.5	327.8	0.30	0.70	78.9	0.17
h1a30	283	313	387	576	0.45	395	0.64	2105 / 1.41	225.9	323.7	0.30	0.70	75.6	0.19
h1a31	300	337	420	606	0.41	433	0.58	2750 / 1.63	213.4	307.6	0.31	0.69	80.3	0.18
10/s														
h1a09	325	358	441	625	0.41	513	0.64	2610 / 1.33	222.3	360.4	0.38	0.62	73.6	0.25
h1a10	441	470	516	600	0.31	358	0.42	1630 / 1.39	173.0	232.8	0.26	0.74	75.1	0.21
h1a11	297	355	435	619	0.39	467	0.66	2675 / 1.43	208.9	361.6	0.42	0.58	75.9	0.25
h1a26	272	319	396	617	0.52	564	0.71	2850 / 1.28	276.8	393.8	0.30	0.70	72.2	0.25
200/s														
h1a18	385 / 343	343	417	636	0.47	430	0.51	1915 / 1.35	255.2	277.7	0.08	0.92	74.1	0.17
h1a19	381 / 331	333	418	644	0.47	385	0.51	1785 / 1.34	256.3	280.7	0.09	0.91	73.9	0.21
h1a20	404 / 345	348	428	647	0.46	410	0.49	1820 / 1.32	252.8	273.8	0.08	0.92	73.2	0.22

Fig. 5-16 shows the complete set of σ - ϵ curves at $T=600^\circ\text{C}$. No evident strain rate effects appear; if any, interestingly they seem to be of a strain softening type, probably due to prevailing thermal softening effects. As shown also in Table 5-5, the tensile strength undergoes a small decrease, whereas the yield stress remains almost invariant. The uniform and fracture strains show a small increase with strain rate, as if the material becomes more ductile at dynamic straining. For the 200/s strain rate the yield point instability appears again.

At $T=600^{\circ}\text{C}$ both ψ and R/D_o remain practically invariant over all strain rates. Quite similar is also the behaviour of the work parameter W_u/W_f .

Table 5-5: Test characteristic values of $\varnothing 3\text{mm}$ specimens of austenitic steel X6CrNiNb1810 at $T=600^{\circ}\text{C}$ and at several strain rates.

Strain rate Specimen	$\sigma_{0.2}$ $\sigma_{\text{upp}}/\sigma_{\text{low}}$	$\sigma_{1\%}$	$\sigma_{5\%}$	σ_u	ϵ_u	σ_f	ϵ_f	$\sigma_{T,\text{max}}/\epsilon_{T,\text{max}}$	W_u	W_f	$W_f - W_u / W_f$	W_u/W_f	ψ %	R/D_o
	MPa	MPa	MPa	MPa		MPa		MPa /	MPa	MPa				
0.002/s														
h1a22	168	193	257	351	0.25	167	0.47	810/ 1.39	74.7	139.2	0.46	0.54	75.2	0.24
h1a23	167	190	261	346	0.24	204	0.43	1015/ 1.46	70.6	129.7	0.45	0.54	76.8	0.21
0.15/s														
h1a34	184	209	276	349	0.21	196	0.39	1120/ 1.64	63.9	116.7	0.45	0.55	80.7	0.18
h1a35	167	193	264	338	0.22	193	0.40	1265/ 1.78	63.4	115.2	0.45	0.55	83.1	0.16
h1a36	163	187	261	340	0.22	198	0.40	1285/ 1.74	65.8	116.7	0.44	0.56	82.5	0.19
10/s														
h1a27	146	170	239	321	0.26	225	0.54	1175/ 1.45	71.3	150.6	0.53	0.47	76.7	0.20
h1a28	188	215	277	333	0.22	241	0.48	1090/ 1.36	66.5	142.9	0.53	0.46	74.3	0.19
250/s														
h1a21	238/ 157	202	254	329	0.27	140	0.53	1235/ 1.96	80.2	154.3	0.48	0.52	85.9	0.17
h1a25	176	195	237	320	0.31	149	0.54	1030/ 1.72	86.3	150.1	0.42	0.57	82.2	0.17

Strain rate effect, specimens $\varnothing 30$ at R.T.

Fig. 5-17 shows all σ - ϵ curves at R.T. Again some strain rate hardening effect is overall observed. Yield stress and ultimate stress exhibit a small increase with increasing strain rate. As seen in Table 5-6, the $\sigma_{1\%}$ and $\sigma_{5\%}$ stresses show also some small increase, while the uniform strain and fracture strain tend to decrease with higher strain rates.

The area reduction parameter ψ exhibits small variations with strain rate. The normalized radius of curvature R/D_o exhibits stronger variations at the intermediate strain rates, but it remains almost invariant for quasi-static and dynamic conditions. The work parameter W_u/W_f shows no variations with strain rate. However, it is noted that the number of data points available is rather poor.

Table 5-6. Test characteristic values of Ø30mm specimens of austenitic steel X6CrNiNb1810 at R.T. and at several strain rates.

Strain rate Specimen	$\sigma_{0.2}$	$\sigma_{1\%}$	$\sigma_{5\%}$	σ_u	ϵ_u	σ_f	ϵ_f	$\sigma_{T,max}/$ $\epsilon_{T,max}$	W_u	W_f	$W_f - W_u$ $/W_f$	W_u/W_f	ψ	R/D _o
	MPa	MPa	MPa	MPa		MPa		MPa /	MPa	MPa			%	
0.001/s														
h3a01	237	270	346	580	0.55	409	0.73	2720/ 1.46	268.0	363.9	0.26	0.74	76.9	0.45
h3a02	250	283	355	578	0.52	433	0.69	2645/ 1.40	256.3	346.9	0.26	0.74	75.3	0.46
h3a03	260	288	356	580	0.55	405	0.75	2695/ 1.45	273.0	379.6	0.28	0.72	76.5	0.45
0.1/s														
h3a04	315	326	388	596	0.51	463	0.64	2170/ 1.15	261.0	337.2	0.31	0.77	68.4	0.58
h3a05	304	323	388	586	0.51	489	0.65	2285/ 1.15	259.4	335.1	0.23	0.77	68.4	0.56
25/s														
h3a08	281	301	369	585	0.38	-	-	- / 1.30	183.9	-	-	-	72.8	0.37
150/s														
h3a09	280	330	383	626	0.45	425	0.63	2080/ 1.22	227.9	337.5	0.32	0.67	70.6	0.45
h3a10	270	318	378	626	0.47	440	0.62	2130/ 1.22	240.0	327.9	0.27	0.73	70.6	0.43
h3a11	280	329	384	622	0.45	568	0.58	2772/ 1.26	227.9	306.8	0.26	0.74	71.5	0.44
h3a12	278	327	390	643	0.47	430	0.62	2240/ 1.29	251.7	337.0	0.25	0.75	72.6	0.45

Temperature effects (for Ø3mm specimens)

At 600°C a substantial reduction of the mechanical resistance is observed with respect to R.T. conditions for all strain rate regimes. Fig. 5-18 shows this behaviour for the quasi-static and dynamic case.

The relevant Tables show the decreasing tendency of the ultimate stress at T=600°C with increasing strain rate and its contrast with the corresponding curve at R.T. The $\sigma_{1\%}$ values remain almost constant over all strain rates, they are, however, a lot smaller (50%) than the R.T. ones. The area reduction parameter ψ has not undergone a big change for these two test temperatures.

Some average values illustrate the situation at this temperature: tensile strength 300MPa (down from 600MPa at R.T.), uniform strain 0.25 (down from 0.50), fracture strain 0.45 (down from 0.80), yield stress 160MPa (down from 350MPa).

Size effects (at R.T.)

Figs. 5-19 shows corresponding σ - ϵ curves of the $\varnothing 3$ mm and the $\varnothing 30$ mm specimens at the strain rate regime 200/s. Some differences in the behaviour of the two specimen sizes are noticed. Stress values of $\varnothing 3$ specimens seem to be in general greater than those of $\varnothing 30$. This behaviour is also encountered at the lower strain rates. The $\varnothing 30$ specimens tend, however, to be more ductile (except in the quasi-static case).

To quantify better the effect, individual parameters are examined separately in the Tables 5-4 and 5-6 over the entire strain rate range. The yield stress does not exhibit substantial differences; at 200/s, however, the $\varnothing 3$ values are well above the $\varnothing 30$ ones. No noticeable differences are present for $\sigma_{1\%}$, while the $\sigma_{5\%}$, values for $\varnothing 3$ seem to be always slightly over the corresponding $\varnothing 30$ values. The ultimate stress shows clearly a stronger effect at 10^{-3} /s, where the $\varnothing 3$ specimen values are by $\sim 10\%$ higher than the corresponding $\varnothing 30$ specimen values; at higher strain rates this difference disappears, Fig. 5-20. Similar is also the behaviour of the uniform strain ($\varnothing 3$ values higher at 10^{-3} /s).

Quite distinct is the behaviour of the two specimens as regards the area reduction and the normalised radius of curvature parameters, Fig. 5-21 and Fig. 5-22, respectively. For ψ the curve of $\varnothing 3$ is always higher than that of $\varnothing 30$ specimens (even by 10%). Further, the first curve is continuously decreasing with strain rate, whereas the latter has no such monotonic behaviour. For the normalised radius of curvature the $\varnothing 3$ specimens curve lies always well below the $\varnothing 30$ curve over all strain rates. For the work parameter no such behaviour is observed.

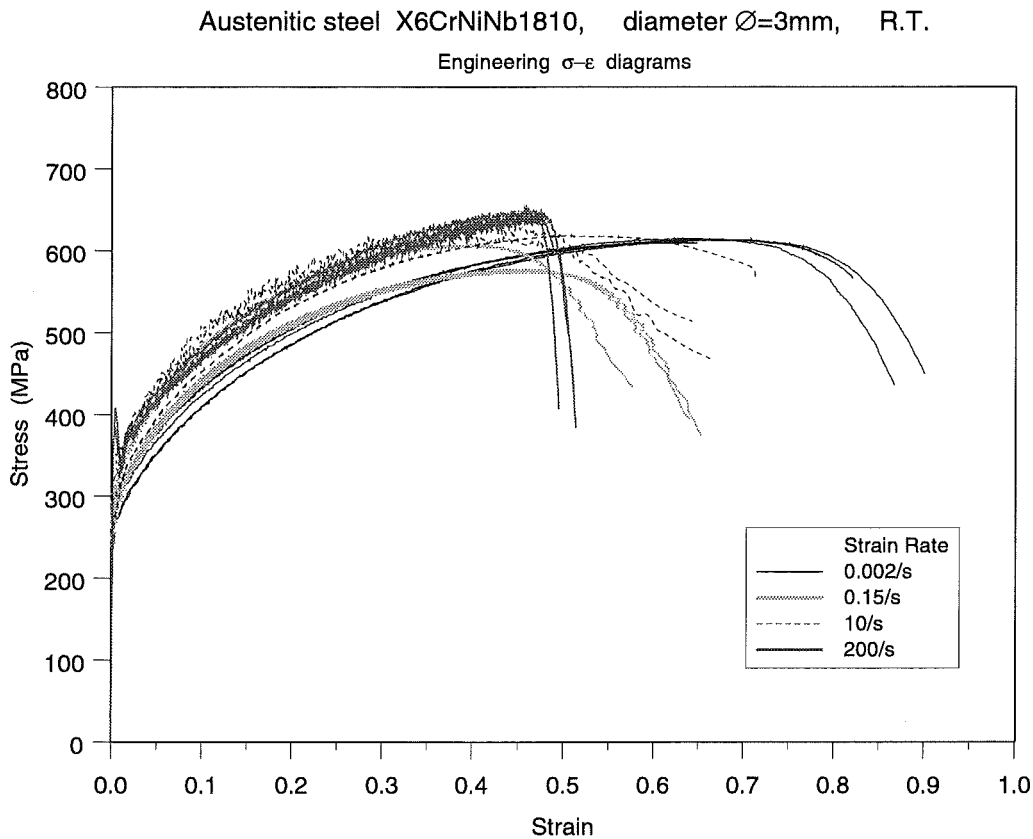


Fig. 5-14

Austenitic steel X6CrNiNb1810, diameter $\varnothing=3\text{mm}$, R.T.

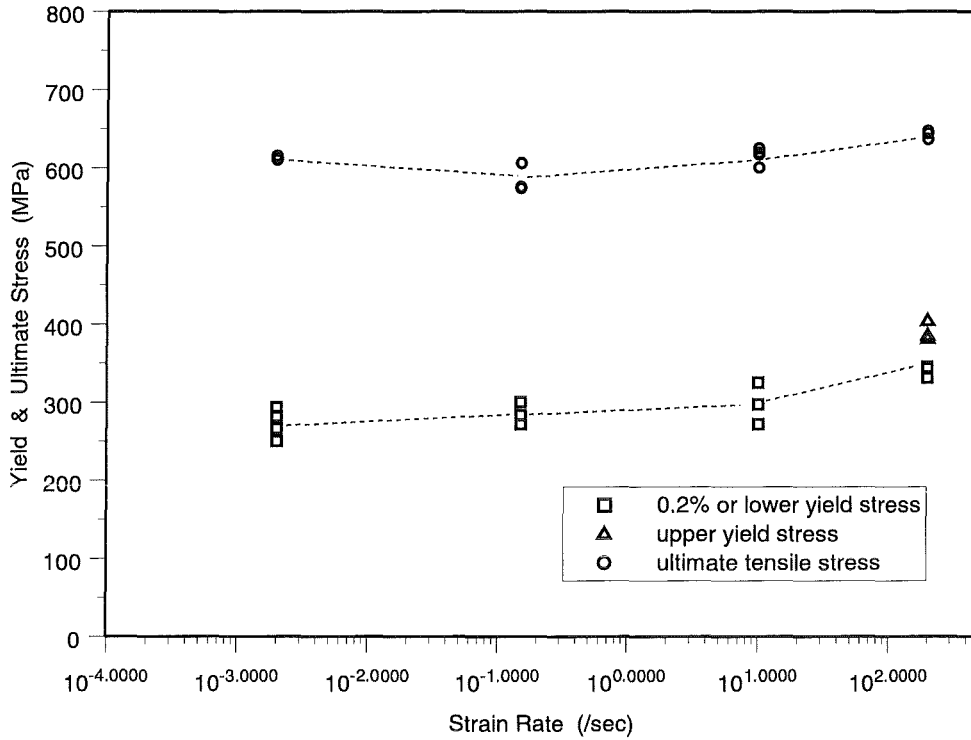


Fig. 5-15

Austenitic steel X6CrNiNb1810, diameter $\varnothing=3\text{mm}$, $T=600^{\circ}\text{C}$
Engineering σ - ϵ diagrams

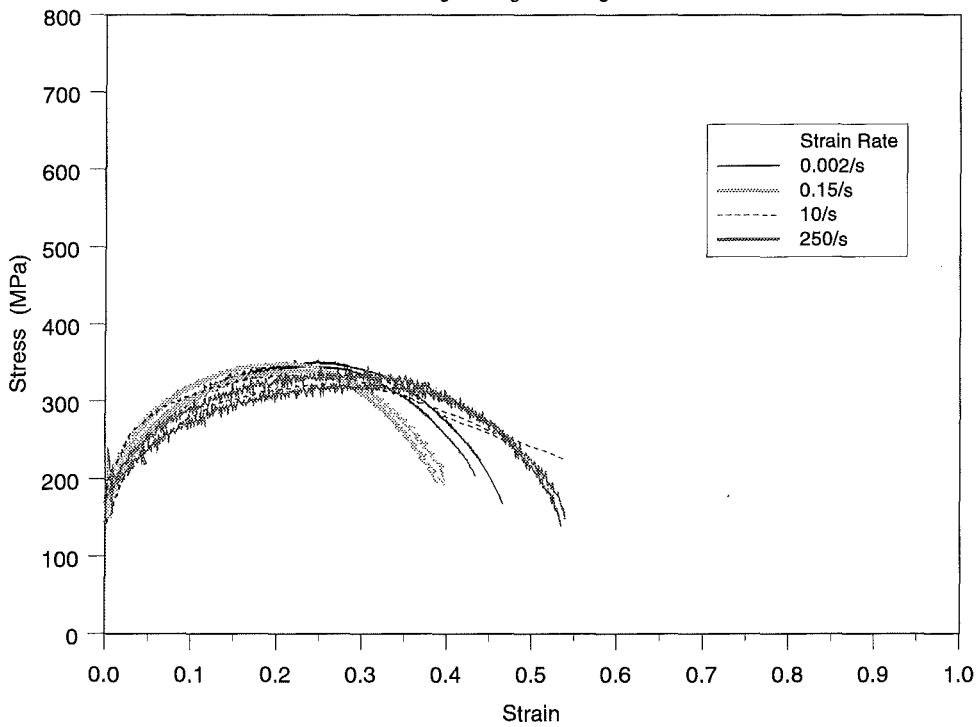


Fig. 5-16

Austenitic steel X6CrNiNb1810, diameter $\varnothing=30\text{mm}$, R.T.

Engineering σ - ϵ diagrams

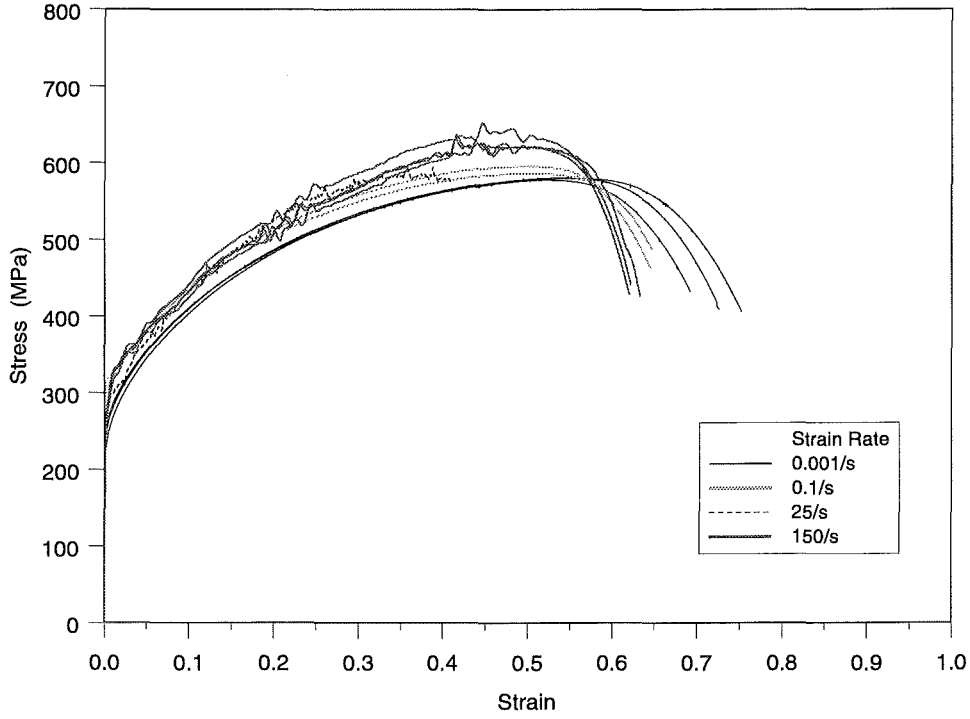


Fig. 5-17

Austenitic steel X6CrNiNb1810, diameter $\varnothing=3\text{mm}$

Engineering σ - ϵ diagrams

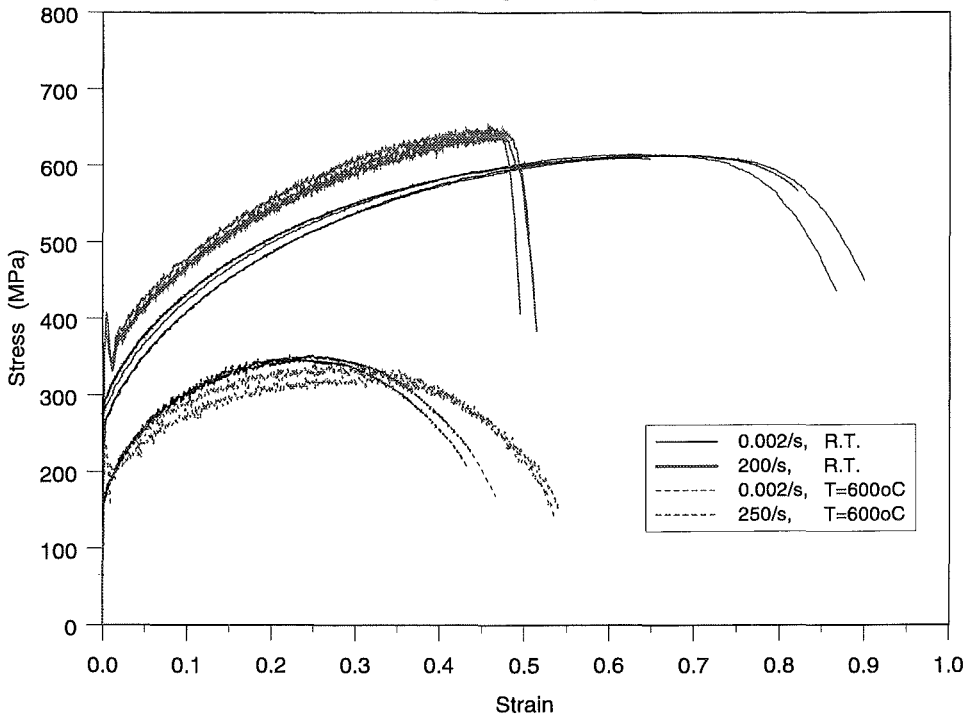


Fig. 5-18

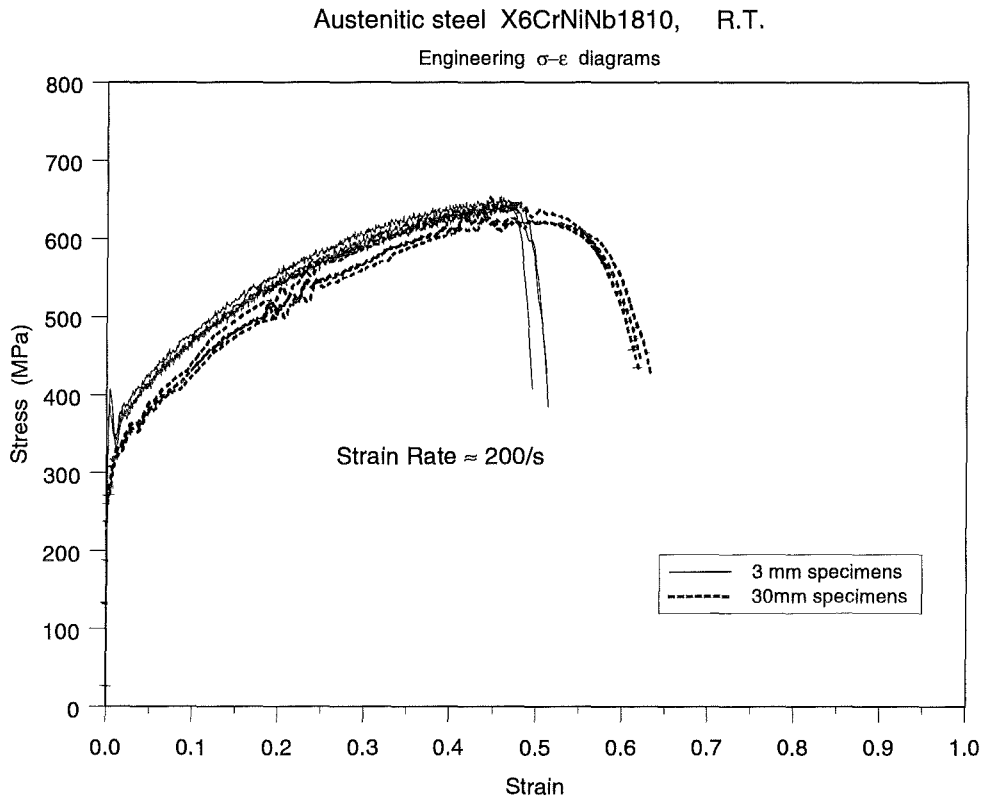


Fig. 5-19

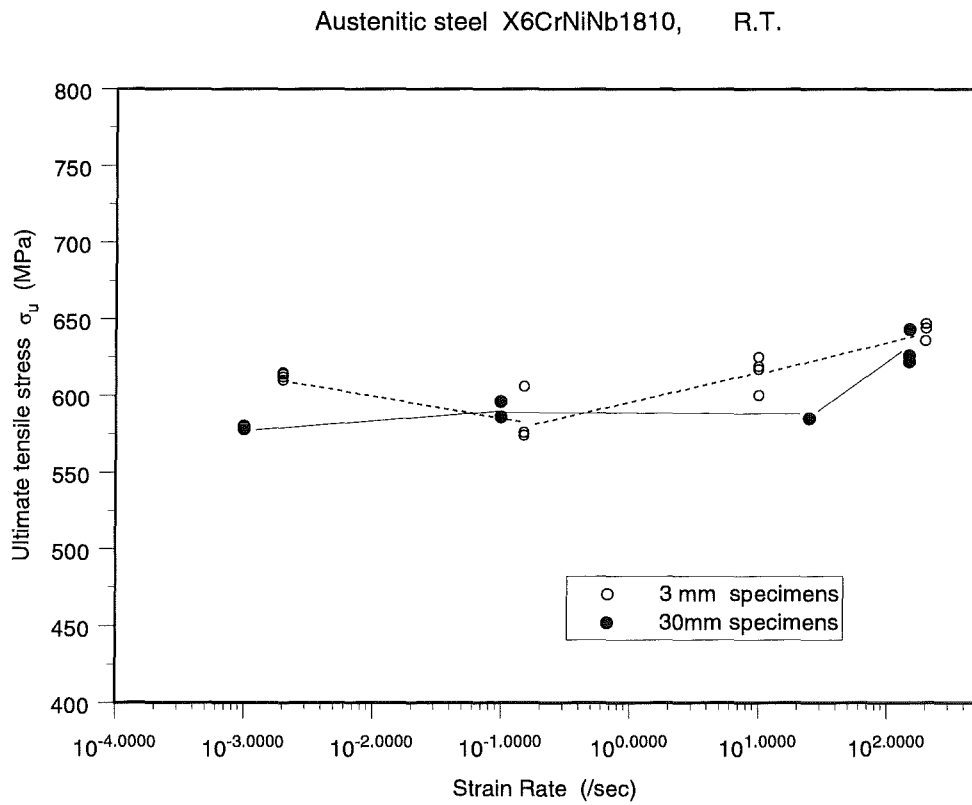


Fig. 5-20

Austenitic steel X6CrNiNb1810, R.T.

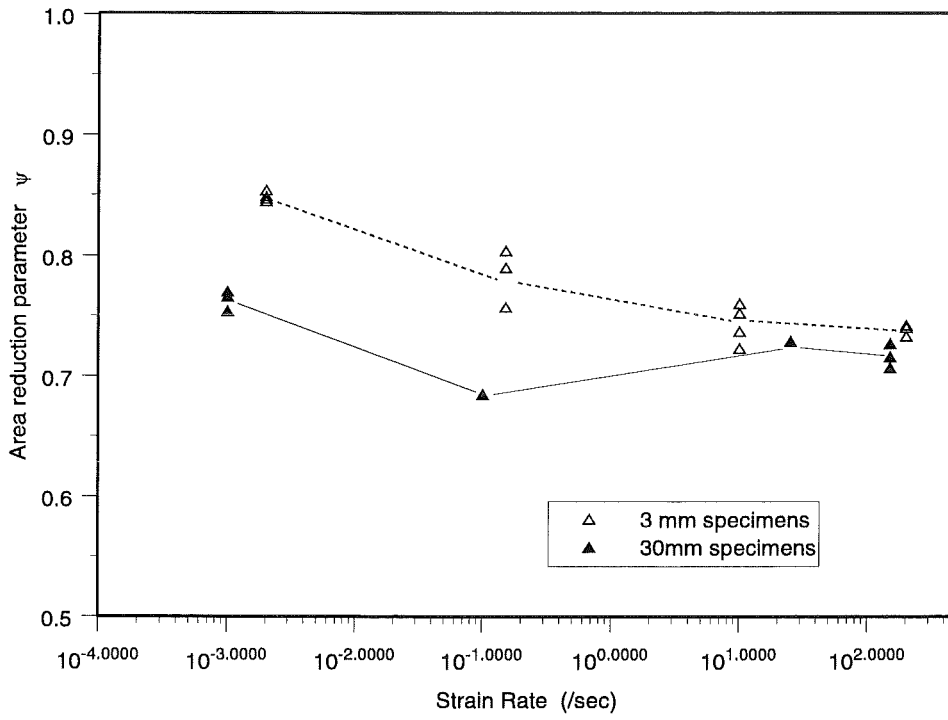


Fig. 5-21

Austenitic steel X6CrNiNb1810, R.T.

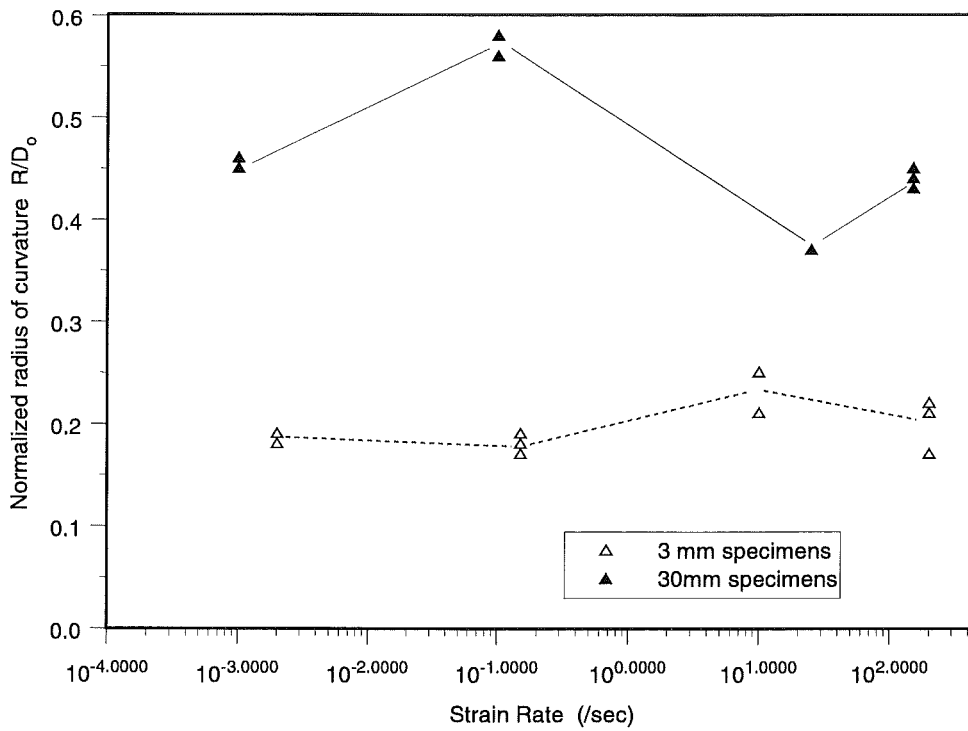


Fig. 5-22

5.2.7 Experimental results - ferritic steel 20MnMoNi55 (1.6310)

This is the vessel head material. The specimens have been constructed from material delivered to the FZK in plates of dimensions 1000x500x70(mm). The chemical composition, as provided by the supplier in the acceptance sheet, is shown in Table 5-7.

Seven of these plates were sent to PSI for the necessary specimen fabrication, and six of them were also used for an extensive material quality assurance verification, Krompholz (1999). This comprised chemical analysis, metallographic investigations, hardness tests, tensile tests and Charpy impact tests. The results indicated an overall good material state with moderate variations over the plates. They also revealed the existence of a noticeable positional influence with regards to the mechanical properties, mainly concentrated along the plates length, but also across their thickness, Krompholz (1999), Probenentnahmeplan (1997).

Table 5-7: Chemical composition of ferritic steel 20MnMoNi55.

C %	Si %	Mn %	P %	S %	Cr %	Ni %	Mo %
0.20	0.28	1.30	0.009	0.002	0.11	0.65	0.47

V %	Al %	N %	Cu %	Co %	Sn %	As %	Ta %
0.005	0.028	0.005	0.03	0.01	0.006	0.008	0.005

Experiments with cylindrical $\varnothing 3$ and $\varnothing 30$ diameter specimens have been performed, according to the pre-established test matrix, at room temperature and at 400°C and at target strain rates: $10^{-3}/s$, $10^{-1}/s$, 10/s, and 200/s. As previously, the produced strain rates have been slightly different. All corresponding stress-strain curves (both engineering and true) have been obtained, and a sub-set of them is used below for generating several graphs for comparison purposes. As before, the Young modulus of these curves has been adjusted to 200GPa for R.T. and to 165GPa for 400°C, respectively.

Characteristic values of tests and specimens have been collected and are reported in Tables 5-8 to 5-10, and a series of full stress-strain curves are also included. The main conclusions from these tests can be summarised below as follows.

Strain rate effects, specimens $\varnothing 3$ at R.T. and at 400°C

Fig. 5-23 shows the complete set of σ - ϵ curves at R.T. As can be seen, there exists a quite distinct strain rate hardening effect. The tensile strength shows a ~15% increase, Fig. 5-24, with increasing strain rate. In the same figure, the yield stress presents an equally substantial increase with strain rate, especially for the 200/s straining.

As noticed also in Fig. 5-23, for the 200/s strain rate a pronounced instability (upper and lower yield points) appears. This time the phenomenon is by far stronger than the austenitic steel's, and starts manifesting itself even at the quasi-static case.

The $\sigma_{1\%}$ and $\sigma_{5\%}$ stresses exhibit a small increasing tendency with strain rate, Table 5-8, which becomes more evident at 200/s.

The uniform strain shows a small variation with strain rate, while the fracture strain decreases with increasing strain rates. This effect is, however, concentrated in the quasi-static to medium strain rate region.

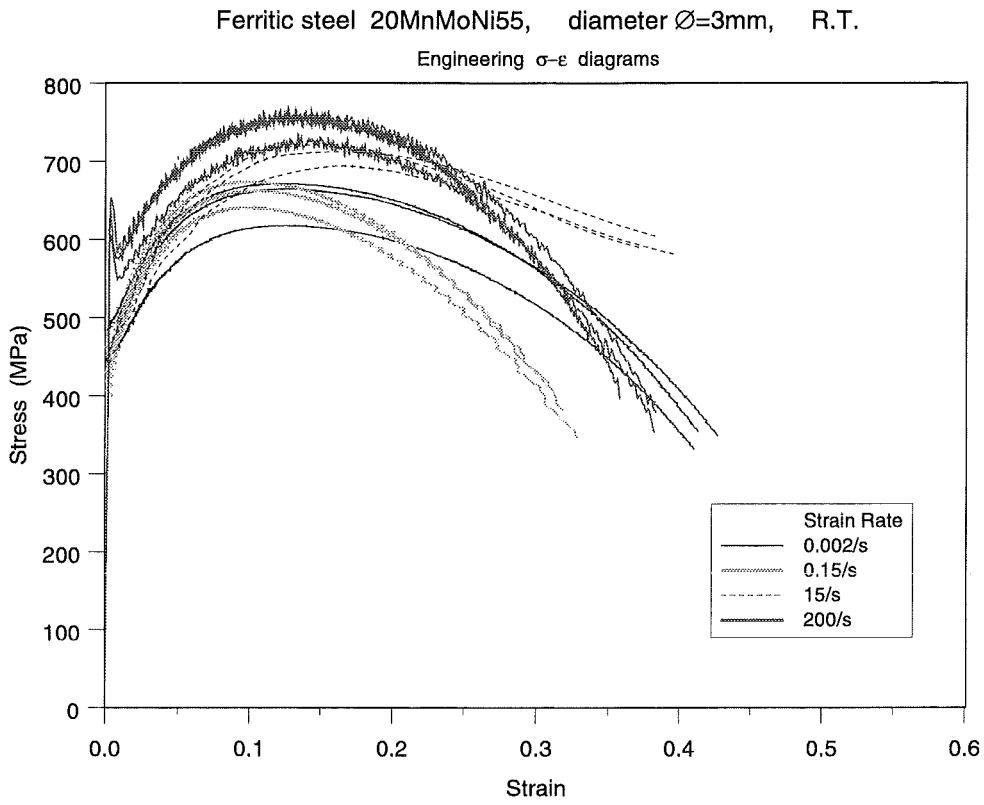


Fig. 5-23

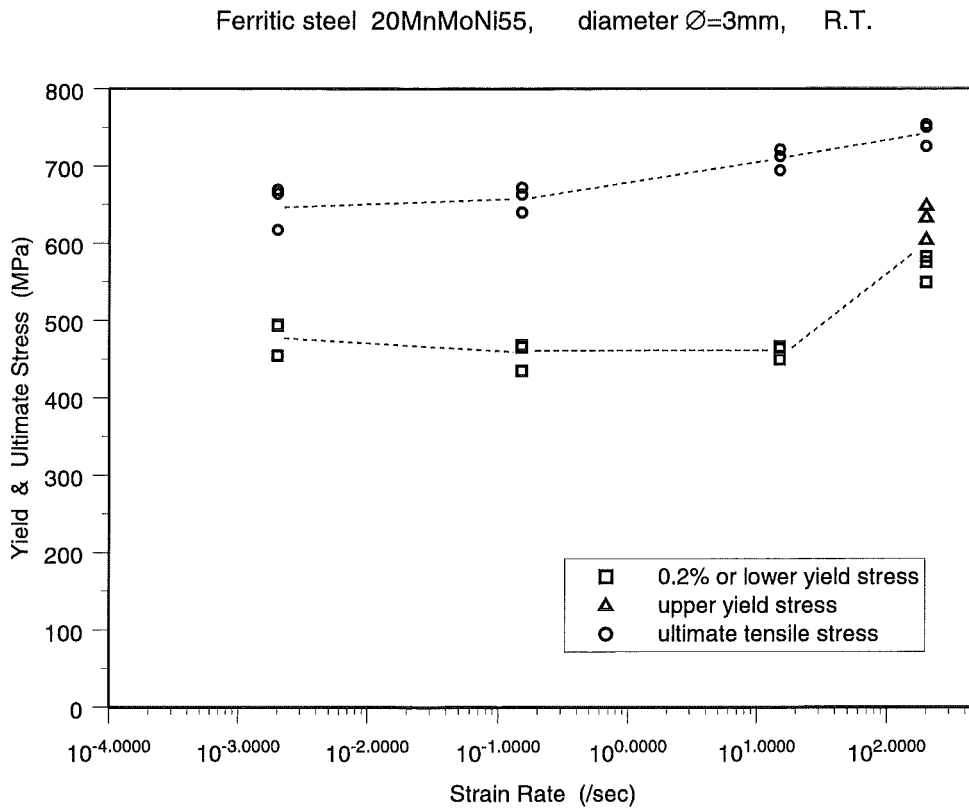


Fig. 5-24

Table 5-8: Test characteristic values of $\varnothing 3\text{mm}$ specimens of ferritic steel 20MnMoNi55 at R.T. and at several strain rates.

Strain rate	$\sigma_{0.2}$													
Specimen	$\sigma_{\text{upp}}/\sigma_{\text{low}}$	$\sigma_{1\%}$	$\sigma_{5\%}$	σ_u	ϵ_u	σ_f	ϵ_f	$\sigma_{T,\text{max}}/\epsilon_{T,\text{max}}$	W_u	W_f	$W_f - W_u / W_f$	W_u / W_f	ψ	R/D_o
	MPa	MPa	MPa	MPa		MPa		MPa /	MPa	MPa			%	
0.002/s														
h1012	494	522	626	669	0.13	353	0.41	1796/ 1.51	77.9	241.2	0.68	0.32	77.8	0.19
h1013	493	509	622	664	0.13	348	0.43	1844/ 1.53	76.3	245.5	0.69	0.31	78.3	0.20
h1017	454	475	575	617	0.13	332	0.41	1811/ 1.58	73.1	220.5	0.67	0.33	79.4	0.19
0.15/s														
h1009	468	509	644	672	0.10	408	0.31	1482/ 1.29	62.7	182.5	0.66	0.34	72.6	0.17
h1011	435	495	629	663	0.11	382	0.32	1498/ 1.36	63.2	183.6	0.66	0.34	74.3	0.17
h1032	465	499	612	640	0.10	345	0.33	1518/ 1.46	57.9	180.6	0.68	0.32	76.8	0.16
15/s														
h1018	466	490	625	712	0.16	603	0.38	2612/ 1.40	104.1	252.1	0.59	0.41	75.3	0.17
h1019	463	502	636	721	0.15	587	0.37	2600/ 1.40	97.9	245.0	0.60	0.40	75.5	0.19
h1023	449	473	594	694	0.17	580	0.39	2485/ 1.36	102.4	251.7	0.59	0.41	74.3	0.20
200/s														
h1002	648/ 582	601	693	750	0.15	380	0.38	1605/ 1.31	103.3	251.0	0.59	0.41	73.1	0.26
h1003	604/ 549	556	661	725	0.15	352	0.38	1347/ 1.25	100.0	239.2	0.58	0.42	71.3	0.21
h1004	633/ 575	585	694	753	0.14	396	0.36	1408/ 1.19	94.1	236.5	0.60	0.40	69.7	0.22

The area reduction parameter ψ is slightly decreasing with strain rate, and the normalized radius of curvature R/D_o remains almost constant with an upwards tendency towards the 200/s. The work parameter W_u/W_f shows a continuous but small increase with strain rate.

Fig. 5-25 shows the complete set of σ - ϵ curves at $T=400^\circ\text{C}$. As previously noticed for higher temperatures, strain rate effects appear to be of a strain rate softening type. As shown in Table 5-9, the tensile strength undergoes a substantial ($\sim 10\%$) decrease, and so does also the yield stress in a non-monotonic manner. The uniform and fracture strains remain almost invariant, and it seems that the material does not lose much of its ductility at dynamic straining. It is also noted that for the 200/s strain rate the yield point instability is present even at $T=400^\circ\text{C}$.

As seen from Table 5-9, at T=400°C both the area reduction parameter and the normalized radius of curvature remain practically invariant over all strain rates. Similarly, the behaviour of the work parameter W_u/W_f presents a small upwards trend.

Table 5-9: Test characteristic values of Ø3mm specimens of ferritic steel 20MnMoNi55 at T=400°C and at several strain rates.

Strain rate Specimen	$\sigma_{0.2}$ $\sigma_{upp}/\sigma_{low}$	$\sigma_{1\%}$	$\sigma_{5\%}$	σ_u	ϵ_u	σ_f	ϵ_f	$\sigma_{T,max}/\epsilon_{T,max}$	W_u	W_f	$W_f - W_u / W_f$	W_u / W_f	ψ %	R/D _o
	MPa	MPa	MPa	MPa		MPa		MPa /	MPa	MPa				
0.002/s														
h1014	426	474	568	627	0.12	306	0.34	1650/ 1.62	68.6	178.0	0.61	0.39	80.1	0.19
h1015	417	464	547	561	0.09	225	0.37	1400/ 1.72	44.7	169.6	0.74	0.26	82.1	0.20
h1016	422	467	556	579	0.10	234	0.42	1550/ 1.76	55.8	201.3	0.72	0.28	82.8	0.18
0.15/s														
h1024	426	479	567	582	0.09	278	0.33	1390/ 1.58	46.1	160.1	0.71	0.29	79.5	0.16
h1033	422	472	560	575	0.10	332	0.32	1265/ 1.32	51.3	159.4	0.68	0.32	73.2	0.18
h1037	440	499	588	600	0.09	336	0.29	1410/ 1.41	46.8	151.6	0.69	0.31	75.6	0.20
15/s														
h1020	402	416	513	544	0.11	459	0.27	1300/ 1.00	55.7	135.9	0.59	0.41	63.3	0.29
h1021	312	382	501	535	0.11	412	0.33	1920/ 1.50	53.1	157.8	0.66	0.34	77.6	0.18
h1022	307	349	475	546	0.15	463	0.37	2410/ 1.59	73.2	185.9	0.61	0.39	79.6	0.16
250/s														
h1006	429/ 379	397	481	507	0.11	270	0.35	1470/ 1.59	49.9	156.5	0.68	0.32	79.6	0.22
h1007	449/ 371	408	489	518	0.12	245	0.32	1230/ 1.56	56.2	144.5	0.61	0.39	79.0	0.19
h1008	385/ 362	392	464	488	0.13	221	0.37	1240/ 1.62	57.0	155.5	0.63	0.37	80.2	0.21

Strain rate effects, specimens Ø30 at R.T.

Fig. 5-26 shows all σ - ϵ curves at R.T for all strain rates. Some new phenomena seem to influence the behaviour this time. Specifically, there is a strain rate hardening effect together with a trend of the strains to increase with strain rate. As seen in Table 5-10, both the yield stress and ultimate stress exhibit an appreciable increase with increasing strain rate. The $\sigma_{1\%}$ and $\sigma_{5\%}$ stresses show only some small increase. However, the uniform and fracture strains

tend clearly to increase with higher strain rates, too; this implies more ductility at higher deformation velocities.

The area reduction parameter ψ exhibits almost no variations with strain rate. The normalized radius of curvature R/D_0 values exhibit a very clear, almost 40%, reduction with increasing strain rates. The work parameter W_u/W_f remains almost constant with strain rate. However, as previously noted, the number of data points is rather poor.

Table 5-10: Test characteristic values of $\varnothing 30$ mm specimens of ferritic steel 20MnMoNi55 at R.T. and at several strain rates.

Strain rate Specimen	$\sigma_{0.2}$ $\sigma_{upp}/\sigma_{low}$	$\sigma_{1\%}$	$\sigma_{5\%}$	σ_u	ϵ_u	σ_f	ϵ_f	$\sigma_{T,max}/\epsilon_{T,max}$	W_u	W_f	$W_f - W_u / W_f$	W_u / W_f	ψ %	R/D_0
	MPa	MPa	MPa	MPa		MPa		MPa /	MPa	MPa				
0.001/s														
h3018	417	447	561	602	0.12	380	0.35	1594/ 1.25	63.9	183.3	0.65	0.35	71.4	0.52
h3027	402	449	574	609	0.11	401	0.30	1411/ 1.11	58.1	162.8	0.64	0.36	67.1	0.54
h3030	416	450	567	599	0.11	395	0.30	1442/ 1.15	57.4	159.7	0.64	0.36	68.4	0.52
h3005*	-	-	-	580	-	-	-	-	-	-	-	-	73.1	0.32
0.1/s														
h3019	473	484	584	633	0.13	420	0.34	1678/ 1.22	78.9	194.5	0.59	0.41	70.5	0.42
h3031	487	486	577	625	0.13	409	0.35	1635/ 1.21	81.4	194.7	0.58	0.42	70.1	0.48
25/s														
h3006	576/ 480	500	603	645	0.12	592 ?	0.21 ?	2305? 1.31	72.8	125.1 ?	0.42 ?	0.58 ?	73.0	0.32
150/s														
h3001	519/ 502	517	591	673	0.16	371	0.38	1505/ 1.24	99.1	227.5	0.56	0.44	71.1	0.33
h3002	590/ 497	515	592	659	0.14	336	0.39	1470/ 1.32	84.3	224.6	0.62	0.38	73.3	0.30
h3003	531/ 497	513	594	681	0.16	369	0.38	1575/ 1.30	98.6	228.8	0.57	0.43	72.8	0.31
h3004	573/ 486	507	587	660	0.14	335	0.38	1470/ 1.33	85.3	218.1	0.61	0.39	73.5	0.31

* Pulling up to maximum load was at 0.001/s strain rate, but necking and fracture occurred in a dynamic manner.

Ferritic steel 20MnMoNi55, diameter $\varnothing=3\text{mm}$, $T=400^\circ\text{C}$
Engineering σ - ϵ diagrams

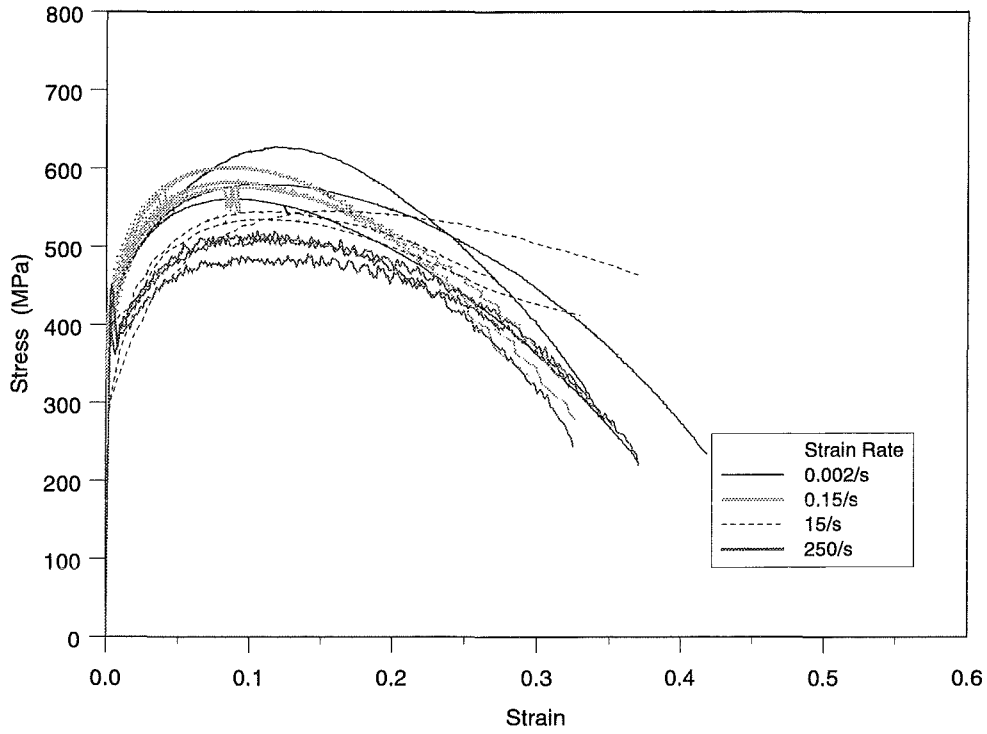


Fig. 5-25

Ferritic steel 20MnMoNi55, diameter $\varnothing=30\text{mm}$, R.T.
Engineering σ - ϵ diagrams

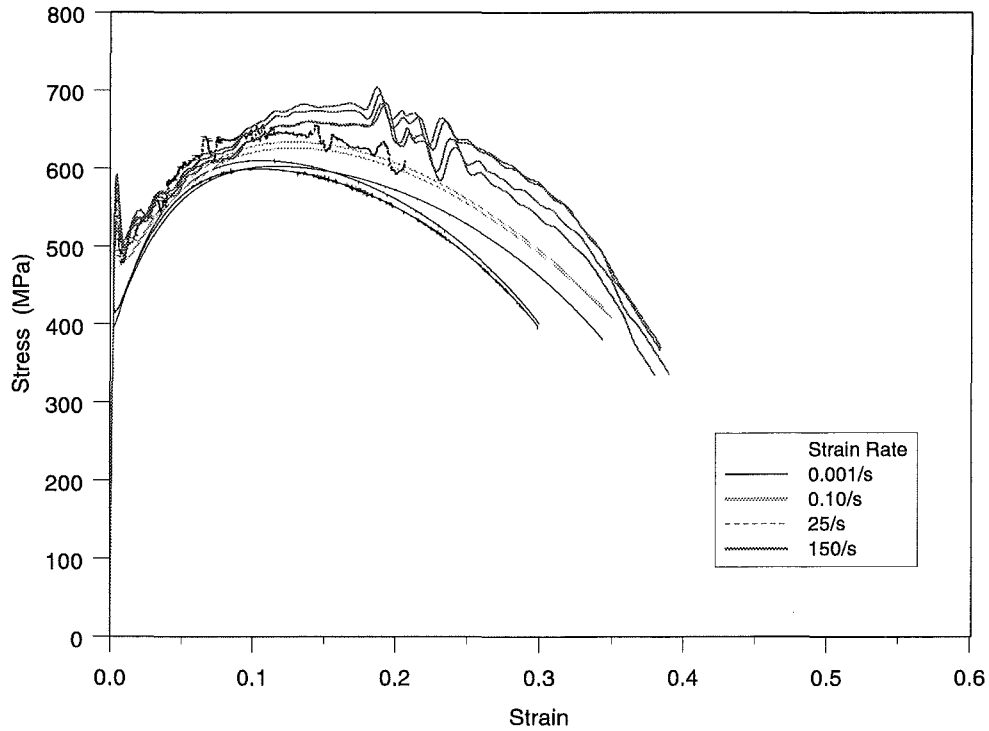


Fig. 5-26

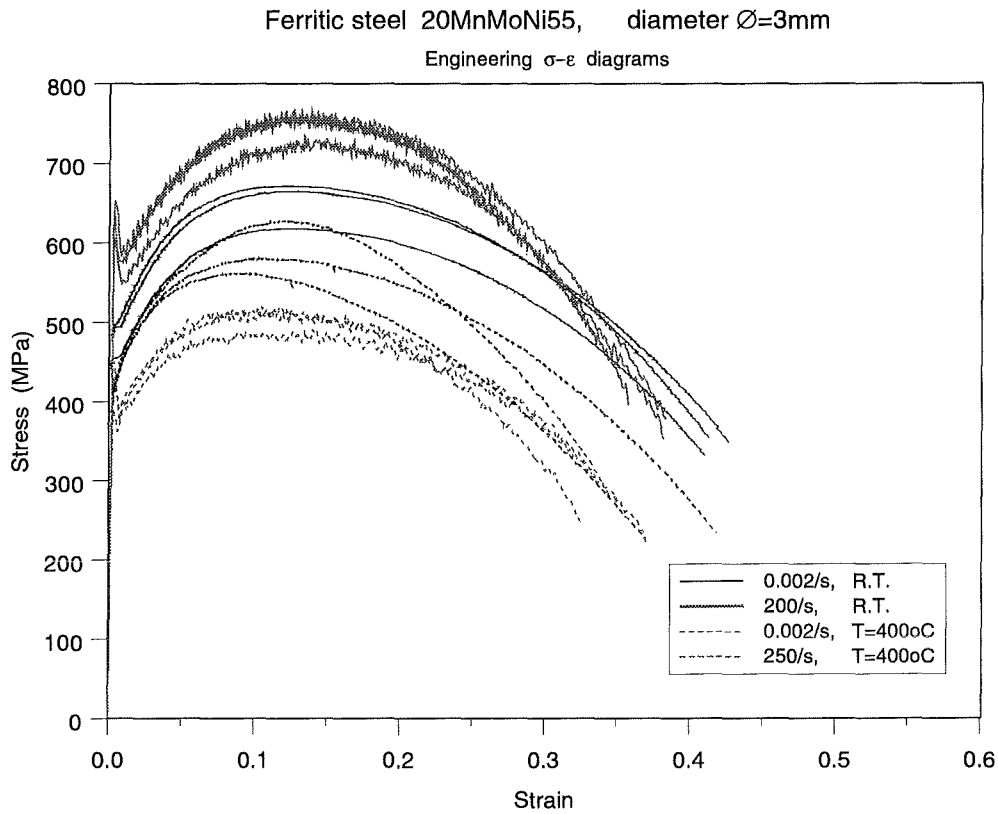


Fig. 5-27

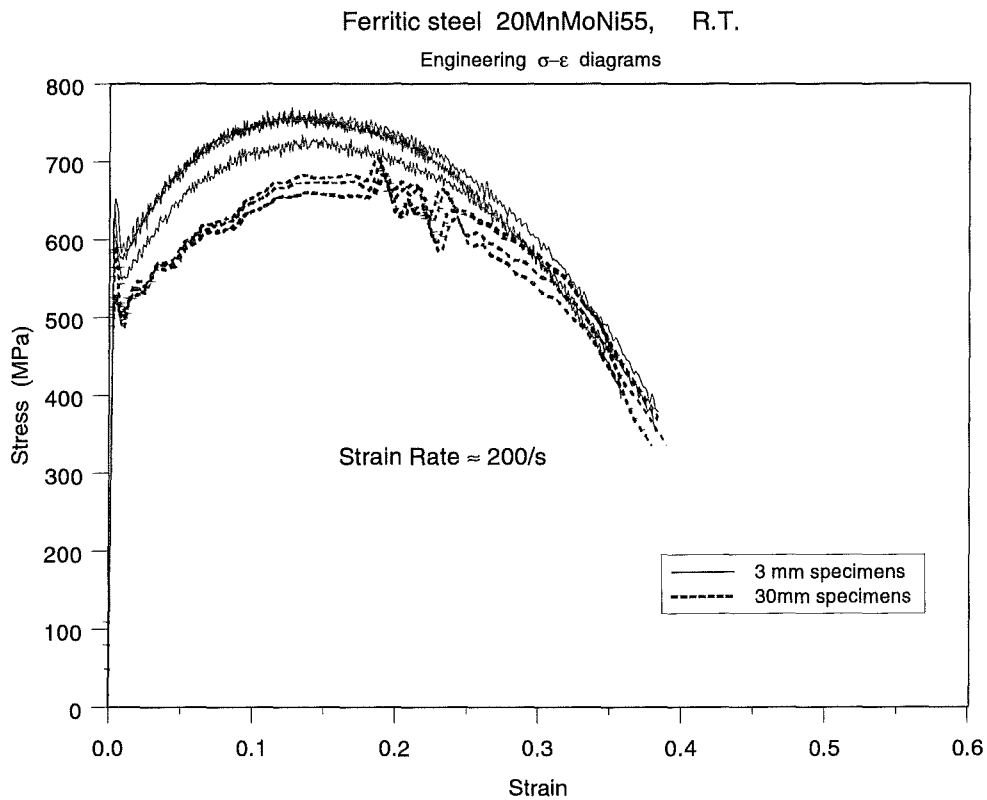


Fig. 5-28

Temperature effects (for Ø3mm specimens)

At T=400°C a substantial reduction of the mechanical resistance is observed with respect to R.T. conditions for all strain rate regimes. Fracture strains, however, are not considerably affected. Fig. 5-27 shows this behaviour for the quasi-static and dynamic case.

The Tables values show the decreasing tendency (strain softening) of the ultimate stress at T=400°C with increasing strain rate and its impressive contrast with the corresponding curve at R.T. (strain hardening). The $\sigma_{1\%}$ values at T=400°C and R.T. demonstrate this strain rate softening and hardening phenomenon, respectively. The area reduction parameter ψ does not undergo any appreciable changes for these two test temperatures, except at 200/s.

Due to the strain hardening effects at R.T. and the softening effects at T=400°C, it is evident that the big differences are manifested at the higher strain rates. To illustrate this situation some average values are quoted: tensile strength at 0.001/s is 589MPa (down by ~10% from 650MPa at R.T.); tensile strength at 200/s is 504MPa (down by ~32% from 743MPa at R.T.).

Size effects (at R.T.)

Fig. 5-28 shows corresponding σ - ϵ curves of the Ø3mm and the Ø30mm specimens at three strain rate regime 200/s. Some differences in the behaviour of the two specimen sizes are noticed. In general, stress values of Ø3 specimens tend to be greater than those of Ø30. Ductility does seem to be considerably affected.

To quantify better the several effects, individual parameters are examined separately over the entire strain rate range. The yield stress exhibits substantial differences at the two extremes of the strain rate range with the Ø3 values being higher there. At mid-range the values intermingle and a weak opposite trend is present (Ø30 values are higher). Like the yield stress, $\sigma_{1\%}$ and $\sigma_{5\%}$ exhibit also differences at the two extremes of the strain rate range with the Ø3 values being higher there.

As mentioned above, the ultimate stress, Fig. 5-29, shows clearly a net size effect with the Ø3 values being by at least 10% higher than the corresponding Ø30 values for all strain rates. No difference in the behaviour of the two specimen sizes is indicated with respect to the uniform strain.

As for the austenitic steel, very distinct is the behaviour of the two specimens as regards the area reduction and the normalised radius of curvature parameters, Fig. 5-30 and Fig. 5-31, respectively. For ψ the curve of Ø3 is always higher than that of Ø30 specimens, and only at 200/s strain rate they come together. Worth noticing is also the fact that the first curve is decreasing with strain rate, whereas the latter is monotonically increasing. For the normalised radius of curvature the Ø3 specimens curve lies always well below the Ø30 curve over all strain rates. This time the Ø30 curve is monotonically decreasing with strain rate, whereas the Ø3 curve shows a slight increase. With respect to the work parameter, no differences are observed for the two specimen sizes.

Ferritic steel 20MnMoNi55, R.T.

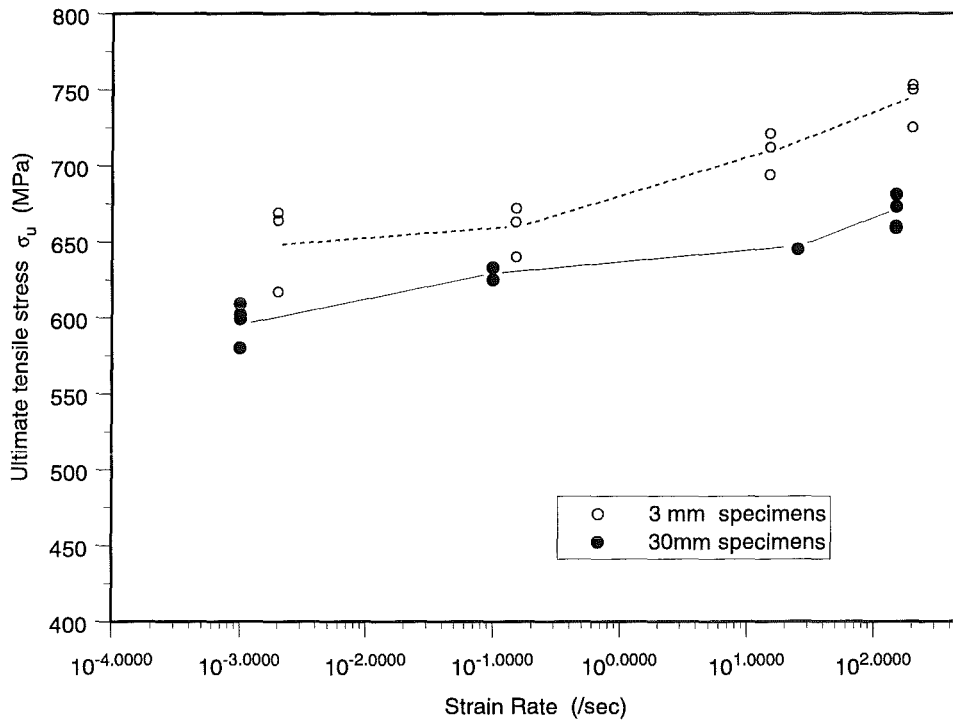


Fig. 5-29

Ferritic steel 20MnMoNi55, R.T.

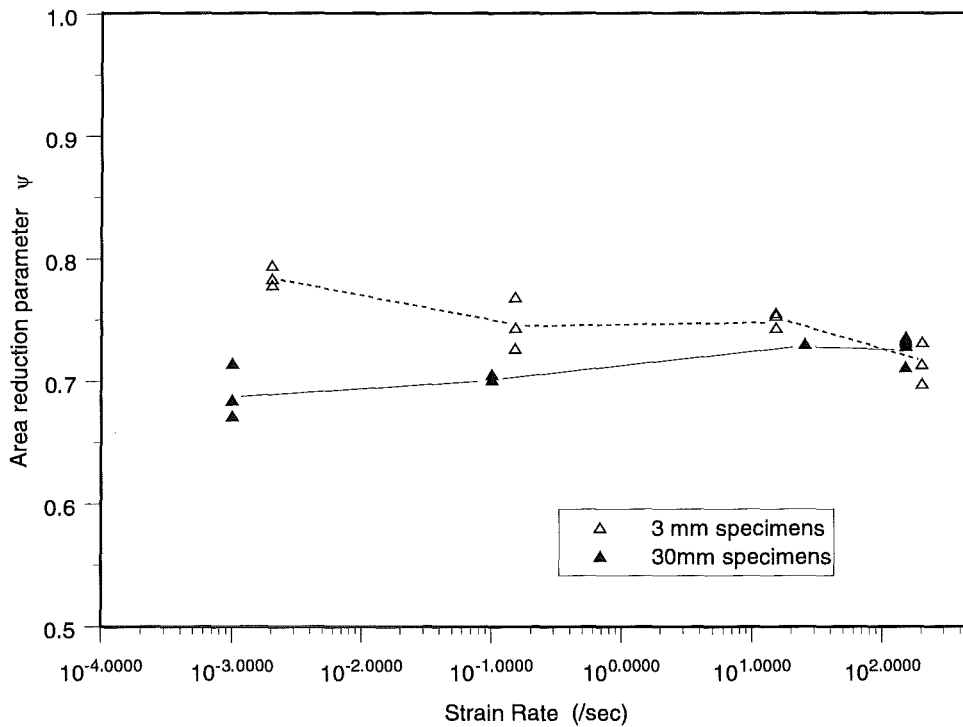


Fig. 5-30

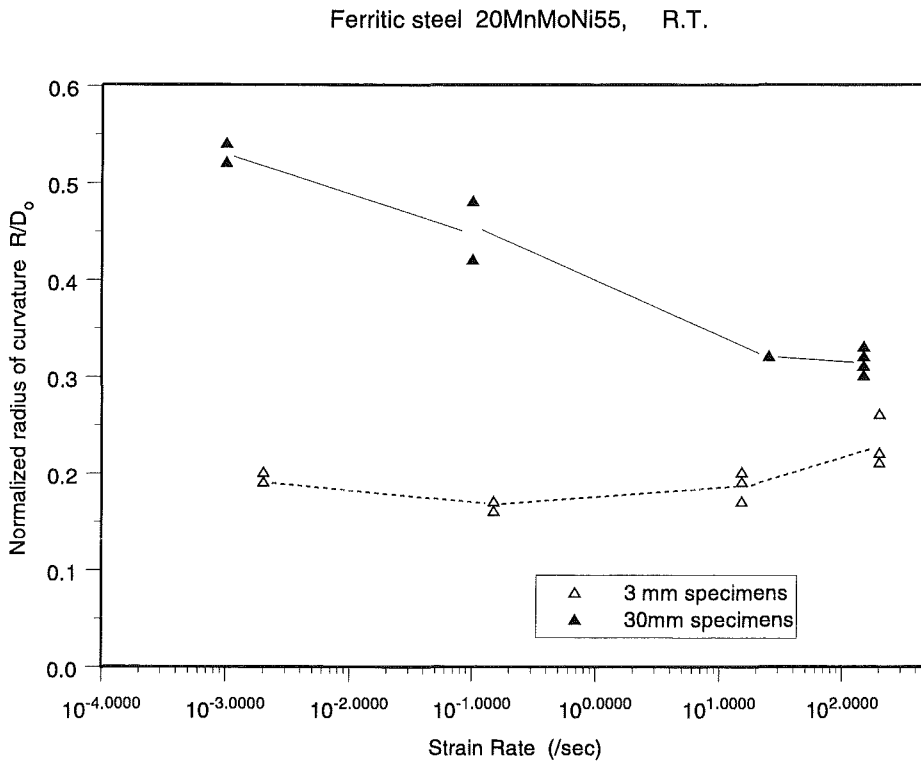


Fig. 5-31

5.2.8 Experimental results - ferritic steel 26NiCrMo146 (1.6958)

This is the material of the bolts used for fixing the vessel head onto the top of the cylindrical reactor vessel. Specimens have been constructed by the JRC from two different heats of material furnished by FZK. Heat 1 includes 15 unused bolts (of the BERDA experiment), and heat 2 a half-cylinder of 340mm diameter and 180mm height. Some specimens have been constructed from both heats, so as to investigate any material production variation effects. Specimens with a two-numeral identification come from heat 1 (e.g. b52), and specimens with a one-numeral identification from heat 2 (e.g. b3).

No supplier's certificate has been provided, but the typical chemical composition of this material is as shown in Table 5-11, *Stahlschlüssel* (1995). Further, no quality assurance tests have been carried out.

Table 5-11: Chemical composition of bolt ferritic steel 26NiCrMo146.

C	Si	Mn	P	S	Cr	Mo	Ni	V	Al
%	%	%	≤ %	≤ %	%	%	%	%	%
0.25-0.30	0.15-0.30	0.30-0.50	0.020	0.010	1.20-1.70	0.35-0.50	3.40-3.80	≤ 0.12	0.020-0.050

Experiments have been conducted, according to the pre-established test matrix, only at room temperature with Ø3mm specimens and at target strain rates: 10⁻³/s, 10⁻¹/s, 10/s, and 200/s, as indicated in Table 5-2. All corresponding stress-strain curves (both engineering and true) have been obtained. It is noted that the Young modulus of these curves has been adjusted to 200GPa.

Characteristic values of the experiments have been collected and presented in Table 5-12. Naturally, since only a single size specimen at R.T. has been tested, the following discussion focuses exclusively on strain rate effects.

Fig. 5-32 shows the complete set of engineering σ - ϵ curves obtained. It can be seen that some strain rate hardening effects are present, which are exposed in more detail in the next figure. The tensile strength shows a constant increase ($\sim 10\%$) with increasing strain rate, Fig. 5-33. The behaviour of the yield stress is less consistent but it shows overall a small increase, too. No yielding instability for the dynamic strain rate appears.

As shown in Table 5-12, the stress $\sigma_{5\%}$ exhibits a constant increasing tendency with strain rate. The stress $\sigma_{1\%}$, however, does not show such a nice behaviour. As more delicate, it is possible that both the $\sigma_{0.2}$ and the $\sigma_{1\%}$ are affected by errors at their determination during the construction of the σ - ϵ diagram.

The uniform strain remains almost invariant with strain rate, while the fracture strain decreases constantly with more accentuation at the dynamic regime.

It is to be noted that for all strain rate regimes the material has a high elastic limit and yield point (over 1000MPa), which lie close to the tensile strength (average 1200MPa). Further, it exhibits a quite short plastic deformation (fracture strain not exceeding 0.25).

As the Table 5-12 values demonstrate, both the area reduction and normalised radius of curvature parameters remain almost invariant over all strain rates. Finally, it is seen that the work parameter W_u/W_f shows a substantial increase, especially towards the higher strain rates.

Table 5-12: Test characteristic values of Ø3mm specimens of bolt ferritic steel 26NiCrMo146 at R.T. and at several strain rates.

Strain rate Specimen	$\sigma_{0.2}$ $\sigma_{\text{upp}}/\sigma_{\text{low}}$	$\sigma_{1\%}$	$\sigma_{5\%}$	σ_u	ϵ_u	σ_f	ϵ_f	$\sigma_{T,\text{max}}/\epsilon_{T,\text{max}}$	W_u	W_f	$W_f - W_u / W_f$	W_u / W_f	ψ %	R/D _o
	MPa	MPa	MPa	MPa		MPa		MPa /	MPa	MPa				
0.001/s														
b3	1121	1167	1204	1209	0.046	775	0.24	1974/ 0.93	50.5	247.4	0.80	0.20	60.7	0.28
b4	1131	1172	1218	1216	0.048	752	0.24	2075/ 0.97	53.7	255.0	0.79	0.21	62.2	0.35
b51	1014	1052	1102	1105	0.052	650	0.29	2235/ 1.19	53.4	276.0	0.81	0.19	69.8	0.23
0.10/s														
b42	1125	1154	1181	1189	0.045	935	0.25	2771/ 1.11	48.8	262.9	0.81	0.19	66.9	0.22
b52	1112	1149	1175	1190	0.042	952	0.25	2665/ 1.10	45.1	232.5	0.81	0.19	66.8	0.19
b82	1118	1156	1181	1195	0.042	972	0.25	2685/ 1.09	45.3	208.2	0.78	0.22	66.3	0.21
10/s														
b31	1017	1092	1169	1179	0.095	1131	0.25	3448/ 1.11	108.0	276.6	0.61	0.39	67.1	0.25
b32	1045	1083	1177	1185	0.082	1132	0.26	3550/ 1.13	90.7	293.3	0.69	0.31	67.7	0.25
b41	1087	1120	1215	1224	0.086	1180	0.25	3263/ 1.01	98.8	287.1	0.66	0.34	63.6	0.27
150/s														
b1	1144	1208	1249	1253	0.051	770	0.13	1700/ 0.84	57.7	152.2	0.62	0.38	56.9	0.32
b12	1145	1176	1230	1237	0.051	672	0.21	2100/ 1.15	57.8	214.8	0.73	0.27	68.5	0.27
b2	1160	1236	1287	1290	0.052	730	0.22	1940/ 0.98	62.3	239.7	0.74	0.26	62.5	0.30
b21	1176	1205	1249	1250	0.052	983	0.15	2670/ 1.07	59.4	175.5	0.66	0.34	65.5	0.27

Bolts ferritic steel 26NiCrMo146, diameter $\varnothing=3\text{mm}$, R.T.
Engineering σ - ϵ diagrams

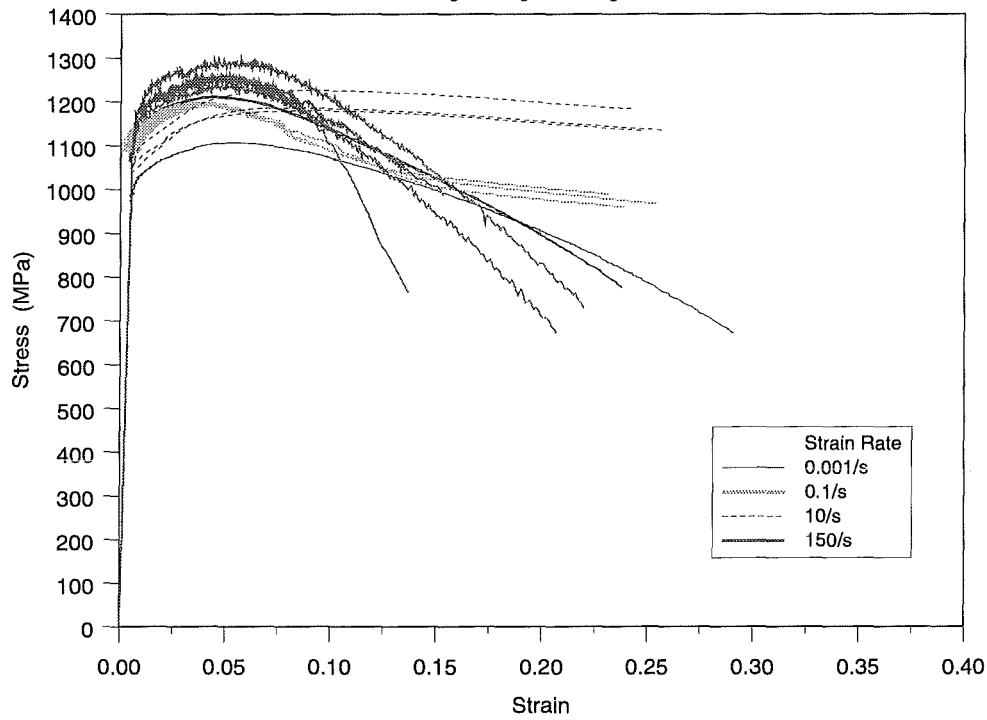


Fig. 5-32

Bolts ferritic steel 26NiCrMo146, diameter $\varnothing=3\text{mm}$, R.T.

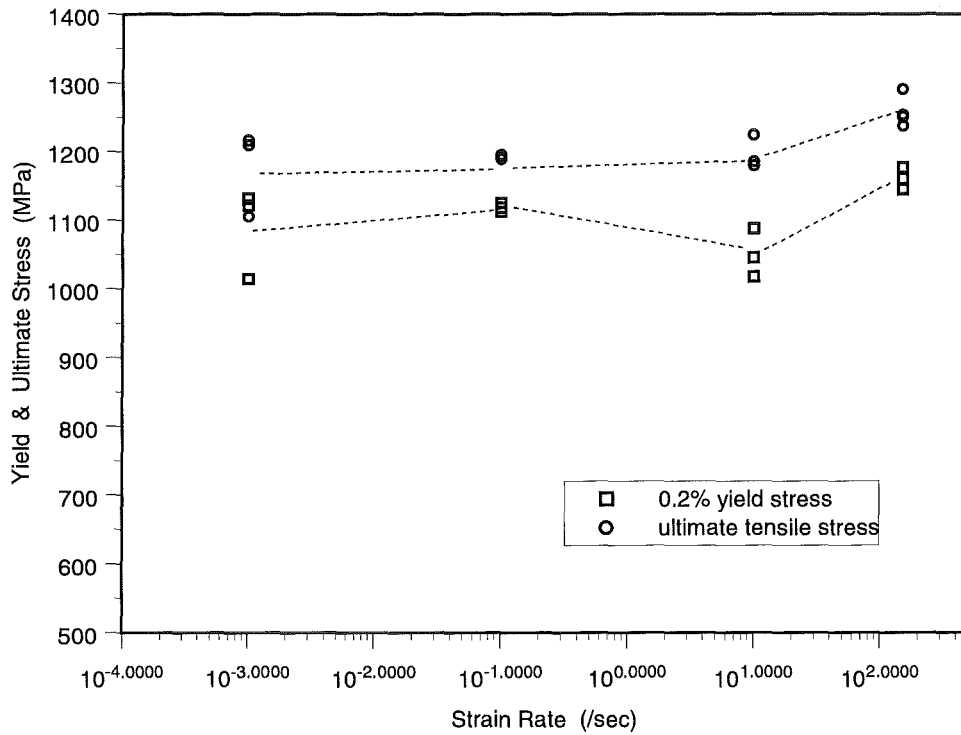


Fig. 5-33

5.2.9 Experimental results – bronze G-CuSn 12

The material (DIN 1705, previously G-SnBz12) has been used for the fabrication of some of the model grid plates for the simulation of the Upper Internal Structure (UIS) in the BERDA experiment. No precise information has been provided, but the typical chemical composition of this alloy is as shown in Table 5-13.

Table 5-13: Chemical composition of bronze G-Cu Sn 12.

Cu	Sn	Ni*	P*	Sb*	Fe*	Pb*	S*	Zn*
85.5-87.5 %	11.0-13.0 %	2.0 %	0.4 %	0.2 %	0.2 %	1.0 %	0.6 %	0.5 %

* permissible additions

Cylindrical Ø3 mm specimens have been constructed by the JRC and twenty tension experiments have been performed, according to the pre-established test matrix, at room temperature and at target strain rates: $10^{-3}/s$, $10^{-1}/s$, $10/s$, and $200/s$. The corresponding stress-strain curves have been obtained, adjusting the Young modulus to 110GPa. Based on them, the behaviour of several parameters have been studied. Fig. 5-34 shows the yield stress and tensile strength of this bronze versus strain rate. The main conclusions of this exercise can be summarised as follows:

No persistent tendencies or strain rate effects appear; the tensile strength (identified as the maximum stress in the engineering stress-strain curve) does not vary noticeably with strain rate; fracture strain values show some small strain rate effect.

The yield stress presents a constant increase with strain rate, which anyway is small in the range of main interest ($10^{-3}/s$ to $200/s$);

Difficulties and reduced reproducibility have been encountered with this testing (attributed to material inhomogeneity and anisotropy due to a relatively large grain size).

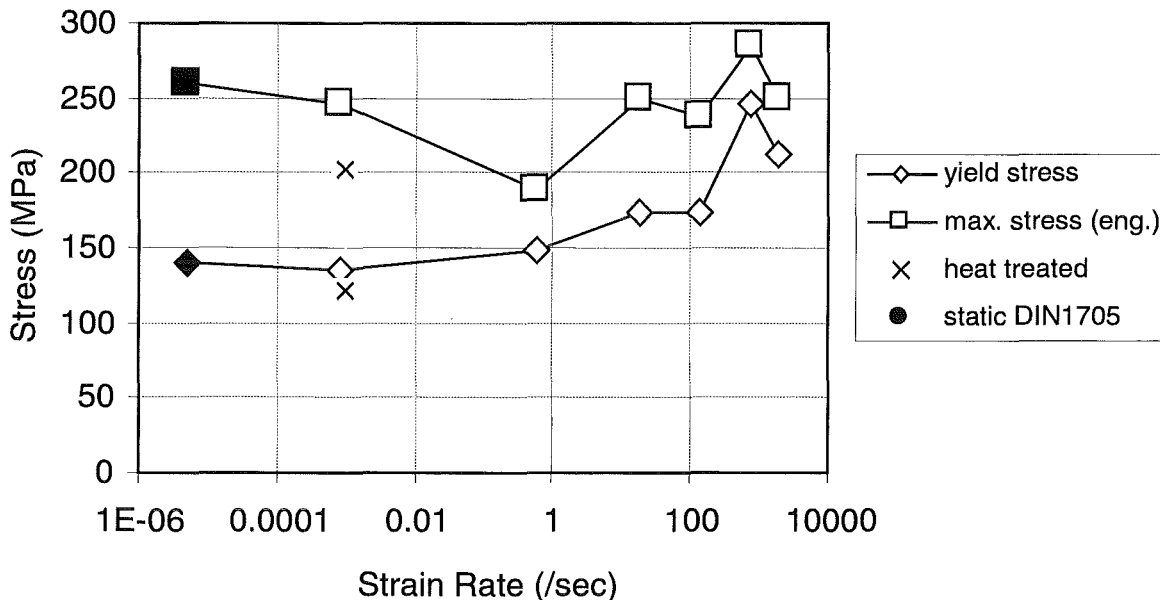


Fig. 5-34

5.2.10 Essential results and conclusions

The results amply demonstrate the degrading influence of temperature; mechanical strengths at 400°C-600°C are reduced by as much as 50% with respect to R.T. conditions. Also shown characteristically is the effect of strain rate, of varying degree for each material. It has been observed that at R.T. the strain rate effect is definitely of a hardening type (strength increase with strain rate by as much as 20%). However, at T=600°C and T=400°C for the X6CrNiNb1810 and 20MnMoNi55 steels, respectively, it is rather of a softening nature and is accompanied by ductility reduction. This strain softening behaviour should probably be attributed to the adiabatic conditions of loading, which become even more accentuated at elevated temperatures, thus rendering the thermal softening dominant, Zener (1994), Dodd (1997).

Size effect tendencies have also been noticed, as revealed by the appearance and comparison of the stress-strain curves of the Ø3 and Ø30mm specimens, and the behaviour of other corresponding parameters derived for these two specimen sizes. Strength resistance of small specimens tends to be greater than that of the big specimens by approximately 10%. More convincing size effects evidence seems to constitute the behaviour of the area reduction parameter and of the normalized radius of curvature, both of which are local quantities associated with fracture. This fact points to the direction that more local quantities may have to be sought and measured, Hsu (1964).

Confirmation of these results would require some further work both experimental and in the analysis of the available data. The situation is particularly sensitive when it comes to the size effects. Specifically, before the above trends can be declared as true size effects, all possible error sources must have been eliminated. In the specific case, from the quality assurance of the original steel plates it is already known that there exist positional influences, which could potentially be masked as size effects and also alter the quantification of the temperature and strain rate effects. This important issue has not been explicitly raised in the present discussion, but an effective analysis in associating mechanical specimen properties and specimen position in the original plate has been undertaken by Malmberg (1999). Finally, some testing with intermediate specimen sizes is considered necessary for filling in gaps of data indispensable for a better interpretation of the observed trends.

Acknowledgement

The RPVSA project was co-financed by the European Commission under the European Nuclear Fission Safety Program 1994 – 1998, contract FI4S-CT95-0002.

During the three years working period of the project the particular research steps were discussed among the partners in semi-annual project meetings and in many additional contacts in-between. If necessary, the program was adapted to changing boundary conditions after consultation with the representatives of the European Commission.

The partners and the coordinator of the RPVSA project appreciated the fruitful cooperation with Dr. A. Zurita, the representative of the European Commission for this project.

References

References to section 1.1

- CAROLI C., Natural convection in homogeneous and stratified hemispherical pools in presence of a volumetric heat source, Report INV-RPVSA(97)-D001, 1997
- CAROLI C., MAGNAUD J.P., Thermal loads on the RPV lower head in case of severe accident with core melt relocation, SMiRT 14, Lyon, France, 1997, paper PW/1
- CAROLI C., MILILLO F., Coupled thermal-hydraulic analyses of the molten pool and pressure vessel during a severe accident, OECD/CSNI Workshop on In-Vessel Core Debris Retention and Coolability, Garching, Germany, March 3-5,1998
- CAROLI C., MILILLO F., Influence of the corium configuration on the lower head thermal behaviour in case of severe accident in a PWR, ENEA, Italy, Report IT-SBE-00008
- EL-GENK M.S., GUO Z., Saturated pool boiling from downward-facing and inclined flat surfaces, Pool and External Flow Boiling, ASME, 1992
- EL-GENK M.S., GAO C., Pool boiling from copper and stainless-steel downward-facing curved surfaces, 2nd European Thermal-Sciences and 14th UIT National Heat Transfer Conference, Rome, Italy, May 29-31,1996
- MILILLO F., CAROLI C., Analysis of accidental scenarios in a PWR with relocation of the molten corium in the lower head of the pressure vessel, 6th ICONE Conference, San Diego, USA, May 10-15, 1998
- THEOFANOUS T.G., SYRI S., The coolability limits of reactor pressure vessel lower head, Proceeding of NURETH-7, Saratoga Springs, USA, September 10-15, 1995
- NOURGALIEV, R.R., DINK, T.N., SEHGAL, B.R., Effect of Fluid Prandtl Number of Heat Characteristics in Internally Heated Liquid Pools with Rayleigh Numbers up to 10^{12} , J. Nucl. Eng. Des. 169 (1997), 165-184
- CAROLI C., MILIOZZI A. and MILILLO F., Thermal-Mechanical Behaviour of the Reactor Pressure Vessel and Corium Molten Pool in a Severe Accident with Core Melt Down, SMiRT 15, Korea 1999, paper P02/2

References to section 1.2 – 1.5

- BHANDARI S., RPVSA Interpretation Benchmark based on RUPATHER Creep Test #4 at 700°C, Framatome, France (1997)
- BHANDARI S., RPVSA Interpretation Benchmark based on FASTHER Test, Framatome, France (1998)
- CARSLAW H. S. and JAEGER J. C., Conduction of Heat in Solids, Oxford University Press, 1959
- CHAMPAIN E. and SAINTE CATHERINE C., Comparison of Results for the RPVSA Interpretation Benchmark on RUPATHER Creep Test at 700°C, CEA Saclay, Report SEMT/LISN/RT/98-024/A, (1998)
- COTONI V. and SAINTE CATHERINE C., Results of the Blind Benchmark based on Rupther Creep Test at 1000°C in the Frame of RPVSA, CEA Saclay, Report DMT/97-217, (1997)
- COTONI V. and SAINTE CATHERINE C., Results of the RPVSA Interpretation Benchmark based on RUPATHER Creep Test #4 at 700 °C, CEA Saclay, France, Report DMT/97-522, (1997)
- COTONI V. and SAINTE CATHERINE C., Comparison of Results of the RPVSA Blind Benchmark based on RUPATHER Creep Test at 1000 °C, CEA Saclay, France, Report DMT/97-286, (1997)

- DEVOS J. , MONGABURE P., SAINTE CATHERINE C. and STRUB C., RUPATHER: A Programme devoted to Modelling the Failure Process of the RPV Lower Head, PVP Conference, Montreal, Canada, July, 1996
- DEVOS J., SAINTE CATHERINE C., POETTE C. and BURLET H., CEA programme to model the failure of the lower head in severe accidents, Nucl. Eng. Des. 191 (1999), 3-15
- DUIJVESTIJN G., Results of the RPVSA/RUPATHER Benchmark No.2, PSI, Switzerland (1997)
- DUPAS P., RPVSA Interpretation Benchmark based on RUPATHER Creep Test #4 at 700 °C, EDF, France, Mail 22/01/98, (1998)
- JENDRICH U. et al., Reactor Pressure Vessel, CEC Final Report on Severe Accidents, 3rd Framework Program, FI3S-CT92-0002, (1996)
- LÄMMER H., RITTER B. and TSAKMAKIS C. , FZK's contribution for the 2nd RPVSA Benchmark, Forschungszentrum Karlsruhe, RPVSA Technical Report INV-RPVSA(97)-D027, (1998)
- LÄMMER H. and TSAKMAKIS C. , FZK's contribution to the 3rd RPVSA Benchmark based on FASTHER Test, Forschungszentrum Karlsruhe, RPVSA Technical Report INV-RPVSA(98)-D036, (1998)
- MILIOZZI A., RPVSA Interpretation Benchmark based on RUPATHER Creep Test at 700 °C, ENEA, Italy, Report CT-SBE-00007, (1997)
- MILIOZZI A., RPVSA Interpretation Benchmark based on Test, ENEA, Italy, Report CT-SBE-00019, (1998)
- MONGABURE P., DESMET M. and MOULIN G., RUPATHER: Essai 4, Rupture en fluage à 700 °C, CEA Saclay, France, Rapport DMT/96-432, (1996)
- MONGABURE P., GOMAS C., DESMET M. and MOULIN G., RUPATHER #9 : Creep Test at 1000 °C and 6.5 bars, CEA Saclay, France, Rapport DMT/97-345 (1997)
- MONGABURE P. and DESMET M., FASTHER: Rupture test under strong thermal gradient and displacement ramp, CEA Saclay, Report SEMT/LISN/RT/98-076/A, (1998)
- NICOLAS L., RPVSA Interpretation Benchmark based on RUPATHER Creep Test #4 at 700 °C, CEA Saclay, France, Report DMT/97-611, (1997)
- OECD-NEA-TMI-2, TMI-2 Vessel Investigation Project, Appendix A, Rapport OECD-NEA, TMI V(93)EG01, (1993)
- SAINTE CATHERINE C., Tensile Tests Characterisation of Pressure Vessel Steel at High Temperatures (20 up to 950°C), CEA Saclay, France, Report DMT/95-236, (1995)
- SAINTE CATHERINE C. and COTONI V., Specification of the RPVSA Interpretation Benchmark based on RUPATHER Creep Test at 700°C, CEA Saclay, Report DMT/97-349, (1997)
- SAINTE CATHERINE C. and COTONI V., Specification of the RPVSA Interpretation Benchmark based on RUPATHER Creep test at 700 °C, CEA Saclay, France, Report DMT/97-349, (1997)
- SAINTE CATHERINE C. and CHAMPAIN E., Specification of the RPVSA Interpretation Benchmark based on FASTHER Test, CEA Saclay, France, Report SEMT/LISN/98-033/A, (1998)
- SAINTE CATHERINE C., RPVSA Interpretation Benchmark based on FASTHER Test, CEA Saclay, France, Report SEMT/LISN/98-065/A, (1998)
- SAINTE CATHERINE C., MONGABURE Ph., LE BER, L., DEVOS J. and BHANDARI S., FASTHER: Failure under Strong Thermal Gradient of RPV Steel, SMiRT 15, Korea 1999, paper P03/1

References to section 2

- BROSI, S. et al, CORVIS. Investigation of Light Water Reactor Lower Head Failure Modes, Nucl. Eng. Des. 168 (1997), 77-104
- DUIJVESTIJN, G., BIRCHLEY, J., Core Melt down and Vessel Failure: A Coupled Problem, Nucl. Eng. Des. 191 (1999), 17-30
- HIRSCHMANN (editor), H., CORVIS: State of Progress - December 1996 (CORVIS Report No 7), (1997)
- REMPE, J.L. et al, Light Water Reactor Lower Head Failure Analysis, NUREG/CR-5642, EGG-2618 (1993)

References to section 3

- AMARASOORIYA, W.H. and THEOFANOUS, T.G., An Assessment of Steam-Explosion-Induced Containment Failure. Part III: Expansion and Energy Partition, Nucl Sci Engn 97 (1987) 296-315
- JACOBS, H., Analytical correlations for Rayleigh-Taylor instability growth, Nucl Tech 71 (1985) 131-144
- KRIEG, R., GÖLLER, B. and HAILFINGER, G., Transient Three-Dimensional Potential Flow Problems and Dynamic Response of the Surrounding Structures, Part I and II, Comput. Phys. 8 2 (1980) 139

References to section 4

- BUNG, H., GALON, P., LEPAREUX, M., COMBESURE, A., A method for the treatment of impact and penetration problems, SMiRT 12, Stuttgart, Germany 1993, Paper B02/1
- DOLENSKY, B., GÖLLER, B., HIRT, A., KRIEG, R., Theoretical models describing the impact loading of a PWR vessel head, Int. Conf. on Advanced Reactors Safety ARS'97, Orlando, Florida (1997)
- DOLENSKY, B., GÖLLER, B., Calculations to interpret the BERDA tests 05, 06, 07 and 09 without upper internal structures, Forschungszentrum Karlsruhe, Internal Report, 1998
- HIRT, A., Rechenmodell zum Aufprall von Kernschmelze auf die oberen Einbauten und den Deckel eines Reaktordruckbehälters, PhD thesis, Universität Karlsruhe (1997)
- DOLENSKY, B., GÖLLER, B., Mechanical Behavior of the Reactor Pressure Vessel Head under Prescribed Static and Dynamic Pressure Loadings, Forschungszentrum Karlsruhe, Internal Report, 1998
- HOFFMANN, G., et al, Essential Results of Model Experiments BERDA I, Forschungszentrum Karlsruhe, Internal Reports on the tests 01 through 11, 1997
- KORNELSON, I., MESSEMER, G., VORBERG, G., Essential Results of Model Experiments BERDA I, Forschungszentrum Karlsruhe, Internal Reports on the tests 12 through 17, 1998 and 1999
- KRIEG, R., MALMBERG, T., MESSEMER, G., STACH, T., STRATMANN, E., Slug Impact Loading on the Vessel Head during a Postulated In-vessel Steam Explosion in Pressurized Water Reactors - Assessments and Discussion of the Investigation Strategy, Nucl. Technol., 111, 369 (1995)
- KRIEG, R., MALMBERG, T., MESSEMER, G., STACH, T., STRATMANN, E., Model Experiments BERDA Describing the Impact of Molten Core Material against a PWR Vessel Head, Int. Conf. on Advanced Reactor Safety ARS'97, Orlando, Florida (1997)
- KRIEG, R., GÖLLER, B., HAILFINGER, G., MESSEMER, G., VORBERG, G., Reactor Pressure Vessel Head Loaded by a Corium Slug - Results of Model Experiments BERDA I, SMiRT 15, Seoul, Korea 1999, paper P02/6
- LETELLIER, A., Contribution à la Modélisation des Impact d'Oiseaux sur les tubes des Réacteurs d'Avions, Thèse de doctorat de l'Université d'Evry, 1996

- LUCAS, G.E., AMARASOORIYA, W.H., THEOFANOUS, T.G., An Assessment of Steam-Explosion-Induced Containment Failure, Part IV: Impact Mechanics, Dissipation, and Vessel Head Failure, Nucl. Sci. Eng., 97, 316 (1987)
- STACH, T., MALMBERG, T., KRIEG, R., Scaled Experiments for a Simple Deformable Structure under Liquid Slug Impact, SMiRT 14, Lyon, France 1997, paper P02/1
- STRUB, C., AUTRUSSON, B., GÖLLER, B. KRIEG, R., Analysis of slug impact against the reactor pressure vessel head. Interpretation of BERDA test 07 with the finite element code PLEXUS, Int. Conf. PVP, Vol. 362, pp. 19-26, San Diego, July 1998

References to section 5

- ALBERTINI, C. and MONTAGNANI, M., Dynamic material properties of several steels for fast breeder reactor safety analysis, EUR 5787 EN, Ispra, 1977
- ALBERTINI, C., BOONE, P.M. and MONTAGNANI, M., Development of the Hopkinson bar for testing large specimens in tension, Journal de Physique, Colloque C5, suppl. au n°8, Tome 46, 1985
- BRIDGMAN, P.W., Studies in large plastic flow and fracture, McGraw-Hill, 1952
- DODD, B., BAI, Y., Ductile fracture and ductility, Academic Press 1987
- ENNIS, P.J., ZIELINSKA-LIPIEC, A., WACHTER, O., CZYRSKA-FILEMONOWICZ, A., Micro-structural Stability and Creep Rupture Strength of the Martensitic Steel P92 for Advanced Power Plant, Acta Materialia, 445, 12, 49-1-4907 (1997)
- HSU, T.C., LITTLEJOHN, G.S., and MARCHBANK, B.M., Elongation in the tension test as a measure of ductility, Proc. Am. Soc. Testing Mats., 65, 874-898 (1964)
- KANEKO, F., MALMBERG, T., Theoretische Analyse eines Ersatzlängenkonzepts für Zugproben nicht-konstanten Querschnitts, Kernforschungszentrum Karlsruhe, KFK-Ext. 8/77-2 (1977)
- KROMPHOLZ, K., Quality assurance of the Austenitic steel X6CrNiNb1810, PSI report TM-49-98-07
- KROMPHOLZ, K., KAMBER, J., KALKHOF, D., Quality assurance for the Ferritic material 20MnMoNi55, PSI, 1999
- LINDHOLM, U.S., High strain rate tests, in Techniques of Metals Research, Vol. V, Part 1, R.F. Bunsmah editor, J. Wiley & Sons, 1971
- MALMBERG, T., Aspects of similitude theory in Solid Mechanics, Part I: Deformation Behavior, Forschungszentrum Karlsruhe, FZKA 5657, Dec. 1995
- MALMBERG, T., KROMPHOLZ, K., SOLOMOS, G., AIFANTIS, E.C., Investigation on size effects in ferritic and austenitic materials, SMiRT 15, Korea 1999, paper L06/5
- MIKLOWITZ, J., The influence of the Dimensional Factors on the Mode of Yielding and Fracture in Medium-Carbon Steel -I, The Geometry and Size of the Flat Tensile Bar, J. Applied Mechanics, Trans. ASME, 70, 274-287 (1948)
- MIKLOWITZ, J., Influence of the Dimensional Factors on Mode of Yielding and Fracture in Medium-Carbon Steel -II, The Size of the Round Tensile Bar, J. Applied Mechanics, 159-168 (1950)
- MOORE, H.F., Tension tests of steel with test specimens of various size and form, Proc. ASTM, 18 part I, 403-421, 1918
- NICHOLAS, T., Tensile Testing of Materials at High Rates of Strain, Experimental Mechanics, 177-185, 1981
- PROBENENTNAHMEPLAN, Werkstoff: 20MnMoNi55; EU-Project F14S-CT96-0024
- REVISIA, PSI report 1997
- RICHARDS, C.W., Effect of size on the yielding of mild steel beams, Proc. Am. Soc. Testing Mater., 58, 955-970 (1958)

- SOLOMOS, G. et al., Tensile properties of bronze G-CuSn12 at higher strain rates, Tech. Note I.98.77, JRC Ispra, May 1998
- SOLOMOS, G., ALBERTINI, C., and LABIBES, K., Experimental Investigation of Strain Rate, Temperature and Size Effects in Nuclear Steels; Part I: smooth cylindrical specimens, Tech. Note, I.99., JRC Ispra, June 1999
- STAHLSCHLÜSSEL, Verlag Stahlschlüssel Wegst GmbH, 1995
- STAINLESS STEELS; quality specifications, DIN 17 440, 1972
- WOOD, D.S., DUWEZ, P.E. and CLARK, D.S., The influence of specimen dimensions and shape on the results of tensile impact tests, Armor and Ordnance report No. A-237 (OSRD No. 3028), 1943
- ZENER, C, HOLLOMON, J.H., Effect of strain rate upon the plastic flow of steel, J. Appl. Phys., 15, 22-32 (1944)